Evidence for the Josephson Effect in Quantum Hall Bilayers

Thesis by

Ian Bairstow Spielman

In Partial Fulfillment of the Requirements
for the Degree of
Doctor of Philosophy

California Institute of Technology
Pasadena, California

2004
(Defended May 10, 2004)

ACKNOWLEDGEMENTS

This thesis is a product of the training, guidance, and overall direction provided by Jim “Idea Factory” Eisenstein. There is part of a graduate education that many advisers neglect, but Jim, to whom I am truly indebted, did not: communication.

This work would truly never had existed without our collaborators Loren Pfeiffer and Ken West. It is their mastery of the science and art of sample growth that ultimately enables this research.

Working in a physics laboratory is never an individual endeavor; the day-to-day interaction with a whole cast of characters was vital to my evolution through graduate school. Thanks to: Mike, for showing that a really good person can succeed in physics; Peter, for “breaking me in” to the Eisenstein lab and showing me the ropes; Ken, for his uncommonly good common (physics) sense; Mindy, for listing to my ceaseless litany of (frequently foolish) ideas; and Tony, for asking all the hard questions and making me reassess my own understanding. Of course, the final product would not have been half as readable as it is without the unwitting proof reading (disguised as “training”) from Lisa, Xerxes, and Laura.

Part of life is lived outside of a physics lab, and I would like to share my most sincere appreciation for my Karate instructor Randy McClure for giving me a (literal) kick in the ass whether I needed it or not.

Foremost thanks, however, go to Jamie, for making every day worthwhile (and for suggesting that I have been in graduate school long enough and might consider actually writing a thesis *now*). To Jamie and baby Camden: thanks for making this the best year of my life.

ABSTRACT

This thesis presents tunneling measurements on bilayer two-dimensional (2D) electrons systems in GaAs/AlGaAs double quantum wells. 2D-2D tunneling is applied here as a probe of the inter-layer correlated quantum Hall state at total Landau level filling factor $\nu_T = 1$. This bilayer state is theoretically expected to be an excitonic superfluid with an associated dissipationless current and Josephson effect.

In addition to the conventional signatures of the quantum Hall effect – a pronounced minimum in R_{xx} and associated quantization of R_{xy} – the strong inter-layer correlations lead to a step-like discontinuity in the tunneling $I - V$. Although reminiscent of the DC Josephson effect, the tunneling discontinuity has a finite extent even at the lowest temperatures (the peak in conductance, dI/dV, is strongly temperature dependent even below 15 mK). The correlations develop when the inter- and intra-layer Coulomb interactions become comparable. The relative importance of which is determined by the ratio of layer separation to average electron spacing. Although this state is theoretically expected to be an excitonic superfluid, the degree to which intra-layer tunneling is Josephson-like is controversial. At a critical layer separation the zero-bias tunneling feature is lost, which we interpret as signaling the quantum phase transition to the uncorrelated state. We study the dependence of the phase transition on electron density and relative density imbalance. In the presence of a parallel magnetic field tunneling probes the response of the spectral function at finite wave vector. These tunneling spectra directly detect the expected linearly dispersing Goldstone mode; our measurement of this mode is in good agreement with theoretical expectations. There remains deep theoretical and experimental interest in this state, which represents a unprecedented convergence in the physics of quantum Hall effects and superconductivity.

CONTENTS

List of Figures

List of Tables

INTRODUCTION

Two-dimensional electron systems (2DES) have proven to be an ideal venue for studying many electron physics. A large perpendicular magnetic field quenches the kinetic and Zeeman energies; in many cases, the dynamics of the resulting system are completely determined by the Coulomb interaction between electrons. In particular, the fractional quantum Hall effect results *essentially* from the importance of Coulomb interactions at high magnetic fields. The addition of a second 2D electron layer parallel to, but a distance d from the first, creates the possibility for completely new, and fundamentally different, quantum Hall states. The bilayer quantum Hall state at total Landau level filling factor $\nu_T = 1$ is the central focus of this thesis.

The importance of Coulomb interactions is magnified in large magnetic fields. Instead of traveling rapidly though the sample at the Fermi velocity, electrons are confined to small cyclotron orbitals. The resulting suppression of the electrons' kinetic energy makes the interactions between neighbors vastly more important. In single-layer systems, the various fractional quantum Hall effects (FQHE) result from quantum states whose physics is entirely due to the subtle dance of $\sim 10^{10}$ strongly interacting electrons.

In the past 25 years the field of 2D electrons has truly come of age, yielding two Nobel prizes: the first one for the discovery of the integer quantum Hall effect (IQHE), and the second for the FQHE. Although all the essential ingredients of the IQHE had been observed before 1980, it was Klaus von Klitzing who made the central observation that when the density of electrons (n) and the magnetic flux (eB/h) are commensurate ($n = \nu eB/h$), the Hall resistance is exactly quantized at an integer fraction of fundamental constants: $R_{xy} = h/\nu e^2$ [1]. The number ν is called the filling fraction. The remarkable feature of the IQHE is that R_{xy} remains quantized at $h/\nu_0 e^2$ over a range of ν centered on integer values of ν_0. The IQHE results from the interplay of Landau quantization of individual electron orbitals and disorder.

Imagine Tsui and Stormer's surprise when, in 1983, they observed a new quantum Hall state at Landau level filling fraction $\nu = 1/3$ [2], 3 times higher in magnetic field than the $\nu = 1$ IQHE[1]. The next year, however, Laughlin correctly explained the $\nu = 1/3$ FQHE in terms of an approximate wavefunction [3] (replete with charge $\pm e/3$ excitations). In 1996 Tsui, Stormer, and Laughlin were awarded the Nobel prize in physics for the discovery and explanation of the FQHE.

These physical effects occur at interfaces between semiconducting (or insulating) materials, at which electrons are confined to 2D sheets. The IQHE was discovered in a silicon transistor, and the FQHE in a higher-quality GaAs device. Since 1983, the quality of GaAs samples has increased dramatically, and patterns have emerged in the distribution in ν of the fractional states. The regular pattern of observed FQHE states led to a new understanding in terms of composite fermions [4]. In this picture $\nu = 1/2$ is a special filling factor, about which FQHE states are symmetrically placed; $\nu = 1/2$ itself is thought to be a Fermi liquid of composite fermions.

These remarkable systems have continued to surprise us with startling new quantum states, such as the recently discovered bubble and stripe phases at high filling factors [5]. Despite the rich physics in a single 2DES, the addition of new degrees of freedom, such as spin or a second 2D layer, can create completely new quantum Hall effects. A large class of multi-component Laughlin-like wavefunctions was proposed by Halperin [6] in 1983 to explain the $\nu = 2/5$ fractional quantum Hall state in a single-layer. Several have been experimentally realized in bilayer systems [7, 8].

The addition of a second layer is superficially similar to a new spin degree of freedom. An electron in one layer can be assigned a pseudospin index $|\uparrow\rangle$, and electrons in the other are assigned $|\downarrow\rangle$. In this language, the electron wavefunction has a spacial part, a real spin part, and a pseudospin part. The crucial difference between spin and pseudospin is that the Coulomb potential between any two electrons is independent

---

[1] Somewhat prophetically, Tsui joked that this was a quantum Hall state composed of charge $e/3$ quarks.

of real spin, but dependent upon layer index and therefore pseudospin. $\nu_T = \nu_1 + \nu_2$ refers to the filling fraction of the system as a whole and is the sum of the individual filling fractions.

Although the $\nu_T = 1$ bilayer state corresponds to $\nu = 1/2$ per-layer, a state at $\nu_T = 1$ is not necessarily surprising. For example, if the bilayer has sufficiently strong inter-layer tunneling then all of the electrons can occupy the symmetric state at $\nu_T = 1$, essentially forming a single component IQHE at $\nu = 1$. In weakly tunneling samples this argument fails, and any QHE at $\nu_T = 1$ must result from nontrivial Coulomb correlations between the layers. The first explicit prediction for a new quantum Hall state was made in 1987 by Chakraborty and Pietilainen [9]. They numerically modeled two parallel $\nu = 1/2$ layers in the absence of tunneling. Their simulations with four electrons per-layer and found evidence for a quantum Hall state.

Stimulated by these numerical results, in 1989 Fertig pointed out several key properties of this bilayer state [10]: first, the ground state of the system can be written as a pseudospin ferromagnet; second, an equivalent description of the ground states is of a excitonic condensate (an exciton is a neutrally charged electron-hole pair); and third, associated with these broken symmetry ground states is a linearly dispersing Goldstone mode. Each of these predictions has been born out by experiment[2]. Shortly thereafter MacDonald and Rezayi predicted that electron-hole bilayers should form an excitonic superfluid when each layer is half filled [11].

The initial experimental work on bilayer electron systems was done by Boebinger *et al.* in 1990 [12]. In these experiments the authors observed that in bilayer systems, the odd integer quantum Hall states systematically disappeared as a function of tunneling strength. This was modeled by MacDonald *et al.*, [13] who described this collapse as a consequence of the interplay between Coulomb interactions and inter-layer tunneling. This model predicted that several states, including that at $\nu_T = 1$, could exist at even when there was no tunneling between layers, and that this state continuously evolves into the strongly-tunneling IQHE of symmetric electrons.

---

[2] Fertig noted that the excitonic condensate was a “good” description of the system. He did not make any predictions regarding superfluid effects such as dissipationless current flow or the Josephson effect.

In a pair of simultaneous publications by Suen *et al.* [7] and Eisenstein *et al.* [8], a new quantum Hall state was discovered in bilayer systems, at $\nu_T = 1/2$. The $\nu_T = 1/4 + 1/4 = 1/2$ state was immediately recognized as significant – no corresponding state has been observed in single component systems. It was later recognized that this detected state was probably the Halperin Ψ_{331} state, which incorporates Laughlin-like correlations between electrons in the same layer, with weaker, but nontrivial correlations between electrons in different layers. Eisenstein *et al.* also noted the appearance of a quantum Hall state at $\nu_T = 1$, was incongruous the earlier observations of Boebinger *et al.* [12]. They argued that the observed state was a new integer state which formed due to Coulomb induced correlations, and not the tunneling gap.

In terms of wavefunctions, the $\nu_T = 1$ QHE state is thought to be well described by the Ψ_{111} wavefunction. Like the Ψ_{331} wavefunction, the Ψ_{111} state includes correlations between layers in addition to those within the individual layers (but unlike the Ψ_{331} state the inter- and intra-layer correlations are of equal importance). In 1992, Wen and Zee observed that the Ψ_{nnn} states have a spontaneously broken degree of freedom associated with charge transfer between layers. In an initial paper, they suggest this versatile state should be an excitonic superfluid [14, 15], and that inter-layer tunneling should have a Josephson singularity. The following year Ezawa and Iwazaki made a similar set of predictions [16].

Unlike conventional "band" excitons where the electron is a finite lifetime excitation from a semiconductors valence band [17], the electrons and holes here have infinite lifetime, making the formation of a excitonic condensate more straightforward. The central focus of this thesis is the experimental detection of these unusual properties via tunneling spectroscopy.

Transport measurements by Murphy *et al.*, in the presence of a parallel magnetic field, $B_{||}$, again found new physics. These measurements showed clear evidence for an unexpected phase transition as a function $B_{||}$ [18]. They found that at small parallel fields the "robustness" of the QHE, as parameterized by the quasiparticle energy gap, Δ, is suppressed rapidly, until at a critical field the suppression becomes much more gradual. To understand the effect of tunneling, Murphy *et al.* studied several samples with different tunneling strengths and layer separations. From these samples they constructed a phase diagram spanning the layer separation - tunneling strength plane and found that, even as the tunneling approached zero, the quantum Hall state persists if the layers are sufficiently close together, i.e., inter- and intra-layer Coulomb interactions are comparable.

The effect of parallel fields was rapidly explained by Yang *et al.* [19], who described the system as a pseudospin ferromagnet. In this language, the transition between two independent $\nu = 1/2$ states and the correlated $\nu_T = 1$ phase corresponds to the development of a finite pseudospin polarization. At small $B_\parallel$, the pseudospin magnetization tends to precess in space with a wavelength proportional to $1/B_\parallel$, this becomes energetically unfavorable as $B_\parallel$ increases, and at a critical $B_\parallel$ there is a transition to a new state where all of the pseudospins once again lie in the same direction.

Although these transport measurements provided evidence that the $\nu_T = 1$ state was in line with theory, no measurement existed to test the more bizarre predictions of Wen and Zee, such as counter-flow superfluidity or inter-layer Josephson tunneling. The following work is the initial 2D-2D tunneling measurements of the $\nu_T = 1$ bilayer state, which clearly indicate a Josephson-like anomaly in the inter-layer tunneling current [20].

This work focuses on six specific measurements:

1. The first measurements, made by Peter Burke and myself, are of the RF conductivity of a 2DES at zero magnetic field [21]. From the RF conductivity data, we extract the plasma modes of the 2DES, which are strongly modified by the presence of a nearby metallic gate.

2. Next we show 2D-2D tunneling data at zero magnetic field. In conjunction with a new sum-rule expression, this data provides a direct measurement of Δ_{SAS} – the splitting between the symmetric and antisymmetric quantum well states.

3. We report our initial measurements on inter-layer tunneling in the $\nu_T = 1$ bilayer quantum Hall state [20]. These data show clear evidence for a Josephson-like feature in the tunneling $I - V$.

4. Next, we investigate the temperature dependence of the $\nu_T = 1$ tunneling feature. The zero-bias conductance is found to be exponential $\sim \exp(-T/T_0)$ in temperature (not activated: $\sim \exp(-T_0/T)$).

5. We measure the dispersion relation of the linearly dispersing Goldstone mode [22] via tunneling spectroscopy. This mode results from the broken symmetry ground state first proposed by Fertig [10].

6. This thesis concludes with an investigation of the effects on tunneling of a relative density imbalance. In this case $\nu_T = \nu_1 + \nu_2 = 1$, but $\nu_1 \neq \nu_2$. We find that a small density imbalance increases the critical layer separation at which the QHE disappears.

These results are divided into several chapters, beginning with introductory material, then continuing to the detection and understanding of the fascinating $\nu_T = 1$ quantum Hall state. The initial chapters serve as introductions to the GaAs/AlGaAs system, relevant experimental methods, and the basic physics of electrons in two-dimensions.

Chapter 1 begins with a discussion of of the GaAs/AlGaAs material system, introducing the technique of molecular beam epitaxy (MBE) through which our samples are grown. These samples are processed via various fabrication techniques yielding structures suitable for resistance, or 2D-2D tunneling measurements. This chapter also introduces the basic band structure of these engineered devices and concludes with the essential concepts of noninteracting 2D fermions both at zero and large perpendicular magnetic fields. Chapter 1 then continues with a description of the basic experimental methods used in our measurements. These measurements are all performed at low-temperature – tens or hundreds of milli-Kelvin – so an overview of the cryogenic apparatus used to obtain milli-kelvin temperatures is included.

Chapter 2 details the 2DES in the context of the simple Drüde model, and goes on to describe a set of experiments performed by Burke *et al.* [21] measuring the AC (GHz) transport properties of a single 2DES. In accordance with the simple model, we observe plasma oscillations in an appropriately sized resonant cavity of 2D electrons. The results are found to be in good quantitative agreement with the simple Drüde model. This chapter concludes with an introduction to noninteracting electrons in a perpendicular magnetic field.

Chapter 3 considers the case of electron tunneling between two nearby 2DES's, and includes a detailed discussion of 2D-2D electron tunneling at zero magnetic field. A new method to directly measure the energy splitting between the ground and first excited state, i.e., the tunneling strength, of the double-layer system is also included in this chapter. The effect of temperature and density, on the tunneling spectra is investigated. Finally, the effects of a perpendicular magnetic field on 2D-2D tunneling are investigated.

Chapter 4 introduces the physics of strongly interacting quantum Hall systems, starting with single-layers and then moving on to bilayers; with special consideration for the case of $\nu_T = 1$. Prior investigations, both experimental and theoretical, are discussed in depth. Tunneling data at this filling fraction is presented which shows a dramatic enhancement of the zero-bias tunnel conductance, and a corresponding step-like feature in the tunneling current. This anomaly is discussed in terms of the physics of superconductors and Josephson tunnel junctions [20].

Chapter 5 considers the dependence of the $\nu_T = 1$ tunneling features on temperature. Deep in the correlated regime, the tunneling conductance is to be sharply peaked at zero-bias, and increases roughly exponentially with decreasing temperature. As the phase boundary is approached, however, the peak first increases then decreases with decreasing temperature. Associated with this suppression at low-temperature, we observe extremely long time constants ($\sim 10,000$ seconds). The suppression and time constants can be explained by contribution to the electronic Zeeman energy by the nuclear field.

In Chapter 6 we use a parallel magnetic field to access the $\nu_T = 1$ spectral function at finite wave-vector, $k = eB_{||}d/\hbar$. A key element of the theoretical understanding of this bizarre quantum fluid is the existence of linearly dispersing Goldstone collective modes. Using the method of tunneling spectroscopy, we have demonstrated the existence of these modes. We find the measured velocity to be in reasonable agreement with theoretical estimates [22]. Contrary to theoretical expectations, however, the zero-bias tunneling feature persists to large parallel fields.

Chapter 7 presents both inter-layer tunneling and Coulomb drag data exploring the dependence of the phase transition on a relative density imbalance between the layers. We find that in the strongly coherent regime the system is further stabilized by imbalance, and that the phase boundary is augmented by the application of a density imbalance. Even at layer separations when the state has vanished, it can be restored by a suitable imbalance.

CHAPTER 1

GAAS-ALGAAS CRYSTALS AND EXPERIMENTAL APPARATUS

Although the focus of this thesis is the exciting collective physics of electrons in two-dimensional (2D) layers, the "laboratory" in which these experiments are performed is an extremely pure semiconductor crystal. Because of their high-quality and well known material parameters, alloys of gallium arsenide (GaAs) and aluminum arsenide (AlAs) are the materials of choice. The detailed parameters of these crystals strictly define our experiments. Within these stringent requirements it is possible to engineer physical structures which confine electrons to nearly perfect two-dimensional sheets.

The experiments described herein were performed at cryogenic temperatures in order to observe the often delicate many-body electron states. The materials can be cooled to 4 K by simply immersing them in liquid helium, to 0.3 K in a pumped ^{3}He cryostat, and to 15 mK in a dilution refrigerator. Even at the lowest temperatures new physics continues to emerge, requiring even more exotic refrigeration.

The materials described herein are grown by molecular beam epitaxy (MBE), a technique by which crystals are assembled with atomic accuracy. Precisely defined structures can be created in the growth direction, while the other two directions remain isotropic. Electrons are then confined at the interfaces between different alloys; depending on the structure, this can yield the single and multiple 2D electron layers which are the central focus of this thesis.

GaAs is a very well-studied and understood material. Decades of materials science has brought this system to a level of maturity which facilitates its use as a host material. Instead of investigating GaAs *per se*, we use the pre-existing body of knowledge about the GaAs system to design our physics experiments.

We can design single or multiple layers of 2D electrons each with custom tailored electronic properties. The structure determines the coupling between these layers, both in terms of tunneling and Coulomb interactions. These custom GaAs/AlGaAs alloys can be exceptionally pure, resulting in electron scattering lengths in excess of 0.5 mm. Our research depends on our fruitful collaboration with Loren Pfeiffer and Ken West who consistently grow the very best GaAs crystals in existence.

As crystal quality has increased, finer and finer details of the interacting electron system have been revealed. This has yielded a host of fundamentally new physical effects in both single and bilayer systems. In single layer systems some of the effects are: the integer quantum Hall effect (IQHE) [23], observed in relatively low quality crystals; the fractional quantum Hall effect (FQHE) [24] found in cleaner materials; and the more recently detected stripe- and bubble-like phases [5] which exist in only the highest quality samples. In bilayer quantum Hall systems a long anticipated type of superfluidity has been detected [20, 25]; the central topic of this thesis is experimental evidence for this atypical state via electron tunneling spectroscopy. The GaAs system is indeed a well-stocked laboratory to study fundamental physics.

This chapter begins with an introduction to the crystal structure of GaAs/AlGaAs materials and the resulting electronic band structure. This introduction emphasizes the properties of mobile electrons within the crystal. This discussion of band structure illustrates how carefully assembled GaAs/AlGaAs layers can create engineered quantum structures, and concludes with a brief menu of the structures used throughout this research.

The introduction to GaAs materials is followed by a discussion of the MBE growth process by which all of our crystals are manufactured. As much an art as a science, the growth of the high-quality crystals has driven research in 2D electrons for decades.

The cryogenic methods involved in cooling from room-temperature (300 K) to 15 mK fill the remainder of this chapter.

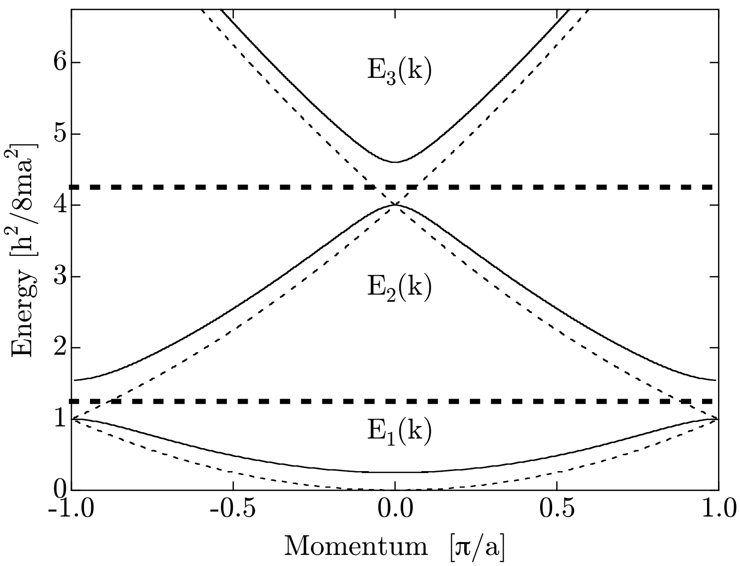

Figure 1.1: Band diagram in Kronig-Penney in first Brillouin zone. Pale dotted line is energy for free electrons.

1.1 Crystal structure

Before discussing the full 3D crystal structure of GaAs, it is helpful to review the consequences of a lattice on electrons in just one dimension. In the physical GaAs crystal, the lattice consists of a periodic potential generated by the regular array of gallium and arsenic atoms. This section focuses on the response of noninteracting electrons to such a potential.

A free electron has a dispersion given by $E(k) = \hbar k^2/2m$. Thus, the energy is quadratic in the wave-vector k. The first effect of the lattice is to limit the crystal momentum to a single zone of the reciprocal lattice. That is, in a crystal any wave-vectors connected by $k + 2\pi n/a$ are equivalent. This reduced zone scheme gives rise to energy bands.

The second result of a finite potential is the opening of gaps in the electron spectra at the zone-boundary. The most simple description of a periodic potential in 1D is the Kronig-Penney (KP) model. In this model the potential is an array of delta functions, the weight of which is a free parameter. Figure 1.1 shows the energy vs. crystal momentum of free electrons (dashed line) and those in the KP model (light-solid line). The result of the potential is to open gaps at the points of intersection in the free electron spectra.

At low-temperature the fermionic electrons will completely fill the lowest unoccupied states, the largest energy of which is called the Fermi energy (E_f). In Figure 1.1 the two dashed horizontal lines indicate two possible Fermi energies (both describing insulators). In one case, the lowest band is completely filled, and any additional electrons will start filling the second band at its minimum at the zone boundary (note that each k state can be filled with two electrons with opposite spins). In the next case, the first two bands are completely filled and the next available state is at $k = 0$ in the third band. Both of these cases are typical for semiconductors; at temperatures above the gap energy, some carriers will be thermally excited from the filled valence band into the empty conduction band. Generally a semiconductor is lightly doped with some material which either donates a small number of electrons to the conduction band, or accepts electrons from the valence band (in which case the carriers are vacancies or "holes" in the valence band).

The final concept described in this picture is that of effective mass. For example, the dispersion of the third band around $k = 0$ can be expanded as $E_3(\delta k) \approx E_3(0) + \hbar^2 \delta k^2 / 2m^*$. m^* is called the effective mass, and like a real mass, describes how a particle responds to a driving force, here in the presence of the lattice. From the figure it is clear that the curvature of the third band is larger than the free electron band, therefore the effective mass is smaller. The concave down top of the 2nd valence band is has less curvature than the nearby conduction band, yielding holes with a larger effective mass.

GaAs and AlAs are both III-V semiconductors with zinc-blend structures as in Figure 1.2 (for a more complete discussion of crystal structure, see for example, Ashcroft and Mermin [26]). The lattice constant of the conventional cubic unit cell is $a \approx 5.6$ Å for GaAs. The GaAs structure is assembled from two face centered cubic (fcc) lattices one of gallium atoms and the other of arsenic. The lattices are offset by a quarter of a lattice constant in each direction: $(a/4, a/4, a/4)$. All of the materials discussed in this thesis are grown on the [100] crystal surface; in the diagram this

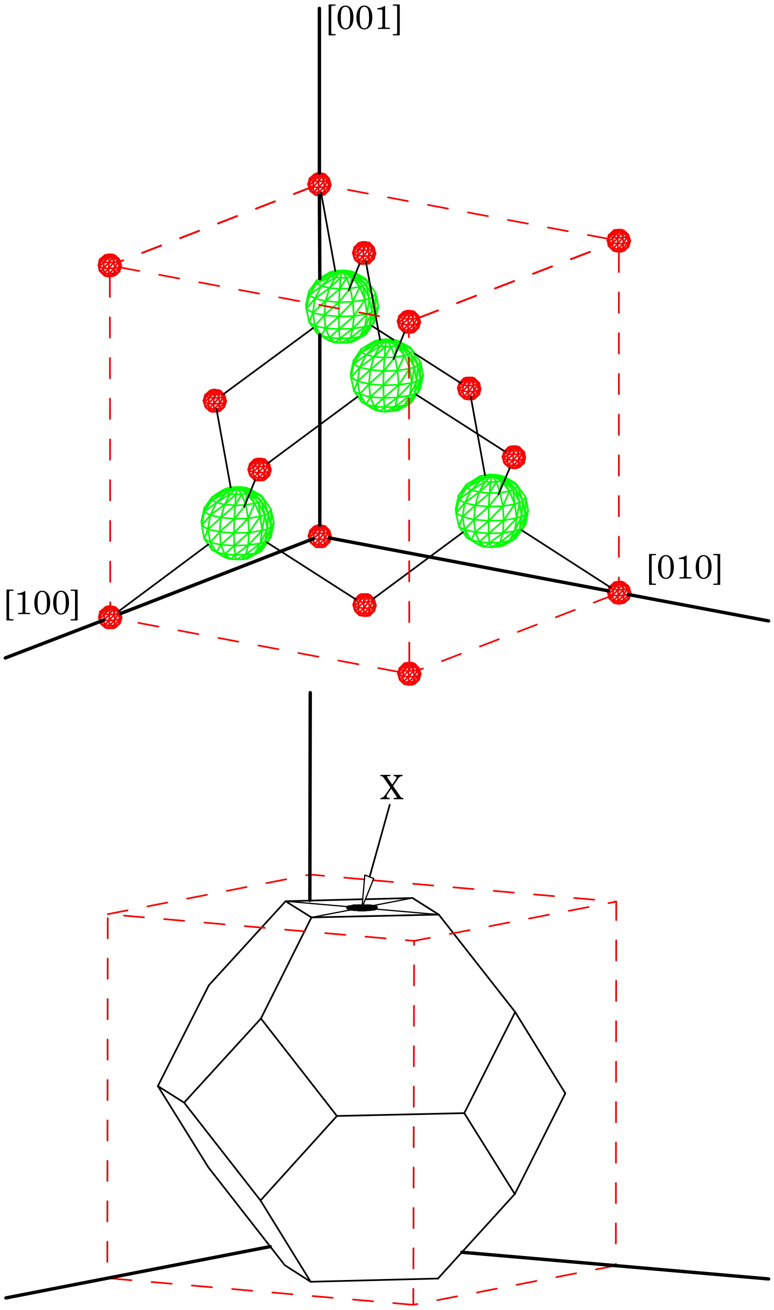

Figure 1.2: Top: GaAs crystal structure (zinc blend), the tetrahedral bonds are shown in black. In this image the two interspersed FCC lattices are clearly visible. Bottom: reciprocal lattice for the FCC structure, note the X point on the edge of the zone; the Γ (not shown) is in the center of the zone.

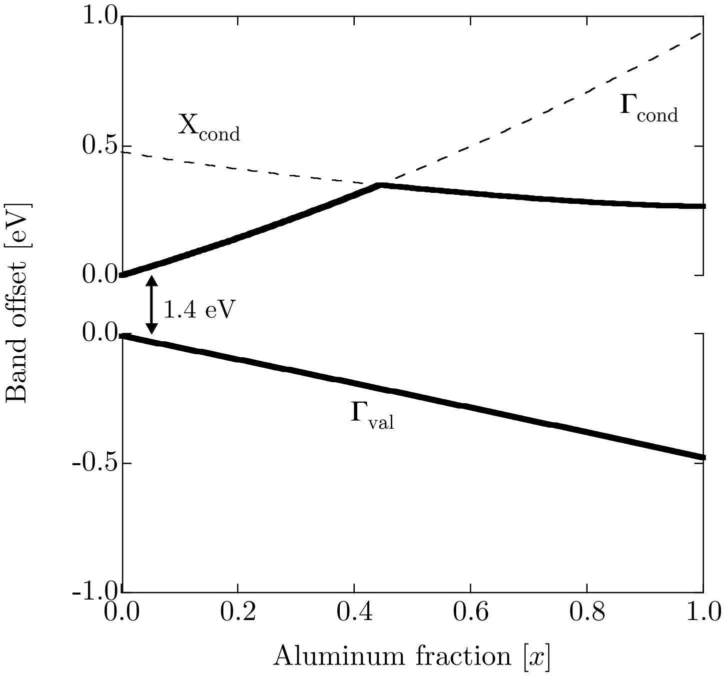

Figure 1.3: Dependence of GaAs/AlGaAs band structure on aluminum fraction (adapted from [27]). Top: band offset in the conduction band. Bottom: offset in valence band. The zeros are offset by the GaAs band gap of 1.4 eV. Note that the valence band maximum is always at the Γ point, while the conduction band minimum shifts from Γ to X at an aluminum fraction of about $x \approx 0.4$.

corresponds to the top of the crystal.

As with the 1D example, the electronic properties of GaAs are best described in the momentum representation and with respect to the corresponding reciprocal lattice. Although conceptually simple, the FCC reciprocal lattice in 3D is much more complex than the simple 1D example.

The first Brillouin zone of the GaAs reciprocal lattice is shown in Figure 1.2; several points of high symmetry in this zone have special names, of which two are relevant here: the Γ point at the center of the zone, and the X point on the edge. In the $\text{Al}_x\text{Ga}_{1-x}\text{As}$ alloy there are local minima in the conduction band at both of these points. When $x < 0.4$ the Γ point is lower in energy than the X point, while for $x > 0.4$ the minimum shifts to the X point.

The band gap and the conduction band energy both change with aluminum concentration x. As a result, a layered structure assembled from sheets of different concentration will create an effective potential landscape for electrons in the conduction band or holes in the valence band. The details of the potential can be engineered by carefully selecting the aluminum fraction (see the data in Figure 1.3). For example, a layer of pure GaAs bounded by $\text{Al}_{0.3}\text{Ga}_{0.7}\text{As}$ barriers will form a potential well.

1.2 BAND STRUCTURE ENGINEERING

The previous section concluded with the central idea of band engineering: combinations of materials with differing band gaps can create controlled potential landscapes for conduction band electrons. In addition to the difference in band gaps between GaAs and AlAs, the effective mass of electrons at the Γ point also differ: $0.068 \times m_e$ for GaAs and roughly $0.15 \times m_e$ in AlAs [28]. Many of the structures described here include layers with an aluminum concentration larger than 0.4, therefore in the region where the X point is the potential minimum. In our samples these layers can serve as tunneling barriers, and we believe the electrons tunnel via the Γ point. Although this has not been directly verified, the observed tunneling conductance scales with aluminum fraction as is expected with the Γ point tunneling barrier. We would expect orders of magnitude more strongly tunneling samples if the smaller X point barrier were relevant.

MBE-grown surfaces are precisely defined at the atomic scale in the growth direction, and are isotropic in the remaining two directions. These structures can therefore be described by a potential $V(z)$; the resulting wavefunctions are plane waves in the $x-y$ plane. The z wavefunction can be solved self-consistently by including both the band potential and the interactions between electrons [29].

Undoped GaAs is an insulator because the Fermi energy lies in the band gap. However, a small concentration of silicon dopant will populate the conduction band. Modern high-quality samples rely on remote doping – the silicon atoms are placed in a sheet remote from the electron gas, and the electrons migrate to the potential trap. This technique was invented by Stormer [30] and it vastly increases sample quality by reducing scattering from the random donor potential[1].

---

[1] Carriers can also be electrostatically drawn into the 2D system using remote metallic gates.

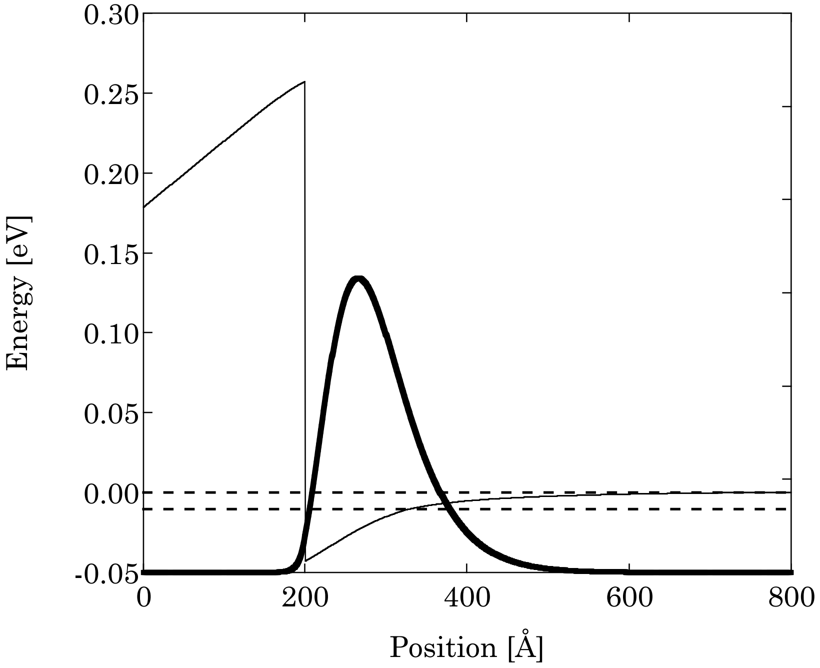

Figure 1.4: Single interface $Al_{0.3}Ga_{0.7}As$ junction. The thin line is the self-consistent trapping potential. The heavy line is the electron density. The dashed lines are the first two eigenenergies (note that the second energy is only just bound).

1.2.1 Heterojunction

A heterojunction is a single interface between $Al_xGa_{1-x}As$ and GaAs, generally with an aluminum fraction $x \approx 0.3$. Above the interface a single-layer of dopants provide the carriers which eventually collect at the interface.

A typical band profile for a heterojunction is displayed in Figure 1.4. This structure consists of an interface between GaAs on the right and $Al_{0.3}Ga_{0.7}As$ on the left. A layer of silicon dopants on the far left contribute a total electron density of 3.0×10^{11} cm^{-2}. The smooth confining potential on the right is not generated by a different material, instead it is the self-consistent potential from the electrons themselves. As the density becomes very small, the trapping potential can become increasingly soft and the wavefunction highly extended.

The linear slope of the potential to the left of the interface is generated from the potential between the remote dopants and the bound electrons. In these samples,

---

Undoped samples provide the possibility for increased sample quality due to the a complete lack of donor scattering. These samples are challenging to fabricate, but provide a controllable electron density coupled with extremely high-quality [31, 32].

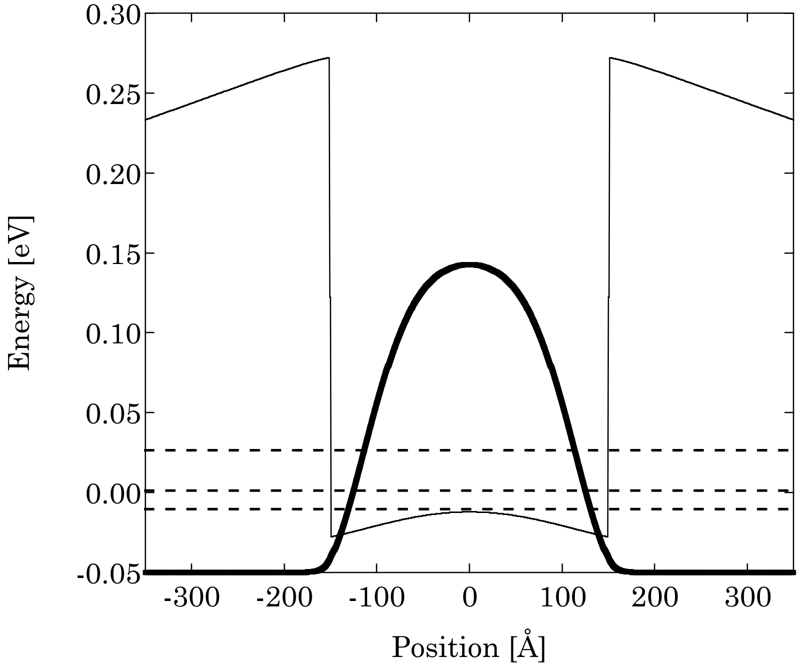

Figure 1.5: Single quantum well assembled from $Al_{0.3}Ga_{0.7}As/GaAs/Al_{0.3}Ga_{0.7}As$. The thin line is the self-consistent trapping potential. The heavy line is the electron density. The dashed lines are the first three eigenenergies.

the electron density is controlled by the setback distance of the dopant layer, not the number of donors. Physically, this means that there is a sufficiently large donor concentration to pin the Fermi energy in the donor layer just below the conduction band edge.

The ground state charge density, $|\psi(z)|^2$, is shown as a heavy line, and the two subband energies are illustrated by dotted lines. It is a generic feature of heterojunctions that the excited states are weakly bound, and that there is often only a single bound state.

In addition to scattering from the remote donors or impurities, a second intrinsic source of scattering is from imperfections in the GaAs/AlGaAs interface, called interface roughness. Because heterojunctions have only one interface, until recently the best samples in the world were all heterojunctions.

1.2.2 Quantum well

Like a heterojunction, the conceptually simper single quantum well (SQW) forms a single sheet of electrons. In the structure in Figure 1.5 the electrons are confined in a GaAs well between $\mathrm{Al}_x\mathrm{Ga}_{1-x}\mathrm{As}$ barriers. In this typical quantum well the well width is 300 Å and the carrier density is $n = 3.0\times10^{11}$ cm^{-2}.

Here the first three bound states are shown by the dotted lines. Notice the roughly quadratic spacing, reminiscent of an infinite square-well potential. Like the heterojunction, an isolated quantum well usually forms a single 2DES, unlike the 2DES formed by a single interface a SQW is symmetric. When the single well is sufficiently wide, it can act like two heterojunctions and effectively form two distinct layers of electrons [33].

In spite of having two interfaces, quantum well samples now hold the record for highest mobility. The number of electron contributed by the donor layer is roughly proportional to the setback between the donor layer and the 2DES. The 2D density is left unchanged by placing the donor layers symmetrically about the well but twice as far away. This increased setback then dramatically reduces the importance of scattering from the donor potential and enhances the mobility.

1.2.3 Double quantum well A double quantum well (DQW) consists of two wells separated by a barrier. This thesis focuses on such samples and discusses in detail the measurement of quantum mechanical tunneling current between the two layers.

The structure in Figure 1.6 consists of two 180 Å wide GaAs quantum wells with a 99 Å wide $\mathrm{Al}_{0.9}\mathrm{Ga}_{0.1}\mathrm{As}$ tunneling barrier. The lowest two energy states are separated by a symmetric/antisymmetric energy gap Δ_{SAS} which parameterizes the tunneling strength. The computed gap for this structure is $\Delta_{\mathrm{SAS}} \approx 0.4$ neV; this calculation includes the effects of the band structure and the differing effective masses in GaAs and AlGaAs. The effective mass both enters into the Hamiltonian via the kinetic term, $(\hbar^2/2m^*)d^2/dz^2$, and leads to a discontinuity in the first derivative of $\psi(z)$ when m^* changes [29].

In general, bilayer samples can be tailored for many specific applications. Very strongly coupled layers (with thin or very short barriers) were used in the initial studies on multicomponent quantum Hall effects [12, 8, 7]. In these studies, the quantity of interest was the magneto-resistances, ρ_{xx} and ρ_{xy}.

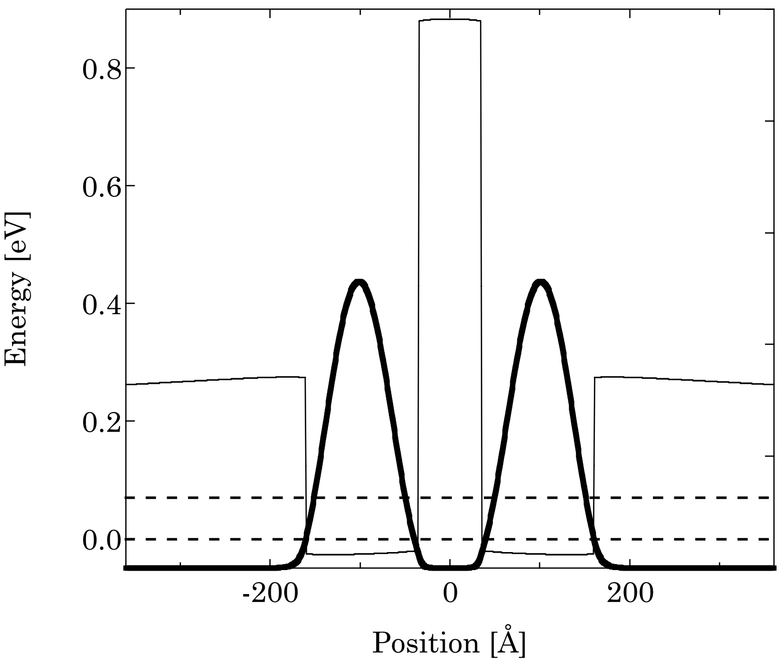

Figure 1.6: Double quantum well: $Al_{0.3}Ga_{0.7}As/GaAs/Al_{0.9}Ga_{0.1}As/GaAs/Al_{0.3}Ga_{0.7}As$. The thin line is the self-consistent trapping potential. The heavy line is the electron density. The dashed lines are the first three eigenenergies. Note that the splitting of 0.4 neV between the lowest two eigenstates is invisible on this scale

In samples with an intermediate tunneling strength, the inter-layer tunneling current can be measured. A selective depletion scheme is used to make separate electrical contact to the two layers [34]. Tunneling measurements are possible when the tunneling conductance is much less than the sheet resistances, so the layers can be considered as equipotentials.

Very weakly tunneling samples are useful for the measurement of Coulomb drag [35]. Here, a current is passed through one layer, and the resulting voltage drop due to inter-layer scattering is measured in the other. A tunneling current leads to a spurious signal.

1.3 Growth

Molecular beam epitaxy is an atomically accurate method of crystal growth in which the constituent elements are very slowly evaporated onto a substrate. By exactly controlling the growth stoichiometry, custom structures are formed from layers

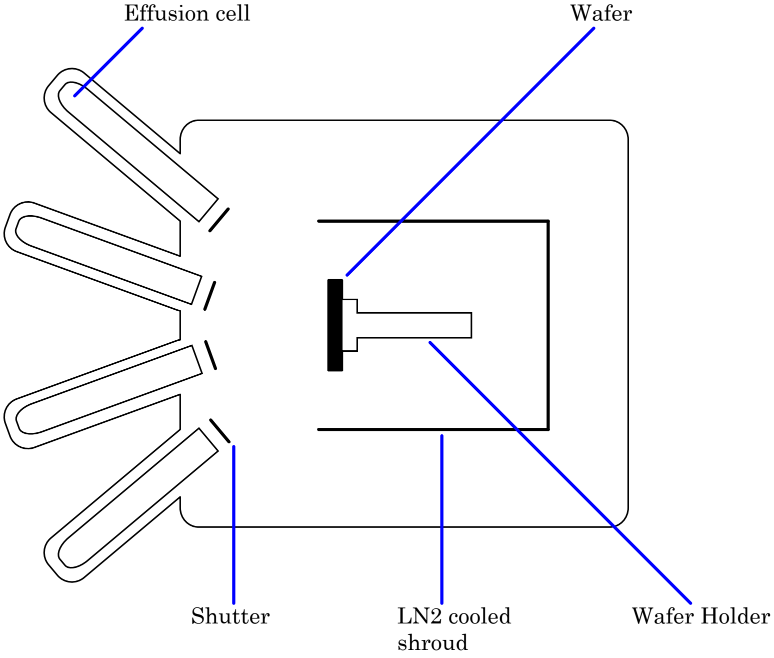

Figure 1.7: Schematic diagram of a MBE chamber.

of GaAs, and $Al_xGa_{1-x}As$.

In the early 1970's, MBE was developed as a new growth technique for high-purity layered semiconductor alloys [36, 37]. MBE can produce high-quality layers with very abrupt interfaces, precise control of thickness, doping, and composition. Because of this high degree of control, MBE is an ideal tool in the growth of high-quality engineered electronic structures.

In MBE, the constituent elements of a semiconductor are deposited onto a heated crystalline substrate to form thin epitaxial layers. The source materials are typically from thermally evaporated elemental sources, resulting in "molecular beams" incident on the substrate. The material sources are independently heated until the desired material flux is achieved, which generally yields a growth rate of only a few Å/s. To obtain high-purity layers, the material sources are extremely pure and the entire process is done under ultra-high vacuum ($\sim 10^{-11}$Torr). The combination of slow growth rates coupled with rapid shuttering of the beams permits atomically abrupt transitions from one material to another.

The growth chamber of a generic MBE system and several of its subsystems are illustrated in Figure 1.7. The sample holder rotates continuously during growth to increase the homogeneity of growth. A liquid nitrogen cooled shroud is located between the chamber walls and the sample holder and acts as pump for many of the residual gasses in the chamber.

Once the blank wafer is placed in the rotating holder, the shutters are opened and closed in a precisely coordinated fashion, which controls the material deposited layer by atomic layer. Depending on the material, the wafer temperature may also be changed during deposition.

Figure 1.8 shows the actual growth layers required to create the bilayer quantum well wafer commonly used in subsequent experiments. The initial layers are called the cleaning superlattice and serve to prepare the surface of the wafer. Following the superlattice is an AlGaAs buffer, and then a silicon dopant layer. The actual DQW is set back from the dopant on the top and bottom to determine the density. A third donor layer follows a brief setback, this layer is designed to populate the surface states of the crystal. Finally the sample is capped with a thin GaAs protective layer.

1.3.1 Processing A 2" wafer of GaAs is not overly useful without some means to contact and control the as-grown 2D layers. Three very useful structures are contacts, gates, and mesas, the detailed fabrication and processing techniques of which are described in Appendix B. Chapter 3 discusses a technique to make separate electrical contact to each of the layers in a multi-layer sample.

An Ohmic contact is made from a material which can diffuse through the top layers and make electrical contact to the 2DEG. Ohmic refers to the fact that such contacts should follow Ohm's law, and not, for example, act as a diode.

It is frequently convenient to use a single sample to study a wide range of carrier densities – a gate is a metalization on the sample surface which, when biased with respect to the 2D electrons, changes the electron density below it.

Finally, we wish to confine the electrons to a suitable geometry. By first masking the desired shape, a chemical etch can dissolve the remainder of the sample surface, leaving a 2DES only under the protected portion of the sample. The final structure

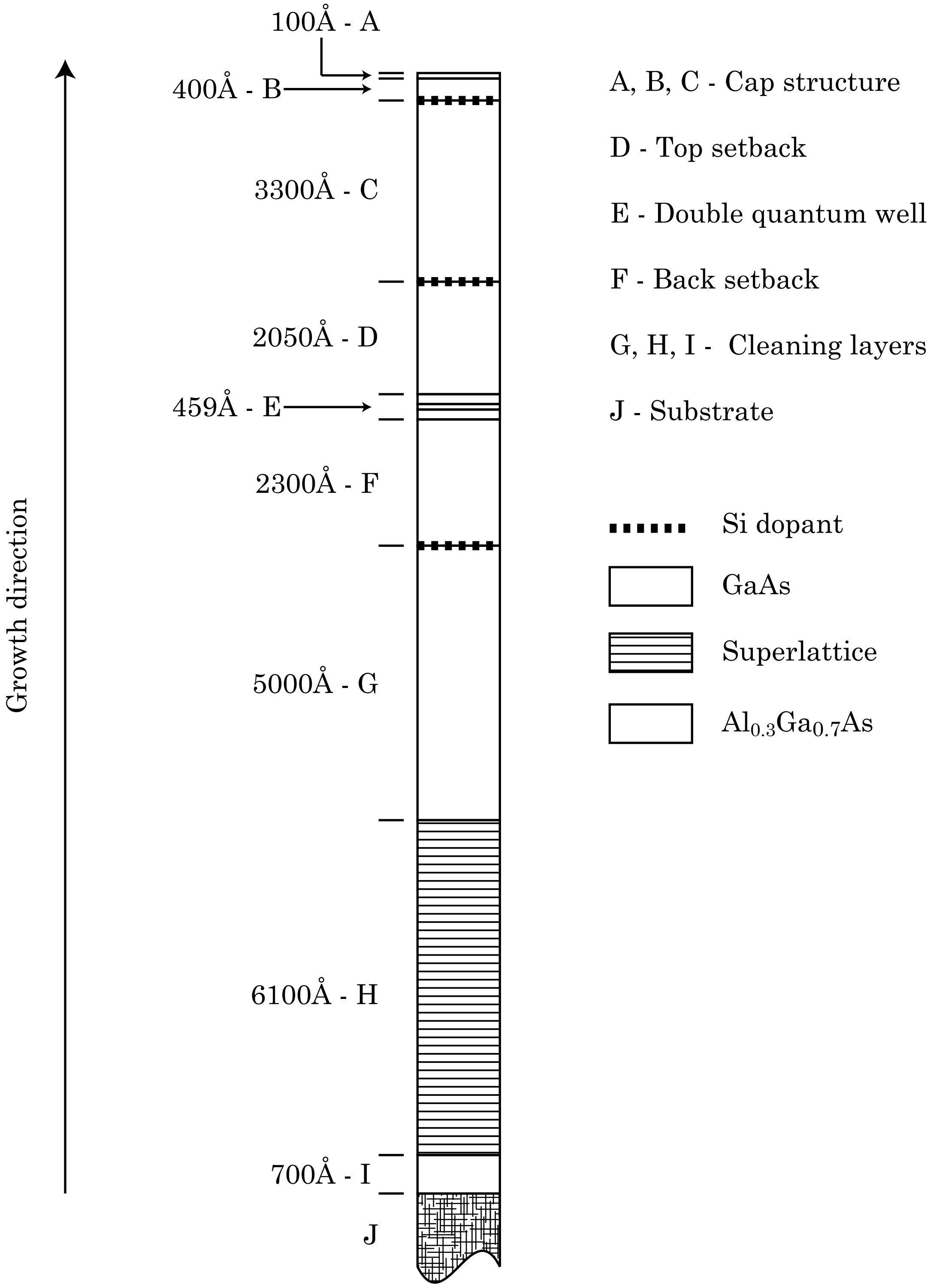

Figure 1.8: Annotated structure of the parent wafer of Sample E.

is called a mesa.

1.4 CRYOGENICS AND MEASUREMENT

Once grown, processed, and connected to a compact chip carrier, the sample is ready for use. Resolving the often delicate, many-electron states requires the ultimate in cryogenic temperatures and high magnetic fields. To that end we employ a series of different, and increasingly complex, refrigeration techniques. In our lab we can cool GaAs crystals below 15 mK. Each cryostat is equipped with a superconducting magnet which provides a magnetic field as large as 16 Tesla.

There are several relevant energy scales which determine the maximum temperature below which various physical effects begin to develop in the 2DES. The first, and generally the largest, is the gap from the ground state to the first excited electronic sub-band, $\Delta E = E_1 - E_0$. At high-temperatures there will be an undesired thermal population of these carriers. For the case of the heterojunction in Figure 1.4 or the SQW in Figure 1.5 this energy is $\sim$ 100 K. In the double quantum well in Figure 1.6, $E_1 - E_0 = \Delta_{\mathrm{SAS}}$ is vastly less than the Fermi energy. Therefore the relevant gap is between these energies and the 2nd excited state: $E_2 - E_1 \approx 400$ K.

Generally speaking, interesting quantum physics does not begin to emerge until the temperature is well below the Fermi energy, E_f; above this temperature the electron gas loses its quantum character and acts like a classical Maxwell-Boltzmann gas. For typical sample densities of 0.5×10^{11} cm^{-2}, the Fermi temperature is $T_f =$ 20 K. Although we generally operate at far lower temperatures, every sample is first tested at 4.2 K simply by dunking it in a liquid helium dewar. By 4 K the electron gas has assumed its Fermi character and we can test the overall operation of our devices. For example: verifying proper contact to the electron gas, testing the functionality of the gates, and frequently measuring the electron density.

In a free electron gas, the importance of interactions between electrons is parameterized in terms of the ratio of the potential to kinetic energy – called r_s. In a 2D degenerate Fermi gas, this ratio is $r_s = m^* e^2 / \left(4\pi\epsilon\hbar^2\sqrt{\pi n}\right)$; for a 2DES in GaAs with a density of 0.5×10^{11} cm^{-2}, this ratio is about 2.5. Fermi liquid theory is thought to

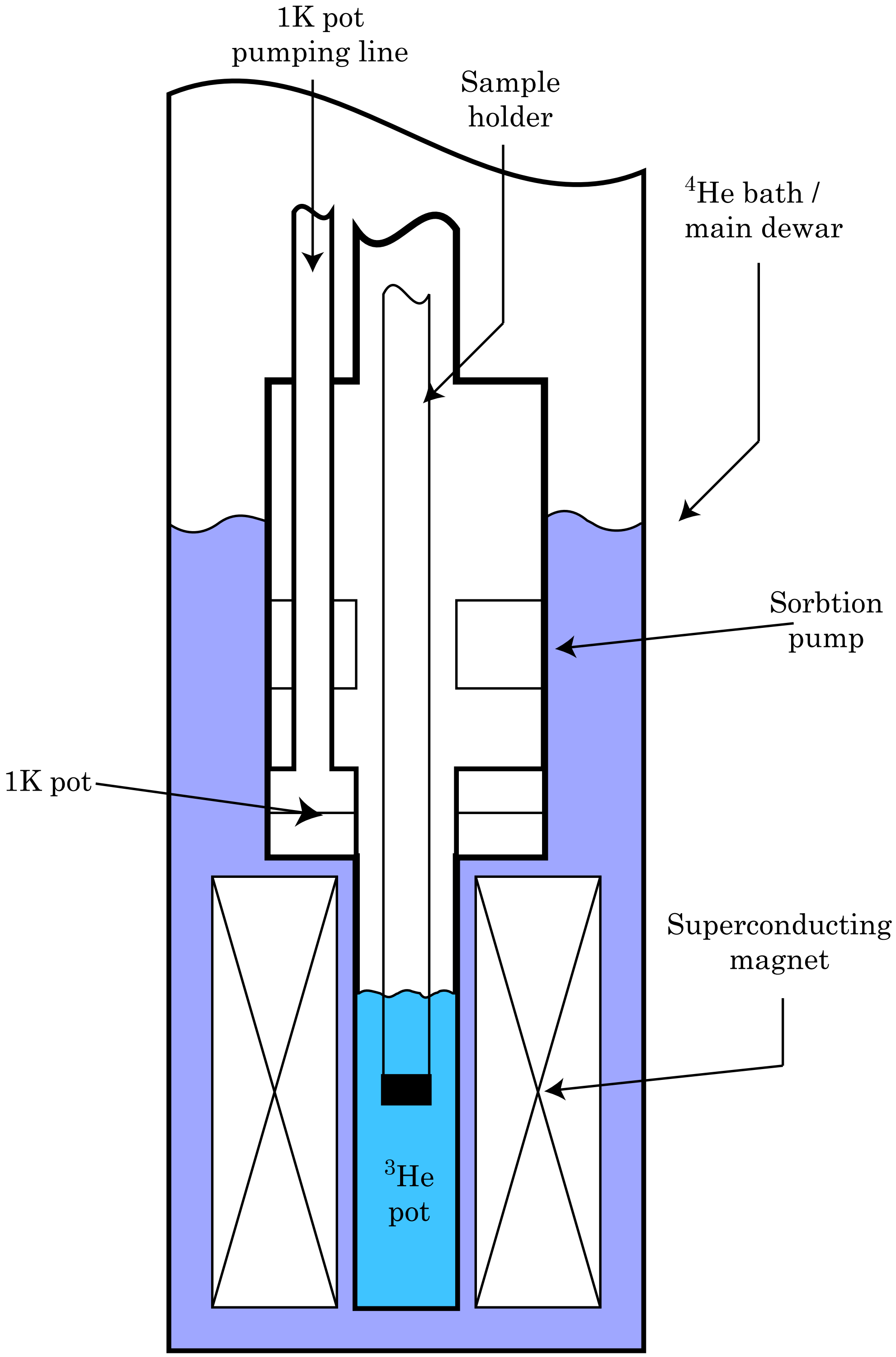

Figure 1.9: Simplified cross-sectional schematic of a typical ^{3}He refrigerator. The sample rests in a pool of liquid ^{3}He in the center of a 9 Tesla superconducting magnet.

be valid for $r_s \lesssim 30$ for 2D electrons (see [38], and references therein), so our system can still be described in a single-particle theory. By decreasing the electron density, r_s can be increased, leading to non-Fermi liquid behavior. Alternately, the application of a large perpendicular magnetic field effectively quenches the kinetic energy, leading to new quantum states dominated by the electron-electron interactions.

At still lower temperatures effects such as the integer and fractional quantum Hall effects begin to emerge. Much of this physics can be studied effectively in a ^{3}He cryostat. Just like evaporating H_2O cools your skin, pumping on a liquid helium bath lowers the temperature. A pumped ^{4}He system can cool to roughly 1 K, while replacing the ^{4}He with the lighter isotope, ^{3}He, reduces this temperature to ~ 0.3 K.

With ever-decreasing temperature and increasing sample quality, more and more exotic and delicate states of the electron system emerge. For example, this thesis details measurements performed in bilayer 2DES in which the system enters a new, superfluid ground state, but only below ~ 500 mK. A dilution refrigerator is required to reach these ultimate low-temperatures. Such a cryostat consists of a circulating mixture of ^{4}He and ^{3}He, which can cool to below 15 mK (for a more detailed discussion of the operation of the ^{3}He and dilution cryostats refer to Appendix C).

1.5 CONCLUSION

In this section, the basic material properties of the GaAs system have been discussed, and those properties which make it suitable as a laboratory for fundamental physics have been emphasized. The use of MBE to grow high-quality GaAs crystals was discussed, and several typical MBE-grown structures were given as examples.

Even at the 15 mK base temperature of a dilution refrigerator, the electron system is continuing to evolve [20] with new physics constantly emerging [39]. Without doubt further discoveries in the highest quality samples wait to be found at yet lower temperatures.

CHAPTER 2

NONINTERACTING ELECTRONS IN 2D

This chapter presents high-frequency conductivity measurements by Peter Burke and myself [21] on a 2DES at zero magnetic field. Electrons in two-dimensions (2D) can be treated in increasing levels of complexity, each introducing new physical phenomena. This chapter begins with the most simplistic description of a two-dimensional electron gas (2DES): the Drüde model. The Drüde model describes a gas of noninteracting, classical electrons, with a phenomenological relaxation time.

To illustrate the surprising success of this model, we measured the frequency-dependent conductivity of a 2DES [21], which is easily computed within the Drüde model. The results of this study compare favorably with experimental measurements both at DC and from 50 MHz to 10 GHz. In this framework, an isolated 2DES behaves as a distributed combination of resistors and inductors. The addition of a nearby conducting gate capacitively coupled to the 2DES completely changes the dynamics of the model and allows for propagating density waves, or “plasmons.” The dispersion and damping of these plasmons is measured, and both are well described by the Drüde result.

The addition of quantum mechanics creates a new layer of complexity, and is the second topic of this chapter. The inclusion of the Pauli exclusion principle alone leads to the formation of a Fermi gas, which dramatically changes the single-electron properties of the system. A perpendicular magnetic field leads to quantized cyclotron orbitals, which at low magnetic fields results in Shubnikov de Haas (SdH) oscillations. When the field is further increased the SdH oscillations continuously evolve into the integer quantum Hall effect (IQHE).

The unifying theme of this chapter is noninteracting electrons. A truly remarkable range of physical effects result from the noninteracting 2D electron gas. Nonetheless, this is just a hint of the rich physics in the interacting 2DEG.

2.1 DRÜDE MODEL

The Drüde model is arguably the simplest description of electrons in a material. The mobile charges are assumed to be noninteracting classical electrons, which scatter from defects (impurities, lattice imperfections, or phonons) on a timescale τ_m. In spite of the stunning naiveté of the Drüde model, it captures many of the essential properties of a 2DES at zero magnetic field (naturally there are exceptions, particularly when the interactions between the electrons cannot be ignored).

In the presence of an external electric field $\mathbf{E}(t)$ and a constant magnetic field $\mathbf{B}$, the classical trajectory, $\mathbf{x}(t)$, of a single charge carrier is described by

$$m^* \frac{d^2\mathbf{x}}{dt^2} + \frac{m^*}{\tau_m}\frac{d\mathbf{x}}{dt} = e\mathbf{E}(t) + e\mathbf{B} \times \frac{d\mathbf{x}}{dt}. \tag{2.1}$$

A phenomenological damping term, m^*/τ_m, has been included; $1/\tau_m$ represents the rate at which scattering events change the momentum. τ_m is often referred to as the momentum lifetime, since it describes how fast momentum states relax.

In two-dimensions it is often convenient to represent the vector $\mathbf{x}(t) = x(t)\hat{\mathbf{x}} + y(t)\hat{\mathbf{y}}$ as a single complex number $z(t) = x(t) + iy(t)$. However, to avoid confusion with the phasor notation used in the time dependence, $\exp(-i\omega t)$, $\mathbf{x}(t)$ will be treated as a regular vector expression.

Equation 2.1 is easily solved in the frequency representation, using the definitions $\mathbf{J}(t) = \sigma\mathbf{E}(t)$ and $\mathbf{J} = en(d\mathbf{x}/dt)$. The resulting Drüde prediction for the AC resistivity tensor $\rho = \sigma^{-1}$ is

$$\rho(\omega) = \begin{pmatrix} \rho_{xx} & \rho_{xy} \\ -\rho_{xy} & \rho_{yy} \end{pmatrix} = \begin{pmatrix} m^*(1 + i\omega\tau_m)/ne^2\tau_m & B/ne \\ -B/ne & m^*(1 + i\omega\tau_m)/ne^2\tau_m \end{pmatrix}, \tag{2.2}$$

where e is the carrier charge, $m^* = 0.068 \times m_e$ is the effective of electrons in GaAs,

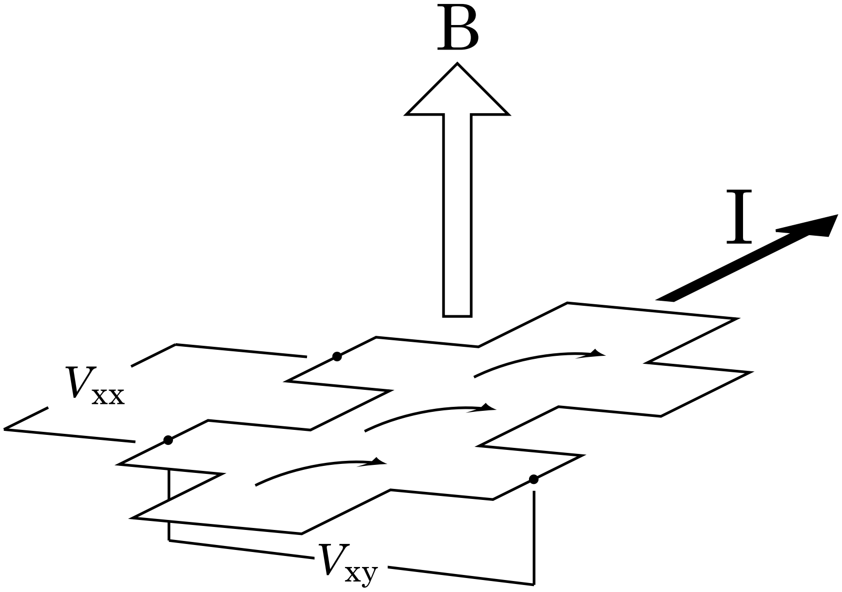

Figure 2.1: Typical Hall bar geometry for transport measurements.

and n is the 2D carrier density. These transport parameters are often measured in the four wire configuration illustrated by Figure 2.1. This section contains several representative numerical results for a “typical” 2DES. The prototypical 2DES is buried 5800 Å beneath the samples surface, has a dielectric constant $\epsilon = 13$, a density $n = 1.5{\times}10^{11}$ cm^{-2}, and a mobility $\mu = 3.5{\times}10^{6}$ cm^2/Vs.

Equation 2.2 has several ingredients. The off-diagonal elements are the Hall resistivity, which depend only on e, n and B. It is often convenient to use ρ_{xy} to measure the electron density, by finding the slope of ρ_{xy} vs. B. The first half of this chapter focuses on zero magnetic field, consequently $\rho(\omega)$ will denote the scalar quantity $\rho_{xx}(\omega)$.

In 2D, $\rho(\omega)$ has dimensions of Ohms per-square[1], or $\Omega/\Box$; for example, a rectangle of length D and width W will have a resistance $R \approx \rho \times (D/W)$. The following relations will neglect this term, in effect assuming a square sample. For GHz frequencies it is conventional to use the symbol Z, the complex impedance, in place of R. $Z = Z_{re} + iZ_{im}$ has a real part which is the usual DC Drüde resistance and a series

---

[1] Consider two squares, one with side L and a second with side $2L$, and with a current I driven through each. The smaller square has half the length, but twice the current density of the larger square. This results in the measured voltage drop being equal.

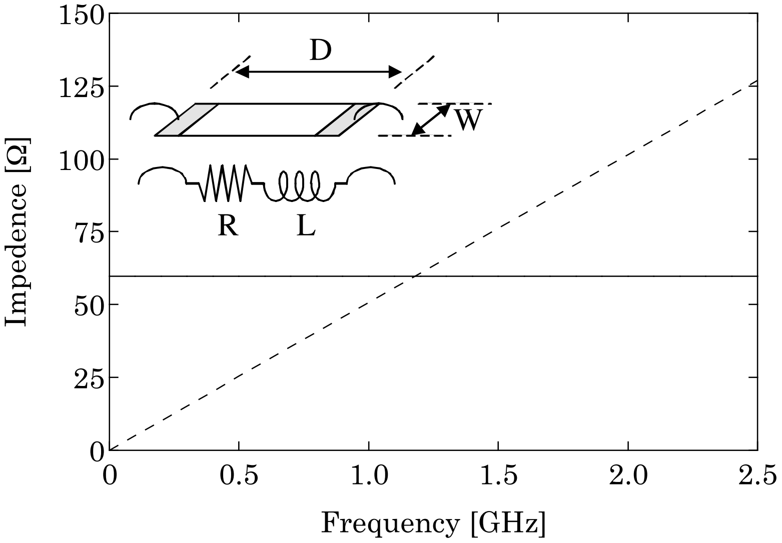

Figure 2.2: Simulated impedance for an isolated 2DES. Solid: real, dashed: imaginary. Inset: equivalent circuit for isolated 2DES. In this case $R = 60\ \Omega$, and $L = 1.6$ nH

imaginary component,

$$Z_{re}(\omega) = \frac{m^*}{ne^2\tau}, \qquad \text{and} \qquad Z_{im}(\omega) = \frac{\omega m^*}{ne^2}.$$

Mathematically, this is nothing more than the impedance of an inductor, whose "kinetic inductance" is $L = m^*/ne^2$. Inductance usually results from energy stored in a magnetic field. However, here it resides in the kinetic energy of the electrons.

Mobility is a measure of a 2DES's quality, defined by $\mu = \tau_m e/m^* = (ne\rho_{\mathrm{DC}})^{-1}$. In the frequency-dependent Drüde model the scattering time τ_m (and therefore mobility) can independently be found using two distinct measurements. The real component of Z is frequency-independent and should therefore give the same information as the zero frequency resistivity. Additionally, the ratio

$$\frac{Z_{im}(\omega)}{Z_{re}(\omega)}\frac{1}{\omega} = \tau_m$$

gives a direct measurement of the scattering time. This second measurement of mobility is related only to τ_m, a single measured quantity, and the ratio is geometry-independent.

In contrast, mobility is conventionally extracted from the DC resistivity, ρ, measured using 4 terminal lock-in techniques. The measured resistance R is a geometry dependent, extrinsic, property of the sample. Two distinct measurements of R_{xx} are required to compute ρ. Current is driven between a pair of contacts, and the voltage drop is measured across the pair of contacts parallel to the current flow. Given four contacts, there are two distinct ways of making this measurement, which give (possibly) different values for resistances $R_{1,2-4,3}$ and $R_{2,3-1,4}$. From these values of resistance, the resistivity can be computed using van der Pauw's equation [40].

In these measurements, the electron density is subsequently required to convert ρ to mobility. The Hall resistance can be used to determine the density. It is often the case that there are undesired parallel channels in the 2DES, and the Hall measurement will include their contribution to the density.

It is more accurate to measure the $1/B$ periodic SdH oscillations of the DC resistivity (or almost any other parameter of the 2DES) vs. magnetic field, see Section 2.5.1 for details. Unlike the Hall effect, the SdH oscillations are insensitive to the carriers in a low-conductivity parallel channel. This difference can lead to discrepancies in the computed mobility.

2.2 RF PLASMONS

The description of a Drüde 2DES is considerably changed by the presence of a nearby metallic gate (Figure 2.3). This variation of the Drüde model can be solved in terms of a distributed LRC transmission line, which supports an attenuated propagating mode.

The inset to Figure 2.3 illustrates this one-dimensional (1D) model. It has parameters r, l, and c: the resistance, inductance, and capacitance per-length. This simple model is solved by first expressing discrete versions of the circuit equations:

$$q_i = c\Delta x V_i, \qquad \frac{dq_i}{dt} = I_{i-1} - I_i, \qquad \text{and} \qquad V_{i+1} - V_i = -\left[r\Delta x I_i + l\Delta x \frac{dI_i}{dt} \right].$$

Assembling these discrete equations into a pair of continuous equations for I and V

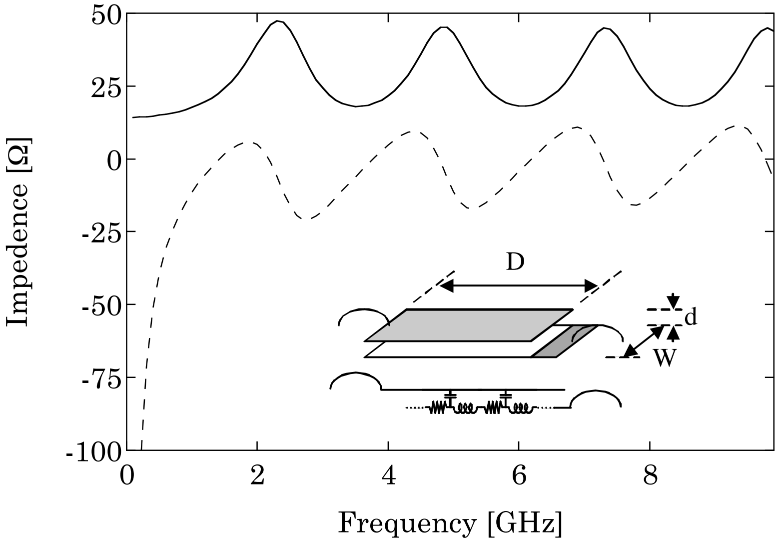

Figure 2.3: Simulated impedance for a gated 2DES illustrating clear plasmon resonances. The solid line correspond to the real impedance, and the dashed line to the imaginary part. Inset: equivalent circuit for a 2DES with a nearby gate. In this case $W = 100\ \mu$m, and $D = 360\ \mu$m.

(with an assumed time dependence of $\exp(i\omega t)$ for all the variables) gives the results

$$\frac{dV^2}{d^2x} = -k^2V, \qquad \text{and} \qquad I = \frac{-1}{(r+i\omega l)}\frac{dV}{dx}.$$

k is a complex wave-number defined by $k^2 = (\omega^2 lc + i\omega rc)$. The solutions $V(x,t)$ can be found by inspection to be $V(x) = A\exp(ikx) + B\exp(-ikx)$.

The wave velocity is related to the real portion of the wave-vector by $v = \omega/k_{\text{re}}$. For an ideal LC transmission line is $v = (lc)^{-1/2}$. Resistive damping reduces the velocity by a factor of

$$\left[\frac{1}{2} + \frac{1}{2}\left(1 + \frac{r^2}{\omega^2 l^2}\right)^{1/2}\right]^{-1/2}.$$

For typical GaAs parameters at 3 GHz the fractional change in velocity is only 0.75%, which can be safely neglected. Inserting the Drüde model results for inductance and capacitance gives the expected velocity,

$$v = \sqrt{\frac{ne^2d}{m^*\epsilon}}. \tag{2.3}$$

The same 2DES would have a wave velocity $v = 2.4 \times 10^6$ m/s, or about 0.8% of the speed of light in a vacuum.

To find the impedance of the device of length D, in Figure 2.3, we apply boundary conditions such that one end of the 2DES is at voltage V_0, and at the other end the current is zero. These boundary conditions result in the impedance

$$Z = -\frac{R + i\omega l}{k} \frac{1}{\tan(\mathrm{kD})}.$$

The measured impedance, Z, in Figure 2.3 clearly shows oscillations which correspond to standing modes within the metal gate/2DES “box”. The width of the bumps results from the lifetime τ_m of the electrons. Again, fitting the Drüde expression to experimental data provides another mechanism to extract τ_m from frequency-dependent impedance measurements.

The modes predicted by the Drüde model are the long wavelength limit of classical 2D plasma modes [41, 42, 43]. For an isolated conducting sheet, the dispersion is given by $\omega^2 = kne^2/2\epsilon m^*$; this result is substantially modified by the addition of a conducting gate a distance d above the 2DES:

$$\omega^2 = \frac{ne^2}{\epsilon m^*} \frac{k}{1 + \coth(kd)}.$$

As $kd \to \infty$ this expression reduces to the Drüde/transmission line result.

2.3 EXPERIMENT

Here I present frequency-dependent conductivity measurements of a single 2DES from 50 MHz to 10 GHz performed by Peter Burke and myself [21]. These data were taken in a top-loading Oxford ^{3}He cryostat with base temperature of 0.3 K. The sample insert was wired with 16 manganin leads (twisted pair) for DC measurements and a single UT34 beryllium-copper coaxial cable (with a silver flash on the inner conductor) for RF measurements to 20 GHz. At this time the cryostat was also equipped with a 15 Tesla Oxford superconducting magnet.

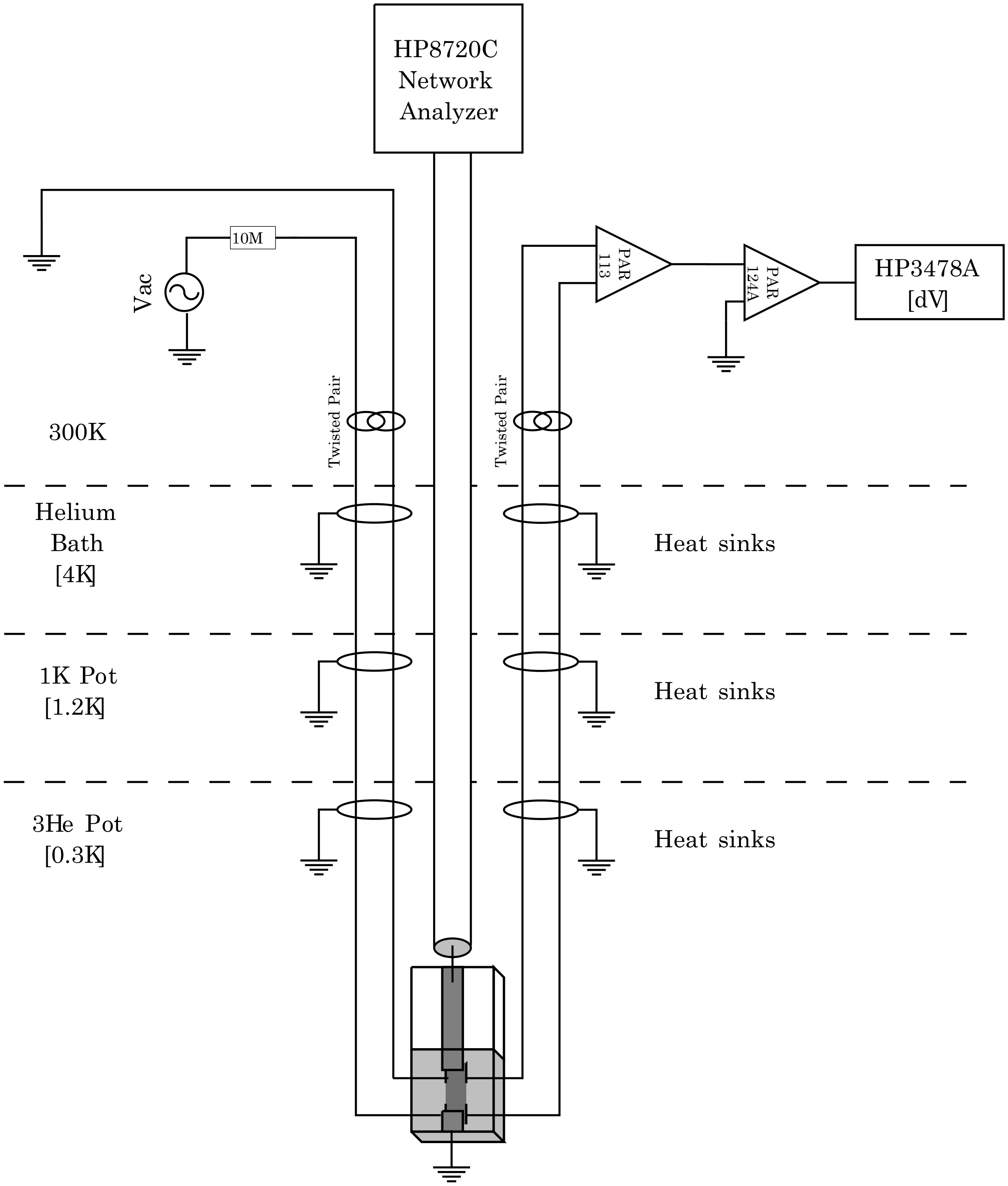

Figure 2.4: A schematic circuit diagram of the experimental setup. The sample is connected on one end to RF ground, and the other to a 50 Ω transmission line followed by a coaxial cable leading from the 0.3 K stage to the HP network analyzer at room-temperature.

The samples were mounted on a header with 16 DC leads and a SMA connector perpendicular to the plane of the samples. The SMA connector linked the sample mount to the coaxial cable; its central pin was soldered to a 50 Ω strip line bridging the gap between the connector and the GaAs sample. The sample was then indium-soldered to the strip-line and terminated by another solder connection to RF ground.

An important concern in this type of experiment is verifying the coaxial cable and applied microwave radiation do not appreciably heat the sample. To provide the best thermal contact possible, the sample is immersed in liquid ^{3}He and the temperature is measured with a Speer 470 Ω resistor. It is easy to heat the sample and the ^{3}He bath by applying excessive microwave power. For powers less than 1 nW, both the Speer temperature and the sample resistance measurements were found to become power independent.

Since the cryostat was equipped with one coaxial cable the impedance of the 2DES was measured in reflection; a more challenging experiment than transmission. Reflection measurements were performed using an HP network analyzer, which records both the magnitude and the phase of the signal.

Extracting the impedance of the sample from the measured reflection requires several steps. The coefficient $\Gamma(\omega)$ is defined as the ratio of reflected voltage to input voltage, and is related to the impedance by (assuming standard 50 Ω coaxial cables)

$$\Gamma(\omega) = \frac{Z - 50\Omega}{Z + 50\Omega}.$$

The impedance computed from the raw data is that of the sample and the coaxial cable in series. This raw data must be corrected in magnitude to include the attenuation of the cable (5dB), and in phase to take into account the finite length of the cable (1.5 meters).

2.4 RESULTS

The results presented here are for the two extreme cases. The first is when most of the sample is ungated, and the second is when the gates cover the majority of

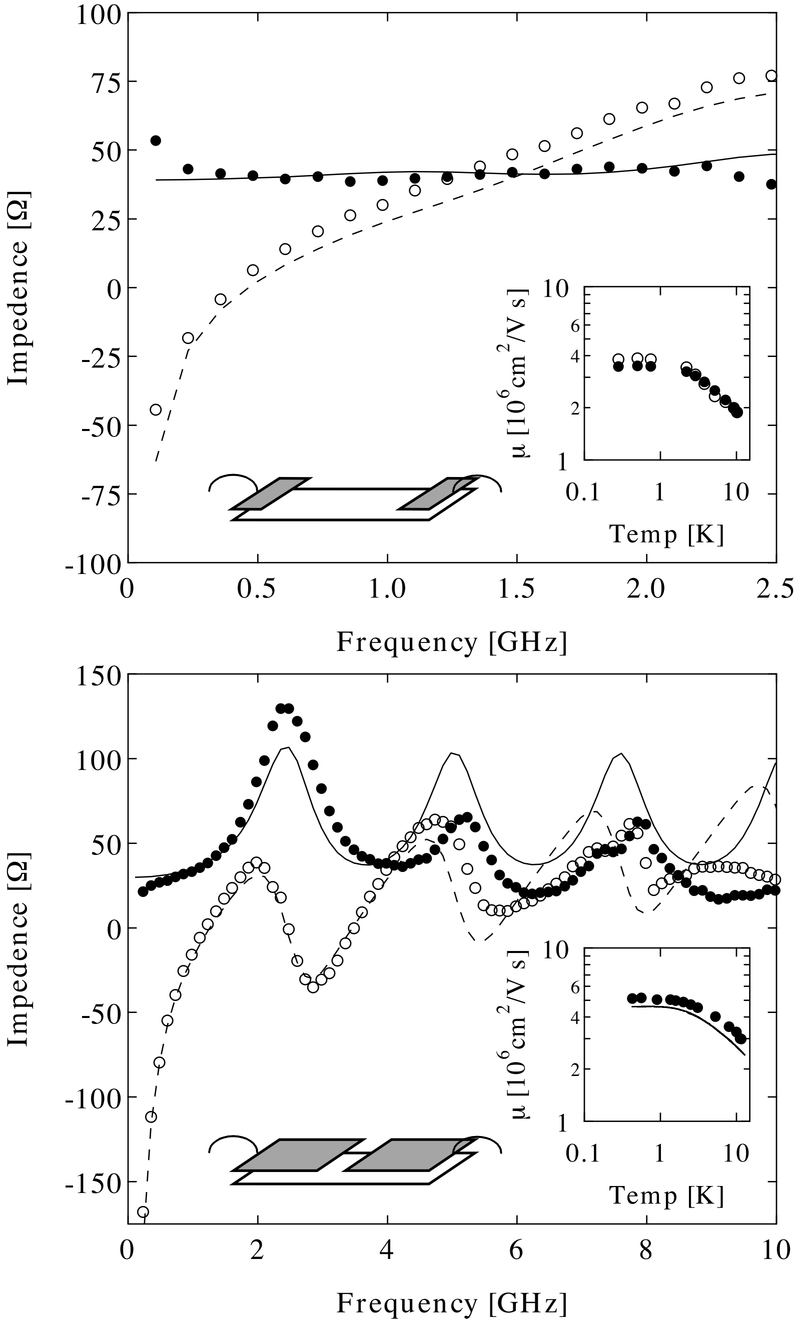

Figure 2.5: In both panels the solid (empty) markers are the real (imaginary) components of the data, while the solid (dashed) lines are real (imaginary) results of a Drüde model calculation. Top: RF conductivity with the majority of the sample ungated. Bottom: RF conductivity with the majority of the sample gated. Note the resonances in the bottom panel corresponding to plasmon standing waves in the sample with wavelength $\lambda = 2L/n$, where n is the mode index and L is the sample length.

the sample (Figure 2.4). In the former, case the system can be considered as two capacitors in series with the AC Drüde impedance. In the second case, the device is essentially two 2DES plasmon resonators in series.

The top of Figure 2.5 contains representative data taken from Sample A in which the majority of the sample is ungated and acts as the series combination of an inductor and a resistor. The continuous curves represent the Drüde model predictions, with the mobility as a single fitting parameter. The 2DES is buried 5800 Å below the sample surface, and has lateral dimensions 510×2560 μm. The gates are 330 μm and 680 μm long. The measured electron density is 1.5×10^{11} cm^{-2}, and the mobility from the fit is 3.8×10^{6} cm^2/Vs, while the mobility from the ratio Z_{im}/Z_{re} is 3.3×10^{6} cm^2/Vs. The inset shows the comparison of these two different measurements of mobility vs. temperature, and confirms good agreement between the two.

Sample B, taken from the same wafer as Sample A, was fabricated to measure the plasma modes in the fully gated geometry. In this case, the mesa is 100×780 μm, and the gates are 360 μm in length. The resulting ungated region is 60 μm in length. The overall slope to the imaginary part of the data results from this ungated region. Again, the data was fit using the mobility as the only free parameter, which was found to be 3.9×10^{6} cm^2/Vs, in agreement with the results of the previous section. The inset to the figure shows measured mobility using this fitting technique vs. temperature, which is in good agreement with the data from the ungated sample.

To complete this experiment, the dependence of the plasmon dispersion on electron density is measured. The dotted line in Figure 2.6 is the dispersion predicted by Equation 2.3. The solid markers are the velocity extracted from a fit to the plasmon model, while the empty markers are from the location of the first peak in $Z_{re}(\omega)$ vs. frequency. It is unclear why the measured results always over-estimate the model predictions, however, the data are still in surprisingly good agreement with the simple model.

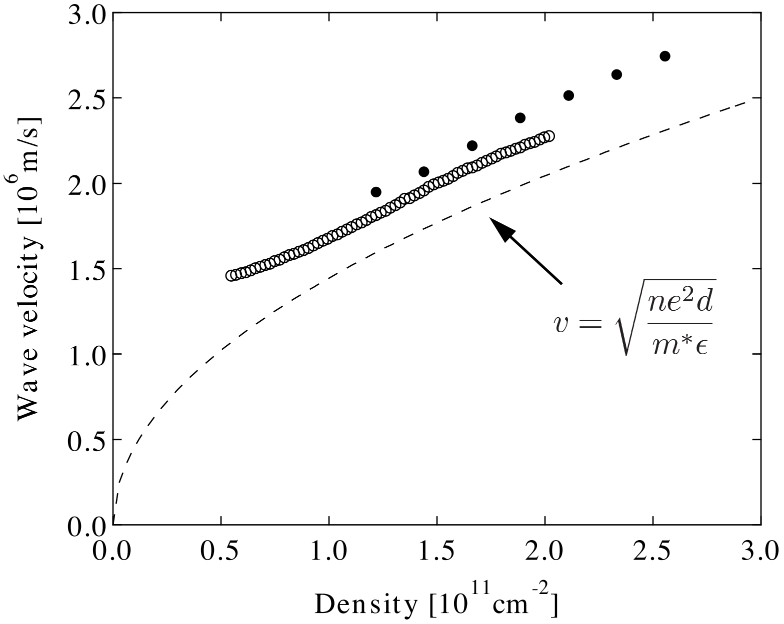

Figure 2.6: Observed wave velocity (markers) compared to model results (dashed line). The solid markers correspond to a fit to the Drüde model result, while the empty markers used the location of the first resonance in Z_{re} vs. f

2.5 Quantum mechanical electrons

The final section of this chapter is a brief summary of some important properties and relationships in a noninteracting *quantum* 2DES. The zero temperature properties of quantum electrons in 2D are first discussed in the absence of a magnetic field, then extended to the case of a field perpendicular to the plane of the 2DES.

Suppose we have a square 2DES with side L; the single particle solutions have energy $E = \hbar^2 k^2 / 2m^*$ and are plane waves confined to set of discrete wave-numbers by the finite sample size: $k_x = 2\pi n / L$ and $k_y = 2\pi m / L$. Together with the electron spin, each pair (k_x, k_y) describes a single quantum state. Electrons are fermions, so each such state can contain at most one electron.

The ground state of N_e electrons is the configuration which minimizes the energy; in 2D this corresponds to filling a circle of momentum states with radius $k_f^2 \geq k_x^2 + k_y^2$ with electrons. The Fermi momentum k_f, and equivalently the Fermi energy $E_f = \hbar^2 k_f^2 / 2m^*$, therefore determines the number of electrons.

The density of electron states in the k_x–k_y plane is $(L/2\pi)^2$; the number of elec-

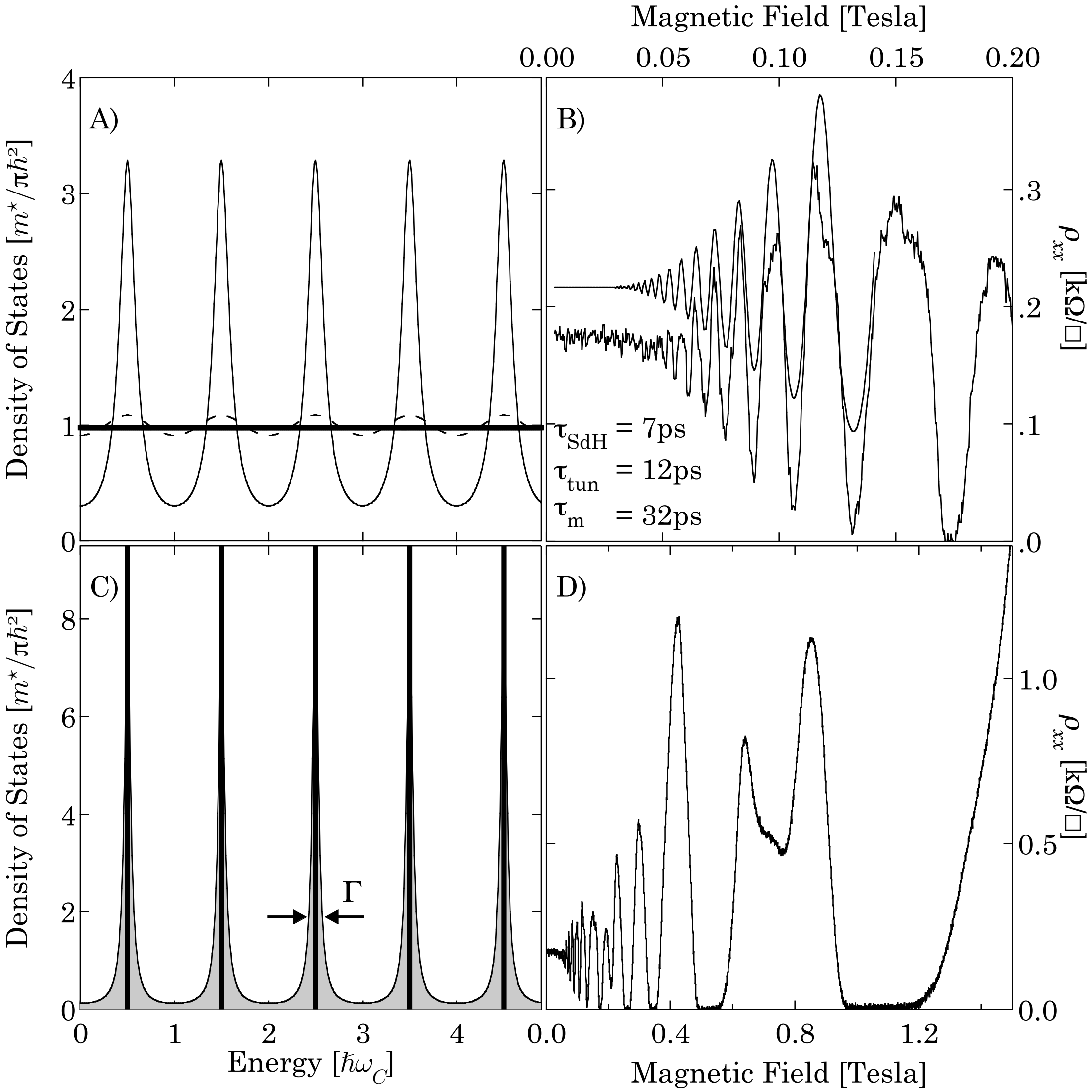

Figure 2.7: A) density of states at nonzero magnetic field with finite disorder, parameterized by Γ (in all of these curves Γ is assumed to be much larger than the spin splitting). Bold: $\Gamma \gg \hbar\omega_c$ in this case the zero field result is regenerated. Dashed: $\Gamma \sim \hbar\omega_c$ here the density of states is periodically modulated around the zero field value. Solid: $\Gamma \ll \hbar\omega_c$ in this case there are large peaks centered on each Landau level index. B) SdH oscillations, data: bottom curve, top: model offset by 50 Ω. C) density of states in the quantum Hall regime. Shaded region indicates localized states and the bold vertical lines are extended states. D) typical quantum Hall data, ρ_{xx} vs. B.

trons (in both spin states) with momentum less than k_f is easily found to be

$$\begin{aligned}\frac{N_e}{L^2} &= \frac{k_f^2}{2\pi} \\ &= \frac{m^*}{\pi\hbar^2}E_f.\end{aligned}$$

Evidently the states are uniformly distributed in energy, i.e., the 2D density of states $g(E)$ is constant and equal to $g(E) = m^*/\pi\hbar^2$. For free 2D electrons this quantity is quite uninteresting; a fixed δE will always result in the same δn. As we will see shortly, a perpendicular magnetic field dramatically changes $g(E)$.

The application of a magnetic field to classical electrons yields objects in circular orbits, all at the cyclotron frequency $\omega_c = eB/m^*$, and the cyclotron radius $r_c = \sqrt{2m^*E}/eB$. Scattering can determine when the magnetic field is relevant. If scattering events occur rapidly, i.e., if $\omega_c < 1/\tau_m$, then the electron trajectory is a set of almost straight segments and can be considered to be at zero field. As ω_c becomes larger, however, the electron can complete full orbits and the magnetic field becomes very important.

Quantum mechanically the detailed wavefunction describing an electron in a magnetic field is dependent on the choice of gauge, however, no measurable quantities can be affected. Here we use the Landau gauge, which is mathematically convenient; in this gauge the vector potential is chosen to be $\mathbf{A} = (0, Bx, 0)$.

The energy spectra is found to be $E_N = (N - 1/2)\hbar\omega_c$, suggesting that the Hamiltonian is closely related to the simple harmonic oscillator (SHO). In the x direction the solutions are the SHO wavefunctions which consist of a Gaussian term modulated by $H_j(x)$, the j^{th} Hermite polynomial. The y part of the wavefunction is a traveling wave; together these form the full wavefunction,

$$\Psi_{N,k} = H_{N-1}\left(\frac{x - x_k}{l_B}\right)\exp\left(-\frac{(x - x_k)^2}{2{l_B}^2}\right)\exp\left(iky\right).$$

This equation has introduced the magnetic length $l_B = \sqrt{\hbar/eB}$, which describes the width of the SHO wavefunctions; note that l_B is not the classical cyclotron radius!

Each energy eigenstate is labeled by two quantum numbers, N and k, however, $\Psi_{N,k}$ is degenerate in the index k, which is related to x_k by $x_k = -{l_B}^2 k$.

An expression for the degeneracy can be computed by assuming the system has lateral dimensions $L \times L$ with periodic boundary conditions in the y direction. The finite system discretizes $k = 2\pi m/L$, and as a result $\Delta x_k = 2\pi {l_B}^2/L$, since the system has finite length in the x direction, the total number of states is $N_e = L/\delta X = L^2/2\pi {l_B}^2$. This leads to the conclusion that each energy eigenstate is macroscopically degenerate with a spacial particle density (in an infinite system each eigenstate is infinitely degenerate) $n = eB/h$.

Although the Landau gauge is perfectly suited for understanding the behavior of noninteracting electrons, the symmetric gauge in which $\mathbf{A} = B \times (-y/2, x/2, 0)$, is more convenient for a later description of interacting systems. For reference, the un-normalized wavefuctions of a single noninteracting electron in the lowest Landau level are given by

$$\begin{aligned} \psi_l &= \exp(-il\theta) r^{|l|} \exp\left(-\frac{r^2}{4{l_B}^2}\right) \\ &= z^{|l|} \exp\left(-\frac{|z|^2}{4}\right), \end{aligned}$$

where $z = (x - iy)/l_B$ is the single complex number conventionally used to describe position in the $x - y$ plane. l determines the angular momentum, in which the noninteracting states are degenerate for positive l.

The configuration of N noninteracting electrons in the lowest Landau level, filling the lowest N angular momentum states, can be expressed as the antisymmetrized product

$$\psi = A\left\{\prod_j^N \psi_j(x_j)\right\} \prod_j^N \exp\left(-\frac{|z_j|^2}{4}\right).$$

This antisymmetrized wavefunction can be explicitly expressed as the Slater determinate,

$$\psi = \begin{vmatrix} 1 & 1 & & 1 \\ z_1 & z_2 & \cdots & z_N \\ & \vdots & \ddots & \\ z_1^{N-1} & z_2^{N-1} & & z_N^{N-1} \end{vmatrix} \prod_j^N \exp\left(-\frac{|z_j|^2}{4}\right).$$

This is a Vandermonde determinant and can be exactly evaluated leading to the simple form,

$$\Psi = \prod_{j<k}^N (z_j - z_k) \prod_j^N \exp\left(-\frac{|z_j|^2}{4}\right). \tag{2.4}$$

It is interesting, that even in the absence of Coulomb repulsion, the electrons avoid each other, with a density-correlation which scales like r^2. This "repulsion" be interpreted as manifestation of the Pauli principle which requires the wavefunction be zero whenever any pair of electrons coordinates are equal.

Electrons also have two spin states, which have been neglected so far. In a magnetic field the two spin states are split by $\delta E = g\mu_B B$. In GaAs the spin splitting much smaller than the cyclotron splitting: $g\mu_B B/\hbar\omega_c = 0.014$ (where $\mu_B = 9.27 \times 10^{-24}$ A $\cdot$ m^2 is the Bohr magneton, and $g = -0.44$ is the Landè g-factor in GaAs). The Landau level index N identifies the orbital states, while the index $|\uparrow\rangle$, or $|\downarrow\rangle$ denotes the spin state. The *Landau level filling factor* $\nu = hn/eB$ is the ratio of the total electron density to the density of magnetic flux quanta (eB/h). Evidently $\nu = 1$ when the lowest spin-resolved Landau level is completely filled, $\nu = 2$ when both spin branches are filled, etc.

2.5.1 Resistance measurements in a weak magnetic field

In the Drüde model we found that the longitudinal resistance ρ_{xx} was independent of magnetic field, and the Hall resistance ρ_{xy} increased in proportion to the field. We are now prepared to see how the quantization of electrons into Landau levels affects the resistance.

Although more sophisticated models for disordered 2DES in magnetic fields exist [38], for the sake of simplicity we will treat a very simple case. To model the effects of disorder, we shall assume that the Landau levels are broadened by a Lorentzian factor, with a half-width Γ. Therefore the broadened density of states is the sum

$$g(E) = 2\frac{eB}{h}\sum_{N=0}^{\infty}\frac{1}{\pi\Gamma}\left[1+\left(\frac{E-E_N}{\Gamma}\right)^2\right]^{-1}.$$

In which the leading factor of two accounts for spin degeneracy, and the Zeeman splitting is neglected (an assumption which is suitable when Γ is larger than the Zeeman gap).

In a weak magnetic field ($\Gamma > \hbar\omega_c$) this summation can be evaluated exactly, resulting in

$$g(E) = \frac{m}{\pi\hbar^2}\left[1-2\exp\left(-\frac{2m\pi\Gamma}{eB\hbar}\right)\cos\left(\frac{2m\pi E}{eB\hbar}\right)\right].$$

The conductivity of a 2DES is simply proportional to the square of the density of states at the Fermi energy. Therefore the shift in $g(E)^2$ will result in a proportional change in the conductivity σ_{xx}, and therefore, ρ_{xx}. This predicts a series of oscillations, periodic in $1/B$, called the Shubnikov de Haas (SdH) effect. The oscillations increase in amplitude with increasing B. At low magnetic field occur they only at even filling factors since $\Gamma \gg g\mu_b B$. The results of this low-field analysis are displayed in panel B) of Figure 2.7 (for more details on this type of analysis see Mani *et al.* [44]). From the fit to measured SdH oscillations we estimate the lifetime $\tau_{\mathrm{SdH}} = \hbar/2\Gamma$ which results in a time of $\tau_{\mathrm{SdH}} = 7$ ps. This time is comparable to the tunneling lifetime, $\tau_{\mathrm{tun}} = 12$ ps, but somewhat less the mobility scattering time $\tau_m = 32$ ps (see Chapter 3 for more details on this discrepancy).

2.5.2 Resistance measurements in a large magnetic field As the magnetic field increases, spin resolved SdH oscillations become visible. The resistance minima of the oscillations continue to deepen until they reach zero, and remain at zero for an extended range of fields centered on integer filling ν. These extended zeros and the accompanying plateaus at $\rho_{xy} = h/\nu e^2$ are the signature of the IQHE.

Using the description of electrons in disorder broadened Landau levels is possible to qualitatively understand the IQHE. Here we again ignore the effect of spin, which in this picture does little more than double the number of available states. Even at high magnetic field, the understanding of the IQHE depends centrally on disorder.

Figure 2.7 panel C) displays the disorder broadened Landau level density of states; the central delta functions contains states which are assumed to be "extended" and can carry current. The body of states surrounding each delta function are further assumed to be "localized" states due to disorder, and are unable to carry current. If the Fermi energy resides in the extended states then the system is conducting; however, as soon as the Fermi energy enters the localized states there are no mobile low-energy excitations and the system becomes insulating – these are the regions where the Hall resistance is quantized and σ_{xx} (and therefore ρ_{xx}) is zero. Evidently, by increasing the number of localized states, the quantum Hall features can span a wider range of filling factors, i.e., a more disordered sample can have stronger and wider integer quantum Hall features.

Like the zeros in ρ_{xx}, the Hall plateaux are extended over a wide range of filling factors centered on an integer ν. It has been argued that whenever there exists a gap to charged excitations, a quantized Hall effect must occur (see [45] and references therein). Once the conductivity drops to zero, no current can flow through the samples bulk. To understand the quantized Hall resistance we turn instead to the edge states.

The top panel of Figure 2.8 shows the Landau level spectrum as a function of position including the effect of an edge. As can be seen from the figure, the energy increases as the edge is approached, and every Landau level that is initially below E_f crosses at some point. Since the conductivity is determined by states near E_f, these "edge states" must determine the observed longitudinal and Hall resistivity's.

Classically, electrons traveling at an abrupt interfaces follow a "bouncing" trajectory along the interface. If $\mathbf{n}$ is the vector normal to the interface, then the electrons travel with an average velocity in the $\mathbf{n} \times \mathbf{B}$ direction. These electrons travel in only one direction at the interface. The corresponding quantum states are chiral edge states – with uni-directional current flow.

From the Laudauer-Büttiker theory of quantum transport [46], we expect each of these channels to contribute a conductivity e^2/h in the absence of scattering. It is remarkable that in the QHE regime this condition holds even on macroscopic length

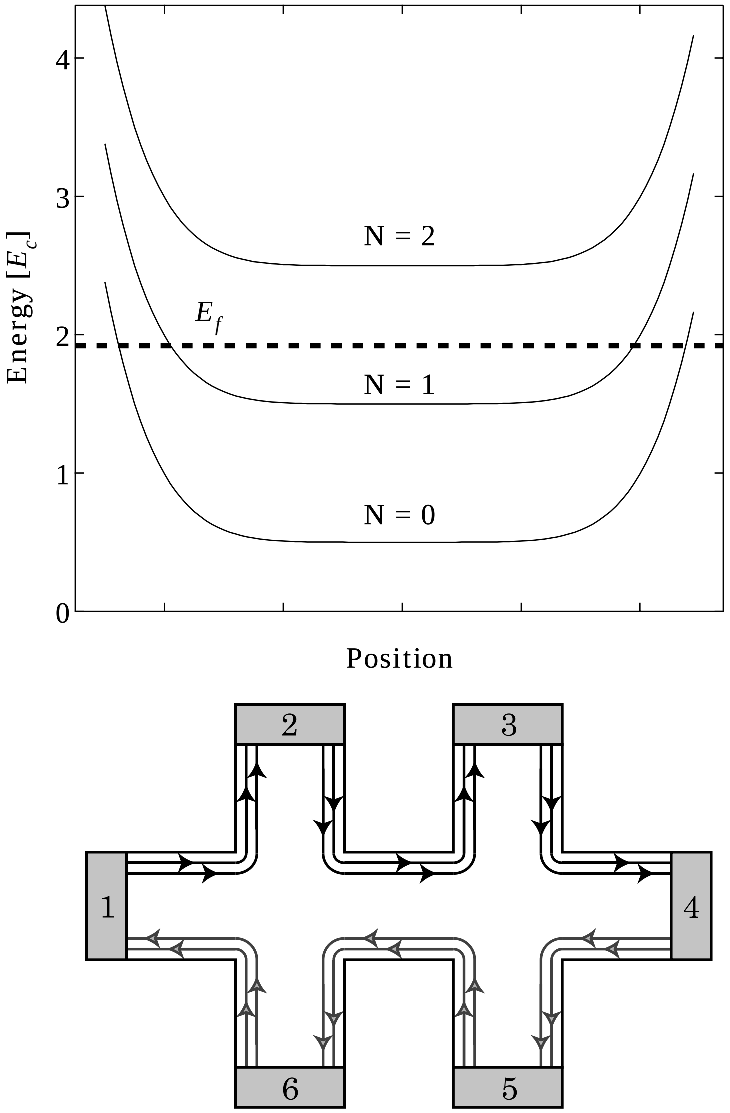

Figure 2.8: The top panel shows the dependence on position of the energy spectra of electrons in units of the cyclotron energy $E_c = \hbar\omega_c$. The dotted line represents the Fermi energy; in this case there are two Landau levels below E_f in the bulk. The bottom panel schematically depicts the edge states resulting from the two occupied Landau levels.

scales. Since the edge states are chiral, a backscattering event must transfer momentum from the edge state on one side of the sample to the counter-propagating state on the other side. For large samples this never occurs. Therefore we can analyze a macroscopic sample in terms of a mesoscopic theory.

In the Laudauer-Büttiker formalism, the net current leaving a contact is given by $I = \Delta V N e^2/h$. N is the number of channels, and ΔV is the difference in potential between the arriving and outgoing electrons.

In the specific case illustrated in Figure 2.8 there are two edge states available. When a current is driven from contact 1 to contact 4, we argue:

1. Since a current I is leaving contact 1: $V_1 - V_6 = Ih/2e^2$;
2. Since no current is sunk in contacts 2 and 3: $V_2 - V_1 = 0$, and $V_3 - V_2 = 0$;
3. Contact 4 is the current sink, so $V_4 - V_3 = -Ih/2e^2$; and
4. No current is sunk by contacts 5 and 6 so: $V_4 - V_5 = 0$ and $V_5 - V_6 = 0$.

These items form a system of linear equations which have the solutions

$$V_1 - V_4 = I\frac{h}{2e^2}, \qquad R_{xy} = V_3 - V_5 = I\frac{h}{2e^2}, \qquad \text{and} \qquad R_{xx} = V_2 - V_3 = 0.$$

The experimental signatures of the quantum Hall effect are correctly understood in this framework. Because the Fermi energy is pinned by disorder between Landau levels, these features are extended over a range of filling fractions. For a more complete discussion, see the text by Datta [47].

2.6 CONCLUSION

This chapter showed RF resistance measurements that are in amazingly good agreement with the predictions of the Drüde model. Peering deeper, there were details of the experiment that need further explanation. For example, the addition of a perpendicular magnetic field in the Drüde model resulted only in a constant R_{xx} and $R_{xy} \sim B$.

To understand the deviations between the Drüde model and the observations, the quantum mechanics of noninteracting electrons were introduced. These additional physics led first to SdH oscillations in the resistance, then at higher fields, the combination of disorder and quantized electron orbitals gave rise to the integer quantum Hall effect.

Chapter 3

2D-2D Tunneling at Zero Magnetic Field

This chapter introduces electron tunneling between two parallel 2DES at zero magnetic field. Although there are a wide range of physics unique to strongly coupled bilayer systems, the data in this chapter reflect a regime where 2D-2D tunneling is used to probe the physics of the individual layers.

The ability to make separate electrical contact to each of the 2D layers [34] opens the door to fundamentally new experiments beyond parallel ρ_{xx} and ρ_{xy} measurements. For example, the inter-layer tunneling current can be measured by making one contact to the top layer and a second to the bottom; a voltage V applied between the layers will result in a tunneling current $I(V)$. In the case of 3D-3D tunneling the current is linear in the voltage, i.e., Ohmic. In the case of 2D-2D tunneling, however, the ratio I/V vs. V is generally observed to be Lorentzian; its half-width at half-max (HWHM), Γ, is directly related to the quasiparticle lifetime in the individual 2D layers.

This chapter will first discuss the structure and fabrication of samples used in such tunneling experiments, then continue describing the measurement circuit, and finally end with an introduction to the physics of electron tunneling between two weakly coupled 2DES's. I/V can be computed in perturbation theory using Fermi's golden rule, resulting in predictions for the width and the magnitude of the tunneling resonance. The low-temperature line width reflects scattering from static disorder, and is compared to the scattering rate from DC mobility measurements.

When tunneling can be treated as a perturbation, it is possible to relate a measured quantity, $\int I/V dV$, to the symmetric-antisymmetric splitting, Δ_{SAS}, of the double

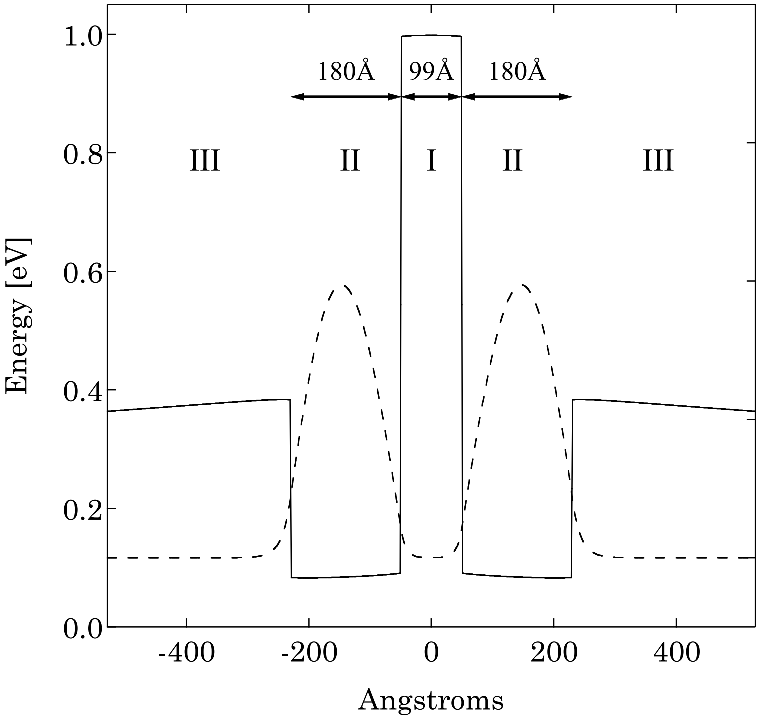

Figure 3.1: Solid: computed conduction band including self-consistent potentials. Dashed: ground state wavefunction for Sample E.

quantum well. Δ_{SAS} can also be numerically computed for a specific structure. The results of these two independent determinations of Δ_{SAS} are within a factor of two.

An analysis of the temperature dependence of the line width, Γ, provides a direct measurement of the electron-electron scattering rate. The initial measurements of Murphy *et al.* [48] were found to be in disagreement with theoretical expectations [49, 50]. More recent calculations by Jungwirth *et al.* [51] and Zheng *et al.* [52] have reconciled the two. Our observations in lower density samples are consistent with the earlier data from Murphy *et al.*

The chapter concludes with a brief discussion of the effects of a perpendicular magnetic field on tunneling. At low fields, the tunneling conductance oscillates in $1/B$, reminiscent of the SdH oscillations in ρ_{xx}. At high fields, the tunneling is suppressed due to a Coulomb pseudo-gap.

3.1 STRUCTURE AND MEASUREMENT

The physical systems under study are double quantum well heterostructures. We make independent electrical contact to each of the wells and measure electron tunneling from one layer to the other. The states labeled by $|\psi_T\rangle$ and $|\psi_B\rangle$ denote an electron in either the top or bottom layer. Neither of these quantum mechanical layer states are eigenstates state of the double-layer system – for the symmetric structure shown in Figure 3.1 – the symmetric combination, $(|\psi_T\rangle + |\psi_B\rangle)/\sqrt{2}$, is the ground state, while the antisymmetric combination, $(|\psi_T\rangle - |\psi_B\rangle)/\sqrt{2}$, is the first excited state. The difference in energy between these states is denoted by Δ_{SAS}. A carrier that starts in one layer will oscillate between them with angular frequency $\omega = \Delta_{\mathrm{SAS}}/\hbar$. When the scattering rate in each layer τ^{-1} is much faster than the tunneling rate, the electrons come to equilibrium in an individual layer between tunneling events. In this limit, the description of independent layers is justified. In other words, $\tau \ll \hbar/\Delta_{\mathrm{SAS}}$. For a high-mobility 2DES, typical scattering times range from 10 to 100 ps; numerical calculations indicate $\Delta_{\mathrm{SAS}} \approx 0.5$ neV in our devices. As a result, an electron scatters about 1000 times between each tunneling event.

The majority of the data discussed in this chapter comes from Sample E, a weakly tunneling GaAs/AlGaAs bilayer consisting of two layers of electrons each with density 0.55×10^{11} cm^{-2} and mobility 1.2×10^{6} cm^2/Vs. This sample consists of two 180 Å GaAs wells (regions II) separated by a 99 Å $\mathrm{Al_{0.9}Ga_{0.1}As}$ barrier (region I). The silicon dopants are set back by 2300 Å of $\mathrm{Al_{0.3}Ga_{0.7}As}$ below and by 2050 Å above. The computed conduction band and resulting ground state wavefunction are illustrated in Figure 3.1.

Figure 3.2 shows a sample in a typical tunneling geometry; two contacts are connected to the top layer and two to the bottom. The central tunneling mesa is a 250 × 250 μm square, covered above and below with evaporated aluminum gates to control the electron density in each. A 40 μm wide arm equipped with top and back depletion gates extends from each side of the central square and is terminated by a AuNiGe Ohmic contact.

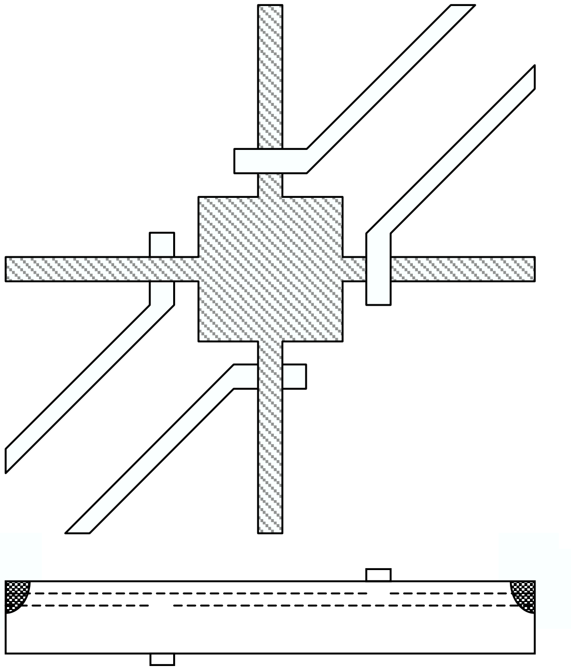

Figure 3.2: Top: top-down view of a sample in the tunneling geometry; bottom: cross section of tunneling geometry

By appropriately biasing the gates above and below the bilayer, electrical contact can be made to each layer individually [34]. For example, a voltage of −0.5 V on a top gate will deplete all the carriers in the nearby top layer, resulting in conduction only through the bottom layer. Depleting the bottom layer with a back gate voltage of −50 V prevents conduction through the back layer (see Figure 3.2). The samples are usually processed as described in Appendix B.6.5, resulting in a sample with back gates set back 50 μm from the 2DES (as a consequence back gate voltages are often −50 to −200 V). A slightly more sophisticated technique (Appendix B.6.6) results in samples only 1 or 2 μm thick.

The measurement circuit (Figure 3.3) consists of two essential parts: bias and detection. The cryogenic elements begin with a set of manganin twisted pairs running from room-temperature. The leads are thermally lagged at several points in the cryostat. Appendix C details the heat sinking and RF filtering installed in the newer, KelvinOx 25 dilution cryostat. The older KelvinOx 400 system is heat-sunk in much the same way, but lacks powder RF filters.

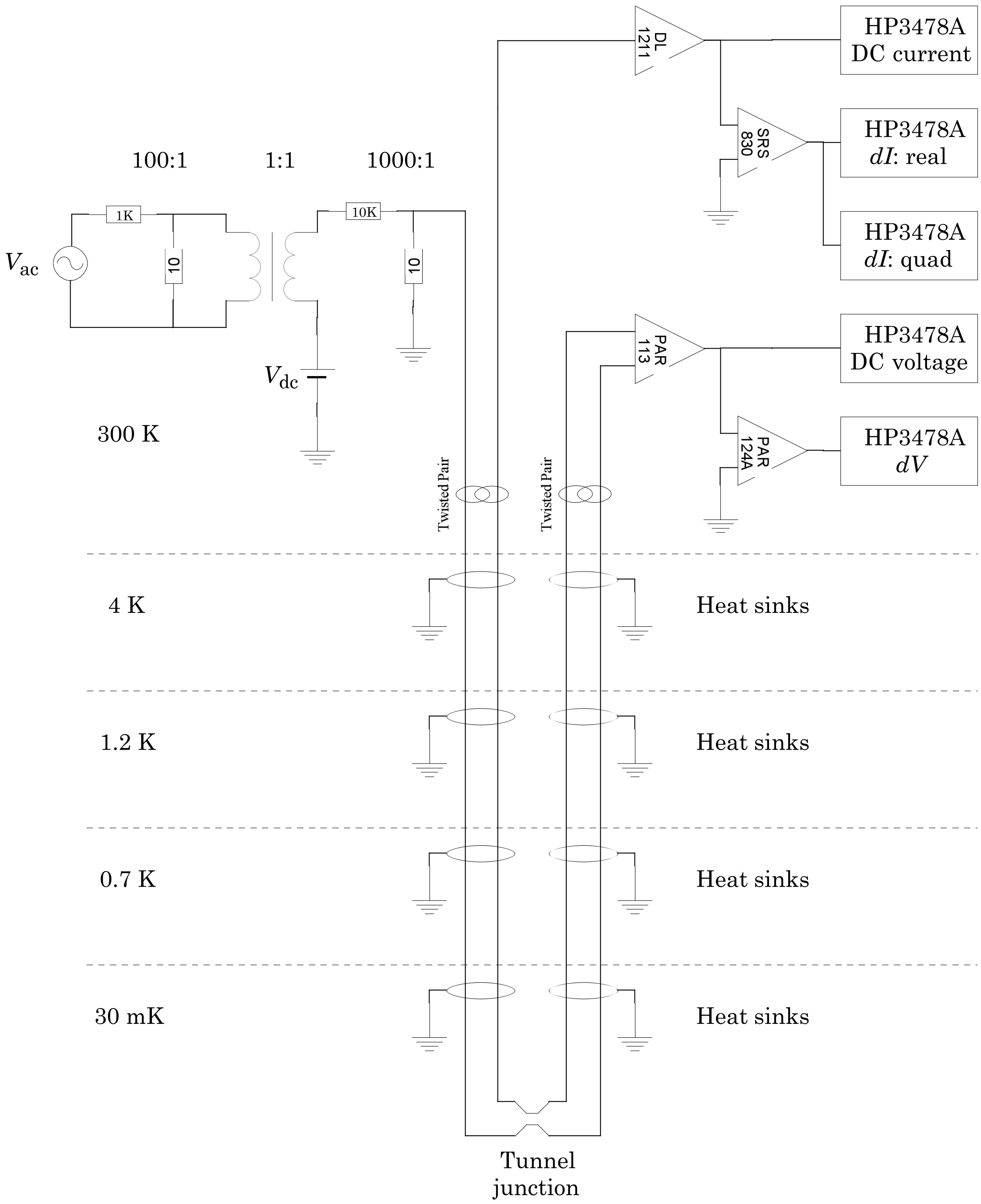

Figure 3.3: Circuit used in tunneling measurements, illustrating the thermal profile and heat sinking for experiments performed in a dilution refrigerator.

The biasing circuit is designed to create a voltage composed of a DC part (generally spanning -1000 to 1000 μV at 2.5 Hz) plus a small sinusoidal AC part (from 0.1 to 10 μV). The initial AC voltage, sourced from the reference channel of a lock-in amplifier (SRS 830 or PAR 124A), has a range of 0.1 to 10 V, and is initially divided by either 100 (as illustrated) or 1000, and added to the DC part of the bias circuit with a 1:1 transformer. The DC voltage source (Kepco 488-122 programmer) has an output range of -10 to 10 V and is either connected directly to one terminal of the transformer (as illustrated), or divided by 10 first. The composite AC+DC signal is fed into a final 1000:1 divider, and connected to one terminal of the tunneling device.

The detection apparatus is also located at room-temperature and detects the current through and voltage across the junction. The current through the tunnel junction is measured with a DL Instruments 1211 low noise current preamp. The amplified signal is fed directly into a voltmeter. In addition, the amplified current signal is measured by a SRS 830 lock-in amplifier, which outputs to DVMs both the real and quadrature part of the AC current signal. The voltage across the tunnel junction is directly measured with a PAR 113 preamplifier, from which both the DC and AC parts are recorded.

Due to the finite resistance of the leads to the sample (this includes both the wires, and the resistance of the 2D arms leading to the central tunneling square), the voltage across the sample can differ from the applied voltage. In many cases, the tunneling resistance is much larger than any lead resistances, and a two terminal measurement can be made.

Detecting the AC current provides an analog measurement of dI/dV, the derivative of the $I - V$, and generally is less noisy than the numerical derivative. The first two terms of the Taylor expansion of $I(V)$ about V_{DC}, with a small AC voltage $V_{\mathrm{AC}} \sin \omega t$ are

$$I(t) \approx I(V_{\mathrm{DC}}) + \frac{dI}{dV} V_{\mathrm{AC}} \sin \omega t.$$

The DC part of $I(t)$ is the usual DC voltage, while the ratio $I_{\mathrm{AC}}/V_{\mathrm{AC}}$ approximates the derivative dI/dV, provided that V_{AC} is smaller than any scale on which there are features in $I(V)$. Finally, any quadrature signal in I_{AC} stems from the inter-layer capacitance.

Perhaps the most challenging aspect of this experiment has been reducing pickup of stray 60 Hz noise. This has been achieved by grounding the cryostat at just one well defined point, and by operating the amplifiers in battery mode. Implementing the first generally yields a rms 60 Hz signal of about 2 μV, which can drop below 0.1 μV when the amplifiers are operated in battery mode. This can be slightly improved by requiring that only twisted pairs span the tunnel junction.

60 Hz pollution is not only a problem in terms of signal-to-noise. In the case of tunnel junctions, voltage noise across the junction changes the measured low-frequency $I-V$ and dI/dV data. This can be understood intuitively by imagining some sharp feature in $I-V$, with the bias voltage oscillating rapidly over a wide range. In this case, a DC measurement of current will be some average over that wide voltage range. Consequently, any AC voltage noise across the tunnel junction must be smaller than the width of the sharpest features in $I-V$.

3.2 2D-2D TUNNELING

Tunneling between two weakly coupled 2DES can be described using a generalized Fermi's golden rule expression (for a general background see [53]). Such an expression is a perturbative result, which is only valid in systems such as ours, in which tunneling events are rare and occur incoherently. Computing the current from one layer to the other essentially counts the number of full states in one layer and pairs them with empty ones in the other (including a leading factor of 2 to account for spin degeneracy). The resulting current density is

$$\begin{aligned} I_{12}(eV) \;&=\; \frac{2e}{\hbar}\overbrace{\int\frac{d^2\mathbf{k_1}}{(2\pi)^2}\int\frac{d^2\mathbf{k_1}}{(2\pi)^2}|t(\mathbf{k_1},\mathbf{k_2})|^2}^{\text{matrix elements for tunneling}}\int_0^\infty\frac{dE_1}{2\pi}\int_0^\infty\frac{dE_2}{2\pi}A(E_1,\mathbf{k_1})A(E_2,\mathbf{k_2}) \\ &\quad\times\underbrace{\delta(E_1+eV-E_2)}_{\text{energy conservation}}\underbrace{n_f(E_1)\left[1-n_f(E_2)\right]}_{\text{filled}\,\times\,\text{empty}}. \end{aligned}$$

I_{12} is the current from layer 1 to layer 2, and I_{21} is the opposite. n_f is the Fermi function, and the spectral function $A(E, \mathbf{k})$ describes the momentum distribution of a state with energy E. Recall the energy eigenstates of the disordered-interacting 2DES are not plane waves. For an ideal, noninteracting system the eigenstates are also momentum states, and $A(E, \mathbf{k}) = \delta(E - \hbar^2 k^2/2m)/2\pi$. The tunneling matrix element, $t(\mathbf{k_1}, \mathbf{k_2})$, between the two momentum states gives the amplitude for tunneling from a momentum state $\mathbf{k_1}$ in the first layer to state $\mathbf{k_2}$ in the second. The total current is the difference $I_{12} - I_{21}$ and can be simplified to read

$$\begin{aligned} I(eV) &= \frac{2e}{\hbar} \int \frac{d^2\mathbf{k_1}}{(2\pi)^2} \int \frac{d^2\mathbf{k_2}}{(2\pi)^2} |t(\mathbf{k_1}, \mathbf{k_2})|^2 \int_0^\infty \frac{dE}{2\pi} A(E, \mathbf{k_1}) A(E + eV, \mathbf{k_2}) \\ &\quad \times \left[n_f(E) - n_f(E + eV) \right]. \end{aligned}$$

This result can be further reduced by evaluating one energy integral, and by assuming that tunneling conserves and is independent of momentum, i.e., $|t(\mathbf{k_1}, \mathbf{k_2})|^2 = t^2 \delta(\mathbf{k_1} - \mathbf{k_2})$ (in a simple single particle model $t = \Delta_{\mathrm{SAS}}/2$). This also assumes that when the bias voltage, V, is applied between the wells the resulting distortion of the barrier is negligible. The resulting current density is (see for example [51])

$$\begin{aligned} I(eV) &= \frac{2et^2}{\hbar} \int \frac{d^2\mathbf{k}}{(2\pi)^2} \int_0^\infty \frac{dE}{2\pi} A(E, \mathbf{k}) A(E + eV, \mathbf{k}) \\ &\quad \times \left[n_f(E) - n_f(E + eV) \right]. \end{aligned} \tag{3.1}$$

Although very general, Equation 3.1, relies on the assumption $\Delta_{\mathrm{SAS}} \ll \Gamma$; in other words, between tunneling events, an electron is in one layer or the other for many quasiparticle lifetimes. Further assumptions are:

1. $k_B T \ll E_f$;
2. The spectral function is narrow compared to E_f [54]; and
3. The spectral function can be written in the form $A(E, \mathbf{k}) = A(E - \hbar^2 k^2/2m)$ (as is the case for Lorentzian broadening at the Fermi surface).

These requirements permit considerable simplification of the tunneling integral, leading to the conductance, $g = I/V$ per-unit area [55]

$$g(eV) = \frac{e^2t^2}{2\pi\hbar}\frac{m}{\pi\hbar^2}\int_{-\infty}^{\infty} dx A(-x)A(eV-x). \tag{3.2}$$

The tunnel conductance is simply the convolution of the spectral functions. This result is independent of temperature, except to the extent that the spectral functions themselves may be temperature-dependent. That is to say, the smearing of the Fermi circle has no impact on the tunnel conductance!

By using the fact that the spectral functions are normalized to 2π, this result can be integrated to find a simple expression relating the total conductance and the tunneling matrix element,

$$\int_{-\infty}^{\infty} g(eV)d(eV) \quad = \quad \frac{2\pi e^2t^2}{\hbar}\frac{m}{\pi\hbar^2}. \tag{3.3}$$

In the case of Lorentzian broadening, the integral is calculable and the resulting relation between lifetime and t^2 was noted by Zheng *et al.* [55]. However, our final expression is independent of the specifics of the spectral functions, such as the scattering time. This integral provides a new way to relate a measurable quantity, the integrated ratio I/V, to the intrinsic tunneling strength. In weakly tunneling samples this was previously accessible only via numerical simulations, not direct measurement.

When a voltage is applied between the layers, charge shifts capacitively. As a result the energy difference between the bottom of the wells (the quantity relevant for momentum conservation) is enhanced by a factor of $1 + 2\pi\hbar^2c/m^*e^2$, where c is the capacitance per-unit area. For the samples described here, this is an 18% effect.

3.3 ELECTRON-IMPURITY LIFETIME

Figure 3.4 illustrates typical tunneling data taken at the nominal per-layer density of 0.55×10^{11} cm^{-2}. The solid curve is the measured differential conductance dI/dV, and the dashed curve is the numerically integrated conductance I/V. In comparison, the dotted trace is a best fit Lorentzian (constrained to be zero at $\pm\infty$),

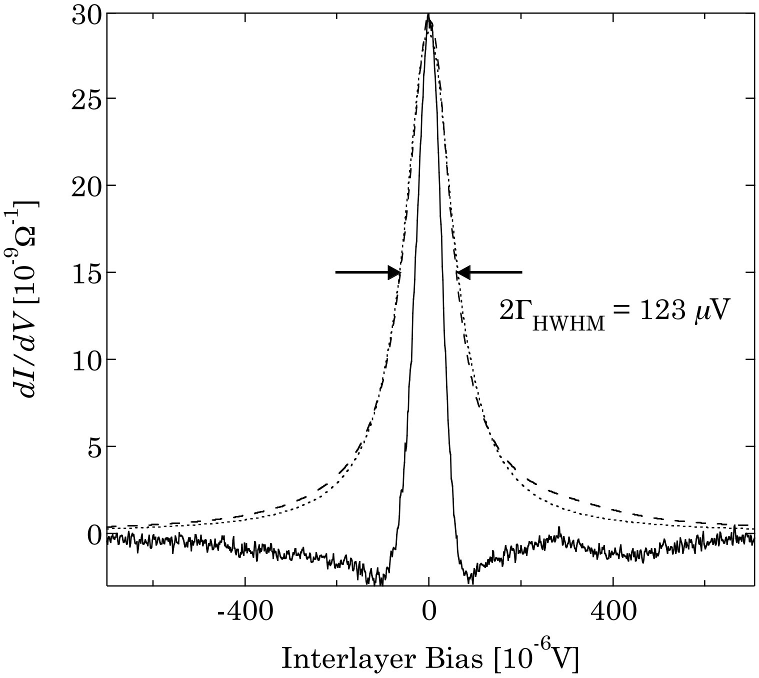

Figure 3.4: 25 mK tunneling data. Solid: dI/dV; dashed: numerically integrated I/V; dotted: Lorentzian fit. The data shown has a line width $\Gamma_{\mathrm{HWHM}} = 61\ \mu$eV

$I/V = G_0/(1+(V/\Gamma)^2)$, showing the good agreement between the expected Lorentzian broadening and experimental observations. The observed half-width is 61 μeV, which fulfills the various approximations required in the proceeding sections.

In the Born approximation the spectral functions themselves are Lorentzian, given explicitly by Zheng *et al.* [55] as

$$A(E) = \frac{\tau}{\hbar}\left[1 + \left(\frac{E\tau}{2\hbar}\right)^2\right]^{-1}.$$

The half-width in I/V is directly related to the spectral functions via Equation 3.2: $\Gamma_{\mathrm{HWHM}} = \hbar/\tau$.

Figure 3.5 compares the quasiparticle lifetime as measured by mobility measurements (solid curve: τ_m) to tunneling (markers: τ_t). The dramatic difference between the two stems from the fact that only large-angle scattering effects the mobility, whereas the tunneling lifetime is limited by all scattering events.

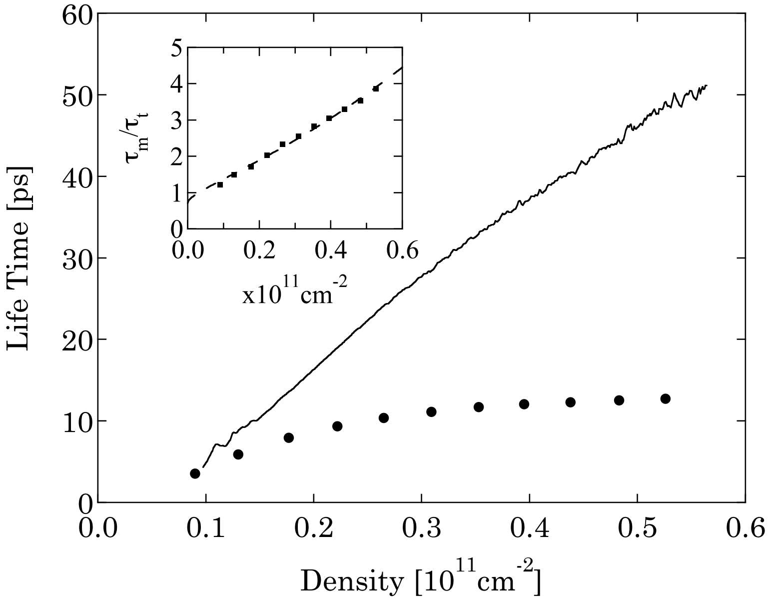

Figure 3.5: Lifetime as measured by tunneling (markers) and as by transport (solid curve). Inset: markers are the ratio between mobility and tunneling lifetimes.

3.4 Measurement of Δ_{SAS}

Although Δ_{SAS} is a property that can be calculated for a given structure, there are considerable uncertainties in the result. These stem both from assumptions in the calculation (the form of the electron-electron interaction assumed), and from physical uncertainties. Examples of these include the exact dimensions of the structure and the aluminum concentration of the barrier.

In the strong tunneling limit, $\Delta_{\mathrm{SAS}} \approx E_f$, it is relatively easy to measure Δ_{SAS}. In the ground state, N electrons are split between the symmetric and antisymmetric states so that the Fermi energies are equal. For identical quantum wells this yields the simple relation, $\Delta_{\mathrm{SAS}} = \pi\hbar^2(n_s - n_a)/m$, between symmetric ($n_s$) and antisymmetric ($n_a$) densities.

In conventional longitudinal transport, R_{xx}, Shubnikov de Haas oscillations are periodic in $1/B$, with frequency $f = nh/2e$; thus computing the Fourier transform of R_{xx} vs. $1/B$ results in a sharp peak at this frequency. Measuring R_{xx} in both layers of a bilayer system in parallel yields densities n_s and n_a [56].

Using Sample G with a 45 Å $\mathrm{Al_{0.3}Ga_{0.7}As}$ barrier and 250 Å wells illustrates this

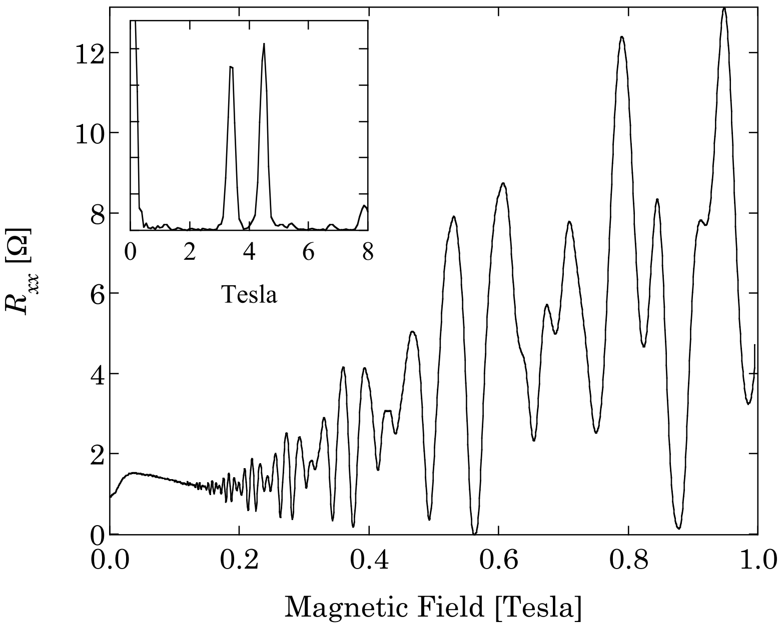

Figure 3.6: Transport data in a strongly tunneling electron bilayer. Inset: Fourier transform of R_{xx} vs. $1/B$. The location of the peaks correspond to the electron density of the symmetric and anti-symmetric states.

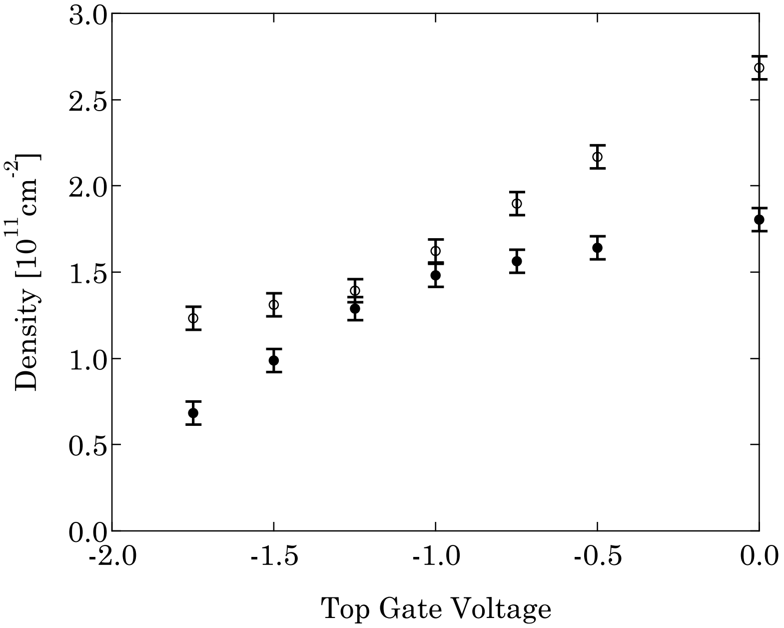

Figure 3.7: Densities as measured from Fourier transform. Includes representative uncertainties of 0.07×10^{11} cm^{-2}.

method of density measurement, and its shortcomings. This sample has total density $n = 4.5\times10^{11}$ cm^{-2}. R_{xx} was measured at $T = 0.3$ K and the external magnetic field was swept from 0 to 1 Tesla at 7 different top gate voltages; the resulting R_{xx} vs. $1/B$ data were Fourier transformed and the locations of the peaks recorded. Representative data is shown in Figure 3.6. As is evident from Figure 3.6, these peaks have a width of about 0.2 Tesla, leading to a minimum resolvable density difference of about 0.07×10^{11} cm^{-2}, or $\Delta_{\text{SAS}} \approx 200$ μeV. The gate voltage dependence of these peaks is shown in Figure 3.7. The value of Δ_{SAS} is extracted from point of closest approach between the two curves. In this case, that distance is smaller than the density uncertainty, illustrating the limitation of this technique.

This method is inadequate for more weakly tunneling devices. Equation 3.3 provides an alternate technique for the measurement of Δ_{SAS} which is useful in the weak tunneling regime. This result ignores the fact that some $(1 - Z) \approx 0.4$ of the spectral density is not located at the Fermi surface, and instead forms a broad background [54]. By measuring only the area under the sharp zero energy feature (for example, by fitting to a Lorentzian and using the area of that function) and thereby explicitly including only the spectral density of the Landau quasiparticles, we can extract Δ_{SAS} by including a factor of Z^2 to account for the excluded spectral weight.

Maintaining $n_1 = n_2$, but at several values of $N_T = n_1 + n_2$, we measure I/V vs. V fit to a Lorentzian. We then integrate I/V vs. V. The data shown does not include a correction for $Z \neq 1$.

Using a self-consistent numerical solver [57, 29], we are able to compute the tunnel gap for these systems under the assumption of $\Gamma - \Gamma$ tunneling; in the AlGaAs system the conduction minimum is at the Γ point when the aluminum concentration is below 40%. Above 40% the minimum moves to the X point at the edge of the Brillouin zone. For the expected structure, the numerics predict $\Delta_{\text{SAS}} = 0.4$ neV, in surprising agreement with experiment. The solver accounts for both Hartree and exchange effects, and includes the differing effective mass of electrons in GaAs $(0.068 \times m_e)$ and AlAs $(0.14 \times m_e$, from Madelung *et al.* [28]).

Figure 3.8 compares the numerical results (scaled by a factor of 2.2) to Δ_{SAS} ex-

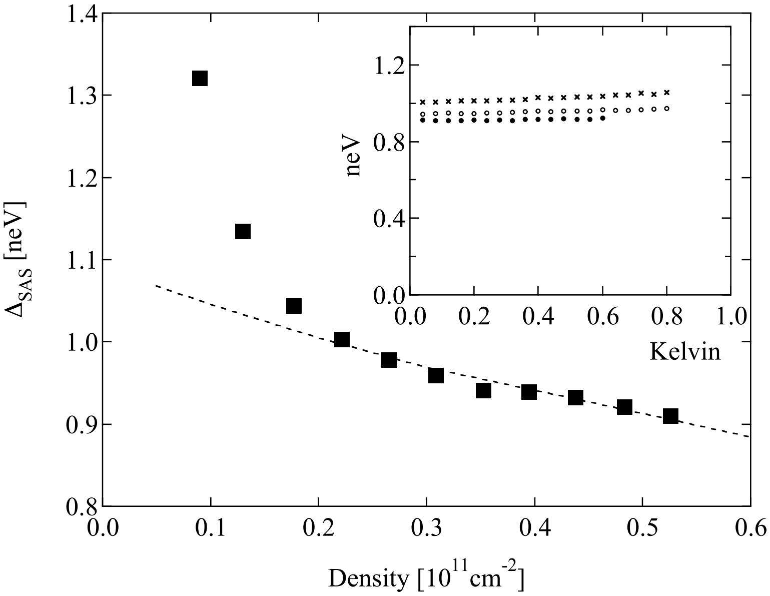

Figure 3.8: Dashed line: tunneling gap from numerical simulations, markers: Δ_{SAS} as measured from tunneling data. Inset: temperature dependence for $n = 0.53{\times}10^{11}$ cm^{-2} (solid circles), $n = 0.35{\times}10^{11}$ cm^{-2} (empty circles), and $n = 0.22{\times}10^{11}$ cm^{-2} (crosses).

tracted from the data using Equation 3.3. The dashed line follows the scaled numerical results, the overall slope of which compares favorably with the measurements. The overall trend of increasing Δ_{SAS} is consistent with the decreasing Coulomb attraction between the carriers and the donors as the density decreases.

The inset to Figure 3.8 shows the measured value of Δ_{SAS} at three different electron densities as a function of temperature. Although the line width increases with temperature (inset to Figure 3.9), the integrated I/V, and hence the computed value of Δ_{SAS}, only changes slightly with temperature. This minimal temperature dependence further supports the idea that the integral of I/V depends almost exclusively on the tunneling strength.

This final fact is remarkable. Equation 3.2 showed that I/V vs. V depends only on the temperature dependence of the spectral function (in the next section we see that this dependence results from the electron-electron scattering time). The integrated I/V is now independent of the temperature dependence of the spectral functions as well!

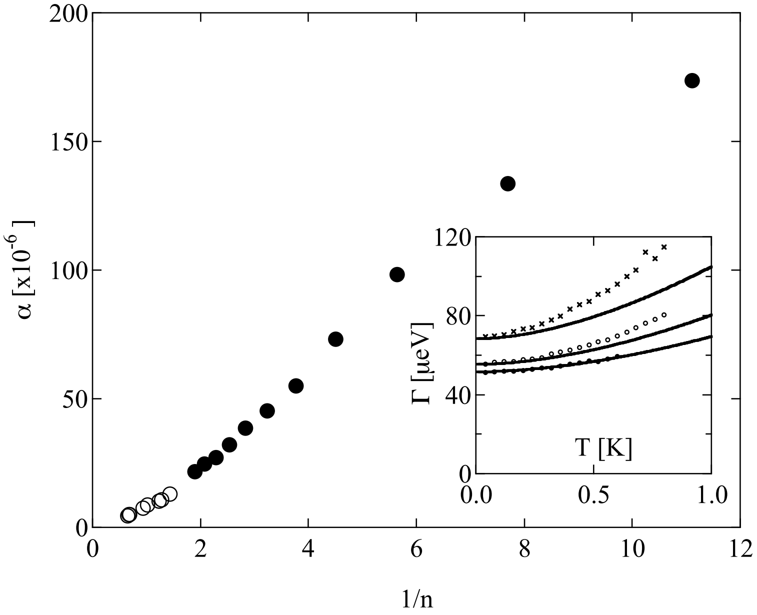

Figure 3.9: α vs. line widths $1/n$. Solid: data from Sample E, empty: data from [48] (note that this data does not include a 12% capacitive correction suitable these samples). Inset: temperature dependence of line width for $n = 0.53 \times 10^{11}$ cm^{-2} (solid circles), $n = 0.35 \times 10^{11}$ cm^{-2} (empty circles), and $n = 0.22 \times 10^{11}$ cm^{-2} (crosses).

3.5 Electron-electron lifetime

The zero temperature line width provides information regarding scattering from static disorder; however, as the temperature increases, the line width also increases rapidly. Since the background disorder is temperature-independent, any change in Γ must result from either electron-electron scattering or electron-phonon scattering. The mobility lifetime τ_m is unaffected by the electron-electron scattering rate, and depends only on electron-impurity and electron-phonon scattering. At all densities it is virtually temperature-independent below 1 K. As a result, electron-phonon scattering can have little effect on the measured tunneling line width in this temperature range.

Experimentally, the data were found to be of the form $\Gamma = \Gamma_0 + \alpha T^2$, where α parameterizes the electron-electron interaction strength. Figure 3.9 shows the good agreement between current experiments at low electron density and earlier measurements at high electron density [48]. The inset shows the measured temperature dependence at three densities: experimental data are designated by points, and theoretical prediction by continuous curves [51]. The high-density trace shows excellent agreement with theory, while as the density decreases, experiment increasingly departs from theory.

One possible explanation for this disagreement is the increasing strength of electron-electron interactions at lower densities. The theory of Jungwirth and MacDonald [51] is a perturbative result which is strictly valid at high densities. We are therefore both reassured that it compares well with experiment at high-density, and not surprised with the low-density deviation.

3.6 2D-2D TUNNELING IN A MAGNETIC FIELD

To this point we have considered tunneling in the absence of a magnetic field. In this section we investigate the consequences in tunneling of a magnetic field perpendicular to the 2D layers. This discussion can be divided into two different regimes. When the magnetic field is small, the magneto-conductance shows oscillations periodic in $1/B$ analogous to the SdH oscillations in ρ_{xx}. At high magnetic fields, however, the zero-bias conductance is suppressed.

As with SdH oscillations in ρ_{xx}, the low-field oscillations in tunneling stem from changes in the density of states squared $g(E_f)^2$ as a function of magnetic field. For more complete models of the effects of disorder on the density of states, see Ando *et al.* [38] and references therein. Using Equation 2.5.1 we can compute the expected tunneling conductance vs. $B_\perp$. The data in Figure 3.10 compare measured tunneling conductance from Sample H to a fit with a scattering time $\tau_{\mathrm{SdH}} = 9$ ps. For these data the density is $n_1 = n_2 = 0.39\times10^{11}$ cm^{-2}.

Figure 3.11-B shows the high-field conductance. Unlike ρ_{xx}, the tunneling conductance becomes suppressed at high-field. This innocuous suppression of zero-bias conductance at high-field is in reality a subtle and relevant effect. To better understand this effect, consider Figure 3.11 which contains typical tunneling data at high-field. These data display current (Panel A) and conductance (Panel B) vs. voltage. In these data, from Sample H, the tunneling conductance and current are strongly

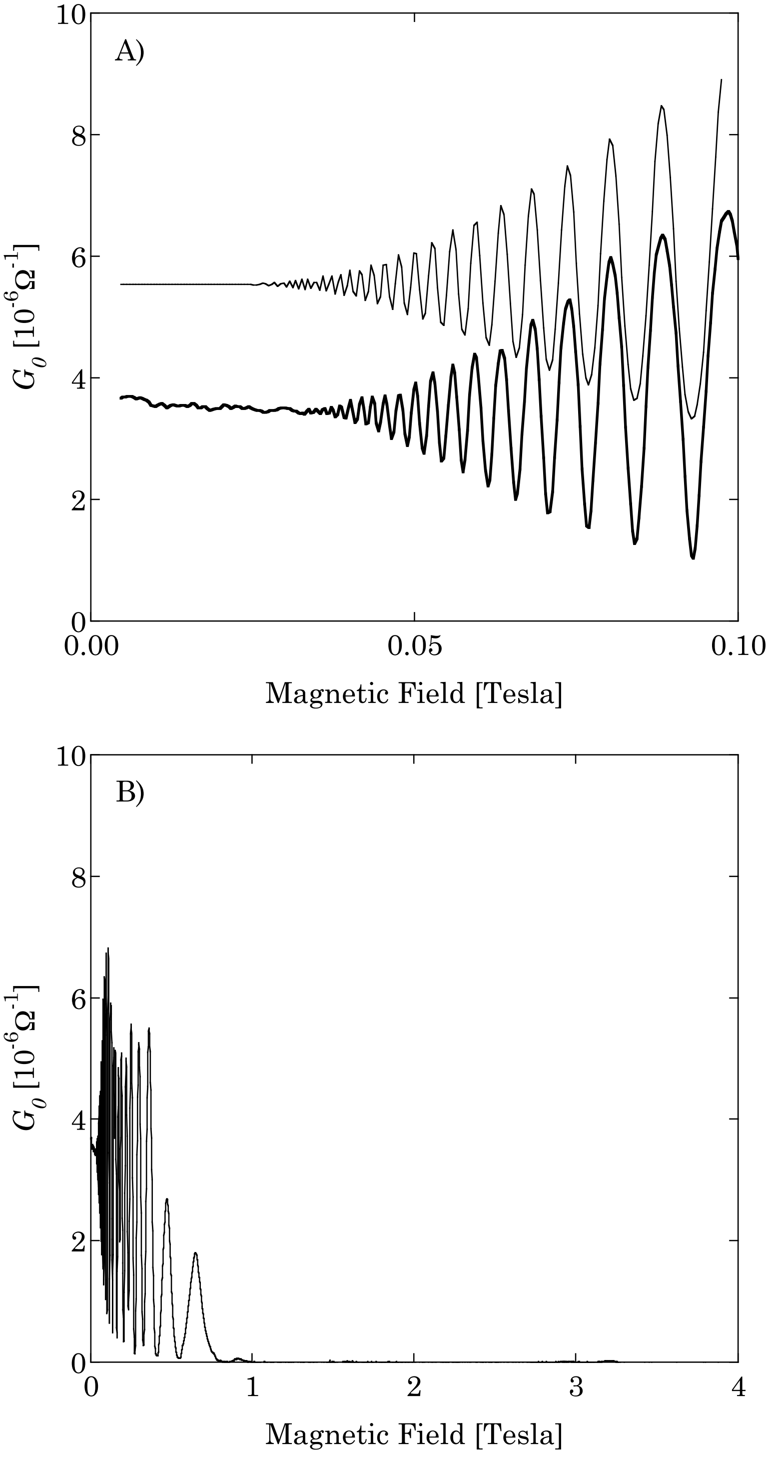

Figure 3.10: Tunneling conductance G_0 vs. B. A) Low-field conductance, Top line: computed conductance using $\tau_{\mathrm{SdH}} = 7$ ps (offset for clarity). Bottom line: measured data, with $n_1 = n_2 = 0.39\times 10^{11}$ cm^{-2}. B) G_0 vs. B at higher magnetic fields showing the strongly suppressed conductance above $B = 1$ T.

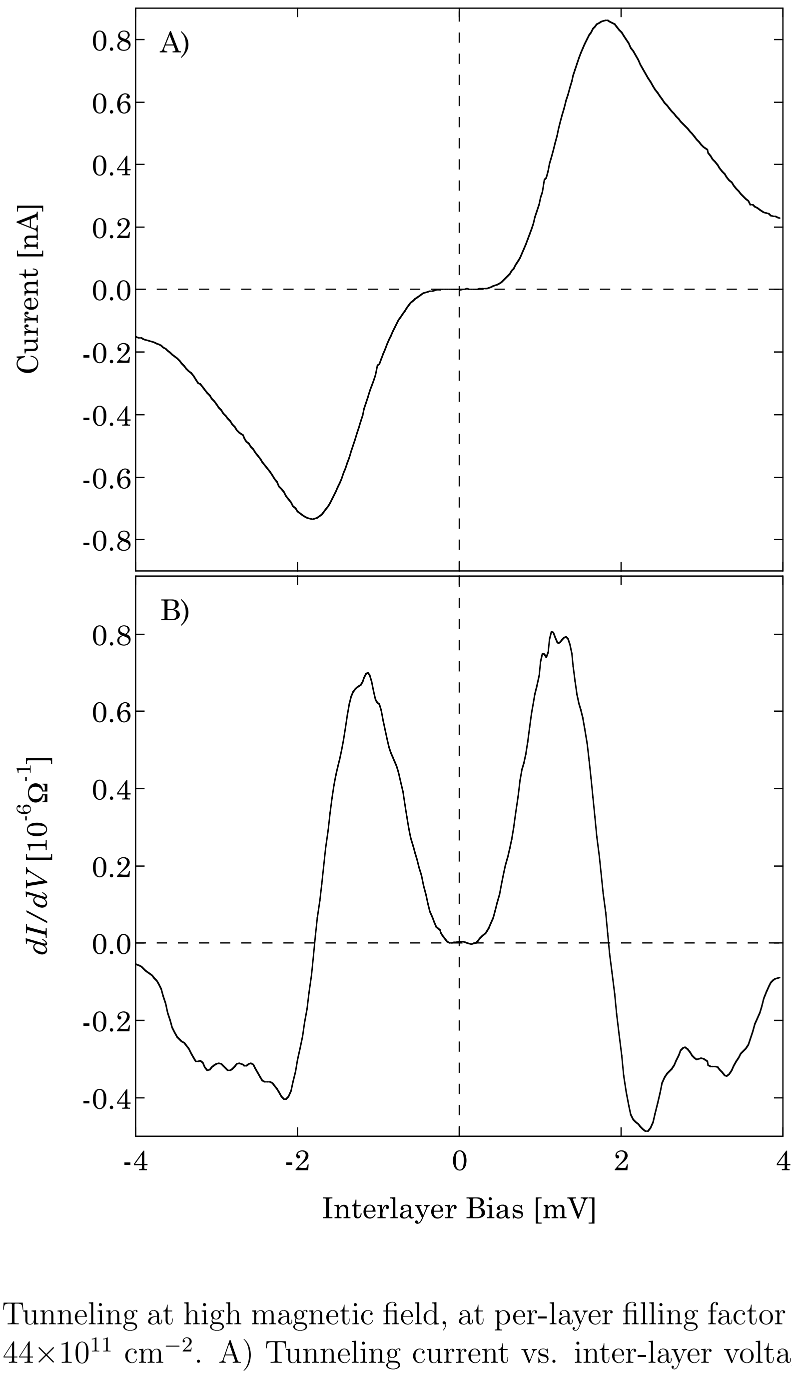

Figure 3.11: Tunneling at high magnetic field, at per-layer filling factor $\nu = 1/2$, with $n_1 = n_2 = 0.44 \times 10^{11}$ cm^{-2}. A) Tunneling current vs. inter-layer voltage. B) dI/dV vs. voltage.

suppressed at zero-bias. In fact, when $\nu < 1$ the tunneling spectra are qualitatively indistinguishable [58, 59]. In a single particle tunneling model, this suppression seems to indicate a gap in the density of states at the Fermi energy. Effect exists over a wide range of filling fractions, including both fractional quantum Hall states (gapped) and the intervening states (ungapped). In particular, it is well known that at $\nu = 1/2$ there is no gap in the density of states, so we must look elsewhere to understand this strange effect.

In a magnetic field, electrons are confined to small orbitals on the length scale of $l_B = \sqrt{\hbar/eB}$, which at high magnetic field becomes smaller than the mean separation between electrons. At large enough magnetic fields, the 2DEG is thought to form a Wigner crystal [60]. Even before the Wigner crystal forms, the instantaneous configuration of electrons resembles the crystalline state. When an electron is suddenly injected between the layers, it enters an interstitial location in the lattice.

Because every electron in the initial N electron system must move slightly to accommodate the new electron, the system relaxes only very slowly to the new state [61]. Even though there is a low-energy configuration with $N + 1$ electrons, that state is unavailable in tunneling, and the external voltage source pays the full energetic penalty for the unfavorable interstitial location.

3.7 CONCLUSION

This chapter has discussed tunneling between two weakly interacting 2DES, both in regard to tunneling strength and to inter-layer Coulomb interactions. Tunneling line width is shown to be an effective probe of the quasiparticle lifetime, both in regard to scattering from static impurities, and to electron-electron scattering. The integrated tunneling data is used to experimentally access the tunneling matrix element $t = \Delta_{\mathrm{SAS}}/2$.

One of the largest uncertainties in the measurement of Δ_{SAS} is the interaction parameter Z, which was estimated to be 0.6 in the range of densities studied. Since Z is a result of highly interacting nature of the 2DES, it seems likely that our direct measurement of the electron-electron lifetime could provide a definite value of Z at any given carrier density. This value might then be fed back into the computation of Δ_{SAS}.

Chapter 4

$\nu_T = 1$ Quantum Hall State

In this chapter we present tunneling measurements between two 2DES's each at $\nu = 1/2$. When the layers are far apart, the tunneling spectra is gapped around zero-bias resulting from the energetic penalty associated with tunneling between two individually correlated, but jointly uncorrelated electron liquids. As the layer separation drops, we observe a resonant enhancement of the zero-bias tunneling conductance [20]. We interpret the formation of a peak in tunneling as the transition to an interlayer correlated state better described by total filling fraction $\nu_T = 1$.

The 1980 discovery of the integer quantum Hall effect (IQHE) and the resulting exact quantization of the Hall resistance in 2D silicon MOSFETs by Klaus von Klitzing [1] was subsequently explained in terms of the interplay of the quantization of electron into Landau orbitals and disorder. These IQHE states are experimentally identified via the quantized plateaus in the Hall resistance at $\rho_{xy} = h/ne^2$ and associated zero resistance features in ρ_{xx}. The discussion of the IQHE in Chapter 1 is now extended to more exotic strongly interacting states in two-dimensional electron systems (2DES).

The IQHE was discovered in a silicon MOSFET with a mobility of 10×10^3 cm^2/Vs. However, as the quality of GaAs devices surpassed silicon, new features reminiscent of the integer quantum Hall effect began to appear. The first such state was observed in a $\mu \approx 100\times10^3$ cm^2/Vs heterojunction by Tsui *et al.* in 1982 [2] at one-third filling, $\nu = 1/3$. As with the IQHE, the quantized Hall resistance corresponded to a minimum in ρ_{xx}, and the Hall resistance was quantized at $3h/e^2$ for a range of filling factors centered on $\nu = 1/3$. This *fractional* quantum Hall effect (FQHE) was explained via an approximate wavefunction the following year by Laughlin [3].

Like the integer quantum Hall states, their fractional cousins are encountered only at particular filling fractions. The addition of a second 2DES parallel to the first opens the door to inherently new bilayer quantum Hall states, generated either by tunneling or by the interplay of inter- and intra-layer Coulomb interactions. In these new bilayer quantum Hall states, it is better to describe the system in terms of the total filling fraction, $\nu_T = \nu_1 + \nu_2$. One such state can exist at $\nu_T = 1$ (when the layer densities are equal this corresponds to $\nu = 1/2$ per-layer).

This chapter begins by introducing both the experimental and theoretical signatures of the FQHE, and continues by discussing the differences involved in bilayer systems. The aim is to understand the completely new quantum Hall states that result when a second, identical, layer is introduced near the first. These new states were initially probed using conventional low-frequency magneto-transport of ρ_{xx} and ρ_{xy}. The central focus of this chapter, however, is 2D-2D tunneling measurements in such bilayer systems at $\nu_T = 1$. Here we explore the parameter space of 2D-2D tunneling defined by magnetic field, density, and temperature.

Finally, the chapter concludes with a brief introduction to the theoretical understanding of the $\nu_T = 1$ quantum Hall state, first as a Laughlin like wavefunction, then as a pseudospin ferromagnet, or an excitonic superfluid.

4.1 The fractional quantum Hall effect

The experimental signature of the fractional quantum Hall effect is very similar to that of the IQHE; each state is identified by the quantized Hall resistance of $\rho_{xy} = h/\nu e^2$, accompanied by a minimum, or zero, in the longitudinal resistance ρ_{xx}. The difference is in the ν's – which are integers for the IQHE and fractions for the FQHE. The first measured fractional state was at $\nu = 1/3$, but since that initial observation the number of fractional states has proliferated.

Figure 4.1 demonstrates the pattern of fractional states which are typical in modern high-mobility samples. The IQHE disorder plays a central role in the formation

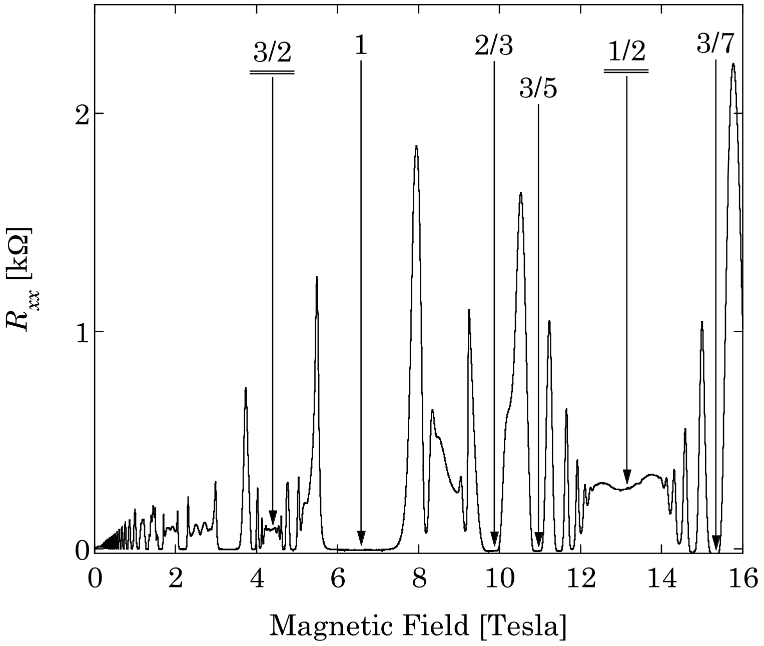

Figure 4.1: Typical FQHE data (unpublished) taken from a high-mobility GaAs quantum well $n = 1.58{\times}10^{11}$ cm^{-2}.

and strength of the states. The FQHE exists only in sufficiently high-quality samples in which the correlated motion of the interacting electron system becomes visible. The remnant disorder in FQHE system then plays the same role as it did in the IQHE leading to features which are extended in filling fraction.

The first observed fractional state, $\nu = 1/3$, was explained by Laughlin's approximate many-body ground state[1] which describes the correlated motion of the interacting electron system [3].

It is not possible to extend the exact 1 and 2 electron solutions to 3 or 100 electrons, but based on their typical form in the symmetric gauge, Laughlin guessed a trial wavefunction for the $\nu = 1/m$ fractional quantum Hall states,

$$\Psi_{1/m} = \prod_{j<k}^{N} (z_j - z_k)^m \exp\left(-\frac{1}{4}\sum_{l}^{N} z_l^2\right) \otimes |\uparrow\uparrow\uparrow \cdots\rangle \,.$$

---

[1] This wavefunction has been shown to be exact for hard-core electrons [62], and exact diagonalizing studies in few-electron systems find the Laughlin wavefunction to be an exceptionally good approximation.

The complex coordinates $z_j = x - iy$ are in units of the magnetic length $l_B = \sqrt{\hbar/eB}$. This wavefunction *assumes* that the electron spins are all Zeeman-polarized by the large perpendicular magnetic field. This is a ubiquitous approximation and the spin part of the wavefunction will not appear in future equations. Likewise, in accordance with convention, the Gaussian factor in each z_l will be omitted in subsequent equations.

Due to the completely symmetric spin wavefunction, the full weight of the Pauli principle falls on the spacial wavefunction. The exchange of any two electrons induces change of sign $(-1)^m$. Any odd exponent, m, therefore gives fermionic statistics; m also selects the filling factor $\nu = 1/m$. This wavefunction predicts several important properties of FQHE states: for example, the lowest energy excitations are gapped and have fractional charge.

At its heart, $\Psi_{1/m}$ is no more than a trial wavefunction, so it is natural (and important) to wonder why and when it is a good approximation of the true ground state. We see that the wavefunction disappears as r^m as any two electrons x_i and x_j are brought close together. This strong avoidance does a remarkable job of minimizing the Coulomb energy.

To understand at what magnetic field $\Psi_{1/m}$ is a sensible guess, consider a "snapshot" of the electron configuration at an instant in time. By freezing all of the electrons at z_k, we can ask about the change in phase when the location of one electron, say z_1, is traced around any other. The final wavefunction is unchanged, except by a multiplicative factor of $1 = \exp(2\pi i m)$, as if there were m lines of magnetic flux quanta, h/e, inside the loop traversed by the electron. As a result, the ratio of total magnetic flux to electron density is m:1, or the filling fraction is $\nu = 1/m$.

It is interesting, that when $m = 1$ the corresponding Laughlin wavefunction Ψ_1, is exactly the ground state wavefunction for noninteracting electrons at filling factor $\nu = 1$ (Equation 2.4. In the absence of inter-Landau level mixing (and with complete spin polarization), this must also be the exact ground state for *any* interaction potential, simply because there is only one way to completely fill a Landau level.

4.1.1 Composite fermions The multitude of FQHE states at filling factors other than $\nu = 1/m$ is elegantly explained in the language of composite fermions [4](for a complete introduction see chapter 7 of [63]). In this picture, the strongly interacting electron system at $\nu = 1/m$ is re-expressed in terms of weakly interacting composite objects, each composed of an electron and two attached flux quanta. This joint object is called a composite fermion (CF). Jain observed that the Laughlin 1/3 state could be re-written as

$$\Psi_{1/3} = \prod_{j<k}^{N} (z_j - z_k)^2 \times \Psi_1.$$

That is the 1/3 wavefunction is an operator acting on the $\nu = 1$ wavefunction[2]. It was Jain's insperation that the wavefunction for different fractional QHE states could be obtained by operating by action of the same operator on wavefunctions at other integer filling ν^*. The new wavefunction is in general at a different filling factor ν, where we have already established that $\nu^* = 1 \rightarrow \nu = 1/3$.

Understaining the composite Fermion picture is tantamount to understand the effect of Jain's operator on an initial state, the important properties of which follow: **Symmetry** The symmetry under particle exchange of the initial wavefunction is unchanged. So a properly antisymmetric initial wavefunction leads to a new antisymmetric wavefunction.

Excitations Although the charged excitation spectrum is changed, no gaps closed nor new gaps opened.

This means that a state that starts as a quantum Hall state presurves the its charge gap, and remains a quantum Hall state. Likewise a ungapped state is mapped to a new gappless state which is not a QHE.

By applying the same procedure which gave the filling fraction for the Laughlin wavefunctions, we see that the ν^* wavefunction is mapped to

$$\nu = \frac{\nu^*}{2\nu^* + 1}.$$

---

[2] Clearly, even number, $2m$, transforms $\nu = 1$ to the Laughlin $2m + 1$ wavefunction. In this discussion we focus only on the most simple case of $m = 1$.

This change in filling factor can be interpreted as the attachment of $2m$ magnetic flux quanta to each electron in the system. These composite objects experience a reduced effective magnetic field of $B^* = B - 2\phi_0 m$ which is the total magnetic field with the field "bound" in CF's removed. At exactly $\nu = 1/2$, $B^* = 0$ and the CF's experience no effective magnetic field; when $B^* \neq 0$ the composite fermions participate in the IQHE at filling factor ν^*. When related to the total filling factor this predicts the location of the fractional quantum Hall states.

Central to this description is the special filling factor $\nu = 1/2$, at which $\nu^* \to \infty$. Since ν is proportional to $1/B$, it is evident that at $\nu = 1/2$, the effective magnetic field is zero. This predicts that at $\nu = 1/2$ in a large perpendicular magnetic field a Fermi surface forms. This surprising fact has been verified experimentally (see the chapter by Willett in [64]). One difference is that due to the assumed complete spin polarization of the electron system, the Fermi wave-vector is expected to be $\sqrt{2}$ larger than at $B = 0$.

From our perspective, there are two aspects of the $\nu = 1/2$ composite Fermi liquid which are relevant. First, it is not a quantum Hall state. This means there is no gap to charged excitations, therefore the resistivity is relatively temperature-independent, and nonzero at low-temperature.

Second, on sufficiently short length- or timescales it is more suitable to think of the system as a set of electrons scattered in an energy minimizing configuration that half-fills the lowest Landau level. In a system with two $\nu = 1/2$ layers in parallel, the measured tunneling conductance still shows the Coulomb gap which characterizes 2D-2D tunneling in a large magnetic field.

In slightly different words, the argument from Chapter 3, is still valid. Since tunneling is essentially a single electron process, when the tunneling electron enters the new layer it has no correlations with its neighbors. It takes a certain amount of time to build up those correlations among its new neighbors that make the system appear as a liquid of composite Fermions. Thus, even though $\nu = 1/2$ has a Fermi surface, tunneling does not show the peaked structure typical of 2D-2D tunneling at zero magnetic field.

4.2 Bilayer quantum Hall effects

The addition of a second 2D layer parallel to the first can fundamentally change the nature of the ground state. When the layers are far apart the system is well described as two independent layers; however, as they are brought close together, electrons in opposite layers can interact either by the Coulomb interaction or through tunneling. Even in the limit of zero tunneling, the Coulomb interactions can create nontrivial collective states which have no counterpart in the individual 2D systems [63, 7, 8].

In bilayer systems it is conventional to refer to the total density and total filling factor: $N_T = n_1 + n_2$ and $\nu_T = \nu_1 + \nu_2$. The simplest case, when $n_1 = n_2$, i.e., equal layer densities, is treated in the present chapter. The effect of a density imbalance is the subject of Chapter 7.

In the limit of very strong tunneling, the gap between the symmetric and antisymmetric quantum well states, Δ_{SAS}, can be much larger than the Fermi energy. In this case, the electrons will aways reside in the lowest energy, symmetric state; these symmetric electrons can participate in the ordinary IQHE and FQHE. In this case, the set of ν_T's which have quantum Hall effects is unchanged from the single-layer case.

As the tunneling strength drops to zero, the two layers might become completely independent; for example, having IQHE only at total filling factor $\nu_T = 2\nu$. This description is only accurate if the layers are weakly coupled, i.e., far apart. However, if they are sufficiently close together, the inter-layer Coulomb interactions can create strong correlations between the layers and form new quantum Hall states.

One such quantum Hall state has been observed at total filling factor $\nu_T = 1/2$ [7, 8] (recall that a single-layer never has a quantized Hall effect at $\nu = 1/2$ or $\nu = 1/4$). Therefore, the addition of a second layer completely alters the physics at certain filling fractions.

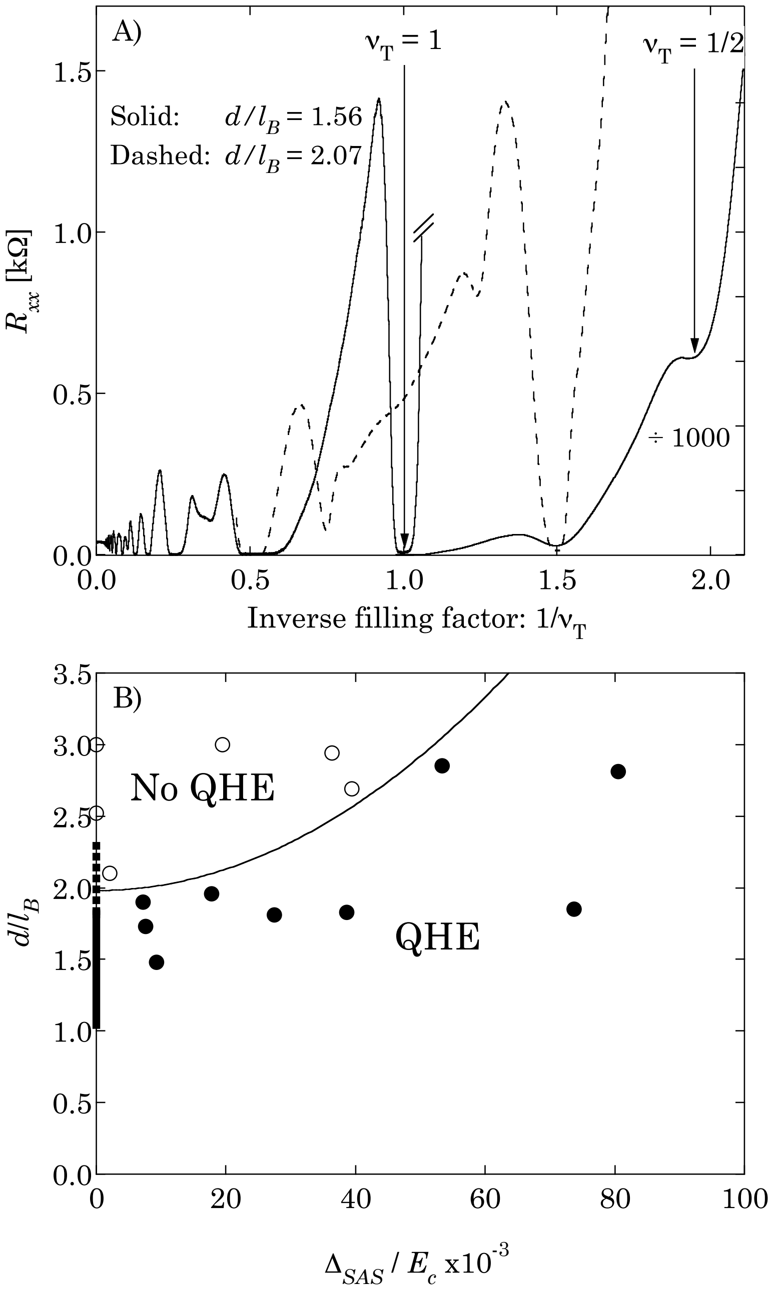

Figure 4.2: A) Typical ρ_{xx} data from Sample H spanning the $\nu_T = 1$ phase boundary at $T = 50$ mK. Solid line: $d/l_B = 1.56$, deep within the coherent state with a well developed zero at $\nu_T = 1$ (also note the weak feature at $\nu_T = 1/2$). Dashed line: $d/l_B = 2.07$ the minimum at $\nu_T = 1$ has completely vanished. B) $\nu_T = 1$ phase diagram. Each circle represents a sample as measured by magneto-transport Murphy *et al* [18]. Solid markers indicate the existence of a quantum Hall minimum, and open markers the lack thereof. The solid line is a proposed parabolic phase boundary based on the transport data. The bold lines on the vertical axis represent tunneling data: the solid portion indicates the existence of a peak in tunneling and the dashed portion indicates its absence.

4.3 QUANTUM HALL EFFECT AT $\nu_T = 1$

Perversely, one of the most interesting bilayer quantum Hall states occurs at total filling factor $\nu_T = 1$. At this filling factor, the lowest spin-resolved Landau level in each layer is half filled with $n_{1,2} = eB/2h$ electrons. When tunneling is strong the appearance of a quantum Hall state is natural. However, in the absence of tunneling the naive expectation is for two independent $\nu = 1/2$ CF liquids. As the layer separation, d, is reduced, the system undergoes a phase transition to an inter-layer coherent state [12, 13, 33].

Both Coulomb interactions and inter-layer tunneling contribute to the strength of this QHE[3]. d/l_B describes the ratio of the inter- to intra- layer Coulomb interactions i.e., $E_{11}/E_{12} \sim (1/\sqrt{n})/(1/d)$. At constant filling factor $l_B \sim \sqrt{n}$, it follows that $E_{11}/E_{12} \sim d/l_B$. Likewise, the tunneling strength is conventionally expressed as the dimensionless ratio of the symmetric-antisymmetric splitting to the mean Coulomb energy, $\Delta_{\mathrm{SAS}}/E_c = \Delta_{\mathrm{SAS}}/(e^2/4\pi\epsilon l_B)$.

Murphy *et al.* [18] located the phase boundary as a function of d/l_B and $\Delta_{\mathrm{SAS}}/E_c$ in a large collection of samples, by inspecting each sample for a QHE at $\nu_T = 1$ [18]. The results of this study are shown in Figure 4.2-B, where the measured phase boundary seems to intersect the vertical axis at $d/l_B \approx 2$. This is a nontrivial fact: even in the complete absence of inter-layer tunneling the electrons still form a inter-layer correlated state.

This QHE state was first observed in conventional transport by detecting a minimum in R_{xx} and a plateau in R_{xy} [8, 7]. Representative resistance vs. magnetic field data are shown in Figure 4.2. These data are taken from sample H, at two values of d/l_B spanning the phase boundary. To allow a direct comparison between two different densities, the data are plotted vs. $1/\nu_T = eB/N_T h$. The dashed trace corresponds to $d/l_B = 2.07$, and there is only the slight depression in R_{xx} at $\nu_T = 1$ reminiscent of a single 2DES at $\nu = 1/2$. However, the solid trace at $d/l_B = 1.56$ features a strong QHE minimum at $\nu_T = 1$.

---

[3] Here E_c and is expressed in MKS units. In the literature, Gaussian units are prevalent.

4.4 Tunneling measurements at $\nu_T = 1$

This section contains the central result of this thesis: a new study of the $\nu_T = 1$ bilayer quantum Hall state and its transition at large layer separation to a compressible phase, using the method of tunneling spectroscopy. Earlier experiments focused on the plane spanned by d/l_B and $\Delta_{\mathrm{SAS}}/E_c$. The samples used in the present investigation are vastly more weakly tunneling than those studied previously. Amusingly, we use tunneling as a probe of the zero tunneling limit. By using weakly tunneling materials, we focus on the state created by nontrivial coulombic correlations. We note that at $d/l_B = 1.60$ the estimated[4] $\Delta_{SAS} = 0.4$ neV is only a tiny fraction of the Coulomb energy, $\Delta_{\mathrm{SAS}}/E_c = 70 \times 10^{-9}$. As a practical consideration, the weak tunneling avoids problems arising from the small sheet conductivities of the 2D layers which develop at high magnetic field (we have measured $\sigma_{xx}^{-1} \approx 130$ kΩ at $\nu_T = 1$). In this section we introduce the dependence of the 2D-2D tunneling at and around $\nu_T = 1$ as a function of inter-layer bias, magnetic field, temperature, and d/l_B.

Samples C, D, and E are all taken from the same wafer, a $\mathrm{Al}_x\mathrm{Ga}_{1-x}\mathrm{As}$ double quantum well (DQW) heterostructure grown by MBE. In these samples, 180 Å GaAs quantum wells are separated by a 99 Å $\mathrm{Al}_{0.9}\mathrm{Ga}_{0.1}\mathrm{As}$ barrier layer; Sample E is discussed in more detail in Chapter 3.1. Unless otherwise stated, any data in this chapter was taken from Sample E.

The electrons are confined to a 250×250 μm square mesa, patterned using standard photolithography. Gate electrodes deposited above and below this mesa allow control over the individual layer densities. The low-temperature mobility of the as-grown sample is 1.2×10^6 cm^2/Vs which falls to 0.4×10^6 cm^2/Vs when the layer densities are reduced to 0.2×10^{11} cm^{-2} (for a complete discussion see Chapter 3). Ohmic contacts (either indium or AuNiGe) are placed at the ends of four arms extending outward from the central mesa. Each of these contacts can be connected to both 2D layers in parallel or to either layer individually. Consequently, both conventional

---

[4] This estimate is based on a self-consistent calculation of the energy levels in the double quantum well, with Γ-point tunneling, a GaAs effective mass of $m^* = 0.067 \times m_e$, and a $\mathrm{Al}_{0.9}\mathrm{Ga}_{0.1}\mathrm{As}$ mass $m^* = 0.14 \times m_e$ [28].

resistivity and inter-layer tunneling measurements can be made on the same sample.

At zero magnetic field the tunneling between the two layers is well described by a Fermi's golden rule expression (Chapter 3). The separate conservation of energy and 2D momentum leads to a Lorentzian resonance in I/V, the half-width, Γ, of which describes the electronic life time, $\tau = \hbar/\Gamma$. At a typical reduced electron density $n_1 = n_2 = 0.3\times10^{11}$ cm^{-2}, this width is 90 μeV and the peak conductance is only 28×10^{-9} Ω^{-1}.

Figure 4.3 displays the central result of this thesis: at $\nu_T = 1$ and 25 mK the tunneling spectra changes qualitatively as d/l_B crosses the phase boundary. This figure contains four panels each at a different value of d/l_B. Although d is constant, the ratio d/l_B can be changed via the layer densities: at fixed filling factor n determines B and thereby l_B. In each case, the individual layer densities were matched by tuning the symmetry of the tunnel resonance at zero magnetic field. The traces were taken at different magnetic fields but at total Landau level filling factor $\nu_T = 1$.

Panels A and B show tunneling in the uncorrelated regime which is dominated by broad features at high-energy and an associated suppression of the zero-bias conductance. This suppression results from the energetic penalty accompanying the rapid injection and extraction of electrons into separately uncorrelated, but individually strongly correlated, electron system produced by Landau quantization [58, 65, 66]. In addition, when an electron tunnels between the layers, it leaves behind a vacancy or hole with charge $+e$. The tunneling suppression is thereby reduced slightly by the electrostatic attraction between the electron and its hole [59]. As the 2D layers are brought closer together the high-energy features move inward, corresponding to an increasing average electron separation. See Chapter 3 for a more in depth discussion of this effect.

When the layers are close enough to support the bilayer $\nu_T = 1$ QHE state, the strong suppression in tunneling is replaced by a resonant enhancement of the zero-bias tunneling. Just below the phase boundary a tiny, yet extremely sharp feature appears at zero-bias (trace C). Finally, deep within the $\nu_T = 1$ phase at $d/l_B = 1.59$, the peak has become enormous and dwarfs all other features in the tunnel spectrum(trace D).

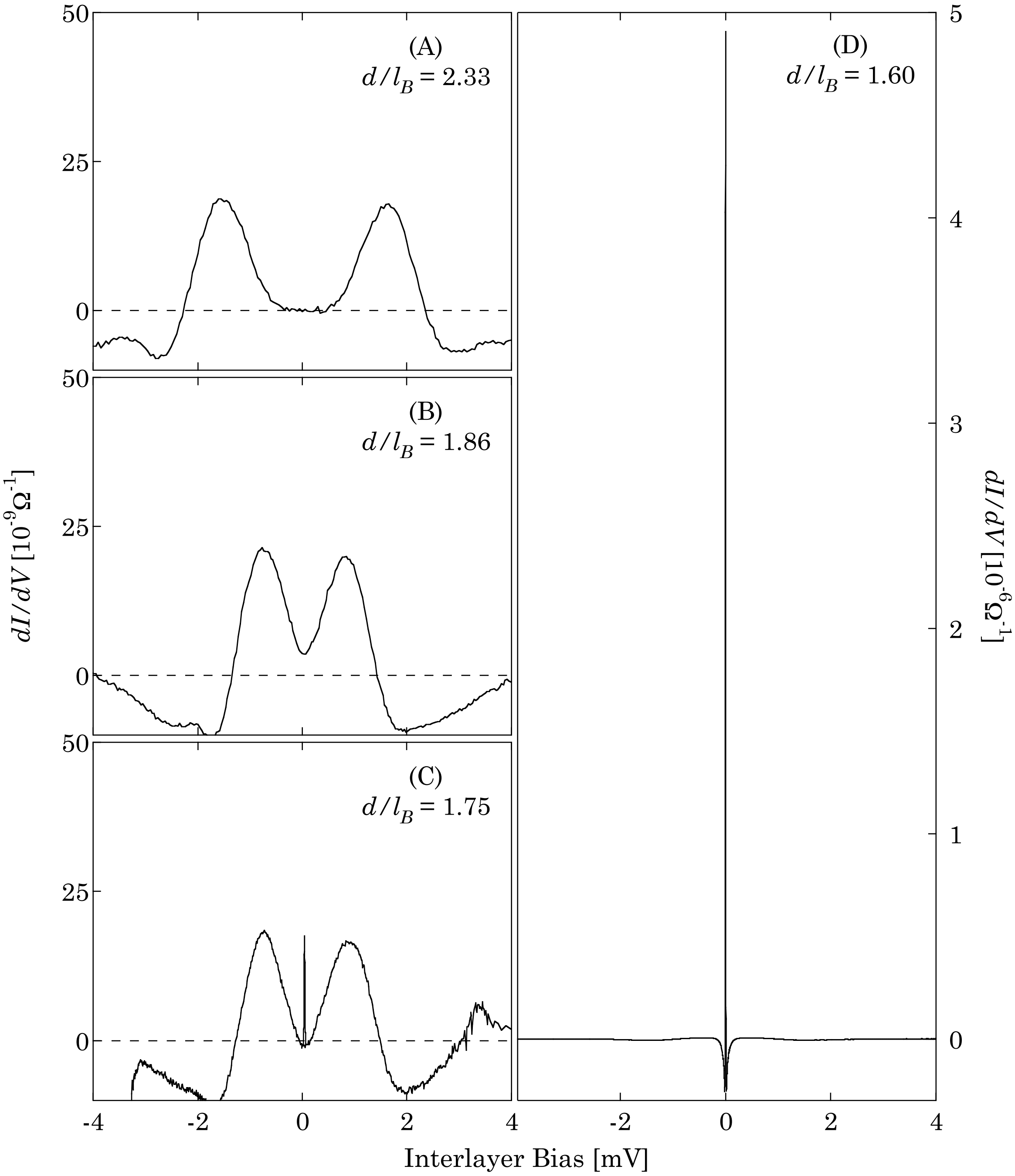

Figure 4.3: Tunneling conductance (dI/dV) vs. inter-layer voltage (V) at $\nu_T = 1$ in a double-layer 2D electron system. Each trace corresponds to a different value of d/l_B, and thus a different magnetic field and density. Panel A, at the largest d/l_B, shows a deep suppression of the tunneling near zero-bias. By panel D, with the smallest d/l_B of the four shown, this suppression has been replaced by a tall peak. Note the scale change in panel D.

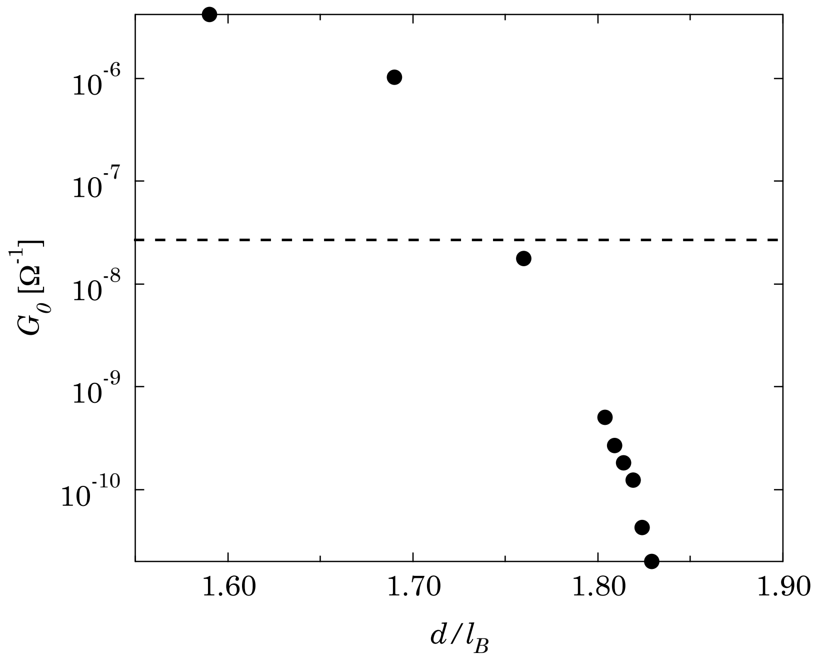

Figure 4.4: Magnitude of the zero-bias tunneling conductance G_0 vs. d/l_B at $T =$ 25 mK. For reference, the dashed line establishes the magnitude of the zero magnetic field conductance.

The height of this peak continues to grow as d/l_B decreases to 1.50 where it exceeds even the zero magnetic field tunneling conductance by a factor of 500[5].

The nominal density of these samples is typically about $N_T = 1.1{\times}10^{11}$ cm^{-2}, which results in $d/l_B = 2.4$ at $\nu_T = 1$. Reducing the density via gating to $N_T = 0.42{\times}10^{11}$ cm^{-2}, gives $d/l_B = 1.45$. The left axis of Figure 4.4 shows the zero-bias tunneling conductance G_0 at $\nu_T = 1$ and $T = 25$ mK, vs. d/l_B. There is a sharp transition near $d/l_{B_{\mathrm{crit}}} = 1.83$ separating two very different tunneling regimes, compared to $d/l_{B_{\mathrm{crit}}} \approx 2$ as observed in earlier transport measurements[6]. Above $d/l_{B_{\mathrm{crit}}}$, the zero-bias conductance is suppressed and the tunneling spectra are qualitatively the same as panel A in Figure 4.3. On the other hand, as d/l_B falls below this critical value a resonant enhancement of the tunneling appears at zero-bias. The magnitude

---

[5] At the lowest densities the tunneling conductance at $\nu_T = 1$ is larger than the sheet conductance of $\sim 1/100$ kΩ. These conductances are measured in a 4-wire configuration. However, the combination of a very narrow and very tall line make an accurate determination of the height and width increasingly difficult as G_0 exceeds the sheet conductivity

[6] Due to the uncertainty in growth parameters, such as barrier and well widths, there is an uncertainty in the exact value of d.

of this peak grows continuously as d/l_B falls.

The right axis of Figure 4.4 shows the d/l_B dependence of the line width (defined as the half-width at half-max of the peak in I/V). At the lowest temperatures and smallest values of d/l_B this width is about 2 μV wide – 25× narrower than the zero magnetic field feature. This dramatic variance from the single-particle lifetime strongly suggests that $\nu_T = 1$ a different mechanism is responsible for the two lifetimes. One explanation could be a transition from single electron to collective physics.

Figure 4.5 shows the magnetic field dependence of the zero-bias tunneling conductance G_0, corresponding to $d/l_B = 2.30$ (40 mK) and 1.59 (25 mK) at $\nu_T = 1$. As in Figure 4.2, the data here is displayed vs. $1/\nu_T$ to facilitate direct comparison of different densities. At small magnetic fields both curves show quantum tunneling oscillations analogous to SdH oscillations in ρ_{xx}. These low-field oscillations are used to determine the 2D density N_T.

The offset trace in Figure 4.5, at $d/l_B = 2.30$, becomes increasingly suppressed at high magnetic field. Again, this is the inhibition of 2D-2D tunneling characteristic of two weakly coupled 2D electron systems at high magnetic field. The solid trace at $d/l_B = 1.59$ differs qualitatively in the vicinity of $\nu_T = 1$. The suppressed tunneling at zero-bias has been replaced with an enormous enhancement centered on $\nu_T = 1$.

Note the small bumps in the $d/l_B = 2.30$ data at high-field. These arise when the system enters or leaves a strong *single-layer* quantum Hall state. In such states the 2D sheet conductivity, $G_s \rightarrow 0$; when the capacitive component of the dI/dV measurement is comparable to G_s there is a parasitic mixing of the capacitive conductance into the real signal. These bumps vanish as the excitation frequency decreases.

To confirm the existence of the conventional QHE, four-terminal ρ_{xx} measurements have been performed in Sample E. As anticipated, a QHE develops in tandem with the peak in tunneling, suggesting that these reflect the same phase transition. The dotted trace in Figure 4.5 shows the observed minimum in ρ_{xx} at $N_T = 0.42\times10^{11}$ cm^{-2} and $T = 40$ mK.

Previous transport measurements found $d/l_{B_{\mathrm{crit}}} \approx 2$, while in the current sample

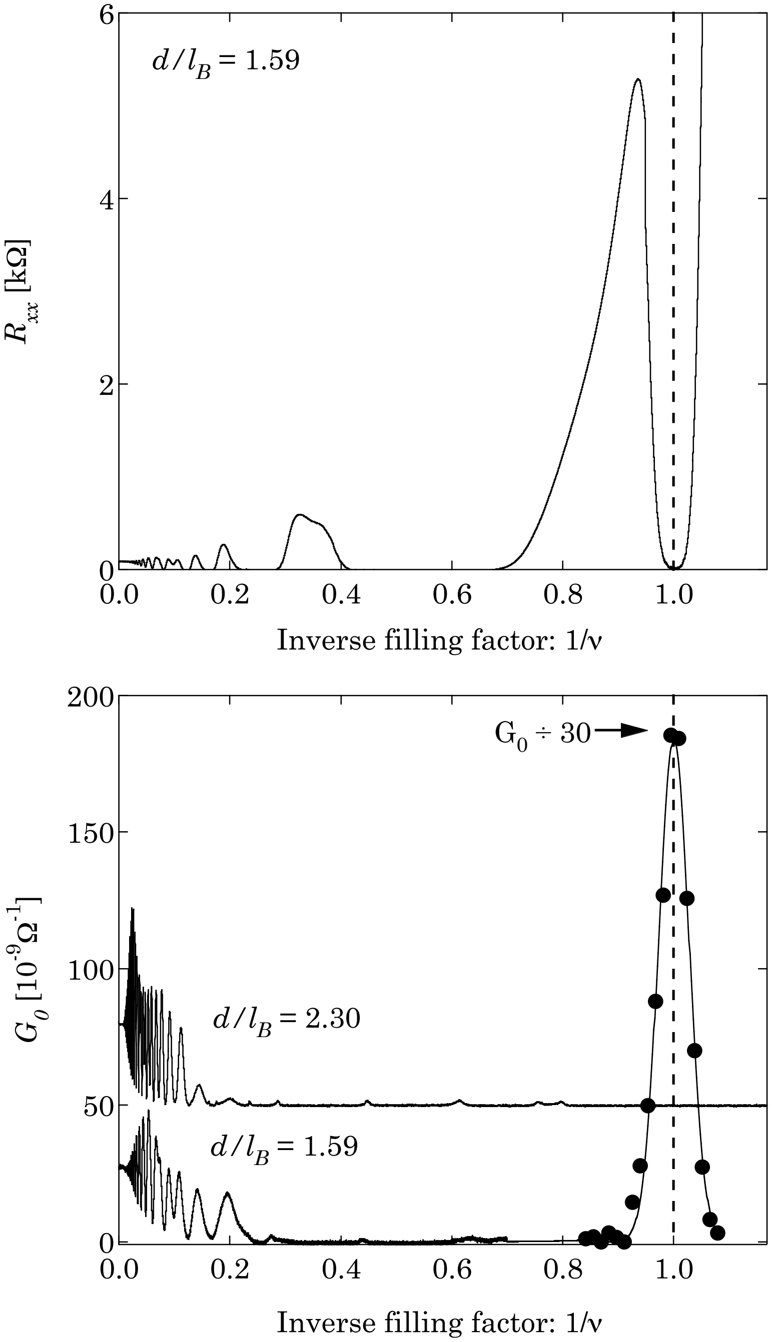

Figure 4.5: Top: ρ_{xx} vs. $1/\nu$, taken at $d/l_B = 1.59$. Bottom: zero-bias tunneling conductance G_0 vs. $1/\nu$. Displaced vertically for clarity, the top trace, taken at $d/l_B = 2.30$ shows no feature at $\nu_T = 1$, while the bottom trace at $d/l_B = 1.59$ has an enormous peak (note the change in scale at $\nu_T^{-1} = 0.7$). Around $\nu_T = 1$ the markers are the zero-bias peak height extracted from individual dI/dV v.s V traces and to solid line is a guide to the eye. Note that the minimum in ρ_{xx} is coincident in field with the peak in tunneling.

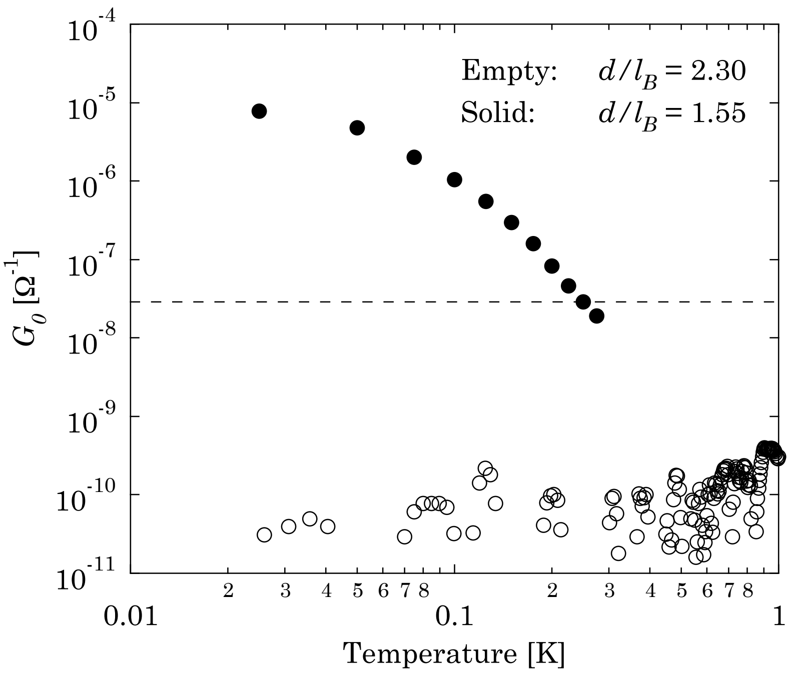

Figure 4.6: Temperature dependence of the zero-bias tunneling conductance at $\nu_T = 1$ at high and low densities. Note that the high-density data has been magnified by a factor of 200. As in Figure 4.4, the dashed line establishes the magnitude of the zero magnetic field conductance.

critical value of approximately 1.83 is observed both via tunneling and transport. In contrast, theoretical estimates assuming infinitely thin wells generally predict yet smaller values [67], typically ~ 1.3 (see Schliemann *et al.* [68] for a discussion). The samples described by Murphy *et al.* [18] had substantially thinner tunneling barriers, therefore the ratio of the well width to the barriers width is larger than in the present samples, making the newer samples more ideal 2D systems.

The temperature dependence of the zero-bias tunneling conductance is displayed in Figure 4.6. Two sets of data are shown, one for $N_T = 1.09 \times 10^{11}$ cm^{-2} and one for $N_T = 0.42 \times 10^{11}$ cm^{-2}. Here we again see a qualitative difference between the tunneling at high- and low-density. At high-density the conductance falls with decreasing temperature. As reported previously, this dependence is consistent with simple thermal activation [58, 65]. The low-density data behave in the opposite fashion, rising as the temperature falls. Once the tunneling peak becomes visible at an onset temperature of $T = 400$ mK, the zero-bias conductance increases in an *exponential* fashion, $G_0 \propto \exp(-T/T_0)$. This growth persists to the to the lowest accessible temperatures,~ 15 mK, and is the topic of Chapter 5.

4.5 THEORETICAL EXPECTATIONS OF $\nu_T = 1$ PHYSICS

When the bilayer system exhibits no QHE at $\nu_T = 1$, the state is well described by two independent $\nu = 1/2$ CF liquids. However, as the inter-layer correlations become strong enough to generate a QHE, the resulting state can be described in terms of a bilayer analogue to the Laughlin state, the Ψ_{111} wavefunction.

This wavefunction is related to two broken-symmetry ground states: a pseudospin ferromagnet, and an excitonic superfluid. Although mathematically equivalent, each of these descriptions highlights different physical aspects of the same state.

4.5.1 Ψ_{111} wavefunction Building on the single-layer case, Halperin proposed a class of wavefunctions in multi-component systems [6, 63, 9] (the second component was designed to be a real spin variable, but it just as well describes electrons in bilayer systems)

$$\Psi_{lmn} = \prod_{j<k}^{N_1}(z_j - z_k)^l \prod_{j<k}^{N_2}(w_j - w_k)^m \prod_{j,k}^{N_1,N_2}(z_j - w_k)^n. \tag{4.1}$$

The variables z_j and w_k denote the location of an electron in either the top or bottom layer. The $l = m = n = 1$ state describes a bilayer state at total filling factor $\nu_T = 1$. Like the $\nu = 1/3$ case, the electrons have nodes when they overlap in the same layers, however, in this trial function electrons in opposite layers also avoid each another. In this wavefunction the number of electrons in each layer is well defined, by explicit construction. Equivalently, both $N_T = N_1 + N_2$ and $\Delta N = N_1 - N_2$ are good quantum numbers.

Wen and Zee observed that some of the Halperin Ψ_{lmn} wavefunctions, including Ψ_{111}, have a broken symmetry associated with charge fluctuations between layers. As with the Laughlin wavefunction, we can compute the magnetic flux penetrating the layers by counting the polynomial powers, and arrive at the pair of equations,

$$\Phi = lN_1 + nN_2, \qquad \text{and} \qquad \Phi = mN_2 + nN_1. \tag{4.2}$$

These two equations can be easily solved for ν_1 and ν_2, the filling factors of each layer,

$$\nu_1 = \frac{m-n}{lm-n^2}, \qquad \text{and} \qquad \nu_2 = \frac{l-n}{lm-n^2}. \tag{4.3}$$

When $l = m = n$ this solution to Equation 4.2 is ill-defined. Instead the difference $\nu_1 - \nu_2$ is unconstrained, while $\nu_T = \nu_1 + \nu_2 = 1/n$. This again suggests that charge transfer between the layers has no energetic cost.

We have seen that when electrons tunneling into highly correlated electron liquids with which they share no initial correlations pay a stiff energetic penalty. This is not the case in the Ψ_{111} state, here electrons in each layer are strongly correlated with those in the opposite, and the third term in Equation 4.1 shows that every object is opposite to a correlation hole in the opposite layer! Instead of a penalty to tunneling, the electrons are encouraged to tunnel.

Although these wavefunctions yield an intuitive explanation of the zero-bias tunneling feature, this intuition falls short in explaining the extremely narrow line-shape. To gain a better feeling of the resonant nature of this peak, we turn to a superficially different description of the $\nu_T = 1$ system: that of a pseudospin ferromagnet.

4.5.2 Quantum Hall ferromagnet Alternately, this quantum Hall state can be described as a pseudospin ferromagnet. A pseudospin index, $|\uparrow\rangle$ or $|\downarrow\rangle$, can be assigned to particles in the top and bottom layers respectively. In the $\nu_T = 1$ coherent state, this local pseudospin variable can become coherent over a long length scale leading to a polarization in the $x - y$ pseudospin plane, i.e., $|\psi\rangle = |\uparrow\rangle + \exp(i\phi)\,|\downarrow\rangle$.

Since the pseudospin variables correspond to the layer index, the z component of the magnetization, m_z, equals 1 for an electron in the top layer and -1 for an electron in the bottom. Likewise, m_x and m_y measure the x and y components of the magnetization. The proposed phase-coherent polarization has a net magnetization lies in the pseudospin $x-y$ plane, i.e., $m_z = \langle \sigma_z \rangle = 0$. $|\psi\rangle$ is not an eigenstate of m_z, infact, the value of m_z is maximally uncertain – every electron is completely perfectly mixed between the two layers.

The entire trial wavefunction can be written as

$$|\Psi\rangle = \prod_{j=1}^{N_T} \left[\mathbf{a}^{\dagger}_{k_j,\uparrow} + e^{i\phi} \mathbf{a}^{\dagger}_{k_j,\downarrow} \right] |0\rangle \, , \tag{4.4}$$

where $\mathbf{a}^{\dagger}_{k,\uparrow}$ and $\mathbf{a}^{\dagger}_{k,\downarrow}$ are creation operators for the $|\uparrow\rangle$ and $|\downarrow\rangle$ states. k is an index which describes the suitable single particle wavefunctions. k might indicate the "momentum" index in the Laudau gauge, or angular momentum in the symmetric gauge (Chapter 2).

The low-energy physics of this model are described by the Hamiltonian [19, 69, 70],

$$H = \int d^2x \left[\rho_s \frac{|\nabla \phi|^2}{2} - \frac{t}{2\pi {l_B}^2} \cos(\phi) + \frac{\beta}{2} |m_z|^2 \right] . \tag{4.5}$$

The gradient term stems from an exchange energy. For the paramaters from Sample E at $d/l_B = 1.6$, Hartree-Fock calculations [70] suggest the following numerical values: $\rho_s \approx 0.005 \times E_c$ which is numerically equal to $\rho_s \approx 400$ mK. The second term of the Hamiltonian is the tunneling energy, where $t = \Delta_{\mathrm{SAS}}/2$, and the third term is a (renormalized) capacitive charging energy, which is $\beta {l_B}^2 \approx 0.15 \times E_c = 1.6$ mK.

The ground state of this Hamiltonian may be viewed as a new kind of easy-plane ferromagnet; in the limit $t \to 0$ the energy is independent of the direction ϕ. Associated with this broken symmetry, a linearly dispersing Goldstone collective mode (a pseudospin wave) is expected [14, 15, 19, 69]. Due to the 2D nature of the system, the finite temperature transition to the ferromagnetic state is expected to be of the Kosterlitz-Thouless (KT) type [14, 15, 19, 69, 71].

The dispersion of the linear Goldstone mode can be computed by investigating the collective mode spectra of Equation 4.5 [19, 69], and when $t \to 0$ the dispersion is given by

$$\omega = \pm \frac{4\pi q l_B}{\hbar} \sqrt{2\rho_s (\beta {l_B}^2)}.$$

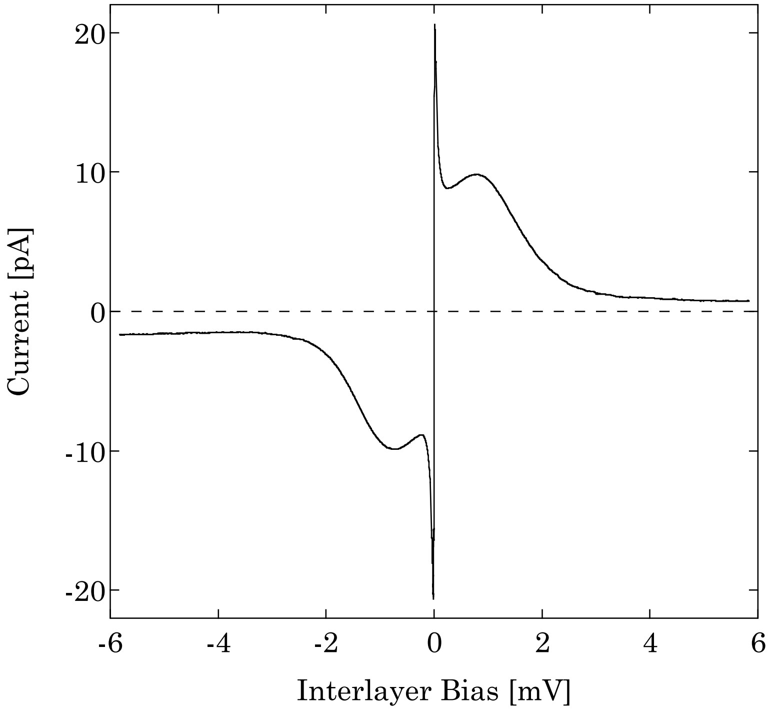

Figure 4.7: $I - V$ data from Sample E at $T = 25$ mK and $d/l_B = 1.45$.

The tunneling term in the Hamiltonian tends to polarize the electrons in the pseudospin x direction, $|\uparrow\rangle + |\downarrow\rangle$. This state is an eigenstate of the tunneling operator, which exchanges electrons between layers. Since there is no energetic cost associated with tunneling electrons we expect an infinite slope in $I - V$ at zero-bias. It is no coincidence that this zero-bias feature in Figure 4.7 greatly resembles the discontinuity in the conventional DC Josephson effect.

In real samples, a gap at zero wave-vector is expected, the size of which is determined by both the single particle tunneling energy Δ_{SAS} and an inter-layer capacitive charging energy [19, 69]

$$\Delta E = 2\sqrt{t\left(t + 4\pi\beta {l_B}^2\right)}.$$

Using our computed value of $\Delta_{\mathrm{SAS}} = 0.4$ neV $= 70 \times 10^{-9} E_c$, and estimates of the charging energy, $\beta {l_B}^2 \approx 0.015 E_c$, the long wavelength pseudospin wave energy is only about 1 μeV. The appearance of the tunneling resonance suggests the existence of a zero wave-vector collective mode which enhances the ability of electrons to tunnel.

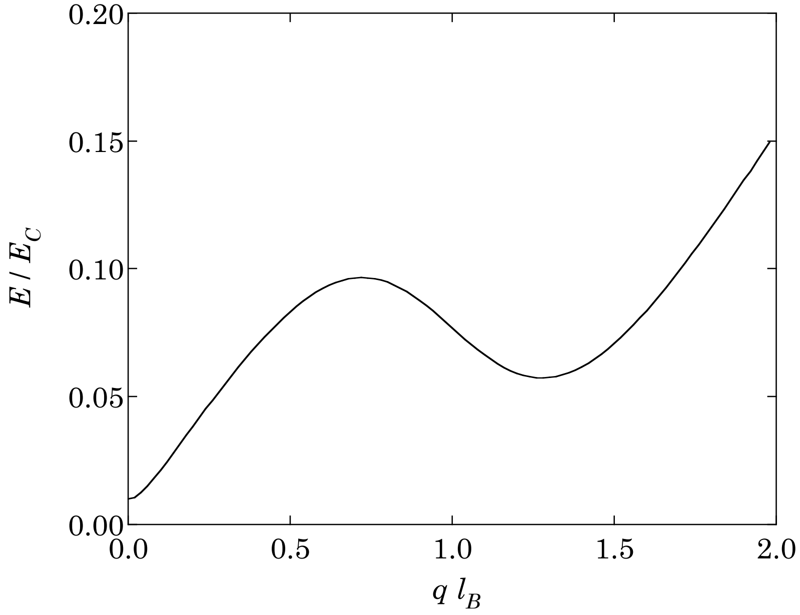

Figure 4.8: Representative pseudospin dispersion in the $\nu_T = 1$ coherent phase after MacDonald [72]. Note the gap near zero-bias, the low-energy linear dispersion, and the roton minima at $ql_B \sim 1.3$.

In particular, only the mode at $q = 0$ is spatially uniform, and therefore can transfer net charge between the layers. Second, the existence of β in the gap tells us that the $q = 0$ mode necessarily incorporate oscillations in the pseudospin z direction, i.e., the movement of charge between the layers.

This ferromagnetic wavefunction function looks completely dissimilar to the Ψ_{111} wavefunction. As we observed above, this not a state of well defined $m_z \sim N_1 - N_2$, while the Ψ_{111} states is an eigenfunction of N_1 and N_2 (and thus N_1 and N_2). Equation 4.5 is a broken symmetry state with respect to the phase ϕ. In spite of these differences, it is deeply related to the Ψ_{111} state [72]. This can be seen as follows. First, rewriting the wavefunction slightly gives (k has been replaced by l, indicating that we plan to use the symmetric gauge)

$$|\Psi\rangle = \prod_{j=1}^{N_T} \psi_{l_j}(x_j) \otimes \prod_{j=1}^{N_T} \left[|{\uparrow_j}\rangle + e^{i\phi} |{\downarrow_j}\rangle \right].$$

This is the explicit wavefunction created by the operators in Equation 4.5. Neither the spacial nor the pseudospin part of this wavefunction is antisymmetric under particle exchange. To generate the correct symmetry, we first take the Slater determinate of these wavefunctions (since the pseudospin variable are completely symmetric under particle exchange, they are unchanged), leading to

$$|\Psi\rangle = \left|\prod_{j=1}^{N_T} \psi_{l_j}(x_j)\right| \otimes \prod_{j=1}^{N_T} \left[|{\uparrow_j}\rangle + e^{i\phi(x)}\,|{\downarrow_j}\rangle\right].$$

Little seems changed here; however, the determinate of the symmetric gauge wavefunctions (indexed from $l = 0 \cdots N_T - 1$) is a Vandermonde determinate which can be easily be written as an explicit polynomial

$$|\Psi\rangle = \prod_{j<l}^{N_T} (x_j - x_l) \otimes \prod_{j=1}^{N_T} \left[|{\uparrow_j}\rangle + e^{i\phi(x)}\,|{\downarrow_j}\rangle\right].$$

Now we have a polynomial which resembles the spacial part of the Ψ_{111} wavefunction. We can multiply by 1 in the form of $\exp(-iN\phi)$, in which N is an integer, and distribute it into the pseudospin product

$$|\Psi\rangle = \prod_{j<l}^{N_T} (x_j - x_l) \otimes \prod_{j=1}^{N_T} \left[e^{-iN\phi(x)/N_T}\,|{\uparrow_j}\rangle + e^{i\phi(x)(1-N/N_T)}\,|{\downarrow_j}\rangle\right].$$

We now show that the integral over ϕ of this wavefunction is the Ψ_{111}, creating a wavefunction which is completely indeterminate in ϕ. Expanding the pseudospin product and integrating yields

$$\prod_{j<l}^{N_T} (x_j - x_l) \otimes \int_0^{2\pi} d\phi \sum_{j=0}^{N_T} e^{i(N-j)\phi} S\left[|{\uparrow_1}, \cdots {\uparrow_{N_T-j}}, {\downarrow_{N_T-j+1}}, \cdots {\downarrow_{N_T}}\rangle\right];$$

we have introduced the symmetrization operator S. The integral over ϕ selects the one term from this summation in which $j = N$ and we arrive at

$$\prod_{j<l}^{N_T} (x_j - x_l) \otimes S\left[|{\uparrow_1}, \cdots {\uparrow_{N_T-N}}, {\downarrow_{N_T-N+1}}, \cdots {\downarrow_{N_T}}\rangle\right].$$

We see that the pseudospin part counts out an explicit number, N, spins and places them in the top layer and puts the remaining $N_T - N$ in the bottom layer. This wavefunction is a state of definite N_T and ΔN. Now we can encapsulate the pseudospin index by defining $x_i \otimes |\uparrow_i\rangle = z_i$, and $x_i \otimes |\downarrow_i\rangle = w_{i-N}$. Using this replacement on the very first term in the antisymmetrized pseudospin wavefunction gives

$$\begin{aligned}\Psi_{111} &= \prod_{j<l}^{N_T}(x_j - x_l) \otimes |\uparrow_1, \cdots \uparrow_{N_T-N}, \downarrow_{N_T-N+1}, \cdots \downarrow_{N_T}\rangle \\ &= \prod_{j<l}^{N}(z_j - z_l) \prod_{j<l}^{N_T-N}(w_j - w_l) \prod_{j,l}^{N,N_T-N}(z_j - w_l).\end{aligned}$$

Therefore, we have shown that the Ψ_{111} wavefunction and the pseudospin ferromagnet are related. One is a state of definite particle number, and the other definite phase. This is analogous to a conventional Josephson junction between two superconductors, which is in a state of definite phase difference Φ, but an indefinite state of cooper pair difference.

4.5.3 Excitonic superfluid Finally, we describe the system as a Bose-condensate of excitons. In this chapter I have focused on conductance data: dI/dV. The sharp feature in conductance, naturally, corresponds to a step in $I-V$. This step is strongly reminiscent of a Josephson discontinuity. Indeed a third description of this system is in terms of an excitonic condensate: a BCS superfluid of bound electron-hole pairs.

Soon after the BCS theory's successful explanation of conventional superconductivity, it was proposed that in a semiconductor an electron in the conduction band and a hole in the valence band could also form a composite object – an exciton – which could then Bose condense [17]. Although conceptually simple, there is yet to be convincing evidence of a band-exciton condensate for the simple reason that electron-hole pairs tend to rapidly recombine by emitting a photon.

In a 2DES at $\nu = 1/2$, only half of the available states in the lowest Landau level are filled; equivalently, the empty states can be thought of as filled by "holes" in a completely full Landau level. Therefore, two layers of electrons, each at $\nu =$

1/2, can be equivalently thought of as one layer of electrons, and a second layer of holes. Electrons in one layer are attracted to holes in the other, and if the layers are sufficiently close together these objects can bind to form excitons. Formally, we can make a particle-hole transformation in the pseudospin Hamiltonian and arrive at the expression

$$|\Psi\rangle = \prod_{k} \left[1 + e^{i\phi} \mathbf{a}^{\dagger}_{k_j,\downarrow} \mathbf{b}^{\dagger}_{k_j,\uparrow} \right] |0^*\rangle \,. \tag{4.6}$$

$|0^*\rangle$ represents a new "vacuum" composed of the true vacuum for $\downarrow$ electrons, but a full Landau level of $\uparrow$ electrons, from which $\mathbf{b}^{\dagger}_{k_j,\uparrow}$ creates holes in the $\uparrow$ layer. This is reminiscent of the BCS wavefunction for excitons. In this case, the annihilation of a hole physically corresponds to an electron tunneling from the electron layer to the hole layer.

It is predicted that when the excitons Bose-condense, the resulting superfluid will correspond to the dissipation-less flow of charge neutral excitons [14]. This flow yields no net electrical current since a unidirectional current J of excitons corresponds to an electrical current $+J$ in the top layer and $-J$ in the bottom.

This remarkable effect has been experimentally realized by Kellogg *et al.* [25]. A current of ~ 0.1 nA was driven though the top layer and re-routed back in the same direction (symmetric channel) or reverse direction (antisymmetric channel) through the bottom layer. Kellogg observed the regular signature of a QHE when the currents were parallel, $\rho_{xx} \rightarrow 0$ and $\rho_{xy} \rightarrow h/e^2$. When the currents were antiparallel, however, $\rho_{xx} \rightarrow 0$ and $\rho_{xy} \rightarrow 0$. This observation indicates that the current carrying objections in the antisymmetric channel are charge neutral and induce no Hall voltage.

In addition the conductivities (σ_{xx}) in these geometrics are vastly different. At the lowest temperatures $\sigma_{xx,\mathrm{asm}}/\sigma_{xx,\mathrm{sym}} > 10^6$, strongly individuating that the superfluid mode has been detected!

4.6 CONCLUSION

In summary, we have discussed the FQHE in a single 2DES, with an emphasis on the lack of a quantized Hall state at $\nu = 1/2$. The additional complexity introduced by a second 2D layer, however, permits the formation of new quantum Hall states both at $\nu_T = 1/2$ and at $\nu_T = 1$. Even in the limit of vanishing tunneling, an inter-layer correlated quantum Hall state at total filling factor $\nu_T = 1$ can form.

We have examined tunneling in double-layer 2D electron systems as the inter-layer correlations are continuously tuned from weak to strong. A dramatic enhancement of the zero-bias tunneling conductance is observed as the system crosses the phase boundary into the $\nu_T = 1$ quantized Hall state. It seems likely that this peak is intimately connected with the $q = 0$ component of the Goldstone mode of the broken symmetry ground state.

Several facets of the $\nu_T = 1$ tunneling resonance have been introduced here and are the topic of subsequent chapters. The detailed temperature dependence is studied in Chapter 5 and the dependence of the phase boundary on d/l_B and density imbalance is the focus of Chapter 7.

CHAPTER 5

TEMPERATURE DEPENDENCE OF THE $\nu_T = 1$ QHE

In this chapter we measure the temperature dependence of tunneling in the $\nu_T = 1$ quantum Hall state and compare these results to those of a conventional Josephson junction. Contrary to popular belief, a conventional Josephson junction always has a finite, albeit usually minuscule, resistance. This resistance is strongly temperature-dependent and vanishes as $T \rightarrow 0$. For sufficiently small and carefully-engineered junctions this dependence can be measured [73] and is well understood within the context of conventional theory [74, 75]. The results are qualitatively similar to the bilayer $\nu_T = 1$ tunnel junction, in that the conductance peaks both become taller and sharper with decreasing temperature, however, the quantitative behavior of the two systems is sharply disparate.

The zero-bias conductance of a "large" superconducting tunnel junction in the over-damped regime follows an Arrhenius behavior, $G_0(T) \sim \exp(2E_j/k_bT)$. The Josephson energy, E_j, is characteristic energy of the tunnel junction. Evidently, as $T \rightarrow 0$ the conductance diverges; in practice $E_j \gg k_bT$, so that except very close to the transition temperature the conductance is essentially infinite.

In contrast, we find that in the $\nu_T = 1$ quantum Hall junction the conductance is exponential in temperature, $G_0(T) \sim \exp(-T/T_0)$, over as many as three decades in conductance. This simple exponential form extrapolates to a finite value at zero temperature. If this extrapolation is to be trusted, we may conclude that there is no true super-current branch in this system.

Although a single Josephson junction has an activated conductance, granular superconducting arrays can have an exponential dependence. This suggests that per-

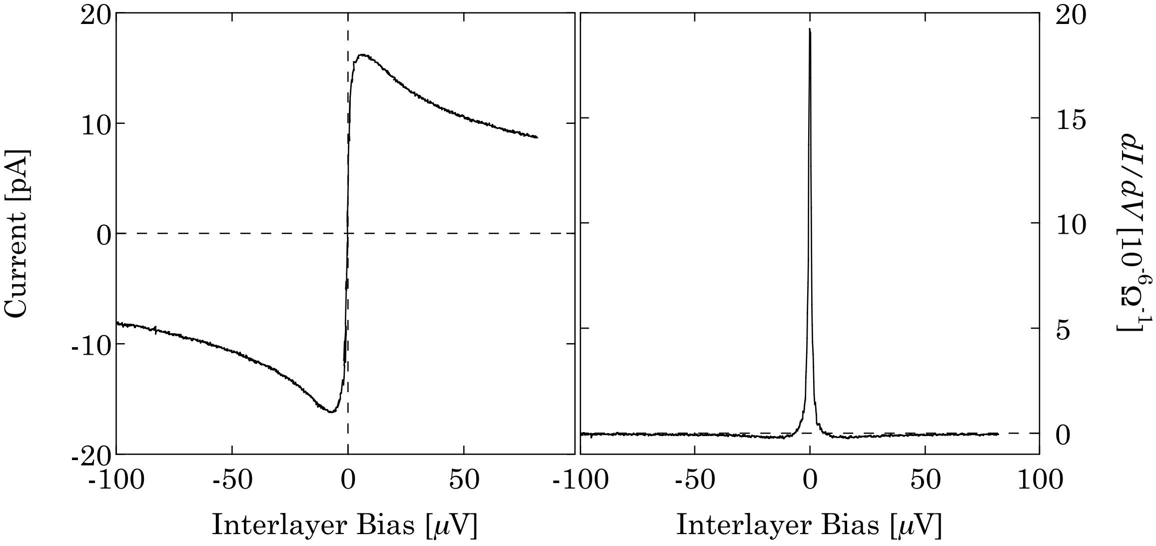

Figure 5.1: Representative $I - V$ and dI/dV data for the $\nu_T = 1$ tunnel junction at $T = 25$ mK and $d/l_B = 1.50$. Note that the line width is clearly nonzero.

haps the strongly disordered quantum Hall system is somehow similar to the granular system.

5.1 Temperature dependence of a Josephson junction

In agreement with theoretical expectations, the observed inter-layer tunneling spectra at $\nu_T = 1$ is qualitatively similar to that of a true Josephson junction [14]. Therefore, we start our discussion with the well known behavior of a "classical" Josephson junction.

In the resistively-shunted junction (RSJ) model, the superconducting circuit is described as an ideal Josephson junction in parallel with a capacitor (an external capacitor in parallel, or just the innate capacitance of the tunnel junction) and a shunting resistor. The resulting dynamics are described by a "tilted washboard" potential with a viscous damping term due to the resistor; at nonzero temperature, this model always leads to a finite (although generally minuscule) resistance.

Figure 5.2-A illustrates the RSJ circuit. Strictly speaking, only the left circuit represents RSJ model. However, the equations of motion for the left and right circuits are equivalent, requiring only a reinterpretation of the voltage and current variables.

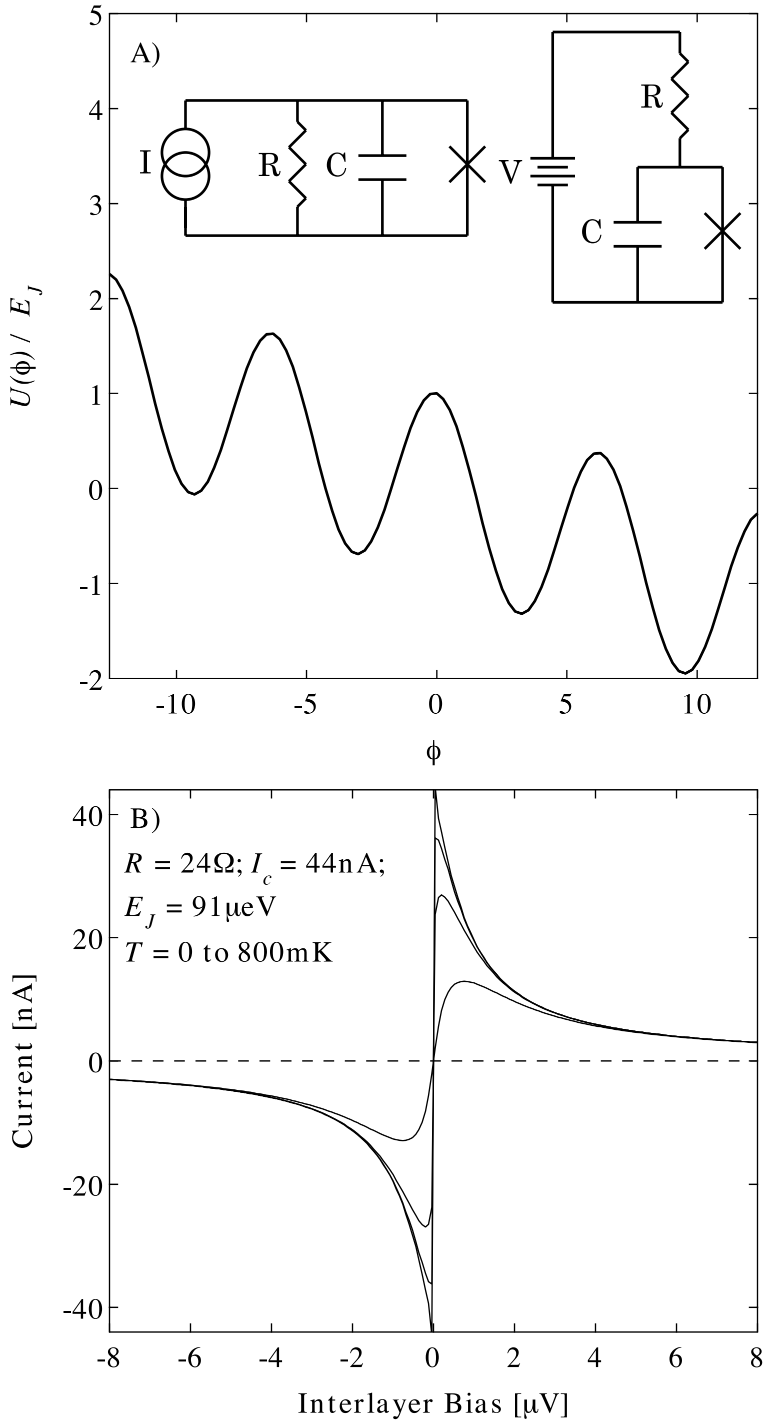

Figure 5.2: RSJ model of a Josephson junction. A) The left circuit is the actual RSJ circuit, while right-hand circuit is a realization more similar to the $\nu_T = 1$ junction. The oscillatory curve represents the potential landscape for the phase ϕ. B) Simulated $I - V$ data for the experimentally realized parameters of Steinbach *et al.* [73]: $R = 24\ \Omega$, $I_c = 44$ nA, and $E_J = 91\ \mu$eV. These curves correspond to $T = 0$, 25, 200, and 800 mK.

The remainder of this section will treat this second case.

A Josephson junction can be considered a nonlinear circuit element obeying Josephson's equations

$$I = I_c \sin\phi, \qquad \text{and} \qquad \frac{d\phi}{dt} = \frac{2e}{\hbar}V,$$

where ϕ is the phase difference between the two superconductors. With the conventional descriptions of resistors and capacitors, this leads to an equation of motion for the phase variable ϕ,

$$\frac{\hbar C}{2e}\ddot{\phi} + \frac{\hbar}{2eR}\dot{\phi} + I_c \sin\phi = \frac{V}{R}.$$

This motion corresponds to the damped oscillations of a particle in the tilted washboard potential illustrated by Figure 5.2, and is described by the potential,

$$U(\phi) = -E_J\left(\cos\phi + \frac{V}{RI_c}\phi\right). \tag{5.1}$$

The Josephson energy, E_J, has been defined as $E_J = I_c\hbar/2e$. We can qualitatively understand the behavior of the junction in two limits. A) When the applied bias is small, the washboard potential is slightly tilted, and the equilibrium value of ϕ is shifted slightly from zero, leading to a DC current $I = I_c \sin\phi$. Since ϕ is time-independent, $d\phi/dt = 2eV/\hbar = 0$, and there is no voltage drop across the junction. B) In the opposite limit, when the applied bias V is large, the phase "rolls" down the steeply tilted washboard, leading to an AC current. As V is further increased, the time-averaged DC current decreases to zero.

When C is small, i.e., the over-damped limit, the model can be solved and the resulting $I - V_j$ and dI/dV_j characteristics are given by [76]

$$I = \frac{1}{R}\left[\sqrt{V_j^2 + I_c^2R^2} - V_j\right], \qquad \text{and} \qquad \frac{dI}{dV_j} = \frac{1}{R}\left[\frac{V_j}{\sqrt{V_j^2 + I_c^2}} - 1\right].$$

V_j is the voltage drop across the junction, not the applied bias. In this model, there is a super-current branch at zero-bias, while slightly away from zero, the current scales like $I(V_j) \sim -|V_j|^{-2}$.

The thermodynamics of a classical object in the potential described by Equation 5.1 can be solved exactly solved [74, 75]. The resulting $I - V_j$ is the ratio of modified Bessel functions

$$I = \mathrm{Im}\left(\frac{I_{1-i\beta E_J v}(\beta E_J)}{I_{-i\beta E_J v}(\beta E_J)}\right), \qquad \text{and} \qquad V_j = R(I_c v - I).$$

This final pair of equations must be solved numerically to acquire a particular $I - V_j$. Figure 5.2-B shows a family of typical $I - V_j$ curves representing the real junction measured by Steinbach *et al.* [73]. In this sample, the normal resistance is $R = 24\ \Omega$, the critical current $I_c = 44$ nA, and the Josephson energy $E_J = 91\ \mu$eV. These curves correspond to $T = 0$, 25, 200, and 800 mK.

Although the zero-bias conductance of the $I - V_j$ can be analytically computed, the low-temperature behavior can be obtained by simple physical considerations. The existence of a potential barrier with height $2E_J$ leads to the expectation that the phase diffuses between wells in an activated fashion. This leads to a finite voltage, and hence a finite conductance in an Arrhenius form given by

$$G_0 = g_0 e^{2T_J/T}.$$

At low-temperatures, the critical current I_c saturates; therefore, the line width, Γ, in dI/dV must simply be proportional to $1/G_0$.

Using this simple model of a Josephson junction, we now investigate the temperature dependence of the $\nu_T = 1$ tunneling feature.

5.2 MEASUREMENT

These experiments were performed in a pair of bilayer GaAs/AlGaAs heterostructures grown by MBE. In these samples, two 180 Å GaAs quantum wells are separated by a 99 Å $Al_{0.9}Ga_{0.1}As$ barrier. Both samples consist of a $250 \times 250\ \mu$m tunneling region with arms extending outward from each side. Gates placed above and below the tunneling region allow for precise control of the electron density, while depletion gates on the arms permit selective contact to each of the two layers. The majority of the results come from Sample E, which has a nominal tunneling strength of 30×10^{-9} Ω^{-1}. When d/l_B is very close to the $\nu_T = 1$ phase boundary, however, the tunneling signal becomes small, and we switch to Sample H[1]. This much more strongly tunneling sample has a zero field conductance of 4×10^{-6} Ω^{-1}.

The data described here was taken in RF filtered and shielded enclosures (see Appendix C for typical details), which, in combination with careful grounding, helped eliminate parasitic distortions of the intrinsic line-shape. Since we do not know, *a priori*, the line shape, our belief that the noise is no longer relevant is based on the fact that line width and peak height both continue to evolve at the lowest temperatures. While in the presence of noise-induced broadening, the height and width both tend to saturate at finite temperature.

In this series of experiments, we investigate the dependence of the $\nu_T = 1$ tunneling feature on temperature and d/l_B. We describe the tunneling peak in terms of its maximum conductance G_0, and its line width Γ_{HWHM} in I/V. In Chapter 3, the half-width of the zero magnetic field feature in I/V was related to the electron lifetime, $\Gamma_{\mathrm{HWHM}} = \hbar/\tau$. In that case, the measured I/V data reflects the convolution of each layers' separate spectral function; as a result the observed peak in I/V is broader than either individual spectral function. In the $\nu_T = 1$ case we purport to directly observe a *single* collective mode: there is no convolution, and it is more suitable to define $\Gamma_{\mathrm{HWHM}} = \hbar/2\tau$.

5.2.1 Observations Figure 5.3 illustrates the temperature dependence of the $\nu_T = 1$ tunneling peak at $d/l_B = 1.50$. Panels A) and B) display the tunneling conductance and current vs. inter-layer bias at four different temperatures: 25, 50, 100, and 200 mK. As a function of temperature, the line qualitatively becomes both shorter and fatter. With the same qualitative eye, the $I - V$ data is strongly reminiscent of that in a Josephson junction.

---

[1] The designed structure of these two samples is the same; however, due to the difference in tunneling strength, we infer that the barrier on Sample H is slightly thinner.

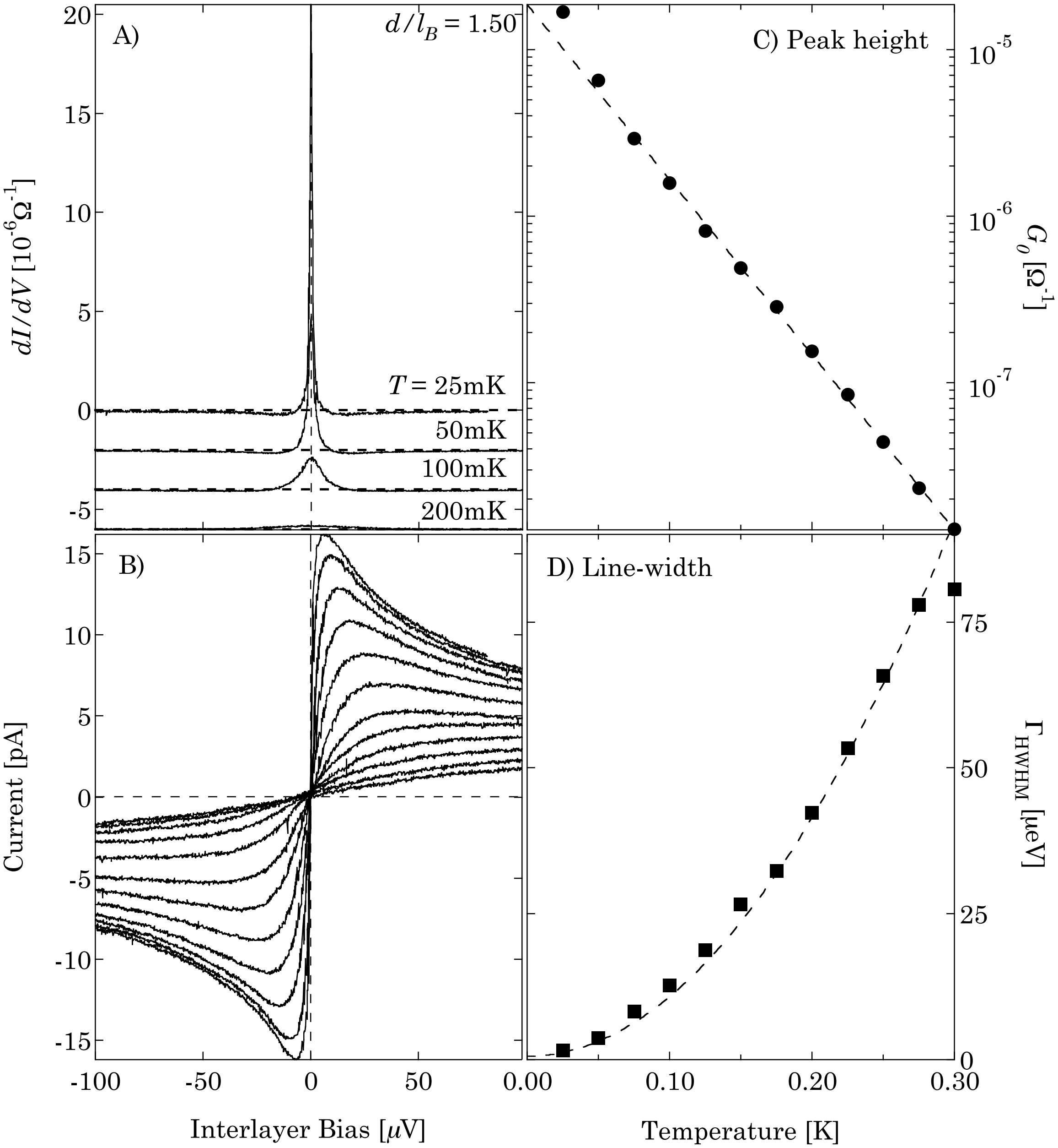

Figure 5.3: Representative temperature dependence at $d/l_B = 1.50$. Dashed lines represent fits to the data. A) Tunneling conductance vs. inter-layer bias at 25, 50, 100, and 200 mK. B) $I - V$ data spanning 25 to 300 mK in 25 mK steps. C) Peak height as a function of temperature, with exponential fit. D) Line width as a function of temperature with quadratic fit.

In Figure 5.3-C, the dependence of the peak conductance vs. temperature is displayed. We make the purely empirical observation that for three decades, the conductance is simply exponential in the temperature: $G_0(T) = g_0 \times \exp(-T/T_0)$. This is very different from the activated behavior seen in the phase diffusion picture. Panel D) shows the apparently quadratic dependence of the line width on temperature. Again, this behavior is theoretically unanticipated, but is reminiscent of the temperature dependence at zero magnetic field.

Figure 5.4 summarizes the temperature-dependent observations as a function of d/l_B. Note that close to the phase boundary, the peak in conductance becomes very small and the measurement becomes noise limited. By switching to Sample H (open markers) we can explore closer to the phase boundary[2].

As illustrated in the top panel of Figure 5.4, the suppression of the $\nu_T = 1$ boundary shows two independent effects. As the phase boundary is approached, the overall conductance scale is reduced and suppressed more rapidly in temperature.

The data in Figure 5.4 shows that the temperature dependence of any given d/l_B can be described only by the two parameters $g(d/l_B)$ and $T_0(d/l_B)$. This description is valid over a wide range of temperatures; however, very close to the phase boundary we observe that the conductance begins to fall with decreasing temperature. We also note extremely long time constants in this range of d/l_B. Upon cooling, the system can take as long as $10,000$ seconds to reach equilibrium. This unusual behavior is not fully understood, and is a topic of ongoing work.

5.2.2 Granular superconductors Although a single Josephson junction shows a qualitatively different temperature dependence than observed here, the resistance of a disordered array of small junctions can have a purely exponential temperature dependence.

In a series of experiments by Frydman *et al.* [77], the four-terminal resistance of a thin, granular superconducting film was found to be exponential in temperature. The

---

[2] Using the growth structure, the critical d/l_B for this sample is measured to be 1.96, compared to 1.83 for Sample E. This suggests that, in combination with the unexpected 100-fold enhancement of the tunneling strength, the *actual* thickness of the barrier (and possibly the wells) is somewhat less than expected.

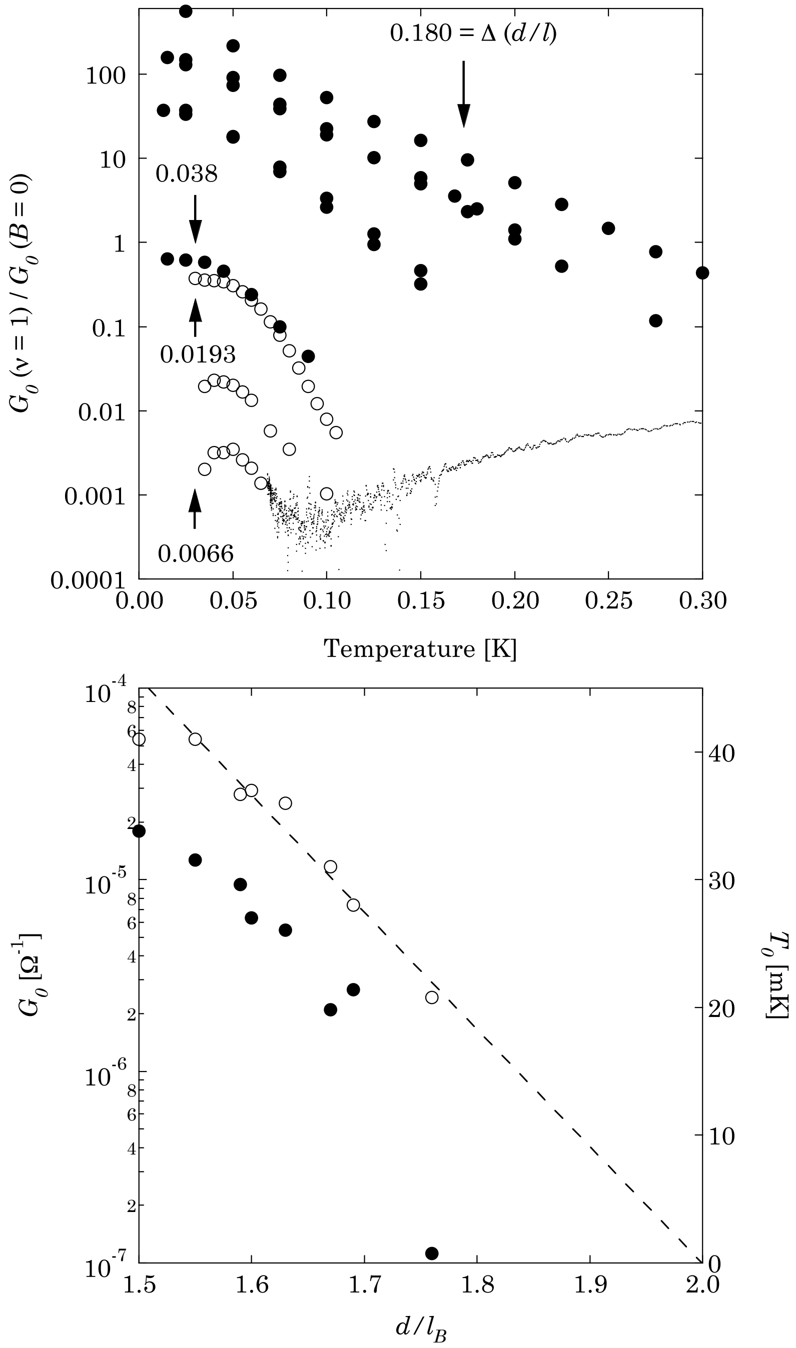

Figure 5.4: Top: peak conductance vs. temperature as a function of $\Delta(d/l_B) = (d/l_{B_{\rm crit}} - d/l_B)/d/l_{B_{\rm crit}}$ for two samples with different tunneling strengths (see text). The solid markers stem from Sample E, and at $\Delta(d/l_B) = 0.180$, 0.126, 0.087, and 0.038 (all using $d/l_{B_{\rm crit}} = 1.83$). Empty markers come from Sample H at $\Delta(d/l_B) = 0.0193$, 0.009, and 0.0066 (all using $d/l_{B_{\rm crit}} = 1.965$). Bottom: dependence on d/l_B of exponential fit parameters from Sample E. Solid: G_0 on the left axis. Empty: T_0 on the right axis, dashed line is a fit to T_0 vs. d/l_B; note that it extrapolates past the phase boundary at $d/l_B = 1.83$.

200 Å superconducting grains are deposited in a ultra-high vacuum (UHV) cryogenic environment, yielding an extremely clean system. The system should be thought of as an disordered array of superconductors coupled via Josephson tunneling.

As the film is cooled, the grains first begin to superconduct at their transition temperature (as observed via local STM measurements of the superconducting energy gap); however, the four-terminal resistance is unchanged. For sufficiently thick films, further cooling leads to the temperature dependence: $R(T) = r_0 \exp(T/T_0)$.

Although the authors do not propose a specific mechanism for this unusual temperature dependence, their computer simulations of finite temperature, diffusive, 1D Josephson junctions arrays, give approximately exponential temperature dependence.

Like this granular system, the bilayer 2DESs are highly disordered. Therefore, it is likely that instead of a single clean superfluid, it may be better considered as a collection of 2D superfluid droplets which are themselves Josephson coupled.

In this scenario, the decreasing temperature gradually increases the length, ℓ, over which grains are phase-coherent. It is noteworthy that while tunneling between many phase-incoherent regions grows in proportion to the number of objects, phase-coherent tunneling tunneling scales as N^2. Thus, as the phase-coherent regions increase in size, the tunneling grows like ℓ^2.

5.3 CONCLUSION

The observed $I - V$ tunneling data at $\nu_T = 1$ is qualitatively similar to finite temperature Josephson tunneling in the diffusive limit. Furthermore, the qualitative dependence on temperature of these $I - V$ curves is similar. Quantitatively, however, they are quite different from one other. The temperature dependence of the tunneling conductance better resembles the four-terminal conductance of a granular array. This similarity may be interpreted as signaling the importance of disorder.

Close to the phase boundary, the exponential temperature dependence is suppressed at the lowest temperatures. Associated with this suppression, the system exhibits extremely long time constants. Preliminary measurements indicate that they stem from the interaction between the 2DES and the nuclear spin system of the gallium and arsenic nuclei.

Chapter 6

Observation of the $\nu_T = 1$ Goldstone Mode

So far, the tunneling experiments at $\nu_T = 1$ have focused on properties of the spectrographically sharp tunneling feature at zero-bias. Since tunneling between two-dimensional (2D) layers conserves both energy and momentum, these measurements probe only those properties of the collective phase that involve no momentum transfer. The application of a magnetic field *parallel* to the 2D planes, however, can impart momentum to the tunneling electrons, which allows experimental access to the finite q collective modes. In this chapter, we present a direct spectrographic measurement of a linearly dispersing collective mode. We argue that this mode is the anticipated Goldstone mode concomitant with the broken symmetry ground state [10, 14, 15].

In the case of tunneling between two parallel 2D layers, the parallel field $B_\parallel$ provides a wave-vector $q = eB_\parallel d/\hbar$, where d is the separation between the 2D sheets. By rotating the sample with respect to the total magnetic field (B), the component of the magnetic field perpendicular to the sample ($B_\perp$) and parallel to the sample ($B_\parallel$) can be independently adjusted *in situ*. This technique has been applied both to 3D-3D tunneling between superconductors [78] and to tunneling in 2D electron systems [79, 80].

The chapter begins by considering the case when the total magnetic field is parallel to the 2D layers, i.e., $B_\perp = 0$. Since dynamics of the individual 2D systems are largely unchanged in the presence of a parallel field, tunneling measurements performed in this configuration can be used to map the 2D Fermi distribution in the $k_x - k_y$ plane [80].

The effect of a parallel field in the $\nu_T = 1$ state is more subtle. When tunneling is strong, a parallel field leads to a phase transition at a critical field ${B_\parallel}^*$, which can be detected in conventional resistivity measurements [18] (Section 6.3). This transition was the first experimental evidence supporting the existence of the superfluid/ferromagnetic order-parameter ϕ [19].

In the ferromagnetic phase, spatial variations of the pseudospin phase, ϕ, govern the low-energy excitations in the system. In addition to the gapped charged excitations that lead to the formation of a quantum Hall effect (QHE), it also possesses Goldstone modes attendant to the broken symmetry ground state [10, 14, 15]. These pseudospin waves are associated with spatial gradients in the phase. When $t \to 0$, they are gapless in the long wavelength limit. By applying a parallel field, we observe the expected tunneling signature of the Goldstone mode at finite applied bias. This chapter focuses on the direct measurement of these excitations.

In addition to the expected finite bias features, we unexpectedly find that the zero-bias peak remains, dominating the tunneling spectra even at large parallel field. The final section of this chapter investigates the dependence on parallel field of this remnant peak. It likely results from the strongly disordered nature of the 2D system, which may well break up into a disordered array of Josephson couped superfluid grains.

6.1 EFFECT OF A PARALLEL FIELD

The consequences of a parallel field can be understood intuitively by considering the effect of the Lorentz force on an electron traversing the distance, d, between the 2D electron layers. When a parallel field $\mathbf{B} = B_\parallel \mathbf{x}$ is applied, an electron with an initial 2D velocity $\mathbf{v}_{2D}$ experiences a force

$$\mathbf{F} = -e\mathbf{v} \times \mathbf{B} = -eB_\parallel \left(v_z \mathbf{y} - v_z \mathbf{x} \right).$$

The time dependence of the **z** variables, $v_z(t)$ and $z(t)$, is

$$v_z(t) = v_y(0)\sin(\omega_c t), \qquad \text{and} \qquad z(t) = \frac{1}{\omega_c}\left[v_y(0) - v_y(t)\right].$$

When the electron traveled the full distance between the layers, i.e., $z(t) = d$, the change in q_y is given by

$$d = \frac{1}{\omega_c}\left[v_y(0) - v_y(t)\right], \qquad \text{and} \qquad \Delta q_y = -\frac{eB_\parallel d}{\hbar}.$$

After each tunneling event the electron's momentum is shifted by Δq. To better understand this process, it is helpful to consider tunneling when $B_\perp = 0$; the 2D dynamics of the individual layers are unchanged by the addition of a parallel field[1]. Therefore, the 2D-2D tunneling can be well understood in terms of the Fermi's golden rule expression from Chapter 3.

Figure 6.1 shows the parallel field dependence of the zero-bias tunneling between two layers with matched density ($n_1 = n_2 = 0.58\times10^{11}$ cm^{-2}). When $B_\parallel = 0$, the signal is maximized and tunneling occurs at the points where the Fermi circles overlap. In contrast, when $B_\parallel \neq 0$, the Fermi circles are shifted with respect to each other and tunneling is only allowed at the two points where they overlap. Finally, when $q = 2k_f$, the edges of the circles briefly osculate, and there is a small enhancement of tunneling before it vanishes.

This data was taken in Sample F, which has 180 Å wells and a 89 Å barrier. At this density, the computed Fermi wave-vector is $2k_f = 1.3 \times 10^8\ m^{-1}$. With the center-to-center well spacing of 269 Å, the location of the secondary peak at $B = 2.89$ T predicts $2k_f = 1.2 \times 10^8\ m^{-1}$. The consistency of this simple picture with the experimental data provides confidence in the understanding of tunneling of a parallel magnetic field.

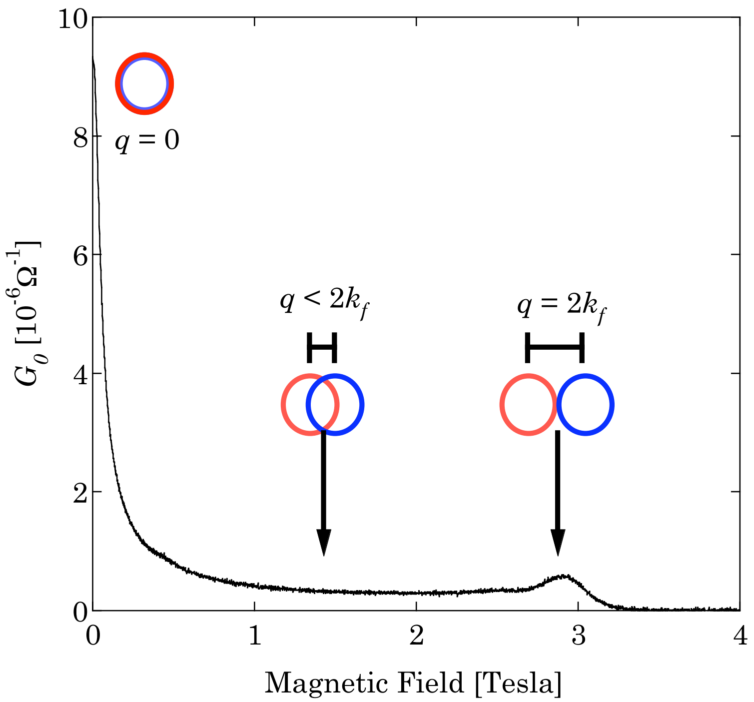

Figure 6.1: 2D-2D tunneling in the presence of a parallel magnetic field, showing clearly the shifting of the Fermi circles with respect to each other.

6.2 A JOSEPHSON JUNCTION IN A PARALLEL FIELD

Although the measurements are in bilayer 2D systems, it is instructive to further pursue the analogy with conventional Josephson junctions. Fogler *et al.* [81] recently pointed out a classic experiment by Eck *et al.* [82] who measured the DC $I - V$ of a Josephson junction in the presence of a parallel magnetic field, $B_{\|}$. The observed DC tunneling current was peaked at finite bias, V^*, and V^* was found to vary linearly with $B_{\|}$.

To understand the features at finite bias, we must include the interaction between the AC tunneling current and the electromagnetic modes inherent in a Josephson junction: the Swihart modes. When the momentum provided by the parallel field, and the energy supplied by the external voltage source, are coincident with the dispersion of Swihart modes, the DC tunneling current is peaked. Recalling that in the presence

---

[1] In reality, parallel fields do affect finite-width 2D systems by mixing between the quantum-wells' subbands.

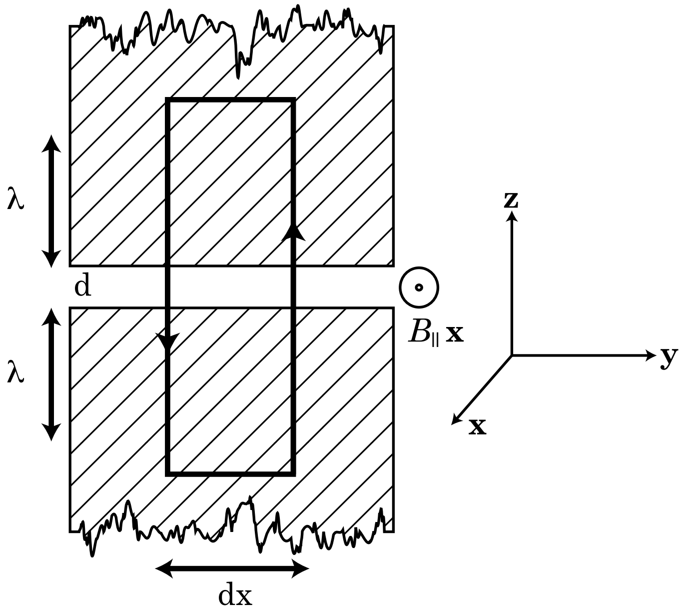

Figure 6.2: SIS tunnel junction with a parallel magnetic field $\mathbf{B} = B_\parallel \mathbf{x}$.

of a parallel magnetic field in the **x** direction, the Josephson equations read

$$j = j_c \sin(\phi(y) - ky), \qquad \text{and} \qquad \frac{d\phi}{dt} = \frac{e^*}{\hbar} V(y,t).$$

k is exactly the wave-vector a cooper-pair acquires when crossing the tunnel barrier, $k = e^* B_\parallel d'/\hbar$ where $d' = 2\lambda + d$. In a superconductor, $e^* = 2e$, and λ is the London penetration depth, i.e., how far the magnetic field penetrates from the insulator into the superconductor.

By considering the surface integral of $\nabla \times \mathbf{E} = -\partial B/\partial t$ bounded by the contour shown in Figure 6.2, and the analogous contour in the $x - z$ plane we arrive at the pair of equations

$$\frac{\partial E_z}{\partial y} = -\frac{d'}{d}\frac{\partial B_x}{\partial t}, \qquad \text{and} \qquad \frac{\partial E_z}{\partial x} = \frac{d'}{d}\frac{\partial B_y}{\partial t}.$$

The $\nabla \times \mathbf{E}$ integral is computed by evaluating the contour integral $\int E \cdot dl$ around the indicated loop. Since the z-component of the electric field is screened within the superconductor, the integral is proportional to d, not $d' = d + 2\lambda$.

A final differential equation can be derived from the **z** component of a second Maxwell equation[2]: $\nabla \times \mathbf{B} = \mu_0 \epsilon_0 \partial \mathbf{E}/\partial t + \mu_0 \mathbf{j}$. Which gives the relation,

$$\frac{\partial B_y}{\partial x} - \frac{\partial B_x}{\partial y} = \frac{1}{c^2}\frac{\partial E_z}{\partial t} + \mu_0 j_z.$$

In these equations, E_z can be identified as the AC potential $v(t)/d$. With this substitution, the three differential equations combine into a single, damped-driven wave equation

$$\left(\frac{\partial^2}{\partial x^2} + \frac{\partial^2}{\partial y^2} - \frac{1}{\bar{c}^2}\frac{\partial^2}{\partial t^2} - \frac{1}{\bar{c}^2 \tau}\frac{\partial}{\partial t}\right) v = \frac{d}{\epsilon_0 \bar{c}^2}\frac{\partial j_z}{\partial t}. \tag{6.1}$$

In this wave equation, the speed of light has been renormalized to $\bar{c}^2/c^2 = d/d'$, and dissipation has been phenomenologically included via a scattering time, τ. In the limit, when the induced AC voltage is much smaller than the applied DC voltage, i.e., $v/V_{\mathrm{DC}} \ll 1$, the phase difference is approximately $\phi_0 \approx e^* V t/\hbar = \omega_J t$. The current in the **z** direction, j_z, must be the Josephson tunneling current. We can compute the current density using the approximate phase $j_z = j_c \sin(kx - \omega_J t)$.

Equation 6.1 permits solutions of the form $v = v_0 \sin(kx - \omega_J t + \Theta)$. Substituting and solving gives for the coefficients v_0 and Θ

$$v_0 = \frac{d j_c}{\epsilon_0 \omega_J}\left[\left(1 - \frac{q^2 \bar{c}^2}{\omega_J^2}\right)^2 + \left(\frac{1}{\omega_J \tau}\right)^2\right]^{-1/2}, \quad \text{and} \quad \tan\Theta = \frac{1}{\omega_J \tau}\left(1 - \frac{q^2 \bar{c}^2}{\omega_J^2}\right)^{-1}.$$

This small AC voltage leads to a correction of the phase $\phi = \phi_0 + v/V_{\mathrm{DC}} \sin(\omega_J t - qx + \Theta)$, which results in a slightly modified tunneling current, $j = j_c \sin(\phi_0 + v/V_{\mathrm{DC}} \sin(\omega_J t - qx + \Theta))$. This perturbed Josephson tunneling current has a finite time-averaged DC component,

$$\begin{aligned} j_{\mathrm{DC}} &= \frac{j_c v_0}{2V_{\mathrm{DC}}} \sin\Theta \\ &= \frac{j_c^2 d}{\epsilon_0 \omega_J V_{\mathrm{DC}}} \frac{1}{\omega_J \tau}\left[\left(1 - \frac{q^2 \bar{c}^2}{\omega_J^2}\right)^2 + \left(\frac{1}{\omega_J \tau}\right)^2\right]^{-1}. \end{aligned}$$

---

[2] For simplicity, this calculation is performed with $\epsilon = \mu = 1$.

Thus, the AC Josephson oscillations, in conjunction with a parallel magnetic field, simulate the low-energy electromagnetic modes. The resulting voltage oscillations lead to measurable peaks in the DC $I - V$ located at $\omega_J = \pm q\bar{c}$. It is important to note that this linearly dispersing mode is the only low-energy excitation of the system. It can equivalently be described as electromagnetic modes in the tunnel junction or modes in the phase difference ϕ.

The expectation for the $\nu_T = 1$ system is very similar, predicting that when $B_{\|} \neq 0$, the zero-bias step in $I - V$ will split into peaks at finite bias [83, 84]. To test this interpretation, we have examined the tunneling spectra at $\nu_T = 1$ after adding a small magnetic field component $B_{\|}$, parallel to the 2D planes, to the existing perpendicular field $B_{\perp}$. The voltage location of these resonances should be $eV^* = \pm\hbar\omega(q)$, where $\hbar\omega(q)$ is the Goldstone mode energy at the parallel field-induced wave-vector q. Since the mode disperses linearly for small q, detection of the splitting will provide a measure of its velocity $\bar{c}$.

6.3 BEHAVIOR AT $\nu_T = 1$

The effect of $B_{\|}$ in ρ_{xx} was investigated by Murphy *et al.* [18]. In these experiments, the transport energy gap, Δ, was measured as a function of parallel field – observations that stimulated the development of the pseudospin model [19, 69, 70]. Murphy noticed that the energy gap first decreased rapidly with parallel field, then saturated at a critical field, B^*.

This transition is easily understood in the pseudospin language; in the presence of a parallel field, the relevant components of the pseudospin Hamiltonian read

$$H = \int d^2x \left[\rho_s \frac{|\nabla\phi|^2}{2} - \frac{t}{2\pi {l_B}^2} \cos(\phi - qx) \right].$$

When $B_{\|}$ is small, the tunneling energy is minimized by a pseudospin, which tumbles in space, $\phi = qx$, leading to an energy density $\rho_s q^2/2$. In contrast, at large $B_{\|}$, a position-independent phase minimizes the energy. In this limit, the average energy density is 0. By setting these simple estimates of the energy equal, we find a critical field

$$B_{\parallel}{}^{*} = B_{\perp}\frac{l_B}{d}\frac{t}{\pi\rho_s}.$$

This equation overestimates, by a factor of only $2\sqrt{2}/\pi \approx 0.9$, the results of more sophisticated calculations [70]. In the transport experiments of Murphy *et al.*, their most weakly tunneling sample was at $d/l_B = 1.8$, with a density of $N_T = 1.26\times10^{11}$ cm^{-2} and a tunnel gap $\Delta_{\mathrm{SAS}} = 2t = 0.8$ K. Based on these parameters, $\Delta_{\mathrm{SAS}}/E_c = 7\times10^3$ and $\rho_s \approx 300$ mK [69], therefore, $B_{\parallel}{}^{*} = 1.1$ T. This prediction is in agreement with the observed transition when the sample was tilted by $\theta^* = 8°$ with respect to the total field, giving $B_{\parallel}{}^{*} = 0.73$ T.

In the current samples, however, $\Delta_{\mathrm{SAS}} \approx 6$ μK, so the critical angle is only $\theta^* \approx 10\times10^{-6}$ degrees. Since we can only control the angle to about $\delta\theta \sim 0.1°$, for all practical purposes, the samples are always in the phase minimizing the gradient energy.

6.4 Experiment

The data in this chapter are taken in Samples D and E. These four-terminal tunneling samples are described in more detail in Chapters 3 and 4. Sample D is used in the experiments at "large" $B_{\parallel}$, i.e., measurements of the $\nu_T = 1$ Goldstone mode. The data from Sample E focuses on the consequences in tunneling of a small parallel field.

In these experiments, a magnetic field, B, is provided by a single superconducting solenoid. The parallel component is generated by rotating the sample by an angle θ with respect to the magnetic field. To maintain a constant filling factor, the total field is adjusted so $B = B_{\perp}/\cos\theta$, yielding a parallel component $B_{\parallel} = B_{\perp}\tan\theta$.

To achieve this, we constricted an 18-pin rotating sample assembly from high-purity silver. The rotation is controlled by a Kevlar string attached on one end to the paddle of the rotator, and the other to a micrometer at room-temperature. By pulling on the string, the paddle rotates; a restoring force is provided by a hand-wound Phosphor-Bronze spring attached to the rotator.

These experiments depend on a quantitative measure of the exact parallel field. Usually, $B_{\|}$ is determined by measuring the SdH oscillations of the 2DES under study. This measures $B_{\perp} = B\cos\theta$, which is insensitive near $\theta = 0$. Instead, the parallel field is accurately determined using a second 2D electron gas sample mounted perpendicular to the tunneling sample. The Hall resistance of this second sample is then proportional to $B_{\|} = B\sin\theta$.

As the following data indicate, the tunneling is very sensitive to tilt, changing considerably when rotated only a single degree. Since the rotator can tilt in only one axis, we first level the sample in the other direction, as measured with a laser reflected from the sample.

6.5 LARGE WAVE-VECTOR: $\nu_T = 1$ GOLDSTONE MODE

Figure 6.3 shows the measured tunneling current I vs. V (top panel) and conductance dI/dV vs. V (bottom panel) at $\nu_T = 1$ and $T = 25$ mK with different parallel fields applied. The data shown in Figure 6.3 corresponds to $n_1 = n_2 = N_T/2 = 0.26\times10^{11}$ cm^{-2} or $d/l_B = 1.61$; similar data have been obtained at various values of d/l_B below 1.84. In addition to the now familiar step in $I - V$ and peak in dI/dV, these data show that the zero-bias feature is suppressed by the application of a parallel magnetic field. Only a few tenths of a Tesla are required to strongly suppress the zero-bias conductance peak.

Upon careful inspection, however, the suppression is accompanied by features moving to higher energy with increasing $B_{\|}$. We associate the location of these features with the anticipated linearly dispersing Goldstone mode. The dotted line in the top panel shows the location in I vs. V where these subtle peaks are located in each trace. It is clear from the bottom panel that the parallel magnetic field has a dramatic effect on the tunnel spectrum. The fine structure, which is magnified in Figure 6.4, first appears as two small peaks in dI/dV positioned symmetrically about $V = 0$ and superimposed on the still substantial flanks of the main zero-bias resonance. As the parallel field increases, these split-off peaks move toward higher energies and become more prominent. At the same time, the zero-bias resonance

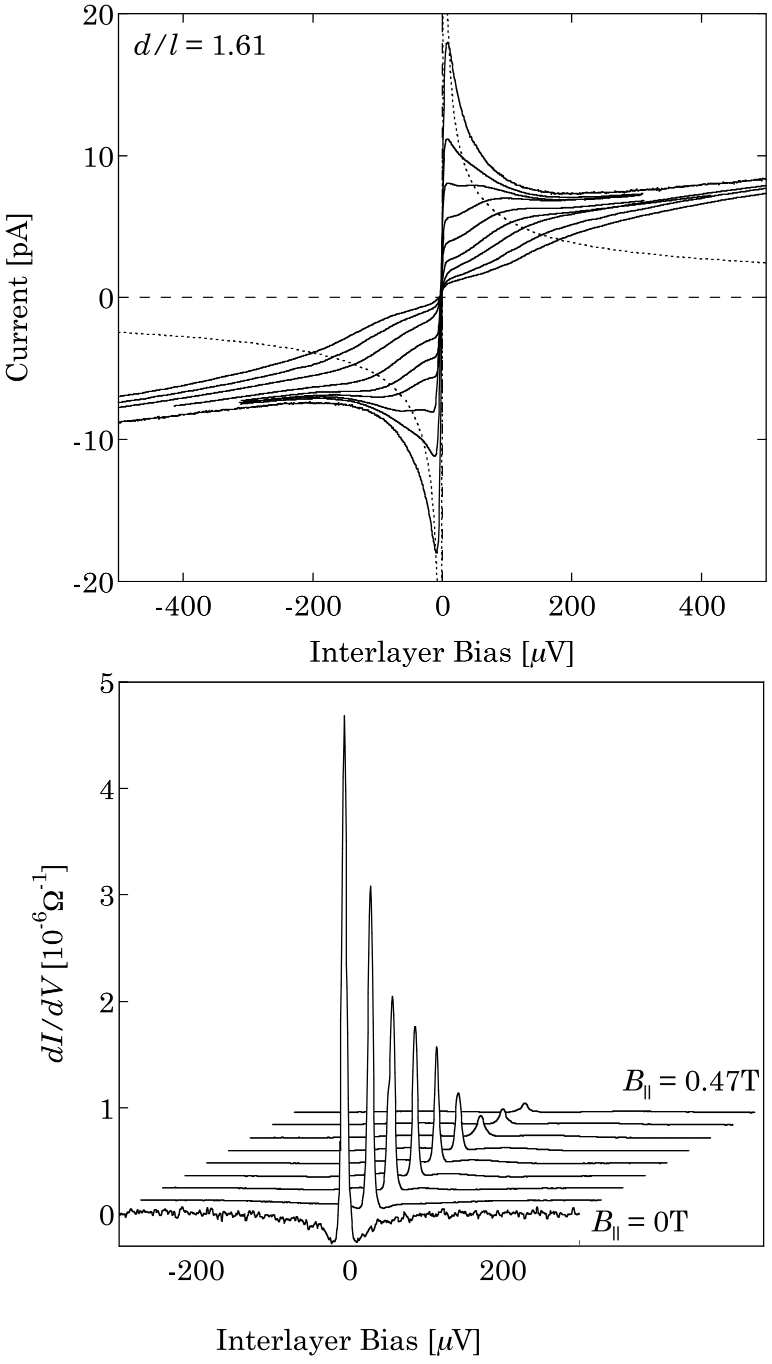

Figure 6.3: Tunneling data at $\nu_T = 1$ and $T = 25$ mK. Total density $N_T = 0.52\times10^{11}$ cm^{-2}, $B_{\|} = 0$ to 0.47 T. Upper panel: $I - V$ vs. inter-layer voltage V. The dotted line indicates the location of the resonance as identified in dI/dV. Lower panel: dI/dV vs. V with $B_{\|} = 0$ to 0.47 T.

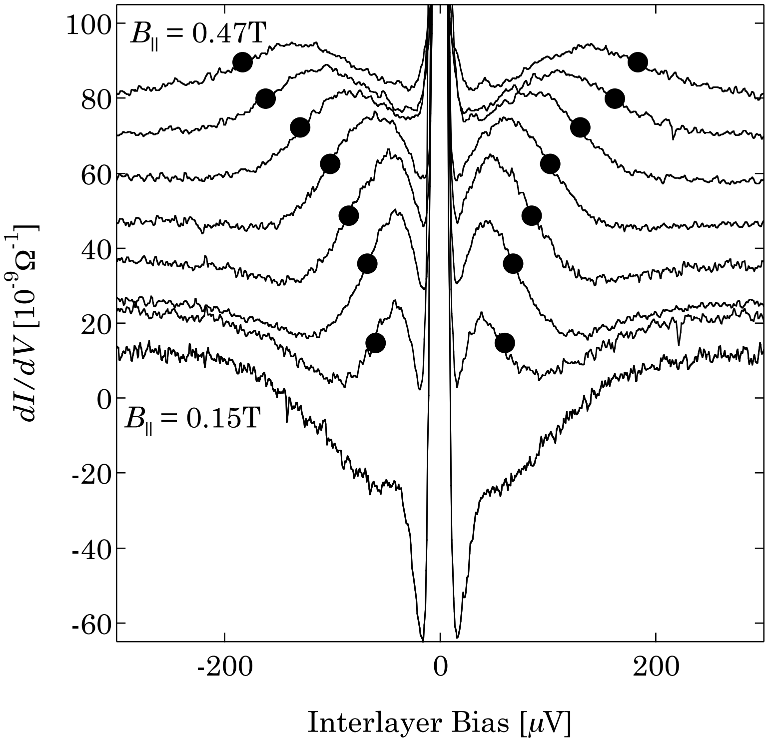

Figure 6.4: Tunneling conductance spectra at $T = 25$ mK and $N_T = 0.52{\times}10^{11}$ cm^{-2} for various parallel magnetic fields. $B_{\|} = 0.11$, 0.15, 0.20, 0.23, 0.29, 0.35, 0.41, and 0.47 T. Dots indicate the positions of the split-off resonances in dI/dV, as identified via maxima in d^2I/dV^2 (Figure 6.5).

weakens steadily. Qualitatively, these split-off resonances have the "derivative" shape theoretically expected [83, 84] for features associated with peaks in $I - V$. Due to the broad, presumably incoherent, background we are unable to identify clear peaks in $I - V$. With this in mind, we identify the energy of the resonances with the voltage V^* at which the derivative of the conductance, d^2I/dV^2, exhibits an extrema (Figure 6.5: top panel). The solid dots in Figure 6.4 show the results of this identification in dI/dV. At high $B_{\|}$, these resonances are lost in the tunneling background.

The top panel of Figure 6.5 shows d^2I/dV^2 as computed numerically from the measured conductance data. The extrema in this data are identified as the location of the resonances and identified with large dots. The bottom panel of Figure 6.5 displays the average energy eV^* of resonances vs. the wave-vector $q = eB_{\|}d/\hbar$. Data for three different densities, $N_T = 0.52$, 0.60, and $0.64{\times}10^{11}$ cm^{-2}, corresponding to

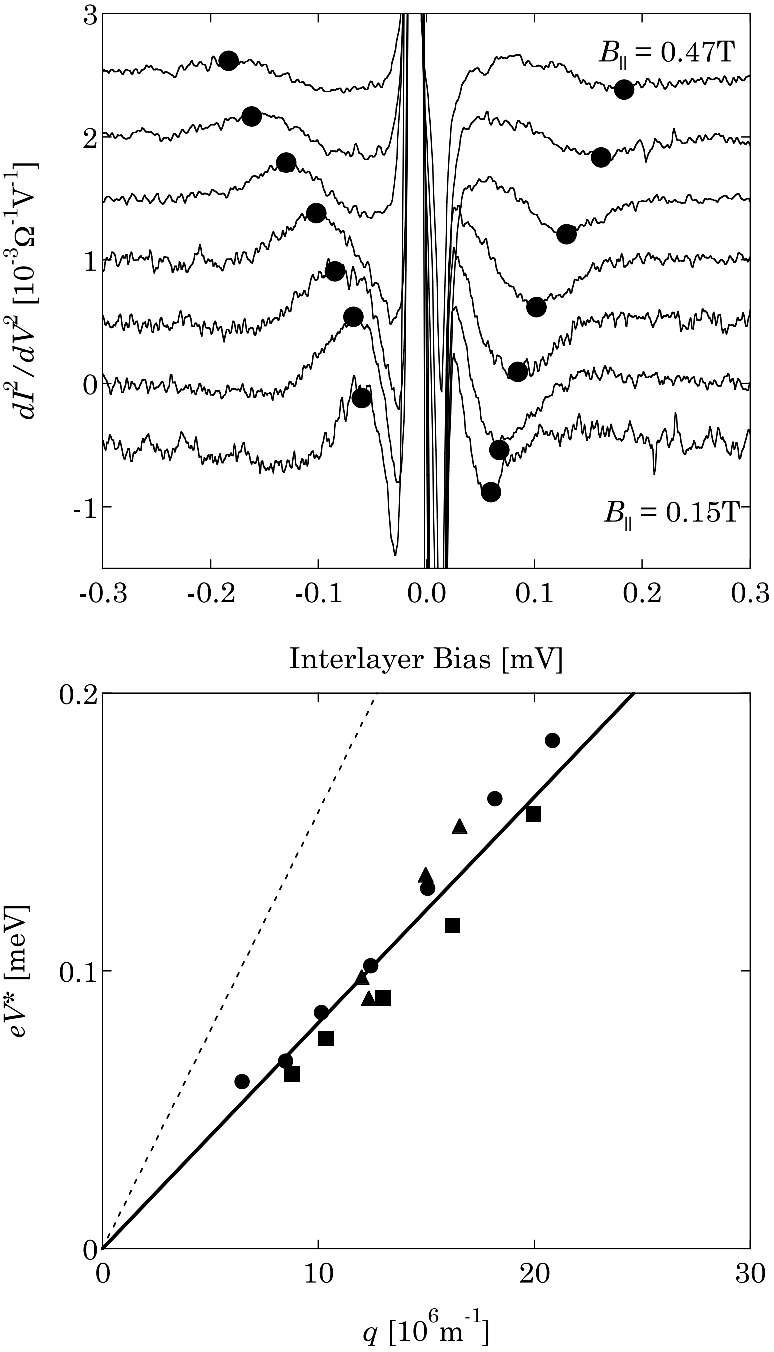

Figure 6.5: Top: d^2I/dV^2 at $d/l_B = 1.59$. The extrema identified with large dots at eV^* are coincident with the peaks in $I-V$, and derivative features in dI/dV. Bottom: energy of split-off peaks vs. the wave-vector $q = eB_{\|}d/\hbar$ induced by the parallel magnetic field. Triangles: $N_T = 0.64{\times}10^{11}$ cm^{-2}. Squares: $N_T = 0.60{\times}10^{11}$ cm^{-2}. Circles, $N_T = 0.52{\times}10^{11}$ cm^{-2}. The dashed line is a theoretical estimate for the Goldstone mode dispersion relation at small q. The solid line is a guide to the eye and corresponds to a collective mode velocity of 14 km/s.

$d/l_B = 1.61$, 1.71, and 1.76, are shown. These data lie on straight lines with a slope identifying the mode velocity $c = 14$ km/s. The dashed line in Figure 6.5 shows an estimate of the dispersion relation of this mode at long wavelengths based on the dispersion relations in Chapter 4. These results, in good agreement with theory, demonstrate the existence of a linearly dispersing collective mode in the bilayer 2D electron system at $\nu_T = 1$.

6.6 SMALL WAVE-VECTOR: DISORDER

The data in Figure 6.3 also possess aspects that are not explained by recent theoretical models [83, 84]. The biggest puzzle is presented by the residual zero-bias conductance peak, which persists to significant $B_{\|}$. In this section, we investigate the behavior of the central peak as it is suppressed, and suggest that disorder may play a role [85].

At zero field, tunneling can be understood in single particle terms and the line width reflects the lifetime of the quasiparticles in the 2D systems [48]. In contrast, the narrow line width and dramatic enhancement in conductance at $\nu_T = 1$ suggests that a collective mode dominates the spectral weight at lowenergy. Additionally, incoherent tunneling cannot explain the strong dependence on parallel field. Tunneling between two uncorrelated layers in a parallel field can be understood much the same way as at zero field. In this case, the single particle wavefunctions described in Chapter 2 lead to an effective change of the tunneling gap,

$$\Delta_{\mathrm{SAS}}(B_{\|}) = \Delta_{\mathrm{SAS}} \exp\left[-\left(\frac{d}{l_B} \frac{B_{\|}}{2B_{\perp}} \right)^2 \right],$$

resulting in a suppression of the tunneling current proportional to ${\Delta_{\mathrm{SAS}}}^2$. In our samples at $d/l_B = 1.63$, the tunneling signal should decrease by 50% at $B_{\|} = 1.61$ T or $\theta = 35°$. The actual conductance, shown in Figure 6.6, is suppressed by half at only 0.13 T, again suggesting that the tunneling feature is a collective phenomena.

In Chapter 5 we suggested that the unusual exponential temperature dependence may be understood in terms of small grains of coherent $\nu_T = 1$ phase Josephson coupled with each other. In this picture, each grain is phase-coherent below the K-T transition temperature, but thermal fluctuations suppress inter-grain coherence. As the temperature drops, the inter-grain coherence increases, which may be parameterized in terms of a coherence length ξ. To better understand this suppression, we again turn to the more well-understood SIS tunnel junction.

Josephson tunneling through a narrow junction of width L, in the presence of a parallel field is described by a Fraunhofer diffraction pattern

$$\begin{aligned} I &= j_c \int_{-L/2}^{L/2} \sin(\phi + qx) dx \\ &= \frac{2j_c \sin(qL/2)}{q} \sin\phi, \end{aligned}$$

which can be identified as the Josephson equation with a critical current modulated by the parallel field. If instead we assume an infinite system, in which two points are phase-coherent with probability $P(x) = \exp(-|x|/\xi)/2\xi$, the analogous computation gives

$$\begin{aligned} j^* &= j_c \int_{-\infty}^{\infty} \sin(\phi + qx) P(x) dx \\ &= \frac{j_c}{1 + q^2\xi^2} \sin\phi. \end{aligned}$$

Here, j^* is interpreted as the current density in a small coherent region of size ξ. The applied q reduces the apparent critical current density by a Lorentzian factor. The half-width of the Lorentzian is directly related to the coherence length by ξ^{-1}. We investigated the dependence on a small parallel field of the central peak in tunneling conductance.

The top panel of Figure 6.6 shows the dependence on a parallel field of the zero-bias conductance peak at $d/l_B = 1.63$, 1.69, and 1.75. To better compare the effect at different values of d/l_B, the strong dependence of G_0 on d/l_B is removed by normalizing the conductance to the value at $\theta = 0$. It is striking that the line-shape at $T = 25$ mK is *independent* of d/l_B (except for the overall vertical scale factor).

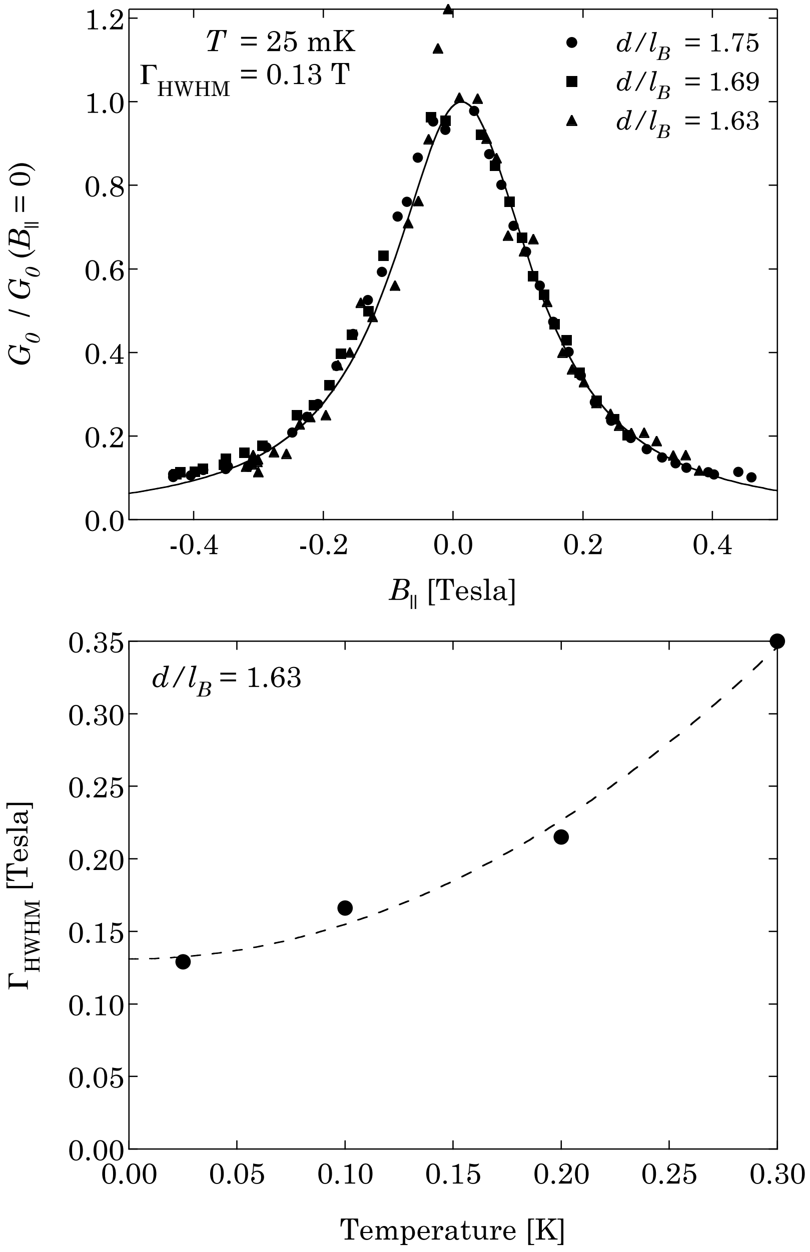

Figure 6.6: Tunneling conductance at $\nu_T = 1$ and $T = 25$ mK. Upper panel: peak conductance vs. parallel field at $d/l_B = 1.63$, 1.69, and 1.75; the solid line indicates a Lorentzian fit. In this data a constant conductance was added from the data. Usually both the conductance and capacitance is measured and any capacitive offsets are removed from the conductance data. In this data set the capacitive data was unavailable but we have made our best effort to correct for this. Lower panel: half-width in $B_\parallel$ vs. temperature at $d/l_B = 1.63$. The dotted line is a quadratic guide to the eye.

The Lorentzian is an extremely good fit to the data, yielding a half-width Γ^3, which is $\Gamma = 0.13$ T, from which we extract a coherence length of only $\xi = 0.2$ μm. This length scale may be reasonable, since it is comparable to the 0.2 μm setback to the silicon donors.

The lower panel shows the temperature dependence of Γ at $d/l_B = 1.63$. The most striking feature of this data is the clear finite intercept as $T \rightarrow 0$. It would be surprising if, suddenly, the gradual temperature dependence changed to permit $\Gamma \rightarrow 0$ below 25 mK. Therefore, the temperature dependence suggests that even at the lowest temperature, the system has a finite and small inter-grain coherence length.

6.7 CONCLUSION

In summary, magneto-tunneling spectroscopy experiments on double-layer 2D electron systems in the $\nu_T = 1$ QHE state reveal a collective mode in the system that disperses linearly with wave-vector at low-energy. The measured velocity of this mode is in reasonable agreement with theoretical estimates for the Goldstone mode of the broken symmetry ground state.

Although rapidly suppressed, the zero energy feature unexpectedly remains at large q. The analysis of this feature suggests that it may be explained in terms of tunneling within small coherent regions. Nonetheless, a theoretical understanding of this remnant peak remains a vexing problem.

---

[3] As stated above, the sample was leveled within 0.5 degrees in the axis perpendicular to the rotation angle. Assuming the existence of a wave-vector, k, from this inadvertent tilt, the width in q is broadened to $\Gamma^2 = \Gamma_0^2 + k^2$. Based on the estimated uncertainty in the tilt angle and the observed line width, this is a 1% effect at $d/l_B = 1.63$.

Chapter 7

Effects of Density Imbalance on the $\nu_T = 1$ QHE

Recent studies of bilayer two-dimensional electron systems (2DES) at filling factor $\nu_T = 1$ are strongly indicative of a quantum phase transition between inter-layer coherent and incoherent states. As the distance between the layers increases, the degree of coherence between the layers decreases, until, at a critical layer separation, the state disappears. The detailed behavior of this transition is central to the understanding of the bilayer-coherent state.

In this chapter, we present inter-layer tunneling data exploring the dependence of the phase transition on a relative density imbalance between the layers and find that in the strongly coherent regime the system is further stabilized by imbalance. Likewise, we find that the phase boundary is moved to larger layer separation by the application of a density imbalance. This result is corroborated by Coulomb drag data taken by Mindy Kellogg.

7.1 $\nu_T = 1$ PHASE BOUNDARY

The location of the phase boundary was first probed by Murphy *et al.* [18] by searching for a minimum in ρ_{xx} at $\nu_T = 1$. Their data explored the plane spanned by d/l_B and Δ_{SAS}/E_c (recall that $E_c = (e^2/4\pi\epsilon l_B)$ is the Coulomb energy). The phase boundary was found to increase roughly quadratically in Δ_{SAS}, but had a nonzero d/l_B intercept of roughly 2. In our weakly tunneling samples, we explored the orthogonal plane spanned by d/l_B and density imbalance, $\Delta N/N_T$.

In Chapter 4, the Halperin Ψ_{111} wavefunction was introducted, which is thought to capture the essential physics of the $\nu_T = 1$ bilayer quantum Hall state. An unusual property of this wavefunction is that it is valid at any individual layer filling fraction ν_1 and ν_2, provided $\nu_T = \nu_1 + \nu_2 = 1$. This observation makes no statement regarding how good a trial function it may be, just that it is a valid question to ask.

In particular, when $\nu_1 = 1/2$ and $\nu_2 = 2/3$, the total system is at total filling $\nu_T = 1$. It is likely that these strong, single-layer, fractional states will dominate the competing ψ_{111} phase. Since the other FQHE states are poorly resolved in our samples (see Chapter 4), we anticipate a strong $\nu_T = 1$ coherent state in the range $|\Delta N/N_T| < 0.3$.

In the language of a pseudospin ferromagnet, $|\uparrow\rangle$ and $|\downarrow\rangle$ denote an electron in either the top or bottom layer. In the balanced, $n_1 = n_2$ ferromagnetic state, the carriers form a coherent inter-layer state described by a macroscopic phase variable ϕ in the state $\left(|\uparrow\rangle + \exp(i\phi)\,|\downarrow\rangle\right)/\sqrt{2}$.

The magnetization of the ferromagnet in the $\mathbf{z}$ direction is proportional to the average charge difference between layers. Thus, when $\langle m_z \rangle = 1$ all of the carriers reside in the top layer. In particular, the $\mathbf{z}$ magnetization is just, $\langle m_z \rangle = (n_1 - n_2)/(n_1 + n_2)$, i.e., the relative density imbalance. By suitably biasing gates above and below each of the 2D layers, we can adjust this ratio while maintaining a constant total filling factor.

7.2 PRIOR STUDIES

Transport measurements have shown density imbalance enhances the charge gap [86, 87, 88], however, these studies are unable to resolve the detailed behavior of the phase boundary.

The initial measurement on density imbalance by Sawada *et al.* [86] used the width of the quantum Hall minimum as a metric for the strength of the QHE. They found that the $\nu_T = 2/3$, and $\nu_T = 2$ effects were rapidly suppressed[1]. This is consistent with the idea that these states are single layer QHE's which disappear when the single-layer filling factor changes. When $\Delta N/N_T \neq 0$, the $\nu_T = 1$ state

---

[1] After an initial strong and rapid suppression vs. $\Delta N/N_T$, Sawada *et al.* **??** found that the $\nu_T = 2$ state gradually became more robust.

was either unchanged (at high initial density), or enhanced (at lower total density). They note that this is consistent with the $\nu_T = 1$ state being described by the Ψ_{111} wavefunction. In their second publication, Sawada *et al.* [87] observe the same effect from temperature-dependent resistivity measurements. By fitting to an activated form, $R_{xx} \sim \exp(-\Delta/2T)$. The resulting energy gap, Δ, increases with increasing imbalance at $\nu_T = 1$.

Tutuc *et al.* measure the effect of a density imbalance on a set of parallel 2D hole layers [88]. Like the measurements of Sawada *et al.* [87], Tutuc *et al.* measured the energy gap Δ. They also find that the $\nu_T = 1$ energy gap increases with imbalance.

Although this result is counterintuitive, the Hartree-Fock theory of Joglekar *et.al.* [67] predicts that the critical layer separation when the $\nu_T = 1$ coherent state disappears, $d/l_{B_{\mathrm{crit}}}$ grows approximately quadratically in $\Delta N/N_T$.

Tunneling has a definite signature when the $\nu_T = 1$ state disappears. We interpret the existence of a resonant peak in tunneling as signifying the existence of the interlayer correlated $\nu_T = 1$ state. Thus, unlike transport measurements, tunneling can be used to probe the dependence of the phase boundary on density imbalance.

7.3 Measurement

Sample described herein is a high-mobility ($\mu = 1.2\times10^6$ cm^2/Vs), molecular beam epitaxy (MBE) grown heterostructure consisting of two 180 Å GaAs wells separated by a 99 Å $\mathrm{Al_{0.9}Ga_{0.1}As}$ barrier. The nominal per-layer electron density, 0.55×10^{11} cm^{-2}, is provided via remotely placed Si dopants set back 2300 Å beneath the bilayer and by 2050 Å above it.

Sample E, with a tunneling geometry, consists of a 250 × 250 μm mesa with four outward extending arms terminated by AuNiGe Ohmic contacts. The layer densities are separately controlled by metallic gates placed above and below the bilayer. Each outward extending arm is also equipped with depletion gates determining which of the two layers, if either, are contacted [34].

Density imbalance, $\Delta N/N_T = (n_1 - n_2)/(n_1 + n_2)$, is the central parameter in this study. The dependence of the layer densities on gate voltages are extracted

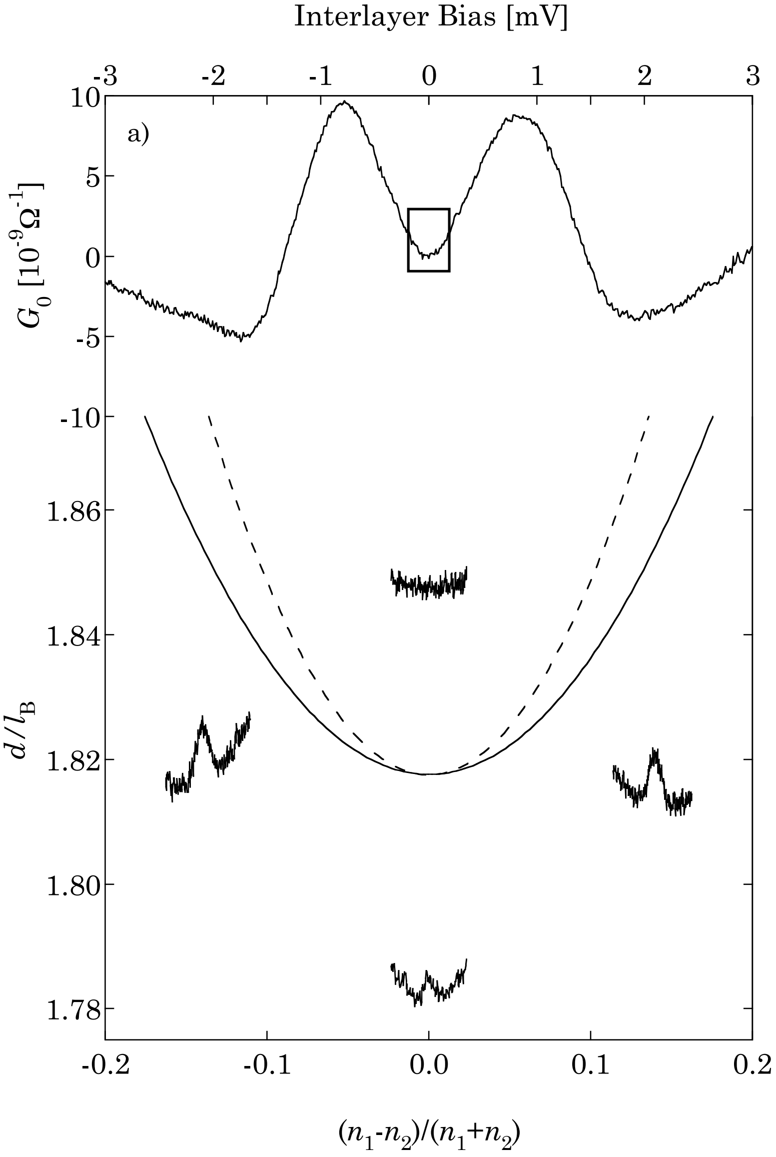

Figure 7.1: Top: dI/dV vs. V at $d/l_B = 1.85$ and $\Delta N/N_T = 0$ illustrating the suppressed zero-bias conductance in the uncorrelated regime. The rectangle around zero-bias bounds the lower conductance traces. Bottom: the bold parabolic curve is the measured phase boundary as a function of $\Delta N/N_T$ and d/l_B. The dotted curve is a theoretical prediction [67] offset from $d/l_{B_{\text{crit}}} = 1.3$ to match the observed transition value. The lower four data traces illustrate the tunneling behavior near the phase boundary. From top to bottom: $d/l_B = 1.834$ and $\Delta N/N_T = 0$; $d/l_B = 1.834$ and $\Delta N/N_T = \pm0.15$; and $d/l_B = 1.804$ and $\Delta N/N_T = 0$.

from low-field Shubnikov de Haas oscillations in either tunneling amplitude or the longitudinal resistivity. At $\nu_T = 1$ the imbalance parameter therefore reflects the application of this calibration and does not result from the direct measurement of the charge difference between the two layers.

Tunneling current ($I - V$) and conductance (dI/dV) are simultaneously measured in a four-terminal geometry. Each layer is connected to two leads; both the voltage drop and current through the sample are independently measured. A small AC excitation is added to the DC bias voltage, and the resulting δI and δV are combined to dI/dV.

Figure 7.1 illustrates our central result. Very close to the $\nu_T = 1$ phase boundary, the application of a density imbalance increases $d/l_{B_{\text{crit}}}$. The bold line represents the phase boundary as measured by tunneling spectroscopy; roughly 200 tunneling traces were inspected for a visible zero-bias tunneling peak, the results of which are well fit by a parabola[2]. In this analysis, conductance peaks larger than $0.2\times10^{-9}\ \Omega^{-1}$ were resolvable. Although our determination of the phase boundary is therefore limited by finite resolution, the same qualitative results have been replicated in a sample with 100× stronger nominal tunneling conductance.

In the incoherent regime, the zero-bias tunneling is suppressed, resulting from the energetic penalty associated with the rapid injection of an electron into a strongly correlated single-layer [66, 58, 65]. In the correlated state, the suppression gives way to a sharp peak centered at zero-bias. Using this peak as the signature of the coherent state, a critical value of $d/l_{B_{\text{crit}}} \approx 1.83$ was measured, below which the dramatic enhancement of the zero-bias tunneling conductance is observed [20].

Figure 7.1 also contains typical tunneling spectra taken at $T = 25$ mK near the $\nu_T = 1$ phase boundary; the full trace ($d/l_B = 1.850$) illustrates the suppressed zero-bias tunneling conductance and broad high-energy features typical of tunneling in the incoherent state. When the densities are imbalanced, the qualitative shape of these

---

[2] A horizontal shift of roughly $\Delta N/N_T = 0.02$ has systematically been applied to the presented imbalance data to preserve the symmetry about zero. Measurements of the tunnel spectra outside of the $\nu_T = 1$ regime indicate thatlayers which have balanced densities at zero magnetic field can become slightly imbalanced at high-field by about 4% (as computed from the asymmetric high-field $I - V$ data [66]).

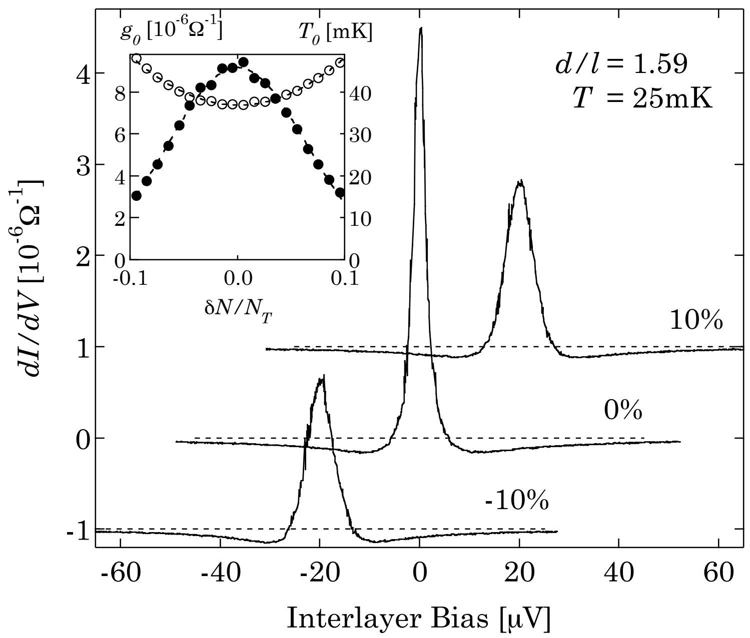

Figure 7.2: Tunneling deep within the $\nu_T = 1$ phase at $d/l_B = 1.59$, $\Delta N/N_T = 0, \pm 0.15$, and $T = 25$ mK (note: the traces are offset for clarity). Inset: exponential fit parameters: solid (left axis) – g_0; empty markers (right axis) – T_0.

features are unchanged, however, the spectral weight shifts, leading to data which is strongly asymmetric about zero-bias.

The lower four tunneling traces in Figure 7.1 span the phase boundary: at $d/l_B = 1.834$ with imbalances of 0 and ± 0.15; and at $d/l_B = 1.804$ with $\Delta N/N_T = 0$. The imbalanced data show a clear peak in tunneling, while at the same d/l_B, when $n_1 = n_2$ the peak is replaced by level valley around zero-bias. In addition, the background is asymmetric in the unbalanced case, reflecting the response of the high-energy tunneling features to a density imbalance. Even deep in the $\nu_T = 1$ phase, the high-energy features remain, having evolved continuously from the gapped structure in the uncorrelated regime. These remnant features show the same type of skewing with imbalance as they do above the phase boundary.

7.3.1 Deep within the $\nu_T = 1$ phase Figure 7.2 illustrates typical tunneling data well below the phase boundary ($d/l_B = 1.59$). In contrast to data taken near the phase boundary, here the tunneling resonance becomes shorter and fatter with increasing imbalance. Conversely, transport data has shown a simple monotonic enhancement of activation energy Δ, vs. $\Delta n/N_T$ [88, 87][3].

Deep in the $\nu_T = 1$ phase, the temperature dependence of the tunneling conductance is well described by $G_0 = g_0 \exp(-T/T_0)$ (see Chapter 5). This indicates the tunneling amplitude can be parameterized in terms of the two variables: g_0 and T_0 (inset to Figure 7.2). The magnitude of the tunneling conductance, described in terms of g_0, decreases with imbalance; conversely, the energy scale T_0 increases. This contrast only becomes evident as d/l_B decreases; at $d/l_B = 1.76$ it is only visible at the lowest temperatures.

7.4 DISCUSSION

This puzzling enhancement of the temperature coefficients suggests that, although connected, the overall integrity of the $\nu_T = 1$ state is not simply related to the magnitude of the low-temperature conductance. One possible mechanism for this was discussed in the introduction – a pseudospin polarization in the m_z direction is expected to decrease the projection onto the $x - y$ plane.

The operator which measures the tunneling current, $tem_y/\hbar$ [55], is proportional to the pseudospin magnetization in the y direction. Based on this, it is plausible that a decrease in the $x - y$ magnetization would be reflected by a decrease in the tunneling conductance.

Since these measurements were performed in the weakly tunneling limit changes in the tunneling strength alone will have little effect on the behavior or integrity of the quantum Hall state.

The upward curvature of the observed phase diagram is in qualitative agreement with the predictions of Joglekar *et.al.* [67]. The results of this theory are show in Figure 7.1 as a dashed line. This result has been translated upward from the predicted transition $d/l_B = 1.3$ to match the experimentally observed 1.83. The central result of an upward curving phase boundary is in agreement with our experiment.

---

[3] Other unpublished data shows the an activation energy which is roughly independent of $\Delta N/N_T$ [89].

7.5 CONCLUSION

In summary, tunneling spectroscopy experiments on double-layer 2D electron systems in the $\nu_T = 1$ QHE have been used to determine the location of the phase boundary between the coherent and incoherent regimes. The enhancement of $d/l_{B_{\mathrm{crit}}}$ with imbalance is in reasonable agreement with theory.

CONCLUSION

The Josephson-like tunneling data presented in this thesis is the first direct evidence [20, 22] for the long-sought excitonic superfluid. Remarkably, we find the excitonic superfluid in a pair of half-filled Landau levels. We have presented several lines of evidence that suggest this tunneling feature must be a collective phenomena.

In parallel with these experiments, Mindy Kellogg [90, 91] has studied the lateral-transport properties of the $\nu_T = 1$ system. In particular, she finds that the symmetric and antisymmetric current channels decouple [90, 91]. In a more recent work, Kellogg *et al* directly measure the predicted counterflow superfluidity. There are two central results of this study: 1) The antisymmetric conductivity is enhanced by six orders of magnitude compared to the symmetric conductivity. 2) Currents in the antisymmetric channel induce no Hall voltage, indicating that the charge carriers are the predicted charge neutral excitons.

This thesis has investigated various properties central to the $\nu_T = 1$ tunnel junction. The results have shown that the inter-layer tunneling current is reminiscent of Josephson tunneling between superconductors. In conclusion, I would like to discuss several directions for future study.

Lower temperature In Chapter 5, we observed that at every d/l_B, when there is a peak in tunneling at $\nu_T = 1$ that peak continues to evolve at the lowest temperatures available in the lab: 15 mK. Central to our understanding of the tunneling feature is its ultimate height and width. A true Josephson junction has infinite conductance and zero line width at zero temperature. A new cryostat has been ordered that should reach 1 mK.

Shapiro steps In the presence of RF radiation, a conventional Josephson junction shows Shapiro steps. We have already attempted to directly illuminate the sample with RF radiation. Unfortunately, only a small amount of power was required to dramatically heat the electron system and destroy the $\nu_T = 1$ state. We are currently working on channeling microwave radiation into the tunnel junction.

Fraunhofer diffraction Chapter 5 alluded to the fact that a narrow superconducting junction in a parallel magnetic field exhibits a Fraunhofer diffraction. This pattern beats when the magnetic flux though the junction is an integer multiple of the magnetic flux quanta. This effect is a direct result of the coherence properties of the superconducting order parameter. We propose an analogous measurement in the $\nu_T = 1$ system.

Other filling fractions When we introduced the Ψ_{111} as a specific example of Halperin a Ψ_{lmn} wavefunction, we noted that a class of these function when $l = m = n$ were all inter-layer coherent. Ψ_{111} is at total filling 1, while the next valid (by the Pauli principle) Halperin state is the Ψ_{333}. This occurs at total filling $\nu_T = 1/3$, which is experimentally challenging. Unfortunately, at the higher magnetic fields required for this state, current samples become insulating.

A second filling fraction of interest is $\nu_T = 3$. Here, both spin branches of the lowest Landau level are completely filled, and we expect to see an analogue of the Ψ_{111} state in the $N = 1$ Landau level. Preliminary tunneling measurements have not observed a state here, but this has not received detailed attention.

Lateral tunneling In the inter-layer tunneling measurements, the data was qualitatively similar to Josephson tunneling. Geometrically, however, the tunneling geometry is nothing like the usual Josephson arrangement. We propose, therefore, to measure the lateral (in-plane) tunneling between two $\nu_T = 1$ systems. To exactly match the Josephson geometry, the tunneling process must involve exciton tunneling, which requires counter-flowing currents.

Nuclear effects We have recently discovered that spin polarization of the gallium and arsenic atoms can dramatically enhance the $\nu_T = 1$ QHE. The electrons and nuclei interact via a weak hyperfine contact interaction, which leads to an effective nuclear magnetic field B_N that acts only on the electron spin (not the kinetic degrees of freedom). We are currently exploring this intriguing effect, which may explain some of the lingering mysteries in our tunneling data.

FINALE

In conclusion, the $\nu_T = 1$ system has proven to be a rich and fascinating system with surprises behind every door. There are many more doors still unopened!

APPENDIX A

SAMPLES

All of the samples used in this thesis are briefly described in this appendix. In many cases several samples were made from the same wafer; to clarify the distinction between these samples, the wafer is described first. This description is followed by a list of each sample made from that wafer. Each of these samples was grown by L. N. Pfeiffer and K. W. West at Bell labs.

WAFER 1

This wafer has a high-mobility single interface, with density of 1.2×10^{11} cm^{-2} and a mobility of about 5×10^{6} cm^2/Vs (the mobility measured using AC techniques in Chapter 2 was found to be 4×10^{6} cm^2/Vs). The sample consists of a single GaAs 250 Å quantum well with $\mathrm{Al_{0.32}Ga_{0.68}As}$ barriers.

SAMPLE A (TRANSMISSION LINE)

Sample used for plasmon transmission line experiment in Chapter 2. The 2DES is confined to a 510 × 2560 μm mesa with a gate covering the first 330 μm and last 680 μm of the sample to capacitively couple RF radiation into the 2DES.

SAMPLE B (RESONATOR)

Sample used for plasmon resonator in Chapter 2. In this sample, the mesa is 100 × 780 μm, and each capacitive coupling gate covers 360 μm of the mesa. This structure leaves a small 60 μm ungated gap in the center of the mesa.

WAFER 2

This is a double quantum well wafer, and has a 180 Å:99 Å:180 Å (GaAs : $\mathrm{Al_{0.9}Ga_{0.1}As}$: GaAs) structure, a nominal density of $N_T = 1.1\times10^{11}$ cm^{-2}, and a mobility of roughly 1.2×10^{6} cm^2/Vs. This wafer has the strange property that samples further from the center have progressively increasing tunneling strength. During growth, the periphery of the wafer is farther from the center of the molecular beams and receives a decreased atomic flux [92]. Due to the decreased flux, the tunnel barrier is expected to be thinner and the tunneling enhanced.

SAMPLE C (TUNNELING)

This sample has a 250 × 250 μm tunneling area and a nominal tunneling strength of $\sim 30\times10^{-9}\ \Omega^{-1}$. The initial publication of the $\nu_T = 1$ effect in tunneling was based on data from this sample [20].

SAMPLE D (TUNNELING)

This sample has a 250 × 250 μm tunneling area and a nominal tunneling strength of $\sim 30\times10^{-9}\ \Omega^{-1}$.

The Goldstone dispersion relation of the $\nu_T = 1$ state was measured in this sample [22].

SAMPLE E (TUNNELING)

This sample has a 250 × 250 μm tunneling area and a nominal tunneling strength of $29\times10^{-9}\ \Omega^{-1}$.

WAFER 3

This is a moderately strong tunneling DQW. The structure is: 180 Å:89 Å:180 Å (GaAs : $\mathrm{Al_{0.9}Ga_{0.1}As}$: GaAs). Note that except for the 89 Å tunnel barrier, this is an exact replica of Wafer A.

Sample F (Tunneling)

This sample was used to test the wafer, with a 250 × 250 μm tunneling area and a nominal tunneling strength of $\sim 5\times10^{-6}\ \Omega^{-1}$.

Wafer 4

This is a weakly tunneling DQW, and includes an etch stop to make EBASE type samples. The structure is: 180 Å:99 Å:180 Å (GaAs : $Al_{0.9}Ga_{0.1}As$: GaAs).

Sample G (EBASE Tunneling)

This sample was used to test the EBASE processing method, and the sub-band densities were extracted using SdH oscillations.

Wafer 5

This double quantum well is a copy of Wafer A, with the same 180 Å:99 Å:180 Å (GaAs : $Al_{0.9}Ga_{0.1}As$: GaAs) structure. Larger setbacks give a decreased nominal density $N_T = 0.9\times10^{11}$ cm^{-2}. Additionally, the tunneling strength of this material at zero magnetic field is roughly 150× larger than expected from Wafer A.

Sample H (Tunneling)

This sample has a 250 × 250 μm tunneling area and a nominal tunneling strength of $4\times10^{-6}\ \Omega^{-1}$.

APPENDIX B

SAMPLE PROCESSING

In this document some basic techniques of GaAs sample processing and preparation are described. “Processing” can vary in complexity from simply cleaving a square sample and annealing indium contacts, to a sophisticated, multistep recipe on both sides of the sample. This guide is divide into two parts; the first describes individual processing steps, and the second is a collection of recipes that apply these steps.

There is vast and daunting literature for processing GaAs materials; however, 99% of what one wants to know is easy to find. The following references are a good starting place [93, 94, 95]. There is extensive literature available on the internet as well, but this information should be considered with a skeptical eye.

B.1 BASICS

The basic tools we use in sample processing include:

1. Tweezers: for the most part, we use metal tweezers from Small Parts [96], however, it is easy to accidentally scratch the surface of a sample with these tweezers, we recommend using a pair of Teflon tweezers from uni-fit [97].
2. Glassware: we use petri dishes to hold our processing solutions. Any small-volume glass (or Teflon) containers will work fine. They should have lids to prevent solvents from evaporating. In addition, it is a good idea to have some beakers and bottles for mixing and storing solutions.
3. Chemicals: most of the recipes in this document describe methods of wet, or chemical processing. Some are fairly robust to small deviations from the recipe,

while others are not. For this reason, it is important to use only chemicals that are known to be uncontaminated. If this means buying a new bottle of acid or H_2O_2, it is worth the expense.

B.1.1 Cleaving Materials grown by molecular beam epitaxy (MBE) usually arrives in the form of a circular wafer of GaAs; in this case, the wafer has a 3” diameter. To conserve valuable material, we cleave small, 3 to 5 mm squares from the host wafer and process these small samples.

Place the GaAs smooth side up on a piece of paper, and scribe a small line where you want the cleave to start. Flip the sample over, and gently press down with the round disk on the back end of the scribe, rolling back and fourth directly over where you made the scratch on the front of the sample. Gradually increase the pressure until the sample cleaves. When done properly, a straight line will form from one end of the material to the other. To extract a square sample from a wafer, first cleave a long bar of material and then cut off individual squares from that. We recently switched to 4×4 mm samples from 5×5 mm samples (saving nearly a factor of 2 in surface area per-sample); however, some older masks still require the larger size.

B.1.2 Sample cleaning Successful processing of a sample requires that the surface be extremely clean. Surface contaminates might be dust that has landed on the sample, GaAs chips from cleaving the sample, or some sort of chemical residue.

Place the sample face up in a petri dish filled with acetone. First squirt the sample gently, and then rub lightly with a q-tip. Transfer the sample to a dish filled with methanol, and again squirt lightly. Remove the sample and blow it dry.

B.1.3 Indium wire-up Find the soldering iron labeled “wire-up,” and if you have your own wire-up tip, place it in the end of the iron. With a razor blade, clean the tip of any dirt or old indium that may be there; then turn the iron on.

If you do not already have a glass slide with indium on it reserved for wire-up, you should make one now. On a glass slide, clearly write “wire-up” and your name. Indium is one of the few metals that wets glass, so get about 1/4” 5N indium wire and spread it all over the surface of the slide using the soldering iron. It is important for making small contacts that this layer be very thin.

Wet your cleaned soldering tip with a small amount of indium from the glass slide (this determines the size of the indium contact; less indium is better). Now touch the iron to your sample. When you remove the iron, a small dot of indium should be left behind. Cut a 1” length of 0.001” gold wire and grab it with tweezers. Hold the tip of the wire on top of the contact and melt the indium with the iron around the wire (this is harder than it seems because the tip of the iron is many times larger than the indium dot and the gold wire). Once the gold wires are attached to the sample, it can be mounted to its final location, again using indium. Indium wets almost everything, so this is generally very easy.

If you hold the gold wire in hot indium for too long, the indium and gold form a very brittle alloy, which generally does not survive any tugging or bending. Be sure and quick when applying heat!

B.2 LITHOGRAPHY

We have two basic tools to create a pattern on the surface of a sample: photolithography, and e-beam lithography. Photolithography involves shining UV light on a photosensitive polymer (photoresist) and then immersing the sample in a chemical developer, which either dissolves the resist that was exposed to light (this is called a positive resist), or dissolves the unexposed region (negative resist). We primarily rely on positive resists. Photolithography is easy and fast, but the resolution is limited to the wavelength of light, here roughly 0.5 microns.

The second technique is e-beam lithography, the idea is the same, except the resist is exposed with electrons instead of light. E-beam lithography can write structures as small as 50 nm, but it works like an etch-a-sketch, where one point is exposed at a time. As a result, e-beam lithography can be quite slow for large structures.

B.2.1 Photolithography: AZ5214E We use the Clariant AZ5214E photoresist and AZ400K developer system for our photolithography. Here is the recipe to apply and develop the photoresist.

1. Put the cleaned sample on the Solitec spinner and turn on the vacuum. There are two vacuum chucks for the spinner; one is large and is used to attach quartz disks to the spinner, and the other is small and is used for the usual 5×5 mm square samples.
2. Press start, and squirt acetone, then methanol on the sample. While it is still spinning, blow it dry.
3. For fine structures (smaller than 10 μm), put a drop of HDMS and spin for 30 seconds at 5000 RPM.
4. Put a drop of resist on the sample and spin for 30 seconds at 5000 RPM.
5. Soft bake for 45 seconds at 100 C on a hotplate.
6. On the mask aligner, expose your sample for 15 seconds with an intensity of 5 mW/cm^2.
7. For fine structures (smaller than 10 μm), immerse the sample in chlorobenzene for 10 minutes.
8. Develop using a fresh AZ5214 developer:H_2O (1:4) mixture for 45 seconds, rinse with H_2O, and blow dry. To keep the developer mixture fresh, it must be stored in an airtight bottle.
9. Visually inspect the pattern under the microscope. If it is not completely developed, return it to the developer until it is.
10. For etches, place the sample on a 130 C hotplate for 60 seconds (longer post-bakes will, in general, result in better etches).

If you are doing some sort of etch, you can now etch the sample, clean the etch solution off the sample, and remove the resist using n-Butyl acetate followed by methanol, and then blow dry.

If you are doing an evaporation, you now evaporate, and then place the sample in n-butyl acetate at 75 C for about 30 minutes. Then place the sample in a petri dish with acetone and squirt the sample until all of the undesired metal has lifted off. In extreme cases, you may need to gently rub the sample with a q-tip, but you run the risk of removing more metal than you want.

B.2.2 Photolithography: polyimid It is sometimes desirable to coat part of a sample with a thin plastic layer, perhaps as an electrical insulator, or simply to protect the surface of the sample. One convenient option is to use a photosensitive polyimid PI-2732 and developer DE-9040 from HD Microsystems [98]. This material is a negative resist, meaning that the polyimid that was exposed to UV light remains after developing. The following instructions will produce a 5 μm film.

1. Put the cleaned sample on the vacuum chuck and turn on the vacuum
2. Press start, and squirt acetone, then methanol on the sample. While it is still spinning, blow it dry.
3. Put a drop of Polyimid on the sample and spin for 30 seconds at 5000 RPM.
4. Soft bake for 3 minutes at 60 C followed by 3 minutes at 95 C on a hotplate, or 75 minutes at 55 C in an oven.
5. On the mask aligner, expose your sample for 15 seconds with an intensity of 5mW/cm^2 (desired dose is 50 to 200 mJ/cm^2).
6. Develop for 150 seconds, rinse for 30 seconds with n-butyl acetate, and blow dry.
7. Cure: Ramp from room-temperature to 200 C at 4 C/min and hold for 30 minutes (in air), then ramp to 350 C at 2.5 C/min and hold for 60 minutes (in nitrogen). It seems that two bakes, one at 200 C and the other at 350 C for the specified times in the annealing station (using nitrogen both times) works well for these steps.

B.2.3 E-beam lithography E-beam lithography uses a small electron beam to write a pattern on the sample's surface. Using our JOEL 840 e-beam microscope and the NPGS software, it is possible to write patterns as small as 50 nm. Unlike photolithography, where the entire pattern is exposed with a single burst of light, the e-beam writes point-by-point. As a result, larger patterns can take hundreds of hours! This section contains two recipes for e-beam lithography, but does not describe how to use the NPGS software, nor how to maintain or use the e-beam microscope.

The exposure depends greatly on the size of the pattern and the details of the substrate, so the exposures suggested below should be considered only as a starting point.

B.2.3.1 Single-layer PMMA The most common resist used for e-beam lithography is PMMA in chlorobenzene. There are many, quite complex, recipes for e-beam lithography that involve several layers of different PMMA solutions. Sometimes, however, it is useful to have a simple recipe. In this case the limitation is that the metalization will not lift off if the thickness exceeds about 800 Å. In terms of final resolution, this recipe is every bit a good as the more fancy ones.

1. Put the cleaned sample on the vacuum chuck and turn on the vacuum.
2. Press start, and squirt acetone, then methanol on the sample. While it is still spinning, blow it dry.
3. Put a drop of PMMA (950 4% solids in chlorobenzene) on the sample and spin for 45 seconds at 2500 RPM.
4. Bake for 60 minutes on a 180 C hotplate.
5. Write the e-beam pattern with an exposure of 270 μC/cm^2 at 35 keV.
6. Develop for 70 seconds in a 3:1 mixture of isopropanol:MIBK. Follow with 30 seconds in isopropanol and 30 seconds in deionized water. During the development, hold the sample with tweezers and swish it around in the solutions. Blow dry.

7. Visually inspect the pattern under the microscope if it is not completely developed, it is necessary to start over. Since the pattern is so small, it can be very hard to find.
8. After the evaporation, lift off the metal in acetone at 50C.

B.2.4 Bilayer PMMA This recipe has two layers of PMMA. The top layer is designed to be hard, so when the resist is developed, it is only dissolved where it was exposed, while the underlayer is rapidly removed. This leads to a large overhang and allows for much thicker metalizations. A 1500 Å evaporation works flawlessly with this resist schedule. The following list describes only what is different from the single-layer resist.

1. Put a drop of PMMA (950 4% solids in chlorobenzene) on the sample and spin for 45 seconds at 2500 RPM.
2. Bake for 60 minutes on a 180 C hotplate.
3. Put a drop of PMMA (495 6% solids in chlorobenzene) on the sample and spin for 45 seconds at 7500 RPM.
4. Bake for 60 minutes on a 180 C hotplate.
5. Write the e-beam pattern with an exposure of 350 μC/cm^2 at 35 keV.
6. Complete as with the single-layer recipe.

There are more complex tri-layer recipes that people have developed for even more stubborn materials. Also, fancy resist schedules are required for angle shadow mask evaporation. The idea here is that a very small pattern is written, and when exposed, the bottom layer is completely dissolved, leaving a suspended pattern on the top. Evaporation is performed once, the metal is oxidized, the sample rotated, and evaporation repeated. This is used, for example, to create SIS tunnel junctions in the construction of single electron transistors.

B.3 WET ETCHES

We use several different wet etches in sample preparation. We might use a slow etch to define a mesa in a controlled manner (Sections B.3.1 and B.3.2), while a fast etch is used to quickly remove hundreds of microns of GaAs (sometimes these go by the name "piranha etch," Sections B.3.3 and B.3.4). There are selective etches that etch GaAs, but not AlAs (Section B.3.5).

B.3.1 Mesa etch: phosphoric acid This is the workhorse etch we use for virtually every sample we process. We use a mixture of H_2O:H_3PO_4:H_2O_2 (50:5:1), which gives a controlled etch rate of 1200 Å/min. Although the exact depth required depends on the detailed structure of your sample, an 8-minute etch is almost always sufficient.

Usually you will have first made a photoresist mask before etching, leaving behind a mesa of defined shape (Section B.2.1).

B.3.2 Mesa etch: sulfuric acid We use a slow sulfuric acid etch exclusively for the preparation of self-aligned contacts, for the simple reason that published recipes for this type of sample used this etch [32]. Phosphoric acid etch would probably work just fine here.

The mixture, H_2O:H_2SO_4:H_2O_2 (80:4:5), gives an etch rate of 4000 Å/min. The etch is completely compatible with the AZ5214E photoresist system.

B.3.3 Fast etch: sulfuric acid For rapidly thinning samples, we use a second sulfuric acid etch: H_2SO_4:H_2O_2:H_2O (5:50:5). This etches at a rate of 4 to 5 μm/min. A typical sample can be thinned from 500 μm to 50 μm in about two hours.

To thin a sample, place a quartz disk on a 130 C hot plate and put some clear wax on the center of the quartz disk. When the wax fully melts, carefully place the sample (side to be etched up!) in the wax and firmly press down with a wooden applicator (take care that no wax gets on the top of the sample). Using a second, sharpened applicator, verify that the sides of the sample are fully coated with wax, so the etch only contacts the top of the sample. Then remove the quartz disk from heat, pressing down on the center of the sample firmly with a wooden applicator until the wax fully hardens. Etch in 30 minute increments, checking the thickness each time, since the etch rate can vary by 50% depending on the exact mixture of the etch.

Sometimes the etched surface takes on a rough rough appearance, and under the microscope looks like sandpaper. This can be avoided by adding small quantities of H_2O_2 [93].

B.3.4 Fast etch: bromine methanol Bromine-methanol is the fastest etch we use, and can thin a sample from 500 μm to 50 μm in about 15 minutes. Unfortunately, this is also a somewhat dangerous procedure and the safety concerns outlined below are essential.

1. Clean a quartz disk with acetone and methanol, both in a petri dish and on the spinner. Take note of the clean face.
2. Cleave and clean three 5×5 mm blank pieces of GaAs each from the same scrap wafer so they have the same thickness.
3. Place quartz disk, clean side up, on the hotplate at 130 C and put three small pieces of clear wax near the edge of the disk, forming an equilateral triangle. Put a fourth piece in the center.
4. Set the three blanks shiny side down in the three wax beads on the periphery of the quartz disk, and the sample also face down, on the center. Press each down firmly with a q-tip. Remove from the hotplate.
5. Clean any wax that may have extruded from under the samples with acetone.
6. **Never allow acetone in the acid hood**
7. Clean the $8 \times 8 \times 1/8$" glass slab and tape the “magic paper” to the plate. Place the slab, paper side up, in the glass dish.
8. Add 15% bromine to methanol (15 ml methanol). Have handy a beaker of H_2O and plenty of methanol.

9. **Wear a face mask, goggles, a lab jacket, long pants, and shoes (no sandals and shorts).**
10. Put a drop of water on the Teflon quartz disk holder and insert the disk.
11. Wet the paper with methanol and pour some bromine-methanol mixture onto the paper.
12. Lightly brush the samples on the paper, tracing figure-eights. To remove from the paper, slide the disk to the edge, but do not lift it off (this will tear the magic paper). When it is working properly, the etch will have a soapy feel underneath as you slide the quartz disk around.
13. When the thickness reaches 250 μm, move the disk to the other side of the holder. Measure the thickness every 15 figure-eights (clean off the bromine-methanol before measuring the thickness).
14. When done, pour the bromine mixture into the white powder, remove the paper from the glass, and rinse the glass, paper, and holder with methanol and H_2O. Clean the work area with the scrubber.

Before attempting the procedure, be sure you are trained by somebody who knows what they are doing. Just following the instructions is not sufficient in this case.

B.3.5 Stop etch: citric acid A citric acid etch, $H_3C_6H_5O_7$:H_2O (5:1), can etch GaAs about 1000× faster than AlAs [99, 100], which is useful to etch until you reach a predefined stop layer. We use this when making EBASE samples (Section B.6.6). It etches GaAs at about 800 Å/min.

B.4 Evaporation

Thermal evaporation is a simple method to deposit a thin metal pattern on the surface of a sample. The idea is simple: the sample (usually with a photoresist pattern) is placed some distance away from a very hot metal source, which evaporates, depositing a thin layer on the sample (usually 0.1 μm to 0.2 μm).

Material and Purity	Symbol	Part #	Density	Z-Factor
aluminum 5N	Al	#10573	2.73 g/cm^3	1.080
chromium	Cr		7.20	0.305
germanium 5N	Ge		5.35	0.516
gold 4N	Au	#13394	19.3	0.381
gold-germanium (88:12)	Au:Ge	#41557	14.68	0.450
indium	In		7.30	0.841
nickel 4N5	Ni	#42333	8.91	0.331
nickel-chromium (80:20)	Ni:Cr	#36298		
silver 5N	Ag	#14153	10.5	0.529
titanium 3N	Ti	#13997	4.50	0.628
zinc	Zn		7.04	0.514

Table B.1: Details of commonly used materials for thermal evaporation [101]. Part numbers refer to the AlfaAesar catalog number.

The source metal usually rests in a tungsten holder firmly clamped between two electrodes. The evaporator can accommodate three different sources at once, and can supply 400 amps. Adjacent to the evaporator is the display for a crystal thickness monitor to measure the metal film is it is grown (see Table B.1 for settings and material information).

B.4.1 Aluminum evaporation and general outline for all evaporations

Aluminum is by far the most common material we evaporate. It is easy and economical (a basket costs far more than two aluminum slugs). It is vitally important to keep the inside of the evaporator clean, so always wear gloves while handling anything that goes inside.

1. Turn on the mechanical pump and set it to backing. Turn on the cooling water, leak protection circuit, and the diffusion pump. The diffusion pump takes about 20 minutes to warm up.

2. Be sure that the main gate valve is firmly closed, then vent the vacuum chamber with nitrogen gas and raise the bell jar.

3. Remove the metal shield and place it on a clean surface. If desired, make a fresh window of glass slides. Verify that the mechanical shutter functions.

4. Tightly clamp a wound tungsten basket (R. D. Mathis [102] Part number B12B-3X.025W) in Position 2 of the evaporator, and place two nuggets of Al in the basket.

5. Attach the sample to a glass slide with a small dab of rubber cement, and place in the sample position of the evaporator. Be sure the glass slide fully covers the hole to avoid any metal reaching the top of the bell jar. Replace the metal shield and slowly lower the bell jar.

6. Rough out the chamber to 100 mTorr, switch over to the diffusion pump, and fill the LN2 trap.

7. After 30 minutes, turn on the power supply, reset the thickness monitor (verify that it is set for aluminum), and set the power to 35%. When the thickness monitor starts to show evaporation, open the shutter and reset the thickness monitor.

8. When the desired thickness has been reached, close the shutter, turn the power to zero, and turn off the supply.

9. Wait 10 minutes, close the high-vac valve, vent and open the chamber as above, remove the sample, close the chamber and rough it out.

10. When done evaporating, turn the diffusion pump and cooling water off, but leave the mechanical pump backing on it until all the LN2 has evaporated.

Aluminum corrodes the tungsten basket, so it is a good idea to evaporate as quickly as possible. A setting of 35% will give a rate of 25 Å/s. For photolithography, or a bilayer PMMA e-beam resist, 1500 Å of aluminum is a good thickness, while for a single-layer PMMA resist, no more than 1000 Å should be grown.

B.4.2 Gold evaporation Evaporating gold is very easy – too easy. Place the gold slugs on a barrier boat (a boat with a region of exposed tungsten surrounded by an oxide barrier, R. D. Mathis [102] part number S35-A0-W). The barrier prevents the gold from creeping over the edges of the boat and either dripping off or evaporating down where it is waisted.

Due to the expense of gold, we have a set of stilts that decrease by 50% the distance from the source to the sample, thus dropping by 75% the quantity of gold required. The sample is considerably closer to the source than the crystal thickness monitor, so the measured thickness 10% less than the actual thickness. For example, if you desire a 1500 Å gold layer, stop when the monitor reads only 1350 Å. During the evaporation, 200 amps will give a rate of about 10 Å/s.

B.4.2.1 AuGe Gold germanium is an eutectic evaporated in the construction of AuNiGe Ohmic contacts. For evaporation it behaves just like gold.

B.4.3 Nickel evaporation Like aluminum, nickel corrodes the tungsten boat during evaporation; however, in this case, the boats may be safely used twice before they are in danger of breaking during an evaporation. We use R. D. Mathis [102] part number S3-.015W for the boats. Nickel evaporates fairly slowly: usually a current of 200 amps will yield an evaporation rate of 4 Å/s.

B.5 OHMIC CONTACTS

The last step required to make a working sample is to make electrical contact to a 2DES. We do this by making "Ohmic contacts" (the term Ohmic indicates that the contacts obey Ohms law, and do not behave like a Schottky diode). We have two general recipes to make Ohmic contact to a 2DES, and one to make weak contact to a N+ cap layer (Section B.5.3).

An Ohmic contact may be either n- or p-type, depending on the carriers contributed by the contacting material. Since we are attempting to make Ohmic contact to n-type GaAs, we use an n-type contact. p-type contacts, at best, would create a p-n junction between the contact material, or more likely would not work at all. The recipes described below are all for contacting n-type GaAs structures.

B.5.1 Indium contacts Making indium contacts is very much like the wire-up discussed in Section B.1.3. You should have a separate glass slide labeled with your name and “n-type,” which should be used only to make contacts. Using the soldering pencil labeled n-type, put small indium dots where you want to make contact to the 2DES. Evidence suggests that the best Ohmic contact is made on the edge of mesas, so be sure the indium bead covers the mesa edge.

Place the sample in the annealing station, and blow forming gas for 2 minutes at 1 SLPM. Maintaining the flow of gas, anneal the sample for 5 minutes at 425C. When the sample has cooled to below 100 C, it is safe to turn off the forming gas and remove the sample. At this point, you should be able to attach gold wires the contacts.

B.5.2 AuNiGe contacts Annealed gold-nickel-germanium (AuNiGe) forms a high-quality evaporated contact to n-type GaAs [94]. The contact resistances are generally found to be much less than indium contacts; however, since they are evaporated, they require more overhead and cannot be created quickly with a solder pencil.

A second advantage of AuNiGe contacts is that they can be made and annealed immediately after the mesa is defined, before any gates are evaporated. Sometimes there may be surface contaminates on the sample when the gates are evaporated. These contaminates then evaporate when the sample is annealed and leave behind bubbles under the gates. Of course, AuNiGe contacts are not perfect, and suffer from two main flaws. The most significant defect of these contacts is called “spiking,” which refers to needles of contact material that can penetrate tens of microns into the GaAs. As long as there are no additional structures directly below the Ohmic contact, this problem can be avoided. Second, AuNiGe contacts have a very uneven surface morphology, which can be a real problem when the exact vertical profile of the contact is important (usually it is not). The uneven surface morphology is only a problem for contacts made using the AuGe eutectic evaporation described below; recipes that rely on distinct layers of Au, Ni, and Ge are smooth.

Following the usual evaporation procedures, define a gate-like region that exposes the desire portion of the mesa (being sure to expose the mesa edge, as this is where Ohmic contact seems to be made). We have several different recipes for AuNiGe contacts. The easiest is made by evaporating Ni and an AuGe eutectic from Alfa Aesar [103].

1. Evaporate 50 Å of nickel at 2 Å/s (200 amps)
2. Evaporate 1350 Å of AuGe at 20 Å/s (200 amps). AuGe is expensive and evaporated on raised stilts; see more in Section B.4.2 on gold evaporation.
3. Evaporate 150 Å of nickel at 2 Å/s (200 amps)
4. Remove sample from the evaporator and anneal for 5 minutes at 440 C (see the notes in Section B.5.1 for more details on annealing).

Before annealing the contacts are smooth, but the annealed contacts have a rough appearance. This is normal; if they end up looking smooth and shiny, then something has gone wrong. There is a second recipe that we often use which changes the evaporation from 50 Å:1350 Å:150 Å (Ni:AuGe:Ni) to 300 Å:1500 Å (Ni:AuGe). There is little difference between these two contact schemes. The former is slightly preferable, as it uses 10% less AuGe.

B.5.3 CrAl contact to N+ This makes a weak (100 kΩ) contact to a heavily doped, or N+, region on the top of some samples. A N+ region conducts and can be used as a gate. The primary advantage of CrAl contacts is that they are not annealed, and can be used to contact only the surface layer of a sample without diffusing down to lower layers. Evaporate 500 Å of chromium followed by 1000 Å of aluminum and lift off as usual.

B.6 RECIPES

The previous sections describe each of the tools and procedures we use to construct various samples. This section contains instructions to make specific samples from start to finish.

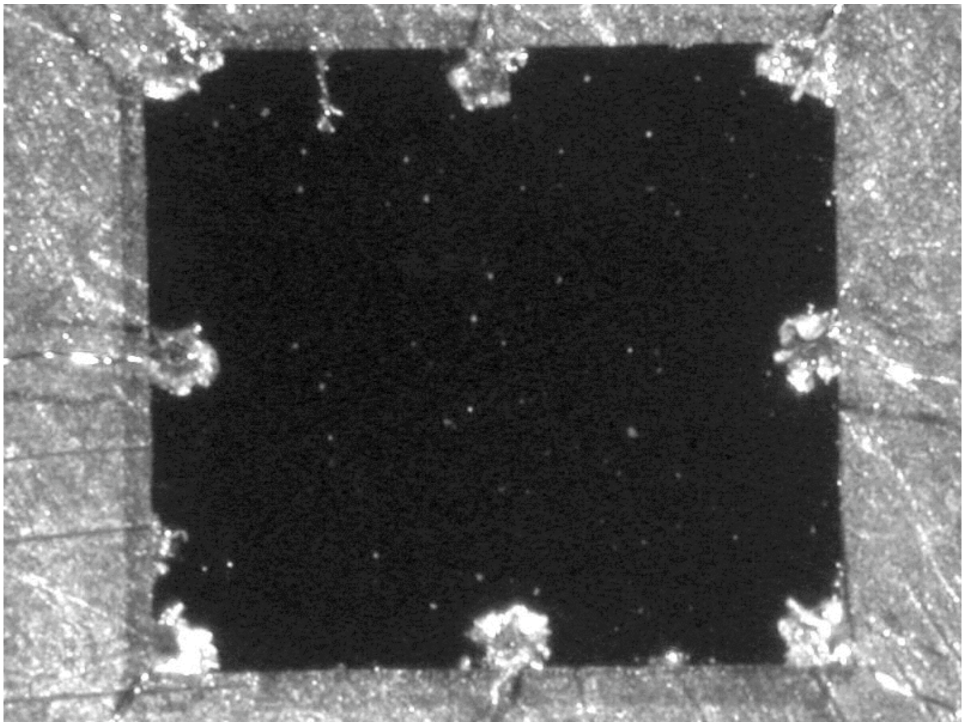

Figure B.1: Photo of a sample with annealed indium Ohmics.

B.6.1 Cleaved sample with annealed indium contacts This is the simplest piece of sample processing possible – a small square of GaAs is cut from the wafer, and some number (usually 8) indium contact are made to the 2DES. This is the type of sample you would use to make conventional transport measurements.

1. Cleave sample from wafer (Subsection B.1.1).
2. Clean sample (Section B.1.2).
3. Make indium contacts (Subsection B.5.1).
4. Wire-up sample.

There are several simple "tricks" we sometimes use with these samples. If we have a single 2DES and we need to change the density we stick the sample to copper tape using vacuum grease and use the tape as a back gate. Since the tape is about 0.5 mm away from the 2DES, several hundreds of volts are required to appreciably change the

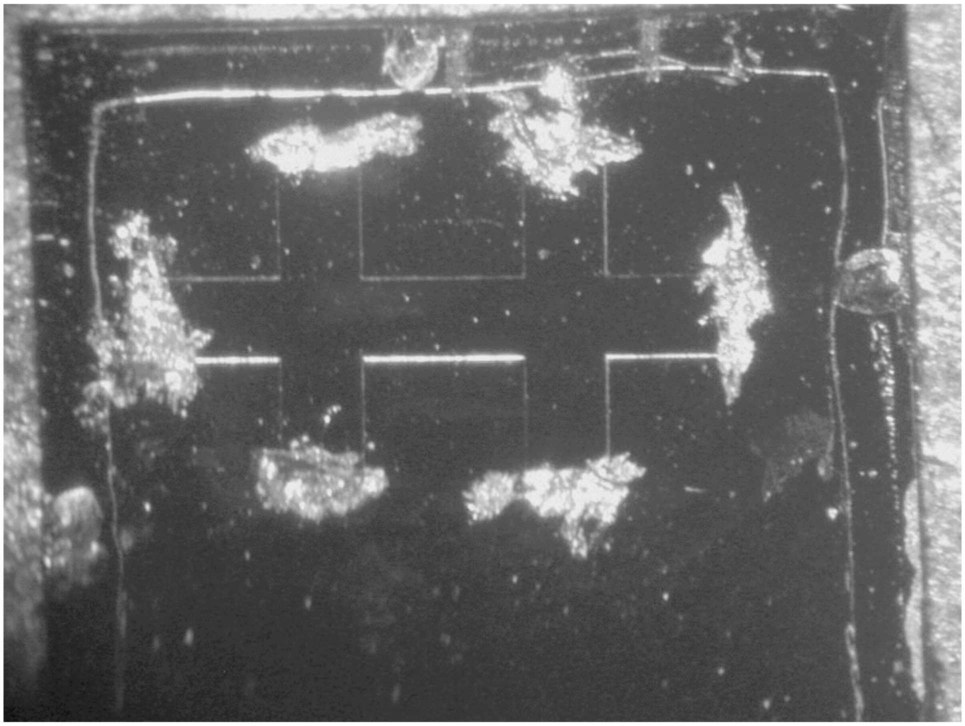

Figure B.2: Photo of a sample with a mesa and annealed indium Ohmics.

density. To gate from the top (useful for bilayer systems, or single-layers when back gating just doesn't work), make radial scribes from the edge of the sample in about 1 mm between each indium contact. We have a piece of semi-insulating GaAs with gold evaporated on it. Cleave a piece of this material that fits on top of the sample but inside all of the Ohmic contacts, and attach it (gold side up) with with a thin layer of grease. Now the gold forms a gate, again 0.5 mm away from the 2DES.

B.6.2 Mesa with indium contacts Adding a mesa to the indium contacts in the previous section, this type of sample is typical for high-mobility 2DES, where illumination is required and gates are ruled out. The structure in Figure B.2 is a Hall bar, a common pattern for transport measurements in high-mobility single or double-layer systems.

1. Cleave sample from wafer (Subsection B.1.1).

2. Clean sample (Section B.1.2).

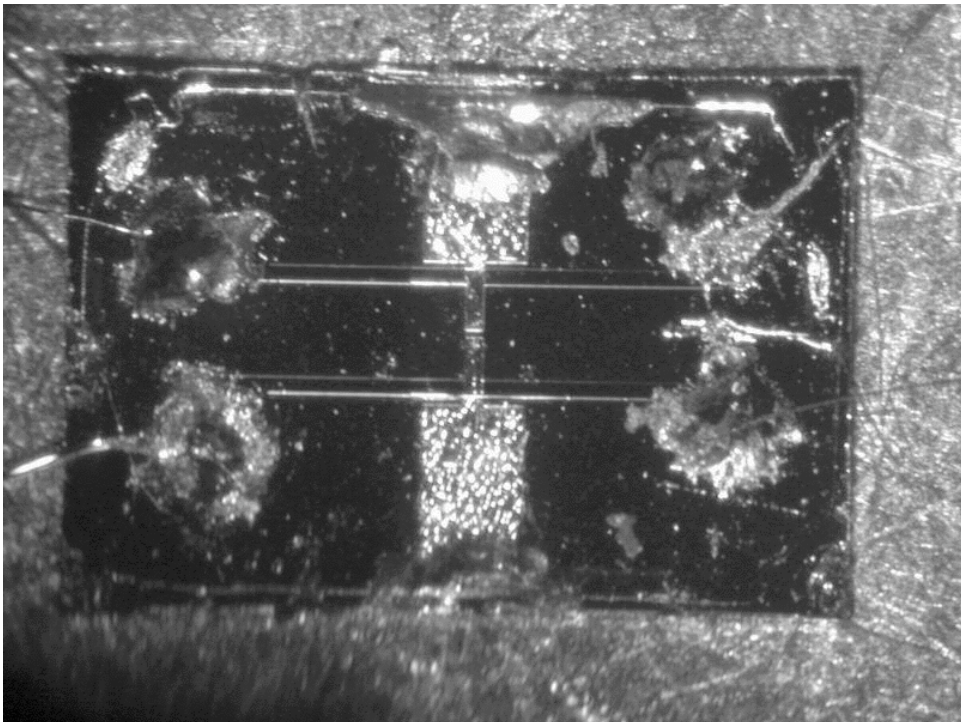

Figure B.3: Photo of a sample with a mesa, annealed indium Ohmics, and an aluminum gate.

3. Define mesa (Section B.2.1).
4. Etch with phosphoric acid etch (Section B.3.1).
5. Rinse with deionized water and blow dry, then remove the photoresist with n-butyl acetate.
6. Clean sample (Section B.1.2).
7. Make indium contacts (Subsection B.5.1).
8. Wire-up sample.

B.6.3 Mesa and gates with indium contacts Again, this recipe increases in complexity by including an aluminum gate. This gate can control the density of electrons below it, but prevents the sample from being illuminated. As a result, samples with gates cannot have as high a mobility as ungated, illuminated samples.

The sample in Figure B.3 is a RF resonator structure used in observing the plasma-density modes of a single 2DES.

1. Cleave sample from wafer (Subsection B.1.1).
2. Clean sample (Section B.1.2).
3. Define mesa (Section B.2.1).
4. Etch with phosphoric acid etch (Section B.3.1).
5. Rinse with deionized water and blow dry, then remove the photoresist with n-butyl acetate.
6. Clean sample (Section B.1.2).
7. Define top-side gate pattern, evaporate aluminum gates, and lift off the metalization (Section B.4.1).
8. Rinse with acetone, methanol, then deionized water.
9. Clean sample (Section B.1.2).
10. Make indium contacts (Subsection B.5.1).
11. Wire-up sample.

B.6.4 Undoped heterostructures Undoped heterostructures are exactly the same as our usual samples, except there is no silicon dopant, and therefore no carriers in the structure. Instead, the Ohmic contacts are used to provide the carriers. A gate is placed above the structure; when a positive voltage is applied to the gate it can, for contacts sufficiently close to the gate, suck carriers in from the doped contact region and form a 2DES in the undoped structure. These samples allow the creation of extremely high-quality samples with variable density [32].

What makes the implementation of this idea difficult is the requirement that the Ohmic contacts be sufficiently close to the 2DES and the gate that the potential of

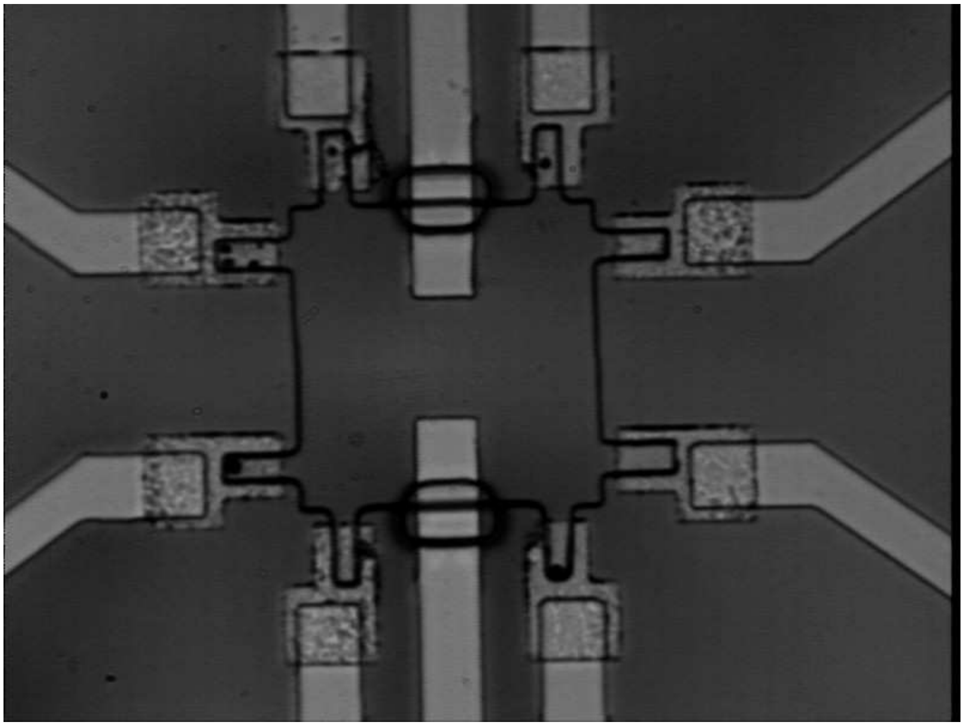

Figure B.4: Photo of a sample with self aligned contacts and CrAl contact to a N+ gate.

the gate can draw carriers from the contact. This is achieved in practice using the technique of “self aligned contacts.” The idea is to use a sample with an N+ layer grown as a gate, then etch the desired mesa shape past both the N+ and the 2DES, creating a gate exactly coincident with a 2DES. Next, a lithography step creates openings where the Ohmic contacts are desired, but instead of evaporating contacts right away, the N+ layer is first etched away, and contacts are immediately evaporated in the resulting pit.

An additional complication of these samples is making contact to the N+ layer. An unannealed CrAl contact is used to make contact; however, the metalization cannot be exposed to the side of the mesa, otherwise it will short to the 2DES at about 0.3 V, when the Schottky barrier has been overcome. Instead, the CrAl traces go over small polyimid bridges at the edge of the mesa.

1. Clean sample (Section B.1.2).

2. Define mesa (Section B.2.1).
3. Etch with a slow sulfuric acid etch (Section B.3.2) for 135 seconds.
4. Rinse with deionized water and blow dry, then remove the photoresist with n-butyl acetate.
5. Clean sample (Section B.1.2).
6. Define polyimid bridges (Section B.2.2).
7. Apply Ohmic contact pattern.
8. Etch with a slow sulfuric acid etch 2000 Å below the contact interface (4000 Å/min).
9. Clean in deionized water and blow dry. It might be possible to clean with some chlorobenzene as well, which could also help harden the resist.
10. Evaporate AuNiGe contacts (Section B.5.2).
11. Evaporate CrAl both as the N+ contact and as the pads and leads for wire-up (Section B.5.3)..
12. Lift off.

The samples produced using this recipe have a very low yield, somewhere between 10% and 30%, where the usual failure modes are shorting between the Ohmic contact and the gate (if they are too close), or contacts don't work at any gate voltage (if they are to far apart). The quality of the contacts also depend strongly on the crystalline axis, so we often find that the contacts on two parallel sides of a square work well, while the other two sides fail completely.

B.6.5 Thinned samples A thinned sample refers to a sample where most of the host GaAs wafer on which the MBE structure was grown has been etched away. We generally do this to allow for selective depletion of bilayer systems, creating tunneling, or coulomb drag geometries, for example.

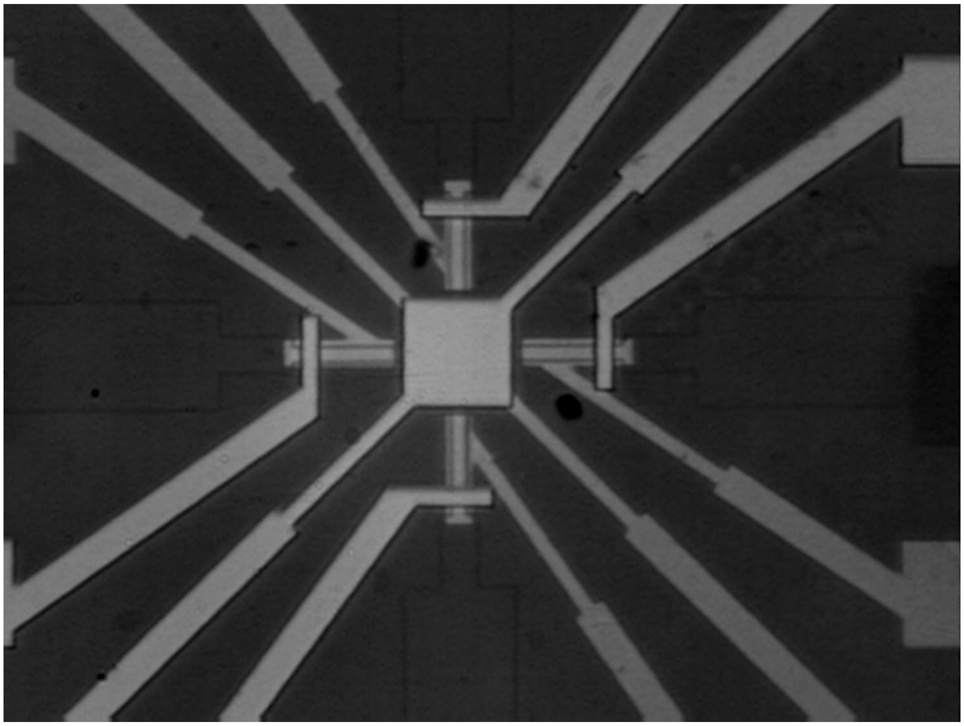

Figure B.5: Photo of Sample E, a 50 μm-thick sample in a tunneling geometry. Both the top and back gates are visible as the sample was imaged in the infrared, where GaAs is transparent.

Figure B.5 is a photo of Sample E, a sample designed primarily for tunneling measurements. This particular sample is 45 μm thick, and the central square, where the tunneling takes place, is 250 μm on a side. The image was taken in the infrared, below the band gap of the GaAs, where it is transparent. The following recipe is generically used to make such thinned samples.

Perhaps the hardest part of making thinned samples is the wire-up stage; it is very easy to destroy the sample by pressing with the solder pencil. For this reason, we often use conducting epoxy to contact aluminum structures, using indium only for Ohmic contacts. This usually works well, but we have recently encountered a problem where the epoxy fails to make electrical contact to the metal.

1. Clean sample (Section B.1.2).

2. Define mesa (Section B.2.1).

3. Etch with phosphoric acid etch (Section B.3.1).
4. Rinse with deionized water and blow dry, then remove the photoresist with n-butyl acetate.
5. For samples requiring AuNiGe contacts, first define Ohmic pattern and evaporate AuNiGe contacts (Section B.5.2).
6. Anneal AuNiGe contacts for 5 minutes at 440 C.
7. Rinse with acetone, methanol, then deionized water.
8. Define top-side gate pattern, evaporate aluminum gates, and lift off the metalization (Section B.4.1).
9. Rinse with acetone, methanol, then deionized water.
10. Thin sample to 40 μm using sulfuric acid etch (Section B.3.3). Leave the sample on the disk.
11. Define back gates, using infrared camera to align to top side structures. Then evaporate Al gates.
12. Rinse with acetone, methanol, then deionized water.
13. Attach gold wires to back-side pads using conducting epoxy and cure for 20 minutes at 100 C.
14. Remove sample from quartz disk (Section B.3.3).
15. Wire-up front side pads using conducting epoxy and anneal for 20 more minutes.

If indium contacts are required instead of AuNiGe, do not attach wires to the back side before removing the sample from the quartz disk. Instead remove the sample, then make Ohmic contact to the front side, and lastly do any required wire-up with conducting epoxy.

There are several difficult parts with the recipe. One of the most challenging parts of making a thinned sample is handling it once it is 50 μm thick. Before it has any wires on it, we carefully transfer it from one surface to another by tilting the surface and shaking it slightly until it slides off. Once a single gold wire has been attached, it may be readily used as a handle.

B.6.6 EBASE samples Epoxy bond and stop etch (EBASE) [100] samples are very much like the free standing 50 μm thick samples, except they are supported by a second piece of GaAs and thinned to 1 or 2 μm. These samples require a special AlAs layer grown during MBE on which a selective etch will stop. To contact the metalization on the original top layer, it is necessary to etch small holes, called vias, though the remainder of the sample. When planning masks for EBASE samples, it is important to allow space for the vias alongside the pads for the back gates. Once the sample is thinned, care should be taken to minimize the contact with acetone.

1. Clean sample (Section B.1.2).
2. Define mesa (Section B.2.1).
3. Etch with phosphoric acid etch (Section B.3.1).
4. Rinse with deionized water and blow dry, then remove the photoresist with n-butyl acetate.
5. Define Ohmic pattern and evaporate AuNiGe contacts (Section B.5.2).
6. Anneal AuNiGe contacts for 5 minutes at 440C.
7. Rinse with acetone, methanol, then deionized water.
8. Define top-side gate pattern, evaporate aluminum gates, and lift off the metalization (Section B.4.1).
9. Rinse with acetone, methanol, then deionized water.
10. Cleave a square larger than the original sample of semi-insulating GaAs.

11. Clean the semi-insulating piece, and when done, place it on a piece of Teflon.
12. Measure and record the thickness of the sample and the semi-insulating piece.
13. Cover the top surface of the sample and the semi-insulating piece with a thin layer of Stycast 1266 epoxy. Place the two surfaces together and press down firmly on the sample with a wooden applicator.
14. Put a small, 5×5 mm piece of Teflon on top of the sample (from bottom to top there should be Teflon, semi-insulating GaAs, epoxy, sample, and Teflon).
15. Place the above in a small vise and gently clamp, taking care that the sample remains in the center of the blank GaAs.
16. Cure for 60 minutes at 125 C in a furnace. When done, remove the sample from the vise and the Teflon.
17. Thin sample to 40 μm using sulfuric acid etch (Section B.3.3). Leave the sample on the disk.
18. Finish with the citric acid stop etch (Section B.3.5) and remove the sample from the disk.
19. Define back gates, using infrared camera to align to top side structures. Evaporate Al gates.
20. Rinse with acetone, methanol, then deionized water.
21. Define and etch via holes.
22. Wire-up sample with conducting epoxy or indium.

Depending on the thickness of the as-grown structure, these samples can be completely transparent when the citric acid etch reaches the stop layer, but this does not mean that the sample was completely etched away. Often one corner or side of the sample will reach the stop layer first. If the whole sample is not exposed in 5 minutes, remove it from the etch, cover the completed region with clear wax, and repeat in 5 minute intervals until the surface is fully exposed; then quickly remove the wax with acetone.

APPENDIX C

INSTALLATION AND OPERATION OF THE KELVINOX 25 CRYOSTAT

This document describes the instillation and operation of the Oxford KelvinOx 25 cryostat located in 051B Sloan. This cryostat has been enhanced over the provided Oxford specifications; it has a base temperature of 28 mK and a cooling power of 50 μW at 100 mK. The sample sits in the center of a 9 Tesla superconducting magnet (11 Tesla when pumping on the λ plate), and is thermally anchored to the mixing chamber with a cold finger designed for maximal thermal conductivity with minimal eddy current heating.

The first section describes the operation of a typical dilution refrigerator, and the second part details the construction of the tail piece, the electrical wiring of the cryostat, and the thermometry. The third section describes the dewar, magnet, and associated thermometry. The discussion concludes with the operating procedures for this system, and details its typical behavior.

C.1 PRINCIPLE OF OPERATION

Most low-temperature refrigeration relies on some form of evaporative cooling, and the dilution cryostat is no exception. For conventional cryogenic liquids ^{4}He, evaporative cooling becomes exponentially less efficient with decreasing temperature. In practice, a pumped ^{4}He system is limited to about 1 K, and a ^{3}He cryostat to roughly 0.3 K.

To understand the operation of, and need for, a dilution refrigerator, it is instructive to understand the failure of pumped helium cryostats (for a more compete argument see, for example, Reif [104]). Such a cryostat consists of a bath of liquid with a low-temperature liquid-vapor interface. A column of vapor extends from the liquid to room temperature where it is pumped. In steady state – constant pressure and temperature – the evaporative cooling power is $\dot{Q} = \dot{N}l$, where $\dot{N}$ is the rate at which atoms cross the phase boundary, and l is the latent heat per-atom. Although l is in general a function of temperature, this argument will assume that it is temperature-independent.

An ideal mechanical pump moves a constant volume of gas per-unit time, which we will call R, the pumping rate (typically given in liters/second). For a pump operating at room temperature, T_{rt}, the ideal gas law predicts a cooling power, $\dot{Q} = PRl/k_bT_{rt}$.

The Clausius-Clapeyron relation provides a second expression involving P and T,

$$\frac{dP}{dT} = \frac{l}{T\Delta v},$$

where $\Delta v = v_g - v_l$ is difference in the per-atom volume (N/V) between the gaseous and liquid phases. Here we simply assume that that liquid is much more dense than the gas ($v_g \gg v_l$), thus $\Delta v \approx v_g = k_BT/P$. When combined with the Clausius-Clapeyron relation, the resulting differential equation is easily solved, and the vapor pressure is found to be $P = P_0 \exp(-l/k_BT)$. P_0 is a material dependent constant, which is much larger in ^{3}He than ^{4}He. Therefore, the cooling power is

$$\dot{Q} = \frac{P_0 lR}{k_bT_{rt}} e^{-l/k_bT}.$$

The strongest effect here is the exponential – changing the pumping speed will not substantially increase the cooling power. Therefore, the low-temperature failure of conventional evaporative cooling stems from the exponentially suppressed vapor pressure. An alternate cooling technique is required to achieve temperatures below about 0.3 K, of which dilution refrigeration is one example.

Below about 0.8 K, the liquid composed of a mixture of ^{3}He/^{4}He phase separates, with the less dense ^{3}He floating on top of the ^{4}He. Even at the lowest temperature, the

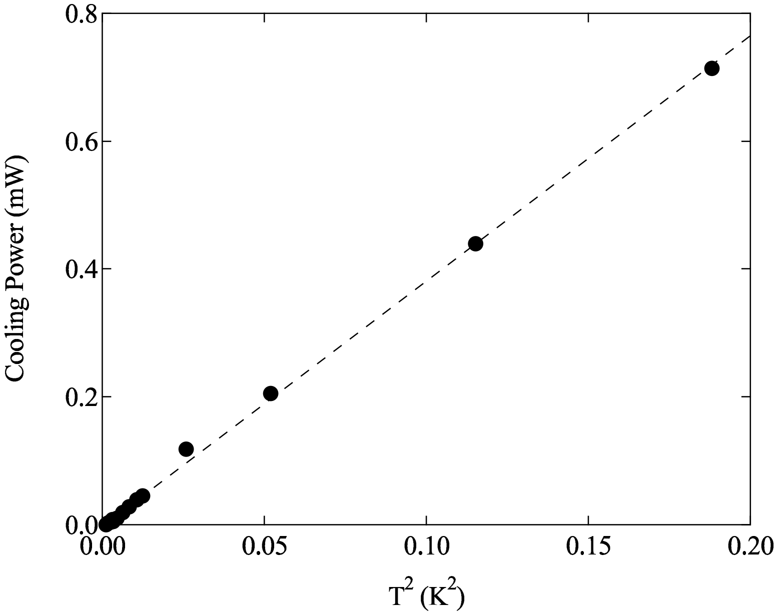

Figure C.1: Cooling power of KelvinOx 25 cryostat vs. temperature with 1.5 mW still power. Dotted line is quadratic fit, yielding a flow rate of 46 μmole/s, and a heat leak of 4.5 μW.

^{4}He phase is composed of roughly 6.6% ^{3}He. Modeling this as ^{3}He "liquid" floating atop a "gas" of ^{3}He (the concentrated and dilute phases, respectively) yields a system which potentially overcomes the limitations of evaporative cooling. Here, the "vapor pressure" is finite at low-temperature. The detailed mechanism of cooling is beyond the scope of this document, but the final low-temperature cooling power in units of Watts is [105]

$$\dot{Q} = 84\dot{n}T^2 + \dot{Q}_0,$$

where $\dot{n}$ is the rate in the moles per-second at which ^{3}He atoms cross the boundary, and $\dot{Q}_0$ is the unavoidable heat leak to the cold stage.

The actual operation of a dilution refrigerator is somewhat more complex than this in-principle discussion would suggest. The dilution cycles consists of a continuously circulating ^{3}He/^{4}He mixture. For the following discussion, refer to Figure C.2, which contains a photo of the KelvinOx 25 cryostat side-by-side with a schematic illustration of the essential parts.

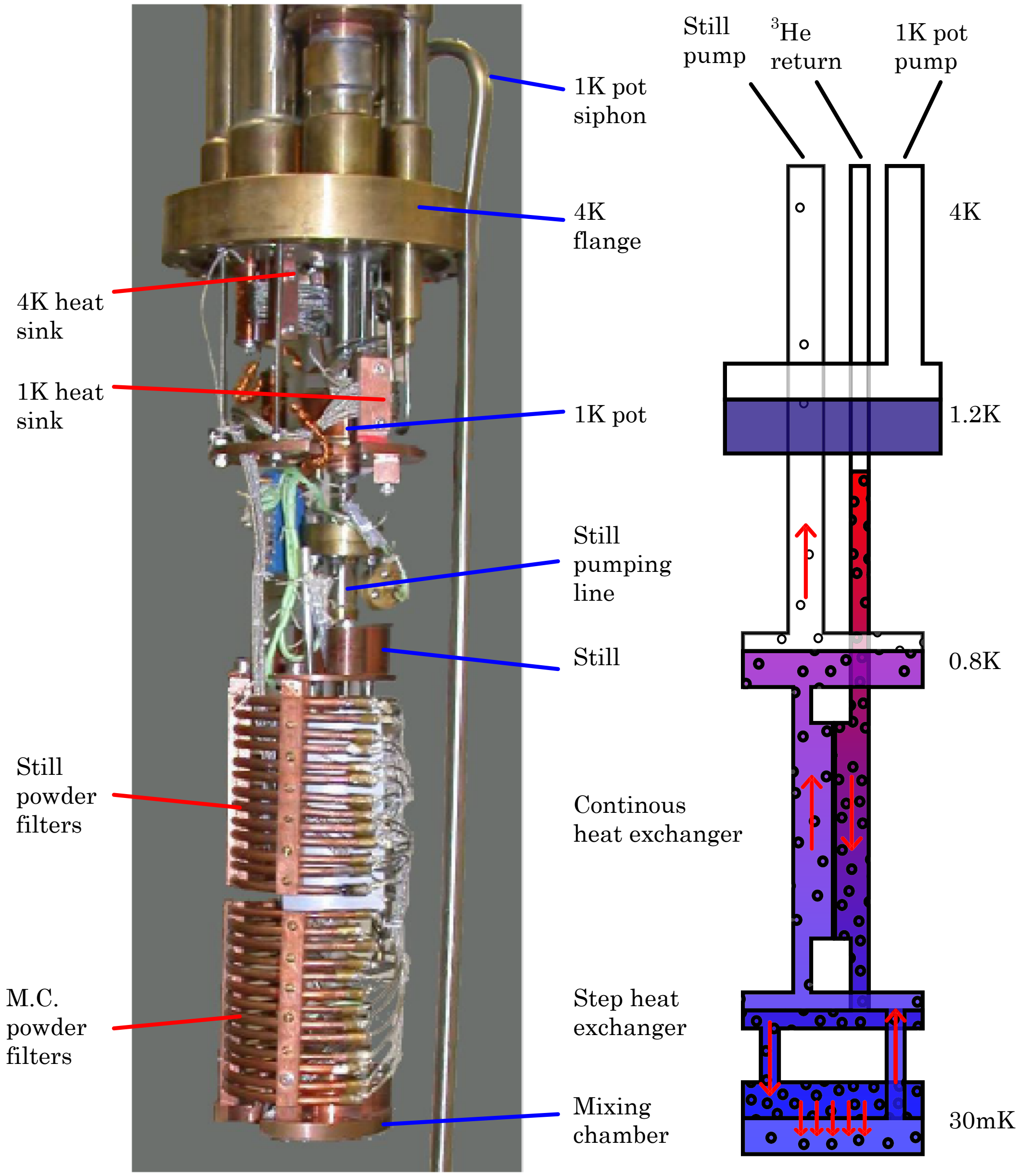

Figure C.2: Left: Annotated photograph of KelvinOx 25 cryostat as currently installed. Right: Schematic for a generic dilution refrigerator.

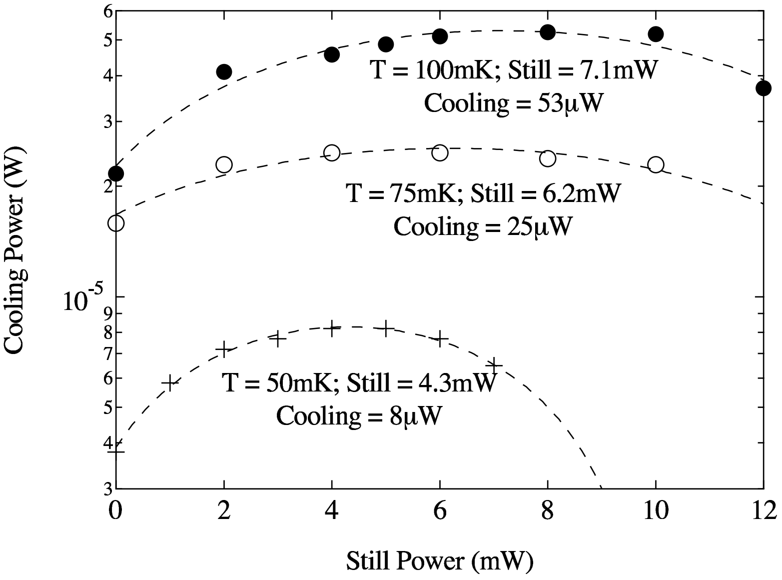

Figure C.3: Cooling power of KelvinOx 25 cryostat at 50, 75, and 100 mK.

C.1.1 Mixing chamber (MC) This is the active portion of the dilution refrigerator and contains the ^{3}He/^{4}He interface. The mixing chamber is connected with two circulation lines: one in the dilute phase, which pumps away ^{3}He atoms, and a second in the concentrated phase for the returning ^{3}He.

C.1.2 Heat exchangers As the dilute phase leaves the mixing chamber it encounters a series of heat exchangers that use the rising mixture to cool the returning ^{3}He. The quality of the heat exchangers is central to a functioning system. This system has a continuous heat exchanger, followed by a single discrete exchanger. The continuous heat exchanger consists of a small stainless capillary tube wound in a coil set within a larger stainless tube. The descending concentrated mixture flows down the coiled capillary, and the acceding liquid flows around the coil.

Just before the mixing chamber, the mixture encounters a single discrete heat exchanger. The two fluids are separated by a thin plastic membrane with pressed silver sinter on both sides. Such a heat exchanger provide extremely good thermal contact.

C.1.3 Still After the heat exchangers, the dilute phase enters the still (at about 0.7 K), which contains a liquid-gas interface and is pumped on by a room-temperature mechanical pump. At this temperature, the vapor pressure of ^{3}He is about 100× larger than that of ^{4}He, so ^{3}He atoms are predominately pumped.

The still temperature strongly influences the performance of the cryostat. As the temperature decreases, the ratio of ^{3}He to ^{4}He atoms increases, which enhances the performance. Even as this ratio increase, the pumping rate of ^{3}He slows, decreasing performance. Due to these competing effects, there is a temperature that maximizes the cooling power. A small heater is mounted on the still to maintain this temperature. The dependence of the overall cooling power on the still temperature is illustrated in Figure C.3.

C.1.4 Room temperature The mixture is pumped through the still pumping line by a sealed pump and then flows through a liquid nitrogen cold trap. Some systems also include a 4 K trap. These traps serve to catch any impurities that may have entered the mixture before it enters cryostat.

C.1.5 Return line The returning mixture reenters the cryostat through the return line and cooled to 4 K as it descends through the bath space. The mixture is further cooled by the 1 K pot, where it passes through a constriction and is liquefied. The liquid mixture is further cooled at the still, then passes through the heat exchangers, where it is cooled by the ascending mixture. The cycle is completed as the mixture reenters the mixing chamber in the ^{3}He rich phase.

The cooling power as a function of temperature has been measured for this KelvinOx 25 cryostat, and is contained in Figure C.1. The fit to the data is a quadratic with a constant offset corresponding to an external heat leak. The fit indicate ^{3}He atoms crossing the interface at 46 μmole/s, with a heat leak of 4.5 μW. This rate can also be computed from the expected pumping speed and measured inlet pressure (0.15 mB) of the Alcatel 2033H mechanical pump (13 l/s). This computation yields a flow rate of 75 μmole/s, which is in accord with the estimates based on the cooling power alone. Any pressure gradient between the thermocouple gauge used to measure the pressure and the pump will increase the predicted pumping rate. In addition, the overestimate may be due either to the finite compression ratio of the pump, or perhaps some ^{4}He in the circulating mixture.

C.2 Thermal link

The mixing chamber of the dilution refrigerator is located about 10" above the center of the superconducting magnet. The tail piece serves both as a mechanical and thermal connection between the mixing chamber and the sample located at field center. To allow for a diverse set of experiments, the tail piece accepts modular sample mounts. As of this writing only one sample mount has been constructed, which includes a set of final heat sinks, and terminates in a standard 18-pin header. Alternate sample mounts might include a rotating stage, or a stage with RF connectors.

To maintain a solid thermal link between the mixing chamber and the sample stage, it is important that the tail piece be constructed of an excellent thermal conductor. The RRR, or residual resistance ratio, is the ratio of the resistance of a material at room temperature to that at 4 K. At 300 K, the resistance is dominated by electron-phonon scattering, and for a reasonably high-quality metal, is independent of electron-impurity scattering (i.e., for the same geometry and the same material; it is a sample independent quantity). At 4 K, however, the resistance is dominated by the electron-impurity scattering; hence, the ratio is a geometry independent measure of the resistance due to electron-impurity scattering. A natural choice would be high-purity copper; unfortunately copper is excluded as a construction material due to a large nuclear heat capacity at low-temperatures and high magnetic fields. Instead, the thermal link is provided by 7 high-purity (5N) silver rods with $RRR = 3500$ (the fabrication of which is described in Appendix D).

The silver rods are welded on one end to a silver plate bolted to the mixing chamber, and on the other end to a silver bolt circle. Both are gold plated 99.95% purity silver.

Since annealed silver is extremely malleable, the tail piece required a supporting superstructure. The silver rods are located inside the main structural element, a 1/2"

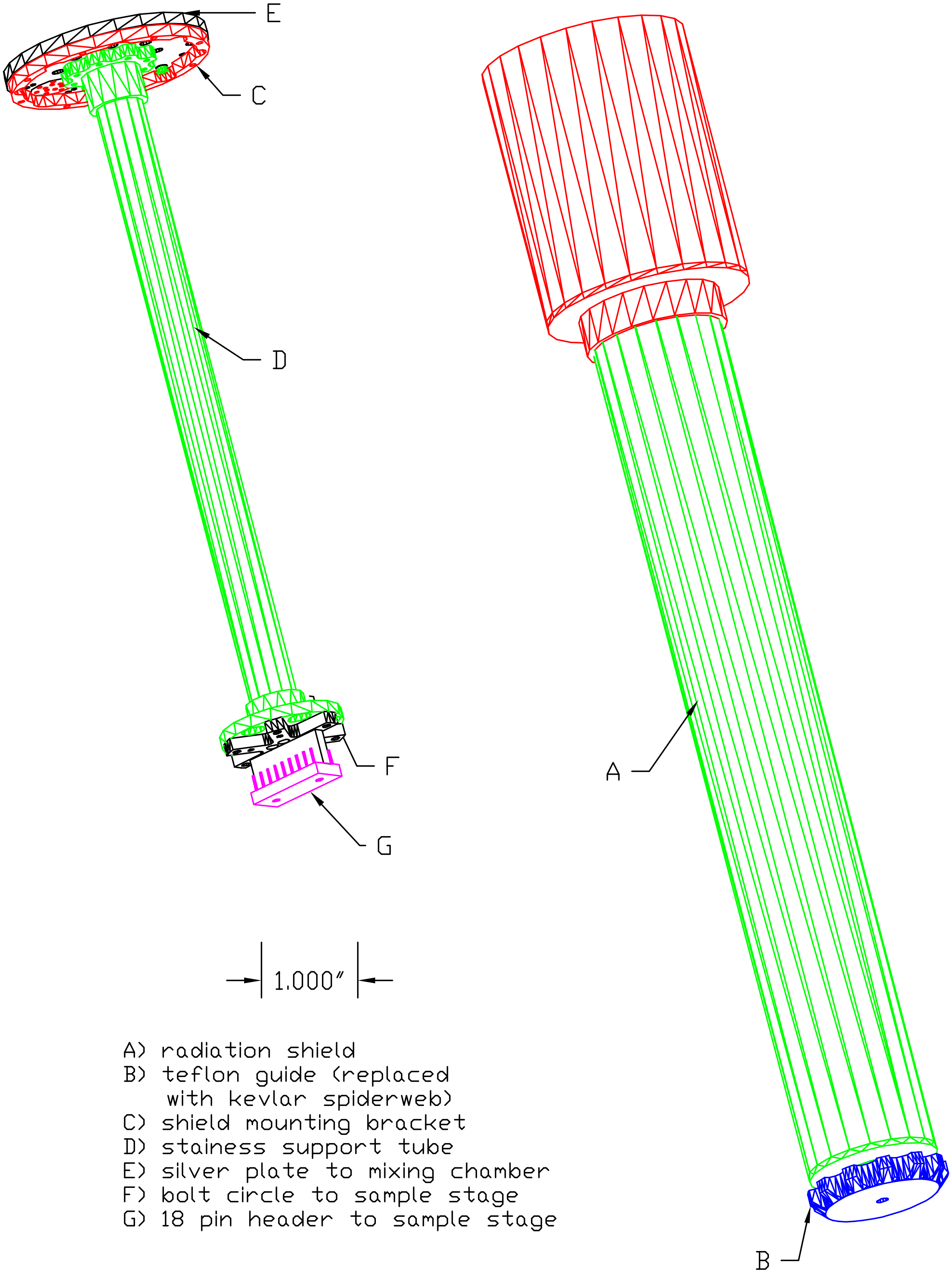

Figure C.4: CAD diagram for KelvinOx 25 tail piece.

Figure C.5: Photo of KelvinOx 25 tail piece, with sample mount attached on the bottom.

diameter thin-wall stainless tube. 304 stainless steel was selected as a cryogenicaly compatible structural material.

The entire assembly fits inside a final radiation shield attached at the mixing chamber. Figure C.4 illustrates the assembled tail piece and radiation shield, and Figure C.5 is a photograph of the installed tailpiece.

Currently the system includes one general use sample mount, which accepts standard 18-pin headers. There are several geometric constraints for any sample mount: it must attach to the cryostat on a 6 place 1.125” bolt circle using 4-40 machine screws. To position the sample exactly at field center it must be located 2.5” from the bolt circle. The whole assembly should be no more than 1.300” in diameter. The sample mount plugs into an 18-pin connector on the tailpiece; the mating connector on the sample mount should elevated 0.730” from the bolt circle. These constraints are more clearly illustrated in Figure C.6.

All contact joints are made with brass screws passing through a silver plate using stainless steel washers. The differential thermal contraction from room temperature for these materials are ($\times 10^{-4}$): 41 (silver), 38 (brass), and 30 (stainless steel). Both stainless steel and brass contract less than silver, so such a joint using either as the screw would always loosen. Since stainless steel contracts less than brass, stainless steel washers effectively tighten the brass screw onto the silver joint. For the silver-brass-stainless system, the stainless steel washers should total 1/3 the thickness of the silver plate.

The sample mount was constructed from three pieces of 99.95% silver. The first two form of a bolt ring with a slot (to decrease eddy current heating), and the third is a rectangle extending perpendicular from the bolt circle (see Figure C.6). The pieces are welded together to make a robust mechanical joint with good thermal conductivity. The heat sinking is described in more detail in Section C.3; two 18-pin connectors are attached to the mount, male on the cryostat side and female for the sample header.

To verify the tail piece was performing properly, the thermal conductivity from the sample stage to the mixing chamber was directly measured at 100 mK. A small

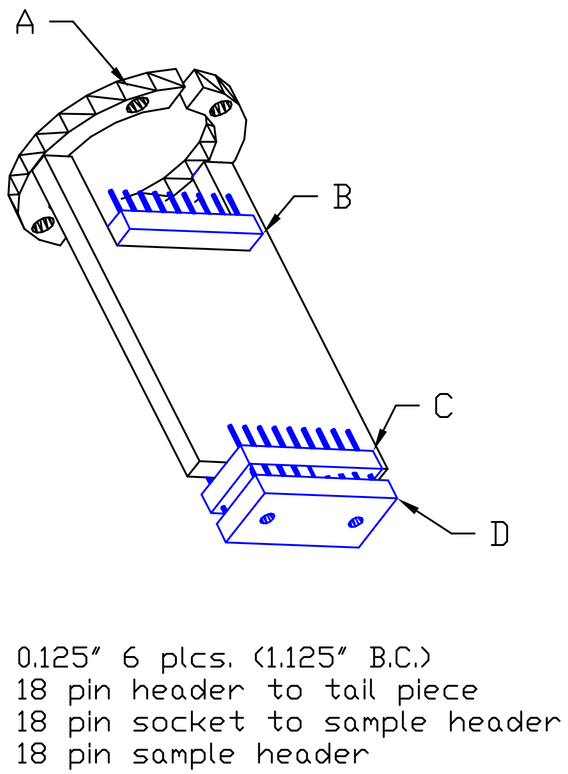

Figure C.6: CAD diagram for KelvinOx 25 sample mount.

Figure C.7: Photo of the KelvinOx 25 sample mount attached to the tailpiece.

voltage was placed across a 10 kΩ resistor thermally connected to the sample stage, and the resulting temperature gradient was measured along the length of the tail piece.

The thermal conductance across the joint connecting the mixing chamber to the tail piece was initially found to be 0.1 mW/K, a factor of 200 larger than the anticipated conductance of the entire tail piece. Before attaching the tail piece, the copper mixing chamber was dark brown; highly oxidized copper could easily have a large thermal resistance.

To remove the oxide, the base of the mixing chamber was etched for 30 seconds in a 1:1 mixture of HNO_3 (nitric acid) and H_2O, polished with an abrasive metal polish[1], and cleaned with acetone and methanol. The new contact joint between the clean copper surface and the gold plated silver base had negligible thermal resistance. The total observed thermal conductance of the tail piece, from the mixing chamber to the sample stage, is 16 mW/K, with the entire measured temperature drop along the silver thermal links.

C.3 WIRING

Particular care was taken in the wiring, heat sinking, and filtering of the DC leads descending from room temperature to the mixing chamber. There are two Bendix connectors on the cryostat; one 18-pin connector used for heaters and diagnostic thermometers (MUX 1,2, and 3), and one 26-pin connector dedicated to the experimental stage.

The 18-pin connector and wiring is original to the system and the heat-sinking is essentially unchanged. All 18 leads are heat-sunk at 4 and 1 K by wrapping the wires around copper bobbins using GE varnish as an adhesive. Since these leads are intended for primarily utility functions, this minimal level of heat sinking is sufficient.

The 26-pin Bendix services the experimental stage, and every effort has been taken to heat sink and isolate the leads properly. To help eliminate pickup, the wires are individually shielded twisted pair, made from a stainless steel outer braid, a Teflon

---

[1] Boyer Brass and Copper Polish, McMaster-Carr [106] part 7096T12.

dielectric, and a pair of Formvar insulated 0.005” manganin wires. The twisted pair was ordered from California Fine Wire Company [107], and was then sent to Cooner [108] to complete the stainless shielding and Teflon dielectric.

These 13 twisted pairs lead directly from room temperature to a pair of clamps on the 4 and 1 K stages. At the still, the first lengths of wire terminates at a set of 13 stainless steel powder filters (see Appendix E), which serve both as RF filters and as heat sinks. The filters are made of 1/8” copper refrigerator tube with a pair of manganin wires coiled inside, filled with stainless power in a epoxy dielectric.

The leads continue past the filters from the still to the mixing chamber and encounter a set of copper powder filters. From these filters, the 13 shielded, twisted pairs, enter the radiation shield attached to the mixing chamber and are heat sunk to copper strips etched on a copper-mylar-copper (180 μm mylar) sandwich.

The final heat sinks are on the removable sample mount and consist of a 5 kΩ metal-film resistor followed by a 500 pF polyester-foil capacitor[2] to ground. This series of heat sinks have proved sufficient to cool the electrons to 28 mK as recorded by a primary coulomb blockade thermometer (CBT) [110]. In the larger dilution refrigerator, a similar heat-sinking arrangement has yielded a CBT temperature of 18 mK.

The filters on each stage consist of 13 independent tubes; this was based on the assumption that the yield of filters would be low. The yield was 100%, and the difficulty was in the connectors to the filters. If at some time it is required to replace the filters on this system, the connectors should be redesigned. Instead of having twist-on connectors (which tend to abrade the solder joints inside the connectors and create shorts to ground); connectors that clamp on would be much better.

C.4 THERMOMETRY

Resistance thermometers are used to monitor temperatures at various stages of the system. The thermometers are measured in a four-wire configuration using a AVS-47 resistance bridge. A 30 μV excitation has proven sufficiently small to avoid

---

[2] 192P series Polyester Capacitor, 0.068 μF Mouser [109] part 75-192P683X9080

self-heating even at the lowest temperatures. This unit has 8 channels labeled "0" through "7." The temperature is regulated via an TS-530A temperature controller, which provides a feedback voltage to a $\sim 500\ \Omega$ wire-wound heater on the mixing chamber.

Two calibrated 1 kΩ Dale RuO_2 thermometers are mounted on the dilution unit. The main thermometer, "Mux 0," is mounted parallel to the magnetic field on the sample stage; its leads are filtered and heat-sunk in the same manner as those leading to the sample stage, and are connected through the same 26-pin Bendix connector. A nominally identical RuO_2 thermometer, "Mux 3", is mounted on the top of the mixing chamber; its leads are wound around a OFHC copper post, to which the thermometer and leads are affixed with Stycast 1266. Both thermometers are calibrated against a Nanoway CBT; the resulting calibration data are shown in Figure C.8. Additional thermometers are located on the still and the 1 K pot. Although their cryogenic readings have been consistent, these thermometers have drifted considerably at room temperature.

The still and mixing chamber are each equipped with Constantin wire wound heaters, with resistances of 510 Ω and 523 Ω respectively.

C.5 DEWAR AND MAGNET

The cryostat is mounted in a model dewar set in a pit in the floor. The top of the dewar is slightly above floor level. Mounted in the dewar is the helium level detector, and two Oxford "10-pin seal" connectors: "A" is wiring for the magnet, and "B" is for the dewar thermometers and heater. There are also two NW25 flanges on the dewar: one for boil-off and the other for the λ plate pump. A needle valve is opposite the λ plate port to control its flow rate. Two high current leads for the magnet complete the dewar wiring.

During operation, the helium level drops by 2%/hour (Figure C.9), and as a result, it needs to be filled every two days. A 60-liter dewar can completely fill the system with 20 liters remaining.

Parameter	Channel	28 mK	4 K	77 K	300 K
Main thermometer	0	22 kΩ	1.268 kΩ	0.999 kΩ	0.999 kΩ
1 K pot thermometer	1	1.4 kΩ	0.980 kΩ	0.578 kΩ	521 kΩ
Still thermometer	2	0.910 kΩ	0.505 kΩ	0.291 kΩ	0.256 kΩ
MC thermometer	3	25 kΩ	1.285 kΩ	0.998 kΩ	0.998 kΩ
Magnet thermometer	4	1.026 kΩ	1.026 kΩ	0.232 kΩ	0.212 kΩ
λ thermometer	4	1.360 kΩ	1.360 kΩ	0.192 kΩ	0.169 kΩ
λ top thermometer	4	1.013 kΩ	1.013 kΩ	0.187 kΩ	0.164 kΩ
Still power	-	1.4 mW	-	-	-
Still pressure	-	0.15 mB	-	-	-
Return line pressure	-	100 mB	-	-	-

Table C.1: KelvinOx 25 thermometry at several useful temperatures. To avoid wasting channels, the four dewar thermometers share channel "4," and have a 3-position rotary switch on the thermometer panel. The 1 K pot and still thermometers have shown some drift in their 300 K and 77 K readings, but are so far reliable at 4 K. The table concludes with the value of several diagnostics at base temperature.

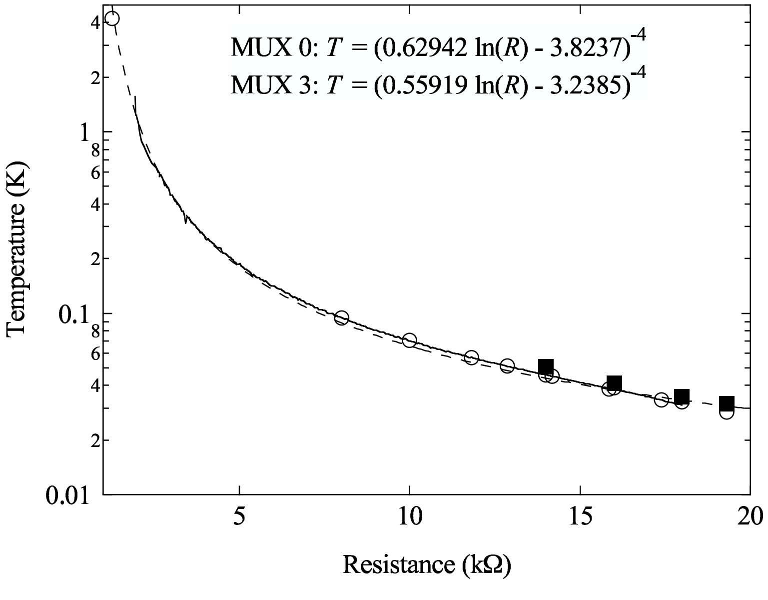

Figure C.8: Calibration of RuO thermometers mounted on the mixing chamber of KelvinOx 25 cryostat. The symbols represent temperature measuring the full dI/dV trace of the CBT thermometer (solid: channel "3," empty: channel "0"); the solid line is temperature extracted from the zero-bias CBT conductance; and the dashed line is a fit to the "MUX 0" data.

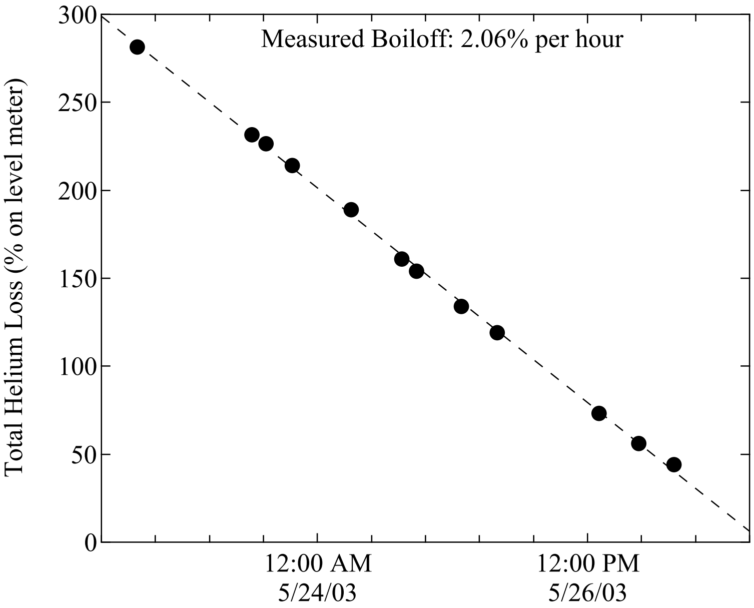

Figure C.9: Measured boiloff for KelvinOx 25 system during operation. The loss is in terms of the measured helium level and records the boil off across several transfers, thus exceeding 100%.

A 9 Tesla superconducting magnet is mounted in the dewar; a field/current ratio of 0.0942 T/A generates the maximum field at 95.55 amps. The magnet is equipped with a persistent current switch heater, which allows the magnet to be selectively placed in persistent mode. This magnet includes cancellation coils that nulls the field at the mixing chamber. At full field, the mixing chamber field is within ±0.004T.

The magnet is controlled with an Oxford PS120-10 power supply. This supply is programmable using a standard serial port, not GPIB. The power supply has been a major problem for this system. Any time there is current in the leads, i.e., not persistent mode, the main thermometers record a dramatic increase temperature. When the current is removed, the temperature instantly drops, suggesting that only the thermometers are being heated. Proper grounding has decreased this effect, but it remains true that reliable temperature readings can only be made in persistent mode, or zero field.

“10-pin seal” B leads to the dewar thermometers (measured in a two wire configuration with a common ground) and heater. The Allen Bradley resistive thermometers are mounted on the magnet top, the λ plate, and 10 cm above the λ plate. Table C.1 summarizes the values of these thermometers at several useful temperatures. The dewar heater consists of two 20 Ω (and 15 Watt) resistors wired in parallel at the bottom of the dewar; such heaters are often useful during the initial transfer to prevent the hydrogen exchange gas from freezing out.

C.6 OPERATION

As installed the KelvinOx 25 has a base temperature of 28 mK and a cooling power of 50 μW at 100 mK; this factor of 2 enhancement over the advertised 25 μW was achieved by installing a wider (NW50 vs. NW25) and shorter pumping line on the still, and by replacing the Oxford provided Alcatel 2012AH pump with an Alcatel 2033H (increasing the free air displacement from 310 L/min to 765 L/min).

Table C.1 contains recommended operating settings, thermometer readings, and pressures at base temperature. The still power setting of 1.4 mW is not optimal for all temperatures; however, it provides acceptable performance across the full operating range of the refrigerator. The cooling power data in Figure C.3 can be used to further optimize the performance.

APPENDIX D

ANNEALED SILVER

Making good thermal contact between different cold parts of cryogenic equipment is essential to the success of any low-temperature experiment. Annealed high-purity silver thermally connects the mixing chamber of a dilution refrigerator to the experimental stage located some 12 to 24" away at the field center of a superconducting magnet.

Copper is an excellent thermal conductor and for experiments at zero magnetic field, it is the best choice for thermal links, however, copper suffers from a large nuclear magnetic moment (and is thus a nuclear coolant: when a magnetic field is swept upwards, entropy is transferred from the spins and the system heats, and in reverse when the field is swept down). Silver has slightly higher thermal conductivity than copper, but more importantly is its lack of a large nuclear magnetic moment. Of course, silver is much more expensive, so it should be only be used when copper is specifically excluded.

D.1 WIEDEMANN-FRANZ LAW

A surprising result of the simple Drüde model of electron scattering is that the electrical and thermal conductivities are related by the temperature times a constant, called the Lornez number, which is independent of material and geometry (it is ironic that this correct result is a lucky accident for Drüde theory, and can be correctly arrived at by treating electrons as fermions). It is therefore sufficient to measure the electrical resistance to ascertain the thermal conductivity of a particular sample.

In the Drüde model (free classical electrons with a damping force $F_{damp} = -mv/\tau$), the electrical conductivity is simply given by $\sigma = ne^2\tau/m$. Likewise, the thermal conductivity in a Fermi gas (in 3D) is computed and their ratio is

$$\frac{\kappa}{\sigma} = \frac{3}{2}\left(\frac{k_B}{e}\right)^2 T.$$

This combination of constans is the Lorenz number, and has a numerical value $L = 1.11 \times 10^{-8}$ WΩ/K^2.

Since the thermal conductivity is related to the electrical conductivity by L, the quality of materials can be assessed by measuring the electrical conductivity R as a function of temperature. A useful parameter is the residual resistance ratio (RRR) defined as the ratio $R_{300\ \mathrm{K}}/R_{4\ \mathrm{K}}$, the resistance at room-temperature divided by that at 4 K. For reasonably pure metals at 300 K, the primary scattering mechanism is phonons (therefore independent of sample quality), while the 4 K conductivity is dominated by impurity scattering. As a result, their ratio gives a geometry independent assessment of the electrical (and therefore thermal) quality. The following equations relating RRR and thermal conductance for copper and silver [105] are potentially very useful (in units of W/Km),

$$\kappa_{\mathrm{Cu}} = (\mathrm{RRR}/0.76) \times T, \qquad \text{and} \qquad \kappa_{\mathrm{Ag}} = \qquad (\mathrm{RRR}/0.55) \times T.$$

The primary assumption in the argument for the Wiedemann-Franz law is that the scattering times for thermal and electrical conductance are the same (the above equations relate RRR to the Wiedemann-Franz thermal conductivities). Observation shows that the Wiedemann-Franz law is well followed by copper, but silver of comparable RRR has only a fraction of the expected thermal conductivity [105].

D.2 MATERIALS

When selecting the size of the material for heat links, a small diameter is important – a changing magnetic field induces eddy currents, and for a solid disk, the amount of heat generated is proportional both to the conductivity and to r^4, in contrast, the thermal conductivity scales as r^2. As a result, a large number of skinny rods minimize eddy current heating while maintaining a large thermal conductivity. Additionally, this suggests constructing large objects (structural supports, for example) out of low-conductivity materials like stainless steel, and then using a large number of thin silver rods for the heat link.

The purity of metals is generally specified as 4N, or 5N – read 4-nines or 5-nines. This means that the sample is 99.99% or 99.999% pure. We start with 5N silver rod with a diameter of 1/8". We have used ESPI [111] or Alfa Aesar [103] as suppliers for this material, but they are prohibitively expensive. For 3N5 silver, Surepure Chemetals [112], is only 25% the cost of these two; we have never tried their 5N silver.

Before processing, the RRR of a typical 5N purity silver rod is about 100. This value can be increased to about 3500 by high-temperature annealing. The literature on annealed silver is sparse [113], and describes a technique of oxygen annealing. The authors found that their sample quality was fundamentally limited by magnetic impurities. When the silver is close to its melting temperature, it tends to form crystal grains, and any impurities migrate to the grain boundaries, eventually limiting the maximal grain size. A small partial pressure of oxygen was found to neutralize the magnetic impurities once they migrated to the grain boundaries. Although the recipe described here [89] does not use oxygen, the quality of samples is similar; our 5N silver (from ESPI) is possibly relatively free of magnetic impurities.

D.3 PREPARING THE MATERIAL

Before annealing, we clean the silver's surface to remove any impurities that might diffuse into the silver during the anneal. First, remove any visible tarnish or dirt with a Scotch-Bright scrubbing pad, then clean with acetone, and methanol, rubbing each time with a paper towel. Immediately before annealing the silver, it should be etched with the following solution for about 5 seconds: 1:1:4 of NH_4OH (ammonium hydroxide):H_2O_2 (hydrogen peroxide, 30%):CH_3OH (methanol). The rod will bubble slightly when immersed in the solution. After the etch, rinse with H_2O, then methanol.

D.4 ANNEALING

Place the cleaned silver on a quartz plate, and slide it into the center of the furnace. Be sure that the silver is fully supported by quartz. After annealing, silver becomes very soft and has a tendency to droop if left unsupported. Close the chamber and flow helium gas at 0.5 SLPM for 30 minutes before starting. At the same time, begin circulating cooling water through the cap.

Setup all three temperature controllers:

- Set the ramp up rate to 3 C/min (press PAR button six times until R1 appears).
- Set the annealing temperature to 860 C (press PAR button seven times until L1 appears).
- Set the annealing time to at least 600 minutes (press PAR button eight times until D1 appears).
- Set the ramp down rate to 3 C/min (press PAR button nine times until R2 appears).
- Start the run (Press PAR twice, and select "run").

Once the chamber is completely cooled, stop the helium flow and remove the silver pieces. They will be very soft; any bending will create dislocations and decrease the RRR. If you inspect them, you should be able to see crystal grains from 1 to 3 mm in size (Figure D.1).

Do not place solder in the furnace. It may be tempting to further anneal a piece of silver for which you have already measured the RRR. If this is required, first file the solder off and repeat the cleaning schedule. Both flux and PbSn solder contaminate the furnace. It is possible to clean out the resulting material plated on the inside of the furnace: tie a piece of Scotch Bright to the end of a long wooden stick and scrub the inside of the furnace tube with acetone, then methanol, then deionized water until it is clean. This process takes about 90 minutes of constant scrubbing.

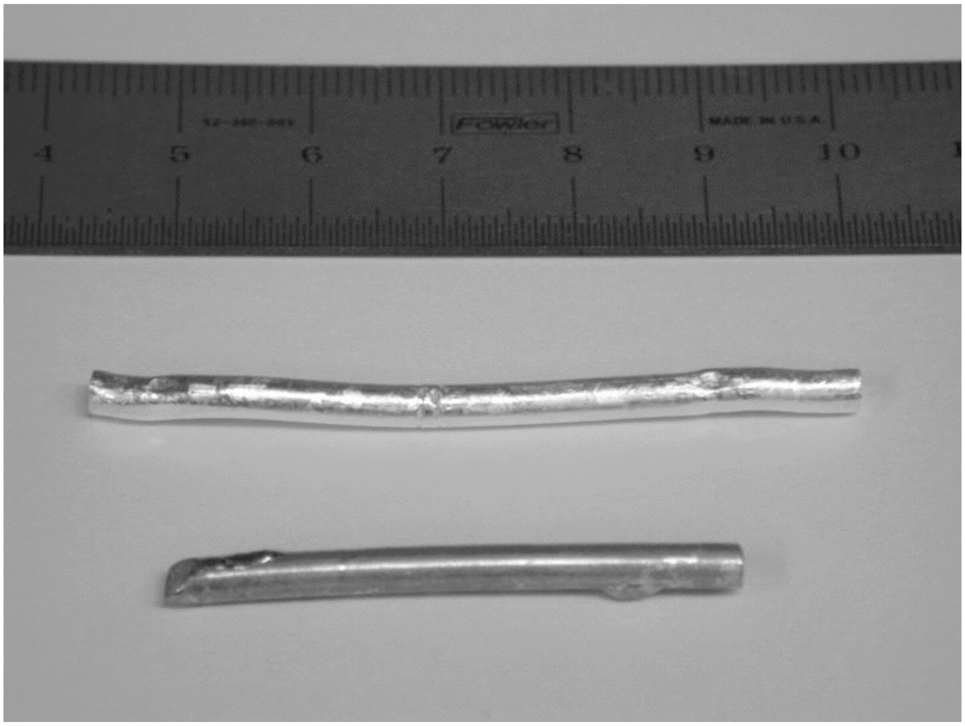

Figure D.1: Typical 5N silver before and after annealing. Note the millimeter-sized grains on the annealed sample (top).

If you plan to anneal with a stainless steel support, be sure to anneal the stainless by itself first as a cleaning step. Likewise brass may be annealed at 860C for use as structural pieces. After annealing, both of these materials leave stains on the quartz plate they were on, indicating that considerable impurities were removed from the metals.

D.5 Measurement of RRR

Before making the final pieces of silver, it is a good idea to anneal a sample from the same batch of 5N silver to verify both that the material is good and that the annealing system is functioning properly. Here the measurement of the RRR for a 1/8" diameter silver rod from ESPI with a length of 8" is described.

It is surprisingly difficult to measure RRRs larger than 1000. If the room-temperature resistance is a typical value of 500 $\mu\Omega$, then at 4 K you would expect a resistance of 500 nΩ. Consequently, it is a good idea to make the test piece as long as possible; in

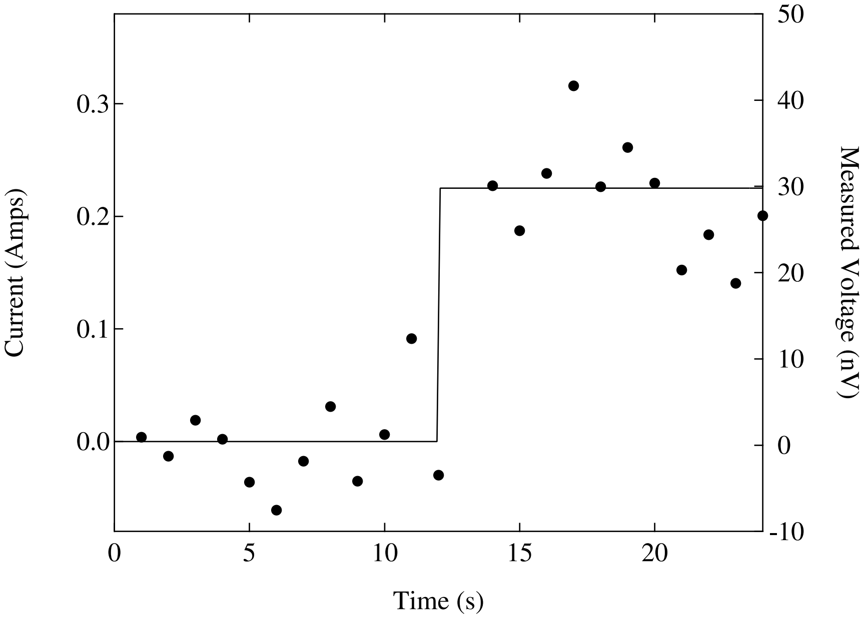

Figure D.2: Measured current and voltage for a highly annealed silver rod at 4 K. The solid line is the current (left axis) and the solid circles are the measured voltages (right axis).

this case 8”. To allow the final piece to fit in the test apparatus, the rod was wound into a 1” diameter coil. The coiled sample was then annealed as described above for 8 hours, and the residual resistance measured.

The resistance of the silver rod was measured in a four-terminal geometry, with the current leads soldered to the ends of the rod, and the voltage probes about 1/4” in from the ends. A simple way to measure the resistance is by applying a slow square wave current pulse (1/4 amp, 15 s period) and measuring the resulting voltage with a PAR113 preamp. The data in Figure D.2 shows the typical result of the measurement averaged 1024 times. From this data, the resistance, and then RRR, can be computed.

Clearly, a larger current excitation will lead to a larger voltage signal. Unfortunately, larger currents eventually heat the sample. Empirically, this heating starts at 1 amp; measurements performed at 1/4 amp are safely in the linear region.

The initial measurements were performed in a ^{4}He dipstick with four copper wires connected to BNCs at room-temperature and soldered to the sample in the helium bath; this scheme never resulted in RRRs larger than 500, which was apparently a

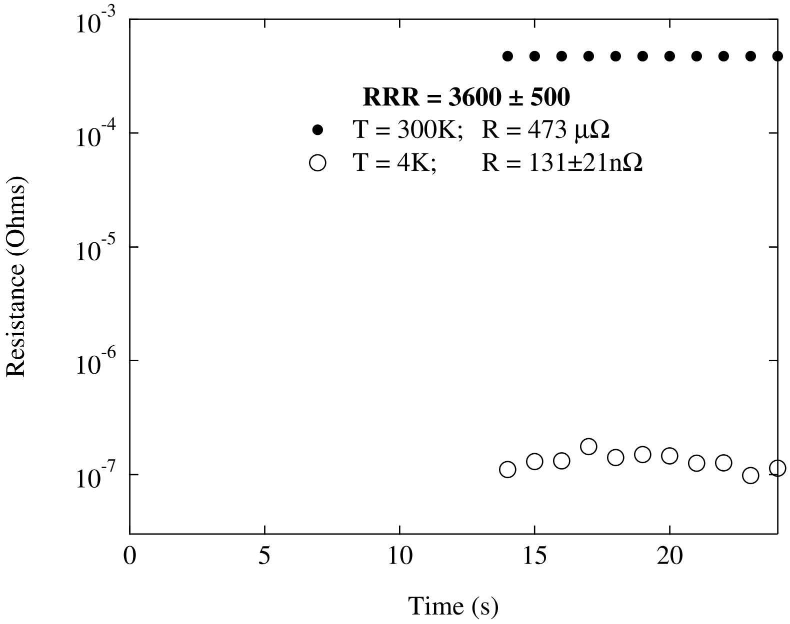

Figure D.3: Measured resistance for annealed silver at room-temperature and 4 K. The solid circles are the 300 K data, and the empty circles are at 4 K.

result of poor heat sinking of the silver rod. To fix this problem, the sample was attached to copper wires which were wound about copper posts and then attached to the copper leads. The above data was measured using this arrangement.

D.6 RESULTS

Silver prepared as described above was used to construct a tailpiece for a dilution refrigerator. The thermal conductivity of this structure was measured and found to be a factor of 10 less than anticipated from the Wiedemann-Franz law. For a RRR of 3500 the thermal conductivity at 100 mK should be 636 W/Km. The thermal link consists of seven silver rods with 1/8" diameter and are 8" long, so the expected thermal conductance is $K = 170 \times 10^{-3}$ W/K. The measured thermal conductance is 16×10^{-3} W/K the factor of 10 discrepancy here would be somewhat disturbing except for two mitigating facts: other silver rods, also prepared using this recipe gave similar thermal conductivities, and the data shown in [105] indicates that high RRR silver can have thermal conductivities depressed by factors of 30 from the Wiedemann-Franz prediction.

Appendix E

Powder Filters

It has become increasingly commonplace to outfit dilution refrigerators with extensive microwave filtering designed to isolate sensitive devices, both from a noisy external environment and from thermal radiation originating in the warmer 4 and 1 K states of the cryostat. In the past 15 years, several types of cryogenic filters have been developed, including: metal powder filters [114, 115, 116], meander line (LRC) filters [117], and wave-guide/coaxial filters filters of several types [118, 119]. Although there are differences in the radio frequency (RF) attenuation of each type of filter, the literature suggests that their performance can be made comparable.

RF filtering was included in the recent rewiring of a small (50 μW at 100 mK) dilution refrigerator. The system in question is intended to be a general-use cryostat with 26 DC leads descending from room-temperature (18 sample, four thermometry, four auxiliary) equipped with RF filters: one thermally lagged at the 1 K pot, and a second at the mixing chamber. The large number of leads, coupled with the extremely limited space, mandates that each RF filter be quite compact. This system will be used in part to measure the transport properties of high-mobility GaAs devices, which often have resistances less than 1 Ω. In these devices, DC resistance is generally measured in a four-wire geometry using low-frequency (5 Hz to 20 Hz) lock-in techniques. Even in a four-wire configuration, large lead resistances, coupled with cable capacitances can pollute measurements of very small resistances. The meander line filters [117], for example, have DC resistances of about 1 kΩ. We decided on metal powder filters based on their compact physical dimensions, relative ease of construction, and minimal DC resistance. This document describes a series of test filters used in preparation for wiring the cryostat.

E.1 Construction

Powder filters consist of an insulated wire embedded in a metal powder/epoxy matrix. When microwave radiation is transmitted though the powder, it induces currents within a skin depth of the metal grains' surface. The vast surface area of the grains allow for a rapid dissipation of RF power.

Many factors contribute to the performance of powder filters; foremost among these is the choice of metal powder, which is the central focus of this study. Two other essential ingredients to the filters are the epoxy filler and the insulated wire. The central wire for these filters was Formvar insulated 0.005" manganin, a commonly used high resistivity alloy[1]. Stycast 1266 was selected as the epoxy filler, based on its desirable cryogenic properties [105], and its low viscosity, which is desirable during the construction stage.

The filters investigated here are constructed from a 1.5 × 0.75 × 0.75" aluminum body with a 1/4" hole running its length. Roughly two meters of 0.005" manganin wire are wound into a 3/16" diameter coil and inserted into the body.

One end of the 1/4" hole is then sealed with a small epoxy cap and cured. The remainder of the cavity is filled with metal power (the 1 μm and 4 μm copper powders have a tendency to clump, making it increasingly challenging to fill the filters), and sealed with epoxy. Before curing, the filter is placed under vacuum. The epoxy will bubble for a time as the air is evacuated from the underlying metal powder. When the filter is removed from vacuum, the ambient atmospheric pressure forces the epoxy into the voids surrounding the metal grains. It is necessary to periodically add epoxy on the top of the filter as the level drops. Once the filters are fully loaded with epoxy, they are cured for 60 minutes at 120 C. The manganin leads are soldered to SMA connectors, which are in turn attached to the end of the enclosure, forming a RF tight device.

---

[1] $\rho \approx 2 \times 10^{-6}\ \Omega \cdot \mathrm{m}$ available from California Fine Wire Company.

By first filling the filter with metal powder, then backfilling with epoxy, we are able to achieve considerably higher densities of metal than by premixing. A mixture with too much metal becomes extremely viscous, and cannot be reliably packed around the wire coil. The filters constructed using the vacuum impregnating technique are ultimately limited in size by the viscosity and working time of the selected epoxy. We find that with Stycast 1266, the maximum length of the filters is about 15 cm.

We constructed five filters (Table E.1), one with stainless steel powder and four with copper powder of varying grain size (all metals are from Alfa Aesar). A sample of each metal powder was imaged in a scanning electron microscope (SEM) and the approximate grain diameter is also listed in Table E.1. The measured grain sizes often differed by as much as 50% from the advertised size.

E.2 Model

There are two mechanisms for the dissipation of RF power in a metal powder. First, an oscillatory magnetic field induces eddy currents in the grains. In addition, an electric field will cause charges to move parallel to the field in the metal grains. Both resistively dissipate power, but when the wavelength is larger than the grain size, magnetically induced eddy currents are the only significant source of dissipation.

If we consider metal grains with average radius a, resistivity ρ, in a linear material with permitivity $\epsilon_0\epsilon$ and permeability μ_0, the magnetization of a single metal grain is a function of the ratio $\alpha = d/\delta_s = d/(2\rho/\mu_0\omega)^{1/2}$. When $d \ll \delta_s$, i.e., low frequencies, the magnetization is purely imaginary and scales like ω. At high frequencies the magnetization is predominately real, and the imaginary part goes as $\omega^{-1/2}$ (for a more complete discussion, see [120]). Starting with a density of N grains per-unit volume gives a bulk magnetization, an effective magnetic permeability can be computed

$$\mu^*/\mu_0 = \left[1 - \frac{3n}{2}\left(1 + \frac{3i}{2\alpha^2} - \frac{3(1-i)}{2\alpha}\coth(i+1)\alpha\right)\right]^{-1}.$$

The term $n = 4N\pi a^3/3$ is the fraction of the volume filled with metal powder. Any quantitative prediction of the model should be regarded with considerable skepticism,

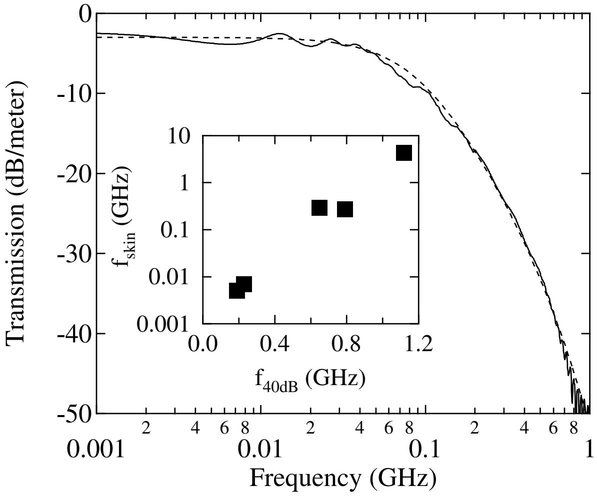

Figure E.1: Transmission data for Filter 1: in units of dB per-meter of manganin wire. Inset: f_{skin} vs. f_{40dB}.

since the model assumes spherical particles at low-density, which is highly idealized. In reality, the metal particles are a random assortment of elliptical grains with aspect ratios as large as 4:1, and the metal powder is tightly packed inside the filters with filling fractions that exceed 50%. It is hoped that the qualitative features of the model will survive these infractions.

The RF powder filters consist of a coaxial transmission line with this lossy dielectric. In the limit where most of the losses occur in the dielectric, the transmission coefficient is just $\gamma = \omega(lc)^{1/2} = \omega(\epsilon\epsilon_0\mu)^1/2$, the imaginary part of which is the attenuation. This result seems to capture the qualitative feature of these filters: the attenuation is proportional to the length of wire, not the length of the enclosure, and the attenuation increases with particle density. A usefully parameter in understanding the performance of the filters is f_{skin}, which is the frequency when $\delta_s = d$ below the frequency eddy currents flow throughout each metal grain, but above it, they only flow within δ_s of the surface.

Figure E.1 compares typical measured transmission to the predication of this simple model. The only adjustable parameter in this fit is f, the filling fraction; in this case, the fit returns an unphysical value of $f = 40$.

This physical picture for the mechanism of dissipation suggests one should choose

Filter	Metal	f_{skin}	f_{40dB}: 300 K	77 K	4 K
1	25 μm S.S.	0.29	0.65	1.1	1.1
2	30 μm copper	0.005	0.19	0.19	0.19
3	25 μm copper	0.007	0.23	-	-
4	4 μm copper	0.27	0.79	0.60	0.57
5	1 μm copper	4.30	1.12	1.25	1.25

Table E.1: Summary of filter information (all frequencies are in GHz). The grain diameters are as observed using a SEM. f_{40dB} is the frequency when the measured attenuation per-meter of wire is 40dB, and f_{skin} is the frequency where the skin depth is the same as the observed grain size.

the grain size and resistance of the metal powder so the skin depth is roughly equal to the grain size at the frequency where the filters should become active. Results for copper and stainless steel can be found in Table E.1.

E.3 MEASUREMENT AND RESULTS

The RF transmission of Filters 1 through 5 were measured first from 50 MHz to 20 GHz using a HP 8720C network analyzer, and then from 1 to 200 MHz using an HP 3577A network analyzer.

The data for each filter appears to follow the same general behavior as in Figure E.1, suggesting each filter can be described by a single figure of merit. f_{40dB} is defined as the frequency where the attenuation per-meter is $-40dB$, and seems to well parameterize the overall performance of a particular filter. The inset to Figure E.1 shows the dependence of f_{skin} on f_{40dB}. Although the trend is the same as expected from our model, the strength of the effect is very different – the model suggests a linear relation between the two, whereas the measured f_{40dB} increases much more slowly.

The temperature dependence is somewhat more difficult to understand. Although the general shape of the data remained unchanged, the dependence on temperature is not what one might expect in the simple model. The attenuation of Filter 1 (25 μm stainless) and Filter 5 (1 μm copper) increases with decreasing temperature; Filter 4 (4 μm copper) shows decreasing attenuation with decreasing temperature, while

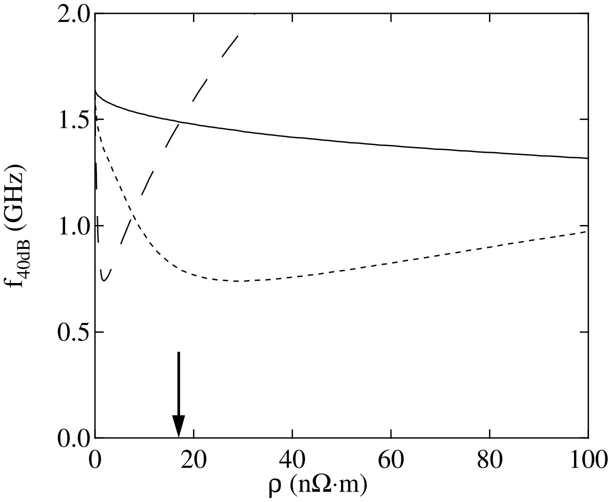

Figure E.2: Predicted resistivity dependence of f_{40dB} for three grain sizes: 40 μm (solid: Filter 2), 4 μm (dotted: Filter 4), and 1 μm (dashed: Filter 5). The arrow corresponds to $\rho = 17$ n$\Omega \cdot$ m, the nominal room-temperature resistivity of copper.

Filter 2 has no change in attenuation (Filter 3 was damaged). That the temperature dependence of the filters can be a function of grain size is understandable in our model. Figure E.2 shows the dependence of f_{40db} on resistivity for the three relevant grain sizes (the parameters for the three curves are based on a fit to Filter 4 at 300 K). If the primary effect of a changing temperature is to diminish the resistivity of the metal, we see that, depending on the grain size and initial resistivity, f_{40dB} can increase, decrease, or remain constant as a function of temperature. The maximum attenuation occurs when the real part in the denominator of the permeability passes through zero, resulting in enhanced dissipation (this is directly analogous to the "anomalous dispersion" in a dielectric, when the frequency of an electromagnetic wave matches a resonate frequency of bound electrons the material). Unfortunately, although Filters 2 and 5 show roughly the dependence predicted, Filter 4 (4 μm copper) does not. It is possible this filter had a lower metal density than expected (as the grain size decreased, the powder no longer flowed easily, and filling the filters became very difficult), which would correctly account for this discrepancy. It should be noted that this analysis excludes the dependence on temperature of the dielectric constant of Stycast 1266, which decreases to 63% of its room-temperature value by

4 K [121].

Although the attenuation of our filters seemed not to particularly depend on the type of metal used, instead depending only on f_{skin}, the choice metal can still be important for other reasons. For example, below 100 mK, stainless steel has a Schottky anomaly [122, 123], leading to a heat capacity that increases with decreasing temperature. The time constant for the thermal relaxation goes as the ratio of heat capacity to thermal conductivity. For a typical filter with lengths scales of about 1 cm, the Stycast 1266/stainless steel combination has a relaxation time of 150 sec at 100 mK, which increases to 900 sec by 50 mK, while for copper the values are 120 sec at 100 mK and 200 sec at 50 mK. Copper is not without its own limitations; at a high magnetic field it has a large heat nuclear capacity. At 1 Tesla and 50 mK, the nuclear heat capacity is comparable to the total heat capacity at zero field, and varies like $(B/T)^2$.

The dielectric constant of the epoxy filler is also important to the attenuation of the RF radiation – like most polymers, epoxies have a dielectric constant of about 3. Our analysis suggests that the attenuation increases like $\epsilon^{1/2}$, so it would be desirable to find a larger dielectric replacement for the Stycast 1266. Additionally, the filters discussed in the study used only manganin wire. It would be interesting to see the effect of wire type on the filter performance; however, if the simple model has any validity, the selection of wire should have little effect on the attenuation.

Based on this work, we suggest 25 μm copper as the powder of choice, based on its performance as a filter, suitability as a heat-sink, ease of construction, and economy. This work considered filters in the absence of an external magnetic field - the presence of a magnetic would introduce a considerable Hall contribution to the conductivity σ, which would have an unknown, and probably deleterious effect on the filters. Consequently, it seems prudent to place the filters in a field free region of the cryostat.

Appendix F

Thomas-Fermi Model

In free space, a charge q produces a potential proportional to $1/r$; this potential is vastly changed if the charge is located within a free electron gas. A classical electron gas perfectly screens the point charge, however, a quantum electron gas screens only imperfectly. The Thomas-Fermi model is a framework within which one can compute approximate screening potentials.

Chapter 3 discusses tunneling between two electron gasses in detail, which provides a direct measurement of the scattering time of electrons, both from other electrons and from static scattering centers. Central to the computation of any scattering rate is the screened potential that defines the interaction of electrons both between other electrons and background disorder.

This appendix presents the Thomas-Fermi model for electron gasses in several spacial dimensional: three-dimensions (3D), two-dimensions (2D), a 2D sheet in a 3D space, and two parallel 2D sheets. These go roughly in order of increasing complexity. Finally, the scattering rate of particles interacting with the computed potentials are computed.

F.1 General framework

The Thomas-Fermi model is a long wavelength approximation, which assumes that every point is in local thermodynamic equilibrium and that the local chemical potential μ is well defined. If we also suppose that the system is in global equilibrium, then the chemical potential can be taken to be everywhere constant.

If there is an external potential, the local density of electrons will change in response to that potential to keep μ constant. For a given μ, the density $n(\mu,\phi)$ of charge q carriers can be computed in any number of spacial dimensions at zero temperature for any total potential ϕ_t,

$$\begin{aligned} n(\mu,\phi) &= 2\int \frac{dk^d}{(2\pi)^d}\frac{1}{1+e^{\beta(E(k)+q\phi_t-\mu)}} \\ &= \frac{2\pi^{d/2}}{(2\pi)^d\Gamma(d/2+1)}k(\mu-q\phi_t)^d \\ &= \frac{2(2\pi m^*)^{d/2}}{(2\pi)^d\Gamma(d/2+1)\hbar^d}(\mu-q\phi_t)^{d/2}. \end{aligned}$$

The third result makes the usual assumption of parabolic dispersion, $E=\hbar^2k^2/2m^*$. The total potential can be expressed as the sum of two parts, $\phi_t=\phi_e+\phi_i$. ϕ_e is the externally applied potential, while ϕ_i is the induced potential resulting from the redistribution of charge carriers. The induced part is simply

$$\begin{aligned} \nabla^2\phi_i &= -\frac{\rho}{\epsilon} \\ &= -q\frac{n(\mu-q\phi_t)-n(\mu)}{\epsilon} \approx \frac{q^2\phi_T}{\epsilon}\frac{\partial n}{\partial\mu}. \end{aligned}$$

The last relation is the Thomas-Fermi differential equation, and results from linearizing the difference in densities. At this point, it becomes convenient to switch to Fourier transformed variables; in term of which the potential is

$$-k^2\phi_i = \frac{e^2\phi_t}{\epsilon}\frac{\partial n}{\partial\mu}.$$

Since the physical quantities of interest are the total and external potential, ϕ_i can be replaced with $\phi_t-\phi_e$, or

$$\phi_t-\phi_e = -\left(\frac{e^2}{\epsilon}\frac{\partial n}{\partial\mu}\right)\frac{\phi_t}{k^2} = -k_{tf}^2\frac{\phi_t}{k^2}.$$

To obtaion this result we made the usual definition of the Thomas-Fermi wave-number, k_{tf}. This leads to the desired result

$$\phi_t = \frac{1}{1+\left(\frac{k_{tf}}{k}\right)^2}\phi_e.$$

Qualitatively, this screening function leaves the potential unchanged at short length scales (large k), and attenuates it at long lengths. There are some usual definitions at this point; $\epsilon_{tf}(k)$ is the Thomas-Fermi dielectric constant, and $\chi_{tf}(k)$ is the polarizability defined by

$$\begin{aligned} \phi_t &= \frac{\phi_e}{\epsilon_{tf}(k)} & \rightarrow & \qquad \epsilon_{tf}(k) = 1+\left(\frac{k_{tf}}{k}\right)^2 \\ \rho_i &= \chi_{tf}(k)\phi_t(k) & \rightarrow & \qquad \chi_{tf}(k) = -\epsilon k_{tf}^2. \end{aligned}$$

Up to this point, the argument is general for any number of dimensions (but not for a sheet embedded in a higher dimension). Now we shall consider the special cases of 2D and 3D electron gasses. In these cases, k_{tf} is

$$\begin{aligned} &\text{2D}: & n &= \frac{m^*\mu}{\pi\hbar^2} & k_{tf}^2 &= \frac{e^2 m^*}{\epsilon\pi\hbar^2} \\ &\text{3D}: & n &= \frac{(2m^*\mu)^{3/2}}{3\pi^2\hbar^3} & k_{tf}^2 &= \frac{e^2 m^*}{\epsilon\pi^2\hbar^2 k_f}k_f^2 \end{aligned}$$

In 2D, the density is linear in μ, so the results are valid even in the limit of large potentials (to the degree that the Thomas-Fermi approximation is valid). One cautionary note, however, is that the Thomas-Fermi model allows the density to continuously pass through zero, where in a real system the density stops changing at full depletion.

For a typical 3D metal (silver: $m^* = m_e$, $n = 5.9 \times 10^{22}$ cm^{-3}, and $\epsilon = \epsilon_0$), the screening length $1/k_{tf}$ is 0.5 Å. In 2D, with $m^* = 0.068 m_e$, and $\epsilon = 13\epsilon_0$, the length is further enhanced to 50 μm.

The case considered above assumes that both the kinetics and electrodynamics are in N-dimensions. In reality the 2DES consists of carriers with 2D kinetics, but which still interact via usual 3D electrodynamics.

F.2 A 2D SHEET IN A 3D SPACE

This section treats a 2D sheet of charge embedded in a 3-dimensional space. Some caution is required to properly distinguish 2D and 3D charge densities. The symbol σ indicates 2D charge density, while ρ is still the overall 3D density. For a sheet lying in the $x-y$ plane located at z_0, these two densities are

$$\rho(x,y,z) = \sigma(x,y)\delta(z-z_0), \qquad \text{and} \qquad -\nabla^2\phi_i(x,y,z) = \frac{\rho(x,y,z)}{\epsilon}.$$

In the Fourier representation, this becomes

$$\phi_i(k_x,k_y,k_z) = \frac{\rho(k_x,k_y,k_z)}{\epsilon k^2} = \frac{\sigma(\mathbf{k_{xy}})}{\epsilon k^2}e^{-ik_z z_0}.$$

The density in the 2D sheet only responds to the potential at $z = z_0$, so integrating out the z part of ϕ and evaluating at z_0 gives

$$\begin{aligned}
\phi_i(\mathbf{k_{xy}},z) &= \frac{\sigma(\mathbf{k_{xy}})}{\epsilon}\int \frac{dk_z}{2\pi}\frac{e^{ik_z(z-z_0)}}{k_{xy}^2+k_z^2} = \frac{\sigma(\mathbf{k_{xy}})}{2\epsilon\,|k_{xy}|}e^{-|k_{xy}||z-z_0|} \\
&= -\frac{e^2m^*}{2\pi\epsilon\hbar^2}\frac{\phi_t(\mathbf{k_{xy}},z_0)}{|k_{xy}|}e^{-|k_{xy}||z-z_0|} \\
\phi_i(\mathbf{k_{xy}},z_0) &= -\frac{k_{tf}}{|k_{xy}|}\phi_t(\mathbf{k_{xy}},z_0)
\end{aligned}$$

In which the Thomas-Fermi wave-vector is defined as $k_{tf} = e^2m^*/2\pi\epsilon\hbar^2$. This result is somewhat different than the pure 3D or 2D results. As with the previous cases the Thomas-Fermi dielectric constant is easily found,

$$\phi_t(\mathbf{k_{xy}},z_0) = \frac{\phi_e(\mathbf{k_{xy}},z_0)}{\epsilon_{tf}(\mathbf{k_{xy}})} \qquad \rightarrow \qquad \epsilon_{tf}(\mathbf{k_{xy}}) = 1 + \frac{k_{tf}}{|\mathbf{k_{xy}}|}.$$

As expected, the small wave-vectors (long wavelength) components are screened, while the large wave-vector (short wavelength) parts are not. However, the screening is much softer than the case of pure dimensions, where ϵ_{tf} is quadratic in k. This means that 2D screening is much less effective than in 3D. Numerically, the screening length is about 50 Å for 2D electrons in GaAs.

F.3 PARALLEL 2D SHEETS IN A 3D SPACE

The argument for a single sheet at z_0 can be extended in a straightforward manner to two parallel sheets located at $z = \pm h/2$. Starting with an expression for the charge density of two sheets,

$$\rho(x,y,z) \;=\; \sigma_T(x,y)\delta(z-h/2) + \sigma_B(x,y)\delta(z+h/2).$$

Using the same argument as for a single-layer, this can be transformed to the Fourier representation, the same k_{tf} defined, and induced potential related to total potential

$$\begin{aligned}\phi_i(\mathbf{k_{xy}},z) &= \frac{1}{2\epsilon}\left(\frac{\sigma_t(\mathbf{k_{xy}})}{|k_{xy}|}e^{-|k_{xy}||z-h/2|} + \frac{\sigma_b(\mathbf{k_{xy}})}{|k_{xy}|}e^{-|k_{xy}||z+h/2|}\right)\\ &= -\frac{k_{tf}}{|k_{xy}|}\left(\phi_t(\mathbf{k_{xy}},d/2)e^{-|k_{xy}||z-h/2|} + \phi_b(\mathbf{k_{xy}},-d/2)e^{-|k_{xy}||z+h/2|}\right).\end{aligned}$$

The induced charge can be conveniently related to the total potential in matrix form, with $\Phi = (\phi(\mathbf{k_{xy}},h/2), \phi(\mathbf{k_{xy}},-h/2))$,

$$\Phi_i = -\frac{k_{tf}}{|k_{xy}|}\begin{pmatrix} 1 & e^{-|k_{xy}|h} \\ e^{-|k_{xy}|h} & 1 \end{pmatrix} \times \Phi_t.$$

In this case, replacing the induced charge with $\Phi_t - \Phi_e$, gives a Thomas-Fermi dielectric matrix defined as

$$\Phi_t = \epsilon^{-1} \times \Phi_e \qquad \rightarrow \qquad \epsilon = \mathbf{1} + \frac{k_{tf}}{|k_{xy}|}\begin{pmatrix} 1 & e^{-|k_{xy}|h} \\ e^{-|k_{xy}|h} & 1 \end{pmatrix}.$$

As $h \rightarrow \infty$, the matrix becomes diagonal, the values of which recapitulate the single-layer results. Given this screening function, it is interesting to consider the effect of the second layer on an isolated point charge located in one layer or the other. The potential due to a free charge located at $x = y = 0$, and $z = z_0$ is

$$\begin{aligned} -\nabla^2 \phi_e &= \frac{e}{\epsilon}\delta(x)\delta(y)\delta(z - z_0) \\ \phi_e(\mathbf{k}) &= \frac{e}{\epsilon}\frac{1}{k^2}e^{-ik_z z_0}. \end{aligned}$$

As the potentials of interest are located at a specific z coordinate, it is necessary to integrate out k_z,

$$\phi_e(\mathbf{k_{xy}}, z) = \frac{e}{\epsilon}\int \frac{dk_z}{2\pi}\frac{1}{k_{xy}^2 + k_z^2}e^{ik_z(z-z_0)} = \frac{e}{2\epsilon}\frac{1}{|k_{xy}|}e^{-|k_{xy}||z-z_0|}.$$

So a charge in the top layer ($z_0 = h/2$) gives the potential

$$\Phi_e = \frac{e}{2\epsilon}\frac{1}{|k_{xy}|}\begin{pmatrix} 1 \\ e^{-|k_{xy}|h} \end{pmatrix}.$$

Using the expression $\Phi_t = \epsilon^{-1} \times \Phi_e$, the total potential on both the top and bottom layers can easily be computed,

$$\Phi_t = \frac{e}{2\epsilon k_{tf}}\frac{\frac{k_{tf}}{|k_{xy}|}}{(1 + \frac{k_{tf}}{|k_{xy}|})^2 - e^{-2|k_{xy}|h}}\begin{pmatrix} 1 + \frac{k_{tf}}{|k_{xy}|} - e^{-2|k_{xy}|h} \\ \frac{k_{tf}}{|k_{xy}|}e^{-|k_{xy}|h} \end{pmatrix}$$

. Again, as $h \to \infty$, the result for an isolated layer is reproduced.

Figure F.1 compares the potential for several different cases. The top panel contains the potential for the top layer (where the charge resides), and the bottom panel for the bottom layer. Several different values for h are plotted. The screening due to a remote second layer has little effect on the potentials in the initial layer, both for charges in the first and second layers.

F.4 POTENTIAL SCATTERING

In this section, the scattering rate of particles interacting with the potentials $\phi_t(k)$ is computed. Using these screened potentials, it is possible to compute the lifetime of electron-like quasiparticles. Following the argument in [51] (a similar argument

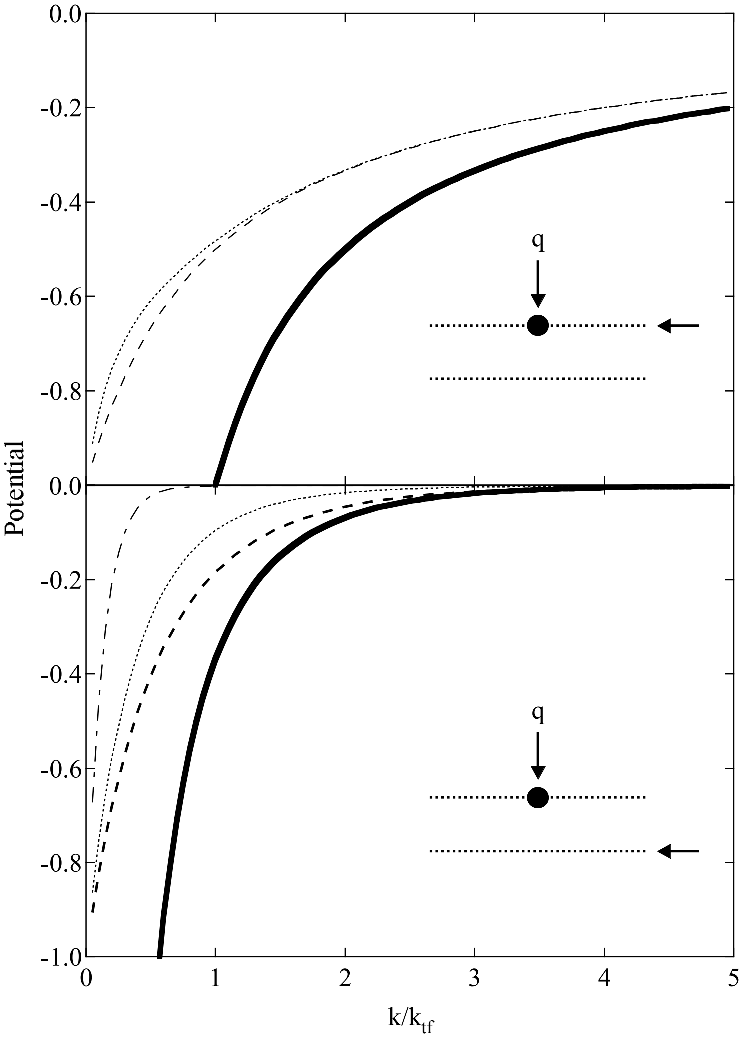

Figure F.1: Screened potential (units of $e/2\epsilon k_{tf}$) from a single test charge in the top layer of a bilayer system. Bold: no screening; dashed: screening from a single-layer; dotted: screening from bilayer system (50 Å separation); and dot-dashed: screening from bilayer system (300 Å separation). Top panel: test charge is in the same layer where potential is measured; bottom panel: charge is in the other layer.

appears in [52]), the scattering function $W = 2\pi \left|\phi_t\right|^2$ can be computed in terms of the interaction parameter $r_s = k_{\mathrm{tf}} / \left(2\sqrt{2}k_f\right)$, $g_0 = 2\epsilon k_{tf}/e^2$ and k_{tf}. For a single-layer, this function is (note that in the approximation this scattering function is spin independent)

$$W(\mathbf{k_{xy}}) = \frac{2\pi}{g_0^2}\left(\frac{k_{tf}/\left|k_{xy}\right|}{1+k_{tf}/\left|k_{xy}\right|}\right)^2 .$$

The scattering rate can be computed from W using a standard Fermi's golden rule integral, which is sharply peaked at $k = 0$ and $k = 2k_f$, allowing the scattering function to be approximated as the average at these two points,

$$W \approx \frac{2\pi}{g_0^2}\frac{1}{2}\left(1+\left(\frac{2k_f}{k_{tf}}+1\right)^{-2}\right) \equiv \frac{2\pi}{g_0^2}w^{fb}.$$

Jungwirth *et al* [51] continue, with a calculation (beyond the scope of this document) of the temperature dependence of the electron-electron scattering rate

$$\begin{aligned}
\frac{\hbar/\tau_e(T)}{E_f} &\approx w^{fb}\frac{\pi}{4}\left(\frac{k_BT}{E_f}\right)^2\left[\ln\left(-\frac{k_BT}{E_f}\right)+\frac{\ln 8}{2}-0.083\right] \\
\Gamma_{ee}(T) &= 2\frac{\hbar}{\tau_e(T)}.
\end{aligned}$$

The latter expression contains a factor of two to account for scattering from both electrons and holes. Figure 3.9 shows these results as a function of temperature at three different r_s (and therefore densities).

Bibliography

[1] K. von Klitzing, G. Dorda, and M. Pepper. New method for high-accuracy determination of the fine-structure constant based on quantized Hall resistance. *Physical Review Letters*, 45:494–497, 1980.

[2] D. C. Tsui, H. L. Stormer, and A. C. Gossard. Two-dimensional magnetotransport in the extreme quantum limit. *Physical Review Letters*, 48:1559–1562, 1982.

[3] R. B. Laughlin. Anomalous quantum Hall-effect – an incompressible quantum fluid with fractionally charged excitations. *Physical Review Letters*, 50:1395–1398, 1983.

[4] J. K. Jain. Composite-fermion approach for the fractional quantum Hall effect. *Physical Review Letters*, 63:199, 1989.

[5] M. P. Lilly, K. B. Cooper, J. P. Eisenstein, L. N. Pfeiffer, and K. W. West. Evidence for an anisotropic state of two-dimensional electrons in high Landau levels. *Physical Review Letters*, 82:394–397, 1999.

[6] B. I. Halperin. Theory of the quantized Hall conductance. *Helvetica Physica Acta*, 56:75–102, 1983.

[7] Y. W. Suen, L. W. Engel, M. B. Santos, M. Shayegan, and D. C. Tsui. Observation of a $\nu = 1/2$ fractional quantum Hall state in a double-layer electron-system. *Physical Review Letters*, 68:1379–1382, 1992.

[8] J. P. Eisenstein, G. S. Boebinger, L. N. Pfeiffer, K. W. West, and S. He. New fractional quantum Hall state in double-layer 2-dimensional electron-systems. *Physical Review Letters*, 68:1383, 1992.

[9] T. Chakraborty and P. Pietilainen. Fractional quantum Hall-effect at half-filled Landau-level in a multiple-layer electron-system. *Physical Review Letters*, 59:2784–2787, 1987.

[10] H. A. Fertig. Energy-spectrum of a layered system in a strong magnetic-field. *Physical Review B*, 40:1087–1095, 1989.

[11] A. H. MacDonald and E. H. Rezayi. Fractional quantum Hall effect in a two-dimensional electron-hole fluid. *Physical Review B*, 42:3224–3227, 1990.

[12] G. S. Boebinger, H. W. Jiang, L. N. Pfeiffer, K. W. West, and S. He. Magnetic-field-driven destruction of quantum Hall states in a double quantum-well. *Physical Review Letters*, 64:1793–1796, 1990.

[13] A. H. MacDonald, P. M. Platzman, and G. S. Boebinger. Collapse of integer Hall gaps in a double-quantum-well system. *Physical Review Letters*, 65:775–778, 1990.

[14] X. G. Wen and A. Zee. Neutral superfluid modes and magnetic monopoles in multilayer quantum Hall systems. *Physical Review Letters*, 69:1811, 1992.

[15] X. G. Wen and A. Zee. Tunneling in double-layered quantum Hall systems. *Physical Review B*, 47:2265, 1993.

[16] Z. F. Ezawa and A. Iwazaki. Quantum Hall liquid, Josephson effect, and hierarchy in a double-layer electron-system. *Physical Review B*, 47:7295–7311, 1993.

[17] L. V. Keldysh and Y. V. Kopaev. Possible instability of semimetallic state toward Coulombic interaction. *Soviet Physics Solid State*, 6:2219, 1965.

[18] S. Q. Murphy, J. P. Eisenstein, G. S. Boebinger, L. N. Pfeiffer, and K. W. West. Many-body integer quantum Hall-effect – evidence for new phase-transitions. *Physical Review Letters*, 72:728–731, 1994.

[19] K. Yang, K. Moon, L. Zheng, A. H. MacDonald, S. M. Girvin, D. Yoshioka, and S. C. Zhang. Quantum ferromagnetism and phase-transitions in double-layer quantum Hall systems. *Physical Review Letters*, 72:732–735, 1994.

[20] I. B. Spielman, J. P. Eisenstein, L. N. Pfeiffer, and K. W. West. Resonantly enhanced tunneling in a double layer quantum Hall ferromagnet. *Physical Review Letters*, 84:5808, 2000.

[21] P. J. Burke, I. B. Spielman, J. P. Eisenstein, L. N. Pfeiffer, and K. W. West. High frequency conductivity of the high-mobility two-dimensional electron gas. *Applied Physics Letters*, 76:645, 2000.

[22] I. B. Spielman, J. P. Eisenstein, L. N. Pfeiffer, and K. W. West. Observation of a linearly dispersing collective mode in a quantum Hall ferromagnet. *Physical Review Letters*, 87:036803, 2001.

[23] K. von Klitzing. The quantized Hall effect. *Reviews of Modern Physics*, 58:519–531, 1986.

[24] R. B. Laughlin, H. L. Stormer, and D. C. Tsui. Nobel lecture: The fractional quantum Hall effect. *Reviews of Modern Physics*, 71:863–895, 1999.

[25] M. Kellogg, J. P. Eisenstein, L. N. Pfeiffer, and K. W. West. Vanishing Hall resistance at high magnetic field in a double layer two-dimensional electron system. *cond-mat/0401521*.

[26] N. W. Ashcroft and N. D. Mermin. *Solid State Physics*. Harcourt Brace College Publishers, 1976.

[27] E. T. Yu, J. O. McCaldin, and T. C. McGill. Band offsets in semiconductor heterojunctions. *Solid State Physics – Advances in research and applications*, 46:1–146, 1992.

[28] O. Madelung and M. Schulz. *Intrinsic properties of Group IV elements and III-V, II-VI and I-VII compounds*. Springer, 1987.

[29] F. Stern and S. Das Sarma. Electron energy levels in GaAs $-$ $\mathrm{Ga_{1-x}Al_xAs}$ heterojunctions. *Physical Review B*, 30:840, 1984.

[30] R. Dingle, H. L. Störmer, A. C. Gossard, and W. Wiegmann. Electron mobilities in modulation-doped semiconductor heterojunction superlattices. *Applied Physics Letters*, 33:665–667, 1978.

[31] B. E. Kane, L. N. Pfeiffer, K. W. West, and C. K. Harnett. Variable-density high-mobility 2-dimensional electron and hole gases in a gated gaas/al$_x$ga$_{1-x}$as heterostructure. *Applied Physics Letters*, 63:2132–2134, 1993.

[32] B. E. Kane, L. N. Pfeiffer, and K. W. West. High-mobility gaas heterostructure field-effect transistor for nanofabrication in which dopant-induced disorder is eliminated. *Applied Physics Letters*, 67:1262–1264, 1995.

[33] Y. W. Suen, J. Jo, M. B. Santos, L. W. Engel, S. W. Hwang, and M. Shayegan. Missing integral quantum Hall-effect in a wide single quantum-well. *Physical Review B*, 44:5947–5950, 1991.

[34] J. P. Eisenstein, L. N. Pfeiffer, and K. W. West. *Appl. Phys. Lett.*, 57:2324, 1990.

[35] T. J. Gramila, J. P. Eisenstein, A. H. MacDonald, L. N. Pfeiffer, and K. W. West. Mutual friction between parallel 2-dimensional electron-systems. *Physical Review Letters*, 66:1216–1219, 1991.

[36] A. Cho. Film deposition by molecular beam techniques. *Journal Vacuum Science Technology*, 8:S31–S38, 1971.

[37] A. Cho and J. Arthur. Molecular beam epitaxy. *Prog. Solid-State Chem.*, 10:157–192, 1975.

[38] T. Ando, A. B. Fowler, and F. Stern. Electronic-properties of two-dimensional systems. *Reviews of Modern Physics*, 54:437–672, 1982.

[39] J. P. Eisenstein, K. B. Cooper, L. N. Pfeiffer, and K. W. West. Insulating and fractional quantum Hall states in the first excited Landau level. *Physical Review Letters*, 88:076801, 2002.

[40] L. J. van der Pauw. *Philips Res. Rep.*, 13:1, 1958.

[41] F. Stern. Polarizability of a 2-dimensional electron gas. *Physical Review Letters*, 18:546, 1967.

[42] A. Eguiluz, T. K. Lee, and J. J. Quin. *Physical Review B*, 11:4989, 1975.

[43] S. Das Sarma and A. Madhukar. *Physical Review B*, 23:805–815, 1981.

[44] R. G. Mani and J. R. Anderson. Study of the single-particle and transport lifetimes in gaas/al$_x$ga$_{1-x}$as. *Physical Review B*, 37:4299–4302, 1988.

[45] A. H. MacDonald. *Introduction to the physics of the quantum Hall regime.* Elsevier Schence B.V., 1995.

[46] M. Buttiker. Symmetry of electrical conduction. *IBM Journal of Research and Development*, 32:317–334, 1988.

[47] S. Datta. *Electronic transport in mesoscopic systems.* Cambridge university press, 1995.

[48] S. Q. Murphy, J. P. Eisenstein, L. N. Pfeiffer, and K. W. West. Lifetime of 2-dimensional measured by tunneling spectroscopy. *Physical Review Letters*, 52:14825, 1995.

[49] C. Hodges, H. Smith, and J. W. Wilkins. *Physical Review B*, 4:302, 1971.

[50] G.F. Giuliani and J.J. Quinn. *Physical Review B*, 26:4421, 1982.

[51] T. Jungwirth and A. H. MacDonald. Electron-electron interactions and two-dimensional-two-dimensional tunneling. *Physical Review B*, 53:7403–7412, 1996.

[52] L. Zheng and S. Das Sarma. *Physical Review B*, 53:9964, 1996.

[53] H. Smith and H. Hojgaard Jensen. *Transport Phenomena*. Oxford University Press, Walton Street, Oxford OX2 6DP, 1989.

[54] R. Jalabert and S. Das Sarma. *Physical Review B*, 40:9723, 1989.

[55] L. Zheng and A. H. MacDonald. Tunneling conductance between parallel two-dimensional electron systems. *Physical Review B*, 47:10619–10624, 1993.

[56] X. Ying, S. R. Parihar, H. C. Manoharan, and M. Shayegan. *Physical Review B*, 52:R11 611, 1995.

[57] J. M. Blatt. *J. Comp. Phys.*, 1:382, 1967.

[58] J. P. Eisenstein, L. N. Pfeiffer, and K. W. West. Coulomb barrier to tunneling between parallel two-dimensional electron systems. *Physical Review Letters*, 69:3804, 1992.

[59] J. P. Eisenstein, L. N. Pfeiffer, and K. W. West. Evidence for an interlayer exciton in tunneling between two-dimensional electron systems. *Physical Review Letters*, 74:1419, 1995.

[60] P. D. Ye, L. W. Engel, D. C. Tsui, R. M. Lewis, L. N. Pfeiffer, and K. W. West. Correlation lengths of the Wigner-crystal order in a two-dimensional electron system at high magnetic fields. *Physical Review Letters*, 89:176802, 2002.

[61] R. Cote and A. H. MacDonald. *Physical Review Letters*, 65:2662, 1990.

[62] S. A. Trugman and S. Kivelson. *Physical Review B*, 31:5280, 1985.

[63] S. Das Sarma and A. Pinczuk, editors. *Perspectives in Quantum Hall Effects: Novel Quantum Liquids in Low-Dimensional Semiconductor Structures*. Wiley-Interscience, 10475 Crosspoint Blvd., Indianapolis, IN 46256, 1996.

[64] O. Heinonen, editor. *Composite Fermions*. World Scientific, 1998.

[65] J. P. Eisenstein, L. N. Pfeiffer, and K. W. West. *Surf. Sci.*, 305:393, 1994.

[66] K. M. Brown, N. Turner, J. T. Nicholls, E. H. Linfield, M. Pepper, D. A. Ritchie, and G. A. C. Jones. Tunneling between 2-dimensional electron gases in a strong magnetic-field. *Physical Review B*, 50:15465–15468, 1994.

[67] Y. N. Joglekar and A. H. MacDonald. *Physical Review B*, 65:235319, 2003.

[68] J. Schliemann, S. M. Girvin, and A. H. MacDonald. Strong correlation to weak correlation phase transition in bilayer quantum Hall systems. *Physical Review Letters*, 86:1849–1852, 2001.

[69] K. Moon, H. Mori, K. Yang, S. M. Girvin, A. H. MacDonald, L. Zheng, D. Yoshioka, and S. C. Zhang. Spontaneous interlayer coherence in double-layer quantum Hall systems – charged vortices and Kosterlitz-Thouless phase-transitions. *Physical Review B*, 51:5138–5170, 1995.

[70] K. Yang, K. Moon, L. Belkhir, H. Mori, S. M. Girvin, A. H. MacDonald, L. Zheng, and D. Yoshioka. Spontaneous interlayer coherence in double-layer quantum Hall systems: Symmetry-breaking interactions, in-plane fields, and phase solitons. *Physical Review B*, 54:11644–11658, 1996.

[71] A. Stern, S. Das Sarma, M. P. A. Fisher, and S. M. Girvin. Dissipationless transport in low-density bilayer systems. *Physical Review Letters*, 84:139–142, 2000.

[72] A. H. MacDonald. Private communication.

[73] A. Steinbach, P. Joyez, A. Cottet, D. Esteve, M. H. Devoret, M. E. Huber, and J. M. Martinis. Direct measurement of the Josephson supercurrent in an ultrasmall Josephson junction. *Physical Review Letters*, 87:137003, 2001.

[74] Yu. M. Ivanchenko and L. A. Zil'berman. *Sov. Phys. JETP*, 28:1272, 1969.

[75] V. Ambegaokar and B. I. Halperin. *Physical Review Letters*, 22:1364, 1969.

[76] J. B. Ketterson and S. N. Song. *Superconductivity.* Cambridge university press, 1999.

[77] A. Frydman, O. Naaman, and R. C. Dynes. Universal transport in two-dimensional granular systems. *Physical Review B*, 66:052509, 2002.

[78] D. J. Scalapino. Pair tunneling as a probe of fluctuations in superconductors. *Physical Review Letters*, 24:1052, 1970.

[79] J. Smoliner, W. Demmerle, G. Berthold, E. Gornik, and G. Weimann. Momentum conservation in tunneling processes between barrier-separated 2d-electron-gas systems. *Physical Review Letters*, 63:2116–2119, 1989.

[80] J. P. Eisenstein, T. J. Gramila, L. N. Pfeiffer, and K. W. West. Probing a 2-dimensional Fermi-surface by tunneling. *Physical Review B*, 44:6511–6514, 1991.

[81] M. M. Fogler and F. Wilczek. Josephson effect without superconductivity: Realization in quantum Hall bilayers. *Physical Review Letters*, 86:1833–1836, 2001.

[82] R. E. Eck, D. J. Scalapino, and B. N. Taylor. Investigation of microwave radiation emitted by Josephson junctions. *Physical Review Letters*, 13:15, 1964.

[83] A. H. MacDonald A. Stern, S. M. Girvin and N. Ma. Theory of interlayer tunneling in bilayer quantum Hall ferromagnets. *Physical Review Letters*, 86:1829–1832, 2001.

[84] L. Balents and L. Radzihovsky. Interlayer tunneling in double-layer quantum Hall pseudoferromagnets. *Physical Review Letters*, 86:1825–1828, 2001.

[85] Z. Q. Wang. *cond-mat/0306553*, 2003.

[86] A. Sawada, Z. F. Ezawa, H. Ohno, Y. Horikoshi, Y. Ohno, S. Kishimoto, F. Matsukura, M. Yasumoto, and A. urayama. Phase transition in the $\nu = 2$ bilayer quantum Hall state. *Physical Review Letters*, 80:4534, 1998.

[87] A. Sawada, D. Terasawa, N. Kumada, M. Morino, K. Tagashira, Z. F. Ezawa, K. Muraki, T. Saku, and Y. Hirayama. Continuous transformation from spin- to pseudospin-type excitation. *Physica E*, 18:118–119, 2003.

[88] E. Tutuc, S. Melinte, E. P. De Poortere, R. Pillarisetty, and M. Shayegan. Role of density imbalance in an interacting bilayer hole system. *Physical Review Letters*, 91:076802, 2003.

[89] J. P. Eisenstein. Private communication.

[90] M. Kellogg, I. B. Spielman, J. P. Eisenstein, L. N. Pfeiffer, and K. W. West. Observation of quantized Hall drag in a strongly correlated bilayer electron system. *Physical Review Letters*, 88:126804, 2002.

[91] M. Kellogg, J. P. Eisenstein, L. N. Pfeiffer, and K. W. West. *Physical Review Letters*, 90:246801, 2003.

[92] L. N. Pfeiffer. Private communication. 2004.

[93] Paul H. Holloway and Gary E. McGuire. *Handbook of compound semiconductors: growth, processing, characterization, and devices.* Noyes Publications, Park Ridge, N.J., 1995.

[94] Ralph E. Williams. *Gallium arsenide processing techniques.* Artech House, Dedham, Mass., 1984.

[95] S. Adachi and K. Oe. *Journal of the Electrochemical Society: Solid-State Science and Technology*, 130:2427, 1983.

[96] Small Parts Inc.; 13980 N.W. 58th Court; P.O. Box 4650; Miami Lakes, FL; 33014-0650; 1-800-220-4242; http://www.smallparts.com.

[97] UniFit; 260-E Main Street; Redwood City, CA 94063; 650-363-2000; http://www.unifit.com.

[98] HD MicroSystems, LLC; PO Box 80010; Wilmington, DE 19880; 1-800-346-5656; http://www.hdmicrosystems.com.

[99] Jong-Hee Kim, Dae Ho Lim, and Gye Mo Yang. *Journal Of Vacuum Science Technology B*, 16:558, 1998.

[100] M. V. Weckwerth, J. A. Simmons, N. E. Harff, M. E. Sherwin, M. A. Blount, W. E. Baca, and H. C. Chui. *Superlattices and Microstructures*, 20:561, 1996.

[101] Sycon instruments stm-100/mf thickness/rate monitor manual, 1997.

[102] R. D. Mathis Company; 2840 Gundry Ave.; Signal Hill, CA 90755; 1-562-426-7049.

[103] Alfa Aesar; 30 Bond Street; Ward Hill, MA 01835; 1-800-343-0660; http://www.alfa.com/.

[104] F. Reif. *Statistical and Thermal Physics.* McGraw-Hill, New York, 1965.

[105] F. Pobell. *Matter and Methods and Low Temperatures.* Springer-Verlag, Berlin, 1995.

[106] McMaster Carr; P.O. Box 54960; Los Angeles, CA 90054-0960; 1-562-692-5911; http://www.McMaster.com.

[107] California Fine Wire Company; P.O. Box 446; Grover Beach, CA 93483-0446; 1-805-489-5144; http://www.calfinewire.com.

[108] Cooner Wire Company; 9265 Owensmouth Ave.; Chatsworth, CA 91311; 1-818-882-8311; http://www.coonerwire.com.

[109] Mouser Electronics; 1000 North Main Street; Mansfield, TX 76063-1514; 1-800-346-6873; http://www.mouser.com.

[110] Nanoway Oy; Ylistonmaentie 26; FIN-40500 Jyvaskyla, Finland; +358-14-445 1500; cool@nanoway.fi; http://www.nanoway.fi.

[111] ESPI; 1050 Benson Way; Ashland, OR 97520; 1-800-638-2581; http://www.espi-metals.com.

[112] SurePure Chemetals; 5-W Nottingham Drive; Florham Park, NJ 07932; 1-888-377-3211; http://www.surepure.com/.

[113] A. C. Ehrlich. Oxygen annealing of silver for obtaining low electrical-resistivity – technique and interpretation. *Journal of Materials Science*, 9:1064–1072, 1974.

[114] J. M. Martinis, M. H. Devoret, and John Clarke. *Physical Review B*, 35:4682, 1987.

[115] A. Fukushima, A. Sato, A. Iwasa, Y. Nakamura, T. Komatsuzaki, and Y. Sakamoto. Attenuation of microwave filters for single-electron tunneling experiments. *IEEE Trans. Inst. and Meas.*, 48:289, 1997.

[116] D. Gunnarsson Bladh K, E. Hurfeld, S. Devi, C. Kristoffersson, B. Smalander, and S. Pehrson. Comparison of cryogenic filters for use in single electronics experiments. *Reviews of Scientific Instruments*, 73:1323, 2003.

[117] D. Vion, P. F. Orfila, P. Joyez, D. Esteve, and M. H. Devoret. *J. Appl. Phys.*, 77:2519, 1995.

[118] H. Courtois, O. Buisson, J. Chaussy, and B. Pannetier. *Reviews of Scientific Instruments*, 66:3465, 1995.

[119] A. B. Zorin. *Reviews of Scientific Instruments*, 66:4296, 1995.

[120] J. R. Wait and K. P. Spies. *Geophysics*, 34:789, 1969.

[121] M. Barucci, G. Bianchini, E. Gottardi, I. Peroni, and G. Ventura. *Cryogenics*, 39:963, 1999.

[122] C. Hagmann and P. L. Richards. *Cryogenics*, 35:345, 1995.

[123] K. Schwabb. Private communication, 2001.